Studying the conduction mechanism of stabilised zirconias by means of molecular dynamics simulations

Dario Marrocchelli

PhD in Chemistry

The University of Edinburgh

2009-2010

Declaration

I hereby declare that this thesis is of my own composition, and that it contains no material previously submitted for the award of any other degree. The work reported in this thesis has been executed by myself, except where due acknowledgement is made in the text.

Dario Marrocchelli

Abstract

Stabilised zirconias have a remarkable variety of technological and commercial applications, e.g., thermal barrier coatings, gas sensors, solid oxide fuel cells, ceramic knives and even fashion jewelry. This amazing versatility seems to originate from the creation of atomic defects (oxide ion vacancies) in the zirconia crystal. Indeed, these vacancies, and their interactions with other vacancies or cations, dramatically affect the structural, thermal, mechanical and electrical properties of zirconia. This thesis is concerned with the study of the role of the vacancy interactions on the conducting properties of these materials. This study was performed by using realistic, first-principles based molecular dynamics simulations.

The first system studied in this thesis is $Zr_{0.5-0.5x}Y_{0.5+0.25x}Nb_{0.25x}O_7$. This has a fixed number of vacancies across the series but its conductivity changes by almost two orders of magnitude as a function of x. For this reason, $Zr_{0.5-0.5x}Y_{0.5+0.25x}Nb_{0.25x}O_7$ represents an ideal test-bed for the role of the cation species on the defect interactions and therefore on the ionic conductivity of these materials. Realistic inter-atomic potentials for $Zr_{0.5-0.5x}Y_{0.5+0.25x}Nb_{0.25x}O_7$ were developed on a purely first-principles basis. The observed trends of decreasing conductivity and increasing disorder with increasing Nb^{5+} content were successfully reproduced. These trends were traced to the influences of the cation charges and relative sizes and their effect on vacancy ordering by carrying out additional calculations in which, for instance, the charges of the cations were equalised. The effects of cation ordering were considered as well and their influence on the conductivity understood.

The second part of this thesis deals with Sc_2O_3–doped (ScSZ) and Y_2O_3–doped (YSZ) zirconias. These systems are of great academic and technological interest as they find use in solid oxide fuel cells. Inter-atomic potentials were parametrised and used to predict the structural and conducting properties of these materials, which were found to agree very well with the experimental evidence. The simulations were then used to study the role of the vacancy interactions on the conducting properties of these materials. Two factors were found to influence the ionic conductivity in these materials: cation-vacancy and vacancy-vacancy interactions. The former is responsible for the difference in conductivity observed between YSZ and ScSZ. Vacancies, in fact, prefer to bind to the smaller Zr^{4+} ions in YSZ whereas there is not a strong preference in the case of ScSZ, since the cations have similar sizes in this case. This effect is observed at temperatures as high as T = 1500 K. Finally, it was found that vacancies tend to order so that they can minimise their mutual interaction and that this ordering tendency is what ultimately is responsible for the observed anomalous decrease of the ionic conductivity with increasing dopant concentration. The consequences of such a behaviour are discussed.

Dedicata a nonno Marcello,
con affetto,
Dario

Acknowledgements

First of all, I would like to thank my PhD supervisor, Paul Madden for his guidance and patience. In the past three years and a half, he has thought me a lot on computer simulations and he has given me a great combination of advice and supervision whilst at the same time allowing me enough freedom and independence to grow up as a scientist. He has also tolerated some of the originalities of my personality, my constant moaning about British weather and my bad jokes in my presentations.

I would also like to thank my collaborators and unofficial supervisors from ISIS, Stefan Norberg and Stephen Hull. Thanks for introducing me to the wonders of neutron scattering, RMC and much more and for the nice time we had at the Pack Horse and in Toronto.

Another person who has done a lot for me is Mathieu Salanne, at the University of Paris VI. Thanks very much for hosting me for the past two summers and allowing me to escape from the miserable weather in Scotland. Apart from the obvious meteorological benefits, my visits to Paris were incredibly stimulating and successful as well as very pleasant.

There is also a huge number of people here in Edinburgh who have been extremely helpful. A special thanks goes to my "fake" supervisors, Philip and Carole, who made my stay in Edinburgh comfortable and bureaucracy free. Another thanks goes to my office mates (too many to name them here) who made the past years very pleasant, thanks to stimulating conversations, funny lunches and nice outings.

Another thanks goes to my parents and my family who, though far away, made me always feel loved and supported. The same goes with my friends back in Italy and those spread around the world.

Finally, last but not least, I would like to thank Elena, my future wife, for all the support she has given me in the past years. She was incredibly helpful all the time and has made my PhD studies much easier and enjoyable than they would have been otherwise. I hope in the future I will be as helpful and supportive as she has been so far.

Contents

List of Figures

List of Tables

Chapter 1

Introduction

Ionic compounds normally form insulating solids on account of the closed-shell electron configurations which prevent delocalisation of electrons. However, when in the liquid phase, charge can be transported, in these materials, by the motion of the ions. Some ionic solids, however, demonstrate an *intermediate* behaviour, in which one of the ionic species is very mobile [1]. This phenomenon is termed "superionicity" or "fast-ion conduction". Such compounds exhibit liquid-like conductivities whilst still in the solid state and at temperatures well below their melting points. For this unusual property, these materials are industrially important in batteries, gas sensors and solid oxide fuel cells, *inter alia*.

Of this family of materials, stabilised zirconias are amongst the most attractive ones. Zirconias, in fact, have a remarkable variety of technological and commercial applications, e.g., thermal barrier coatings, gas sensors, solid oxide fuel cells, ceramic knives and even fashion jewelry [2, 3, 4, 5, 6]. This amazing versatility seems to originate from the creation of atomic defects (oxide ion vacancies) in the zirconia crystal. Indeed, these vacancies, and their interactions with other vacancies or cations, dramatically affect the structural, thermal, mechanical and, most importantly, the electrical properties of zirconia. In chapter 2 all the previous experimental and computational studies performed on these materials in the past two decades are reviewed and summarised. The picture that emerges from this review is that, despite the overwhelming importance that defects have on the ionic conduction and other microscopic properties of zirconia ceramics (and related materials), there is currently no ZrO_2-based oxide system where the origin and strength of defect interactions are well understood. Weak scattering contrast and other experimental difficulties [7, 1] together with the computational demands of sufficiently accurate theoretical modeling [8] have both contributed to this situation.

For this reason, a few years ago, a new research project was started. This was a joint collaboration between Prof. Paul Madden at the University of Edinburgh and Dr Stephen Hull at the ISIS Facility, Rutherford Appleton Laboratories. The main goal of this project was to combine advanced experimental techniques (neutron scattering experiments with Reverse Monte Carlo analysis and impedance spectroscopy) with realistic, first-principles based computer simulations, in order to achieve a better understanding of the defect interactions in oxide ionic conductors. This thesis is concerned with the computational work on stabilised zirconias which resulted from this project.

Computer simulation techniques are a growing and exciting field of modern science and have made important contributions towards a better understanding of the conduction mechanism of these materials [1]. The holy grail of computer simulations is the ability to predict a material's structural and dynamical behavior under a wide range of physical conditions. To achieve this, realistic models of the interactions of these materials are required. The introduction of the Car-Parrinello (C-P) method [9], some 25 years ago, permits the modeling of materials without the need for explicit interatomic interaction potentials. The C-P method is, however, computationally expensive, particularly for systems whose accurate modeling requires the explicit representation of a large number of valence electrons. The study of stabilised zirconias, for instance, requires big simulation cells (up to many thousands of ions) and long simulations ($\sim$ 10 ns) and therefore lies outside the range of direct ab initio simulation techniques. For this reason, the introduction of an interaction potential remains a necessary step for the investigation of many finite temperature phenomena, such as ionic conduction. Such potentials will additionally embody some chemical insight (like, for example, information on the size of a certain cation) and therefore allow a rather direct way of accounting for the differences in behavior of chemically related substances, as will be shown in this work.

In this thesis, some of the progress made through the introduction of interaction potentials in the study of ionic conductors is described. At a fundamental level, ionic systems are of interest in that they are at the limit of where one might expect a description of a material based upon non-bonding interactions between closed-shell species to be appropriate. Although the ions have closed-shell electronic structures, they interact very strongly in the condensed phase, with the properties of the ions themselves being very sensitive to changes in their local environment. These environmental effects have been closely studied using ab initio quantum chemistry techniques [10, 11, 12] and much has been learned about the way in which ions respond to changes in their surroundings. By refining these potentials to deal with such effects [13], useful lessons have been learnt for the construction of interaction models for molten salts

[14, 15, 16, 17], and more recently, for some oxide systems as well [18, 19, 20]. These environmental effects and their relative importance together with the simulation and data analysis techniques used throughout this thesis are described in chapter 3.

$Zr_{0.5-0.5x}Y_{0.5+0.25x}Nb_{0.25x}O_7$ is the first system discussed in this thesis. This material has a fixed number of vacancies across the series but its conductivity changes by almost two orders of magnitude as a function of x [21]. At the same time, the local structure of these materials, as evinced from electron and neutron diffuse scattering experiments, changes quite significantly from one material to the other [21, 22]. Y_3NbO_7 (x = 1), for instance, is the one with the lowest conductivity across the series and with the most disordered structure, whereas $Zr_2Y_2O_7$ (x = 0) has the highest conductivity and the most ordered structure. For these reasons, $Zr_{0.5-0.5x}Y_{0.5+0.25x}Nb_{0.25x}O_7$, though not an ideal candidate for some of the above-mentioned technological applications, represents a perfect test-bed for the role of the cation species on the defect interactions and therefore on the conducting and structural properties of these materials. In chapter 4, the parameterisation, on a purely first-principles basis, of realistic inter-atomic potentials for $Zr_{0.5-0.5x}Y_{0.5+0.25x}Nb_{0.25x}O_7$ is described and these potentials are then validated against a series of experimental data both on the structural and conducting properties of this system. In the next chapter these potentials are used to study the effects different cations have on the vacancy behaviour and how these effects are responsible for the observed differences in the conducting and structural properties of $Zr_{0.5-0.5x}Y_{0.5+0.25x}Nb_{0.25x}O_7$.

The second half of this thesis is dedicated to the study of Sc_2O_3–doped (ScSZ) and Y_2O_3–doped (YSZ) zirconias. These materials show very high ionic conductivity coupled with good mechanical properties and, in the case of YSZ, they are also cheap. For these reasons, these systems are of great academic and technological interest as they find use, primarily, in solid oxide fuel cells. A solid oxide fuel cell is an electrochemical conversion device that produces electricity directly from oxidizing a fuel, usually hydrocarbons. Advantages of this class of fuel cells include high efficiencies, long term stability, fuel flexibility, low emissions, and cost. The largest disadvantage is the high operating temperature (750 - 1000 C$^\circ$) which results in longer start up times and mechanical/chemical compatibility issues [5]. This problem could be solved by lowering the fuel cell operating temperature by $\sim$ 200 K, the so-called Intermediate Temperature-Solid Oxide Fuel Cell (IT-SOFC), but this would require solid electrolytes with higher ionic conductivities than the ones presently used [5]. For this reason, a significant research effort has been made in the past years to understand the conduction mechanism in these materials and to devise new, more conducting systems which would meet the requirements for IT-SOFCs.

When ZrO_2 is doped with aliovalent cations, such as Y^{3+} and Sc^{3+}, these locate substitutionally on the Zr^{4+} sites and consequently a fraction of the oxygen sites become empty to retain overall charge neutrality. These oxide vacancies are responsible for the very high values of the ionic conductivity observed in these materials. However, their conductivity does not increase indefinitely as a function of the dopant concentration but peaks at a concentration of approximately 8 - 13% [23]. Also, it is found that the ionic conductivity of these materials depends strongly on the dopant cation species [23]. To date, the reasons why this happens are not well understood. Such an understanding is however of great importance as this might point towards new directions to further optimise these materials and increase their conductivity. In chapter 6 the parameterisation of realistic potentials for Y_2O_3 - ZrO_2 - Sc_2O_3 mixtures is described and these are then validated by reproducing the large amount of experimental data (single crystal and powder neutron scattering [7, 24], impedance spectroscopy [25, 26, 23, 24] and quasielastic neutron scattering experiments [7]) available for these materials. Chapter 7 then focuses on the conduction mechanism of these materials and on the role that vacancy interactions have on the conductivity. Two phenomena, which are thought to influence the conductivity of these materials, are considered: the way a vacancy interacts with a cation [27, 23] and the way a vacancy interacts with another vacancy [7, 8, 28]. Their influence on the conducting properties of these materials and their relative importance are studied.

Finally, in the appendix of this thesis, two papers are reported, which concern with the high pressure and temperature behaviour of amorphous and liquid GeO_2. These papers were produced by the author of this thesis during his PhD and are methodologically related to the work described here. However the scientific issues which are to be resolved in dealing with the properties of GeO_2 are very different, and therefore a different set of properties were examined. For this reason, it was felt that incorporating these papers into the main body of this thesis would distract the reader from the major issue, ionic conductivity, and also significantly increase the length of this work.

Chapter 2

Ionic conductors

Ionic conductors are compounds that exhibit exceptionally high values of ionic conductivity within the solid state. Indeed, their conductivities often reach values of the order of 1 Ω^{-1} cm^{-1} (for T $>$ 1000 K), which are comparable to those observed in the molten state [1]. For this property ionic conductors find use in a wealth of technological applications such as gas sensors [2], Solid Oxide Fuel Cells (SOFCs) [4, 5] and lithium batteries [29], *inter alia*.

Understanding the causes of this very high conductivity, and the factors which affect it, has provided one of the major challenges in the field of condensed matter science [1]. For this reason many different techniques (neutron scattering, electron diffraction, impedance spectroscopy, NMR, computer simulations, *etc.*) have been used to try to elucidate the conduction mechanism in these materials. Although a clearer picture of this phenomenon has emerged in the past decades, there are still some open questions [1].

Oxide-ion conductors are, as the name itself suggests, ionic conductors in which the mobile species is the oxide ion. These materials have received much attention in the past years because of their use in SOFCs. Yttria stabilised zirconia $(Y_2O_3)_x$–$(ZrO_2)_{1-x}$ (with $x \sim 0.08$) is, for instance, the current choice for the electrolyte in SOFCs. In the next section an overview of the properties of some oxide-ion conductors will be provided. Firstly the available literature on stabilised zirconias will be summarised, since these are the main focus of this thesis. This will then be followed by a short overview of the properties of some of the other oxide ion conductors, such as doped CeO_2 and lanthanum gallates. Finally, at the end of this chapter, the working principles of a solid oxide fuel cell, its advantages over conventional power generation systems and the current challenges will be described.

2.1 Oxide-ion conductors

Cubic, fluorite-structured, binary compounds of stoichiometry AO_2 are of interest as oxide-ion conductors, especially when some of the host cations are replaced by species of a lower valence to produce anion-deficient phases like $A^{4+}_{1-y}B^{3+}_{y}O_{2-y/2}$. These compounds have charge compensating vacancies which allow the remaining anions to move more rapidly throughout the crystal and this leads to impressive values of the ionic conductivity ($\sigma > 0.1\ \Omega^{-1}$, at T = 1500 K) as observed in M_2O_3-doped ZrO_2 (M = Sc or Y) and M_2O_3-doped CeO_2 (M = Y or Gd).

At the simplest level the ionic conductivity would be expected to increase with the number of vacancies, but this is not the case. For example, in $Zr^{4+}_{1-y}Y^{3+}_{y}O_{2-y/2}$ the conductivity decreases with increasing y for $y > 0.16$ and, furthermore, for a given y, the value of the conductivity depends on the identity of the dopant cation. For example, $Zr^{4+}_{1-y}Sc^{3+}_{y}O_{2-y/2}$ is a better conductor than $Zr^{4+}_{1-y}Y^{3+}_{y}O_{2-y/2}$. These effects are due to the reduced mobility associated with the ordering of the vacancies, which may be influenced by vacancy-vacancy, vacancy-cation and cation-cation interactions.

2.1.1 Stabilised zirconias

The Zr^{4+} ion, in ZrO_2, because of its small ionic radius, prefers a seven-fold coordination. For this reason, pure zirconia, ZrO_2, adopts the monoclinic baddelyite structure [M-ZrO_2, space group $P2_1$ /c [30]] under ambient conditions, with the Zr^{4+} in a distorted seven-fold coordination. However, on increasing the temperature, ZrO_2 transforms to a tetragonally distorted fluorite structure [T-ZrO_2, $P4_2$ /nmc [31]] at T = 1370 K, with Zr^{4+} surrounded by eight anions, but with two slightly different Zr^{4+} – O^{2-} distances. Perfect eightfold coordination is achieved at T = 2643 K with a transformation to a cubic fluorite structured phase [F-ZrO_2, $Fm\bar{3}m$ [30], followed by melting at T = 2988 K. The fluorite structure involves a face-centred cubic arrangement of cations. As can be seen in figure 2.1, these cations form tetrahedral and octahedral holes. In an ideal fluorite structure, the anions occupy all the tetrahedral sites and leave empty the octahedral ones. This structure is therefore quite open and this facilitates ionic mobility. It therefore comes as no surprise that most of the best ionic conductors possess this kind of structure.

Pure ZrO_2 is not a good ionic conductor. However, when divalent (Ca^{2+}, Mg^{2+}) and/or trivalent (Gd^{3+}, Y^{3+}, Yb^{3+}, Sc^{3+}) cations are added to this material, these locate substitution-

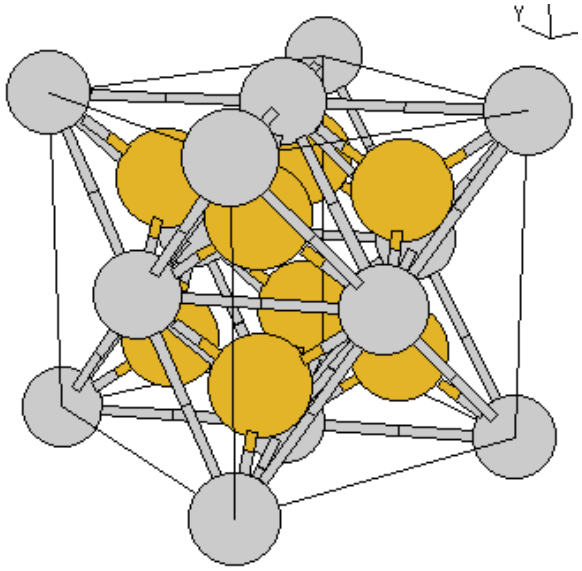

Figure 2.1: *The cubic fluorite structure for a compound of stoichiometry AO_2. Grey spheres are the cations, whilst the yellow ones are the anions.*

ally on the Zr^{4+} sites and consequently a fraction of the oxygen sites becomes empty to retain overall charge neutrality. The effect of this doping is twofold. On one hand, doping ZrO_2 with bigger cations stabilises the fluorite phase at lower temperatures and for this reason these materials are usually dubbed "stabilised zirconias". On the other hand, the introduction of oxygen vacancies increases the mobility of the remaining anions and leads to exceptional values of the ionic conductivity [32, 25, 26, 23].

The dissolution of a trivalent cation into the fluorite phase of ZrO_2 can be expressed by the following equation in Kröger-Vink notation:

$$Y_2O_3(ZrO_2) \rightarrow 2Y'_{Zr} + 3O^x_O + V^{\cdot\cdot}_O \tag{2.1}$$

The addition of two trivalent dopant cations creates one vacancy. The vacancy concentration is given by the electro-neutrality condition ($2[Y'] = [V^{\cdot\cdot}_O]$), implying that the vacancy concentration is linearly dependent on the dopant level. The ionic conductivity can be expressed by [33]

$$\sigma = en\mu, \tag{2.2}$$

where n is the number of mobile vacancies, μ their mobility and e their charge. In the case of oxide ion conductors and assuming *uncorrelated* motion of the vacancies, equation 2.2 can be

re-expressed as

$$\sigma = A/T[V_O^{\cdot\cdot}](1 - [V_O^{\cdot\cdot}])e^{-E/k_BT}, \tag{2.3}$$

where E is the activation energy, k_B is the Boltmann constant, T the temperature in Kelvin and A a pre-exponential factor. This equation shows a maximum for a vacancy concentration $[V_O^{\cdot\cdot}] = 0.5$, although in reality, the maximum in conductivity in these materials occurs at much lower vacancy [1] (dopant) concentration as can be seen in figure 2.2 for M_2O_3-ZrO_2 (M = Sc, Yb, Y, Dy, Gd or Eu).

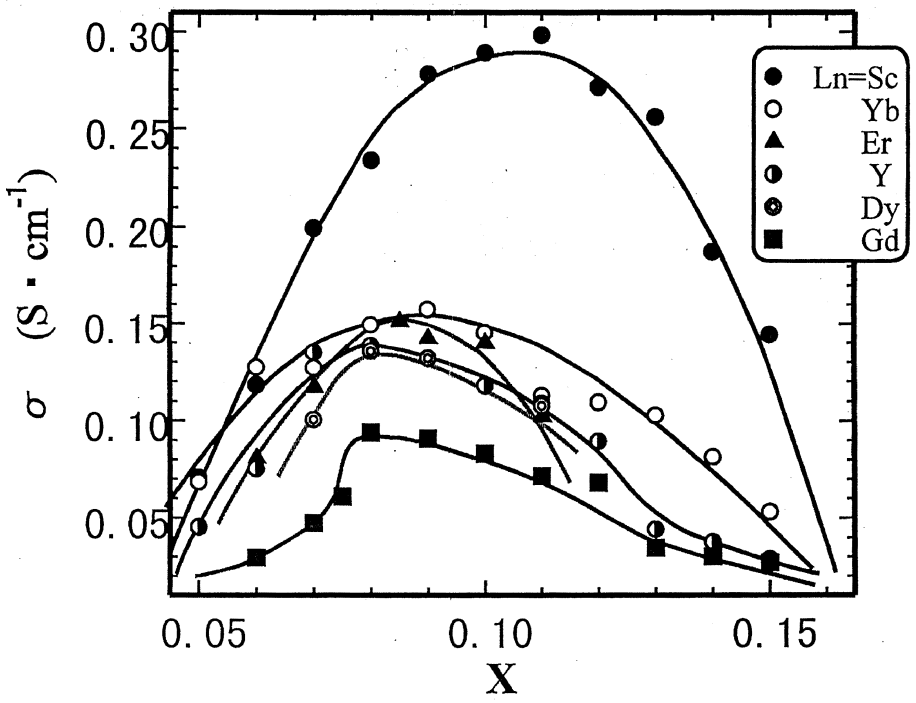

Figure 2.2: *The variation of the ionic conductivity, σ, of $(ZrO_2)_{1-x}$ - $(M_2O_3)_x$ (M = Sc, Yb, Y, Dy, Gd or Eu) vs dopant concentration, x, [23] at 1273 K.*

Yttria-stabilised zirconia (YSZ) has a peak at $[V_O^{\cdot\cdot}] \sim 0.04$. This value is more than *ten* times smaller then expected from equation 2.3. Interestingly, the position of this peak changes according to the dopant species. Scandia-stabilised zirconia (ScSZ) is the material which presents the maximum of the conductivity at the highest dopant content, x = 0.12 (i.e. $[V_O^{\cdot\cdot}] \sim 0.06$). However this value is still about 8 times smaller than expected from equation

[1] When the $(ZrO_2)_{1-x}$ - $(M_2O_3)_x$ formula is used, the vacancy concentration is given by the following expression: $[V_O^{\cdot\cdot}] = \frac{x}{2(1+x)}$. For small dopant concentrations (as in the case of figure 2.2), this equation simplifies to $[V_O^{\cdot\cdot}] \sim x/2$.

2.3. It is also worth noticing that not only the peak position but also the absolute value of the conductivity seems to depend on the dopant species. Once again, ScSZ is the material which presents the best ionic conductivity for a fixed dopant concentration. Also, from figure 2.2, it is clear that YSZ is by no means the best oxide ionic conductor. The reason for its being the current material of choice as an electrolyte in SOFCs is that this material combines a good (though not optimal) ionic conductivity with low electronic conductivity, good mechanical properties, low cost and ease of processing [5].

The nature of the anomalous behaviour of the conductivity observed in figure 2.2, the reasons for its occurrence at such low vacancy concentration and, more generally, the role of the dopant cation species on the conductivity of the materials are still controversial despite being the object of intensive study for the past 20 years. Conductivity measurements point to a relationship between the dopant's radius and the material's conductivity. This can be appreciated in figure 2.3 where the maximum value of the conductivity at 1273 K for a certain dopant versus the dopant's radius is shown. It is clear that the closer the dopant's radius is to that of Zr^{4+}, the higher the conductivity. Quite a similar behaviour is observed for the dopant (vacancy) concentration at which the maximum conductivity is observed vs the dopant radius. This behaviour is usually explained in terms of the elastic strain, which is related to the size mismatch between host and dopant cations. The higher the elastic strain the higher the tendency for vacancies to associate with a certain cation species. Such a tendency is detrimental to the conduction because it will limit the number of mobile vacancies and increase the ion migration enthalpy [23].

There has been a strong debate in the past years as to which cation species vacancies prefer to bind. From a purely electrostatic point of view, vacancies and trivalent dopant cations have a relative charge of +2 and -1 and therefore should attract each other. However, in these materials, elastic interactions result in a repulsion between dopant cations and vacancies [27, 34, 8]. Indeed, in the past two decades, there has been an abundance of contradictory experimental reports (mainly caused by weak scattering contrast and other experimental difficulties) of whether vacancies prefer to bind to dopant [35, 36, 37, 38] or host cations [39, 40, 41, 42]. Recent first-principles simulations seem to have solved the controversy by showing that the repulsive elastic vacancy-dopant interaction prevails over electrostatic attraction and this results in the vacancies binding to the (smaller) host cations [8].

Since vacancies have a relative charge of 2+ and they locally distort the crystal lattice, their distribution throughout the crystal is not random. The best techniques to investigate these ordering tendencies are x-ray, electron and neutron diffraction. Numerous such studies

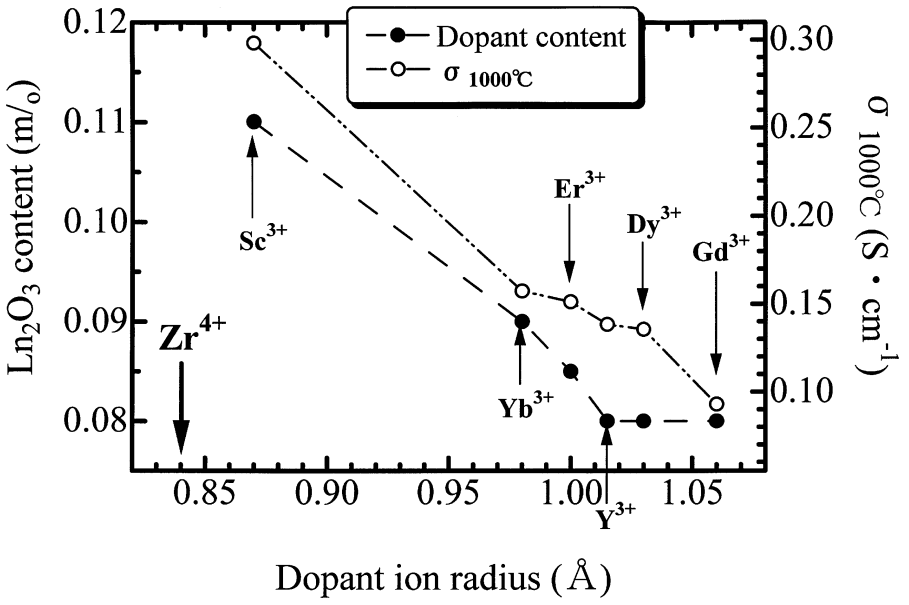

Figure 2.3: *Dopant content at which $(ZrO_2)_{1-x}$ - $(M_2O_3)_x$ presents the maximum in the conductivity vs dopant radius at 1273 K [23]. The maximum conductivity vs dopant radius is reported as well.*

[43, 7, 22, 44, 45, 46] shown that stabilised zirconia systems contain locally ordered regions of vacancies and dopants. The presence of these lattice defects causes extensive relaxation of the ions away from their regular fluorite lattice sites. Goff and co-workers [7] used a combination of neutron and x-ray diffraction data on a single crystal specimen. Some of their neutron data are reported in figure 2.4. The x = 0.10 composition roughly corresponds to the maximum of the conductivity plot for YZO. The figure shows a $\langle 1\bar{1}0 \rangle$ plane in reciprocal space. Sharp intense peaks are seen in the experimental data at the fcc Bragg positions $\langle 002 \rangle$, $\langle 004 \rangle$, $\langle 111 \rangle$, $\langle 113 \rangle$, $\langle 220 \rangle$, $\langle 222 \rangle$, *etc.*. The remainder of the intensity which appears in the pattern is diffuse scattering and is indicative of local structural deformations. At x = 0.10 the most intense diffuse features in the experimental data appear at $\langle 114 \rangle$ and $\langle 112 \rangle$; these are forbidden reflections for the fluorite structure. According to the analysis of Goff *et al.* [7] these peaks are a consequence of local tetragonal distortions of the fluorite structure which occur at relatively low concentrations of Y_2O_3. Recall that in pure ZrO_2, a tetragonal phase is more stable than the cubic one and that Y_2O_3 is added to stabilise the latter. At low Y_2O_3 concentrations local tetragonal distortions with random orientation occur even within a single crystal. The set of data also show a broad, weak feature at $\mathbf{q} = \langle 1.7, 1.7, 1 \rangle$ which is associated with a pattern of lattice deformation about isolated vacancies [7].

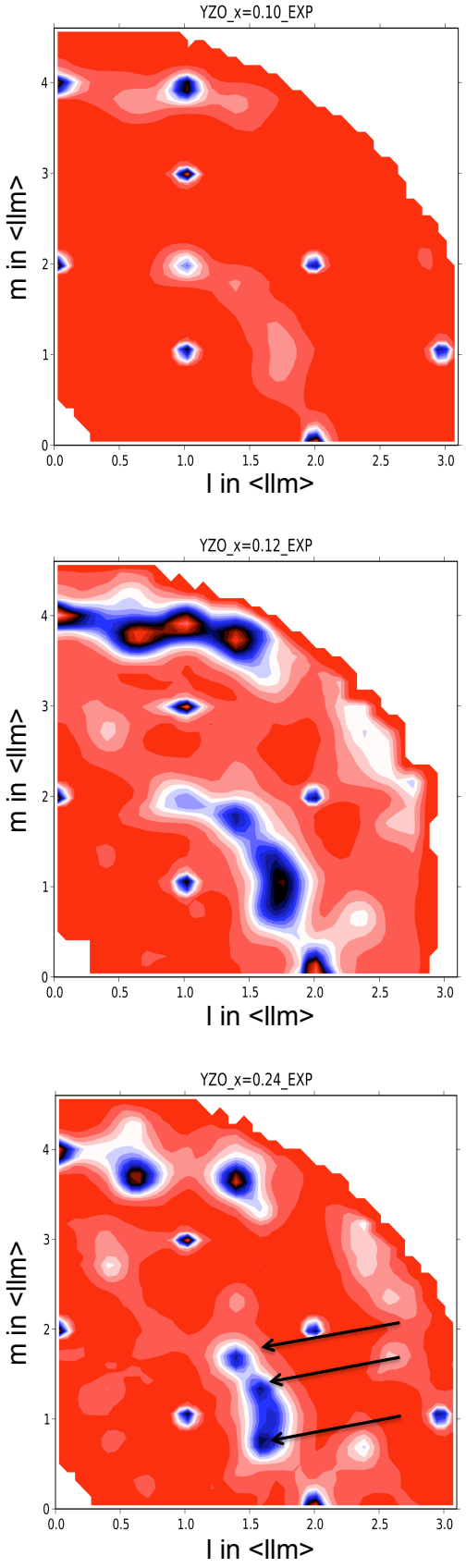

Figure 2.4: *Neutron diffraction patterns, at room temperature, for 10% (top), 12% (middle) and 24% (bottom) YSZ.*

As the Y_2O_3 concentration is increased to x = 0.12 and x = 0.24, the $\langle 114 \rangle$ and $\langle 112 \rangle$ features disappear and the diffuse scattering becomes dominated by new features (highlighted by arrows in figure 2.4) which may be described as belonging to a superlattice at $\mathbf{G} \pm \langle 0.4, 0.4, \pm 0.8 \rangle$, where $\mathbf{G}$ is an fcc Bragg peak position [7]. This pattern was interpreted as caused by the lattice deformations around pairs of vacancies aligned along the $\langle 111 \rangle$ which are themselves ordered along the $\langle 112 \rangle$ direction. This structure is consistent with the most stable arrangement of vacancy pairs found by Bogicevic [8] in his analysis of vacancy-ordering tendencies in YZO.

In view of the above-results, Goff *et al.* concluded that in $(ZrO_2)_{1-x}$ - $(Y_2O_3)_x$ there are three different types of defects within the fluorite lattice. At low yttria concentrations (x < 0.15) there are regions of the crystal $\sim$ 20 Å in size which contain relatively few oxygen vacancies, causing the lattice to undergo slight tetragonal distortion of the type observed in the tetragonal T-ZrO_2. A second kind of defect is isolated oxygen vacancies which then sometimes arrange in pairs along the $\langle 111 \rangle$ fluorite directions, with a cation located between them and extensive relaxations of the surrounding ions. As the yttria content increases, these vacancy pairs pack together in the $\langle 112 \rangle$ directions to form the third kind of defect, aggregates, whose short-range defect structure resembles the long range crystal structure of the ordered compound $Zr_3Y_4O_7$. The aggregates are typically $\sim$ 15 Å in diameter though both their size and number density increases slightly with x. Quasi-elastic neutron scattering measurements [7] show that, on increasing the temperature, these aggregates remain stable up to close to the melting point. On the contrary single vacancies and vacancy pairs become mobile at T $>$ 1000 K and give rise to the high conductivity of the material. In light of these observations, Goff *et al.* [7] proposed that the anomalous decrease in the ionic conductivity with increasing x is a consequence of the decreasing mobility of the isolated defects, possibly due to the blockage by increasing number of static aggregates. It is worth noticing that in this case vacancy-vacancy interactions are proposed as responsible for the drop in the conductivity observed in these materials.

In summary, both vacancy-vacancy and vacancy-cation interactions have been suggested as responsible for the observed behaviour of the conductivity. It remains to be seen, however, how the combined effects of these ordering tendencies determines the temperature-dependent conductivity of a given material and, in particular, how they limit the ability to increase the conductivity by increasing the number of vacancies. Also the relative importance of these effects is still unknown. Answering these questions will be one of the main goals of this thesis.

Simulation studies on stabilised zirconias

A full account of all the simulation studies performed on stabilised zirconias is far beyond the purpose of this thesis. For this reason, in this section, a brief overview of those results which we think contributed the most to the understanding of the conduction mechanism in these materials is provided. For further reading on the subject, the reader is referred to ref. [1] and references therein.

The first systematic studies of the behavior of the defects and their interaction with the dopant cations are found in refs. [27, 34]. Both these works used energy minimisation, with a shell model, to study the energetics associated with cation doping in ZrO_2. The most important result from these studies are the binding energies of a series of dopant cation - oxygen vacancy clusters. These are reported in figure 2.5. The top figure, shows the binding energies for the simplest kind of cluster, a vacancy cation pair, $(M'_{Zr} : V_O^{\cdot\cdot})^{\cdot}$. These energies indicate that, for cations smaller than Sc^{3+} it is energetically favourable for the vacancy to be in a nearest neighbour (nn) position with respect to the substitutional ion, while larger cations prefer next nearest neighbour (nnn) positions. The crossover point, at the Sc^{3+} cation radius, coincides with the minimum binding energy. Interestingly, it was noted that for Sc^{3+}, the next next nearest neighbour (nnnn) configuration exhibits a binding energy that is very similar to both the nn and nnn configurations. This means that as the oxygen vacancy moves away from the Sc^{3+} ions, there is little change in the binding energy until at least after the third neighbour position. This will clearly improve the oxygen migration and it might explain why ZrO_2 doped with Sc^{3+} presents the highest ionic conductivity amongst stabilised zirconias.

If the case where an oxygen vacancy is associated with two dopant cations is considered (a more realistic situation at high dopant concentrations), forming a neutral $(2M'_{Zr} : V_O^{\cdot\cdot})^{\times}$ cluster, very similar results are obtained. These are shown in the bottom part of figure 2.5. Once again, small cations prefer a nn configurations while big cations prefer second neighbour vacancies. The minimum of the binding energies is found at the Sc^{3+} cation radius. These results rationalise the experimental findings shown in figure 2.3. Scandia-doped zirconia shows the highest conductivity because the ionic radius of Sc^{3+} is very close to that of Zr^{4+} and this minimises the lattice strain. In a strain-free lattice, the oxygen vacancies do not have any preferential site, i.e. they do not prefer to bind to a specific cation, and this increases their mobility.

A very elegant study carried out by Bogicevic and co-workers added more insight to the above-mentioned phenomena [8]. In fact, they examined vacancy ordering effects in stabilised zirconias by using first-principles, zero temperature electronic structure calculations. They

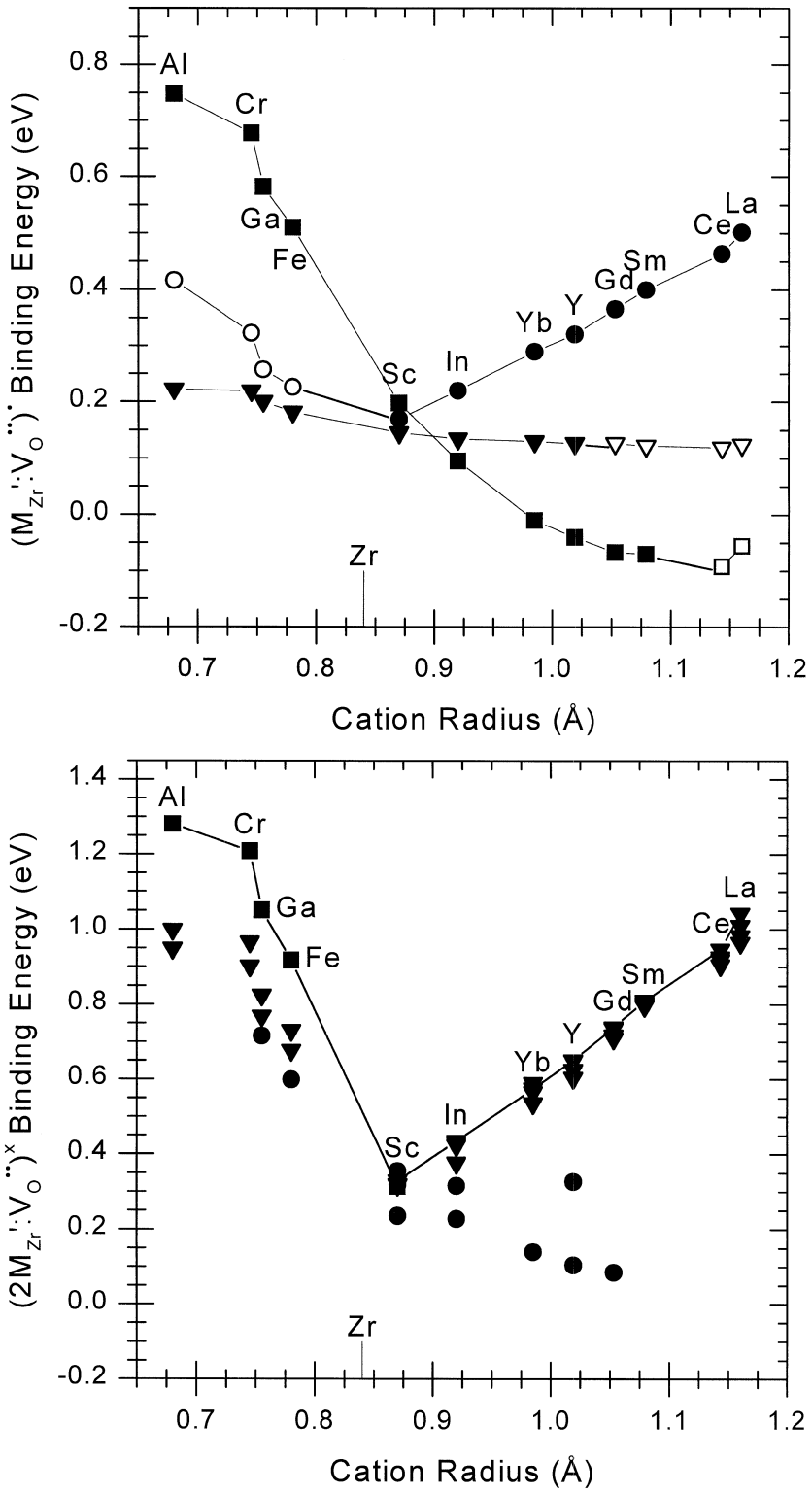

Figure 2.5: *Top: Binding energies of M^{3+} dopant cations to an oxygen vacancy versus the ionic radius of the cation: (■), a nn configuration; (●), nnn configuration; and (▼), nnnn configuration [34]. Bottom: Same figure for the binding energies of $(2M_{Zr}' : V_O^{\cdot\cdot})^{\times}$ clusters [34].*

found that vacancy ordering is most strongly governed by vacancy-vacancy interactions, followed by vacancy-dopant and, weakest of all, dopant-dopant interactions. The influence of the identity of the dopant could be understood in terms of a balance between competing electrostatic and elastic effects, which are associated with differences in the cation charges and radii. They shown that the best way to minimise vacancy-dopant association is to choose dopants where the strain term (*i.e.* the dopant ionic radius relative to that of the host cation) counteracts the electrostatic interaction, rather than simply matching the ionic radii.

All the simulation studies described so far have been performed at zero temperature and, in the case of the electronic structure calculations, on small systems (usually less than 100 atoms). Although the information obtained was very interesting and in some cases it helped rationalise the experimental results, it is desirable to study bigger systems at the temperatures of interest for their technological applications, i.e. T = 750 - 1000 C°. This can be achieved by performing MD simulations on these materials. Refs. [47, 48, 49, 50, 51] contain examples of works where this was attempted. All these studies used simple pair potential (which, as it will be shown, in the next chapters, are not accurate enough) and therefore never attempted a systematic comparison and interpretation of the available experimental data. These works focussed mainly on how the oxygen jump rates are influenced by the local surroundings (i.e. vacancy-cation ordering). In fact, when looking at the diffusion pathways in these materials, it is found that jumps only occur along the $\langle 100 \rangle$ direction. This implies that, during a jump, the oxygen ion comes close to *two* cations, A and B. In the case of YSZ, for instance, jumps can therefore be classified by counting how many jumps are going between two Zr^{4+} cations, one Zr^{4+} and one Y^{3+}, or two Y^{3+} cations, respectively. It is found that jumps through one Zr^{4+} and one Y^{3+}, or two Y^{3+} cations are much more unlikely than what expected on simple statistical grounds. This seems to confirm what was found by static calculations, namely that cations with greater ionic radii are responsible for the localisation of some of the oxygens (i.e. the presence of some vacancy-cation binding effects). This effect is also thought to cause the drop in the conductivity observed in these materials. Indeed, for yttria contents above 10% mol, the decrease of the diffusion coefficient with increasing yttria content (despite the increase of the number of oxygen vacancies) is interpreted as due to the fact that jumps close to lower-valent stabiliser cations are more unlikely that such jumps close to zirconium ions.

The idea that cation-vacancy interactions *alone* are responsible for the drop in the conductivity observed in this materials is almost universally accepted [52, 47, 48, 53, 49, 54, 50] and has been generalised to other doped fluorite systems [48, 54, 50, 55]. However, as discussed above, *two* effects are observed experimentally and are thought to affect the conductiv-

ity: vacancy-vacancy and vacancy-cation ordering effects. MD simulations could, in principle, provide direct information on *both* effects. Vacancies can in fact be identified as explained in section 3.5.3 of this thesis and, from these, radial distribution functions can be extracted. This could tell us about the vacancy-vacancy interaction strength at different temperatures, about the preference for a vacancy to bind to a certain cation species (again as a function of temperature), *etc*. Unfortunately, to date, such information has not been extracted from the MD simulations in [47, 48, 49, 50, 51]. This will be done systematically throughout this thesis.

2.1.2 Co-doping in zirconia

In the past years co-doping of zirconia has been suggested as a way to optimise these materials' properties [56, 46]. As discussed above, scandia-doped zirconia is a very attractive electrolyte material for fuel cells because it has the highest ionic conductivity amongst the zirconia-based electrolytes. However, this material is very difficult to stabilise in the cubic phase over the whole range of working temperature (300 -1200 K) [57], since a rhombohedral phase (or a mixture of rhombohedral and cubic phases) is usually present at low temperature. Adding small amount of Y_2O_3 to this material has been suggested as a way to increase chemical and structural stability and reduce conductivity degradation.

Politova and co-workers studied the effects of co-doping on the stabilisation and ionic conductivity of $(Y_2O_3)_x$ $(Sc_2O_3)_{11-x}(ZrO_2)_{89}$ (x = 1-11) [56]. The addition of yttria was found to significantly improve the phase stability of scandia-doped zirconia. Even 1 mol % of Y_2O_3 addition eliminates completely the rhombohedral and stabilises the cubic structure at room temperature. The addition of yttria was also found to reduce the conductivity, although this effect is not very strong (see figure 2.6). Politova *et al.* also studied ageing effects in these materials. It is well known that if YSZ or ScSZ are annealed at the operational temperature of a SOFC ($\sim 800^\circ$), their conductivity decreases significantly (30-40%) over time (many hundreds of hours). This property is obviously undesirable because it seriously limits the average lifetime and performances of a SOFC. Interestingly, when $(Y_2O_3)_x$ $(Sc_2O_3)_{11-x}(ZrO_2)_{89}$ is annealed for 1500 h at 800°, the samples with x = 1,2 show a very small change in the conductivity, smaller than that observed in pure YSZ or ScSZ. This can be appreciated in figure 2.7.

It seems therefore that $(Y_2O_3)_x$ $(Sc_2O_3)_{11-x}(ZrO_2)_{89}$ (with x = 1,2) is a very promising material for the electrolyte in a SOFC, due to its very high ionic conductivity, stability and low conductivity degradation. For this reason the conduction mechanism of this system will be studied in chapter 7. The only factor hindering its use, at the moment, is the very high price of Sc, which makes this material very costly. However, political and economic changes

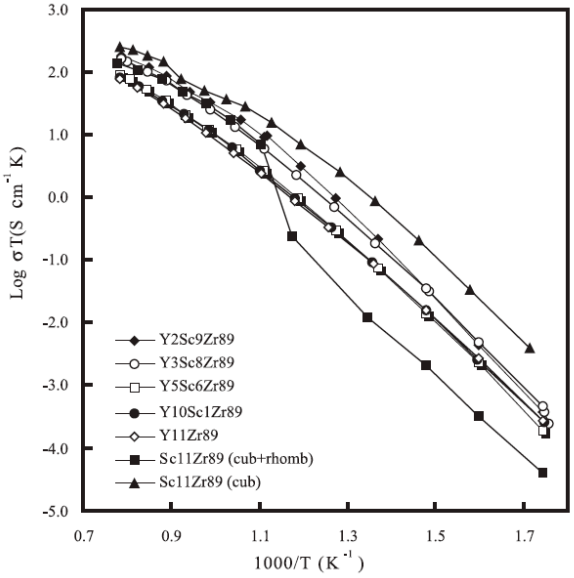

Figure 2.6: *Arrhenius dependencies of the conductivity of $(Y_2O_3)_x$ $(Sc_2O_3)_{11-x}(ZrO_2)_{89}$ [56]. The rhombohedral sample (black squares) shows a sharp step in the conductivity which corresponds to a rhombohedral-to-cubic phase transition.*

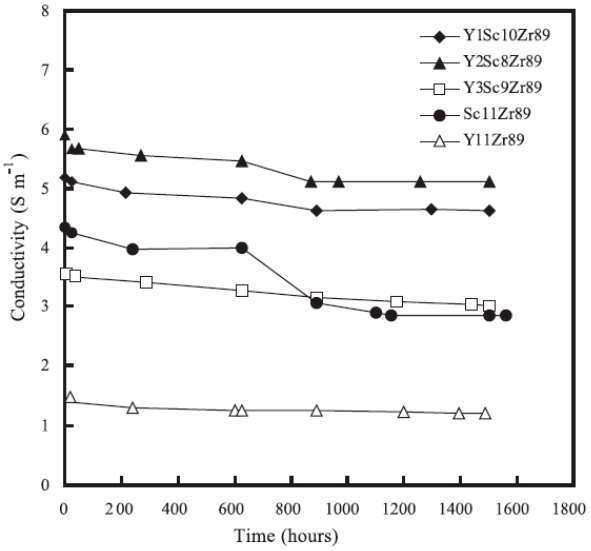

Figure 2.7: *Conductivity versus annealing time at 800° in $(Y_2O_3)_x$ $(Sc_2O_3)_{11-x}(ZrO_2)_{89}$ [56].*

over the last decade have significantly enhanced scandia's availability, thus rendering it worth considering for commercial applications, even though there is still some uncertainty about its ultimate market price [46].

2.1.3 The Y_3NbO_7–$Zr_2Y_2O_7$ system

Doping ZrO_2 with Nb^{5+} is perhaps not the best way to try to improve its ionic conductivity. Nb^{5+} is in fact a very small ion with a higher charge than Zr^{4+} and significant doping levels can only be achieved if Y^{3+} is added at the same time. The resulting material, a mixture of Y_2O_3, ZrO_2 and Nb_2O_5 has three very different cations and this is expected to increase the lattice strain and therefore decrease the conductivity. Despite this, or actually, because of this, the Y_3NbO_7–$Zr_2Y_2O_7$ system represents an ideal testbed to probe the the role of the cation sublattice on the conducting and structural properties.

The $Zr_{0.5-0.5x}Y_{0.5+0.25x}Nb_{0.25x}O_7$ series has been the object of a series of experimental studies [21, 44, 22]. This material has a fixed vacancy concentration across the whole series and this allows the study of the role of the cations without having to worry about a different vacancy concentration. Lee *et al.* [21] were the first ones to study this system systematically. They found that, although the number of vacancies is fixed, the conductivity decreases as x is increased. The difference between the ionic conductivity of the two end members at 1273 K is almost *two* orders of magnitude as can be seen in figure 2.8. Such an impressive change of the conductivity might appear quite mysterious considering that the number of vacancies is fixed across the series. It seems clear that the local cation environment is playing a very important role in this phenomenon. It has also to be noted that the cations are having a much stronger influence on the conductivity than in similar cases, like (ScSZ or YSZ), where the differences are only of a factor of 2-3 [23]. Lee and co-workers tried to relate this behaviour to the structural information obtained from their x-ray diffraction (XRD) measurements. They found that the diffraction patterns presented strong diffuse scattering features at some "forbidden" positions and that the intensity of these peaks varied with composition. This is shown in figure 2.8. It can be appreciated that there seems to be a strong correlation between the local disorder, given by the intensity of the diffuse peak, and the drop in conductivity. The explanation given in their work is that, because of electrostatic interactions, the oxygens vacancies tend to associate with the Y^{3+} ions whilst the oxygens associate with Nb^{5+} ions. These ordering tendencies are also believed to be responsible for the intense diffuse scattering observed in the XRD patterns [21]. It has to be noted that their explanation is in contrast with the results from computer simulation studies on similar materials [27, 34, 8].

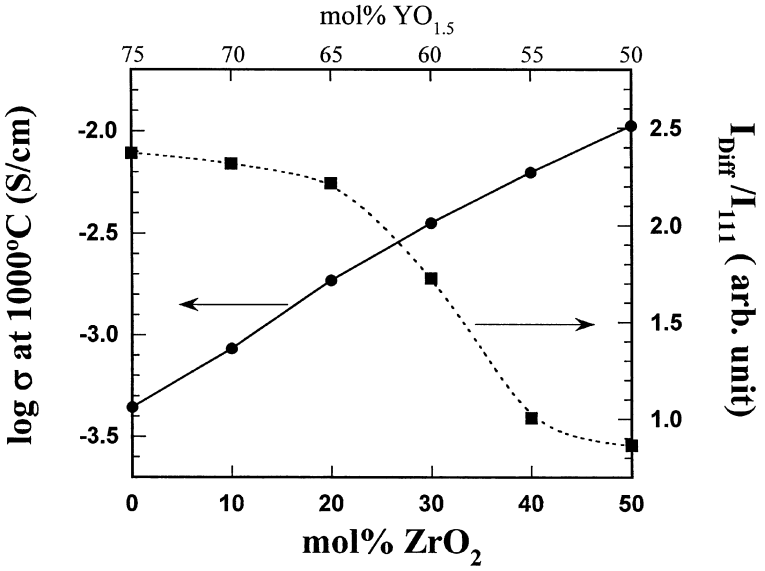

Figure 2.8: *Ionic conductivity (left) and relative intensity of the diffuse scattering (right) versus the ZrO_2 concentration in $Zr_{0.5-0.5x}Y_{0.5+0.25x}Nb_{0.25x}O_7$ [21].*

Garcia-Martin and co-workers [44] studied the microstructure of this system by means of selected area electron diffraction and high-resolution transmission electron microscopy. They found that these materials show modulated fluorite-type structural features which they assigned to partial or short-range ordering of the oxygen vacancies. The modulation of the structure in Y_3NbO_7 is thought to be associated with a partial or short-range pyrochlore-related ordering of the oxygen vacancies (and perhaps the cations). A smooth transition from a pyrochlore-like to a C-type-like diffraction pattern is observed as x is decreased. $Zr_2Y_2O_7$ presents an incommensurately modulated fluorite structure with a weak C-type ordering. Whittle *et al.* [58], however, observe the pattern as 3 peaks centred at $\mathbf{G} \pm \frac{1}{2}\langle 111\rangle$ ($\mathbf{G}$ indicates a fluorite Bragg peak) and interpret it as another type of pyrochlore-like modulated structure. According to Garcia-Martin and co-workers [44], the decrease in ionic conductivity of this system is caused by the fact that the short-range vacancy ordering of the type observed in the pyrochlore structure is more favourable to anion mobility than the C-type arrangement, though no clear explanation of this structure-property relationship has been provided to date.

In conclusion, although the $Zr_{0.5-0.5x}Y_{0.5+0.25x}Nb_{0.25x}O_7$ system has a fixed vacancy concentration across the series, it shows remarkably different structural and conducting properties for different values of x. Also this series has never been the object of any MD study, probably because of the intrinsic difficulty to parameterise accurate inter-atomic potentials for a ternary

mixture of metal oxides. For these reasons, this system is an ideal testbed to study the role that different cations have on the structure and conduction of this material. This system will therefore be the object of a substantial part of the research work described in the next chapters of this thesis.

2.1.4 Other oxide-ion conductors

Stabilised zirconias are probably the most promising oxide-ion conductors to be used in SOFCs. However, in the past years other materials such as doped ceria or the perovskite-structured lanthanum gallates have been suggested as possible electrolytes in SOFCs [4]. The reason for this appears clear by looking at figure 2.9. Both these materials are, in fact, better ionic conductors than YSZ. Unfortunately they also present some serious limitations which, so far, have hindered their use as electrolytes. In this section a short overview of these materials will be given. For further reading on this subject, the reader is referred to chapter 4 in ref. [33] or to refs. [4, 5].

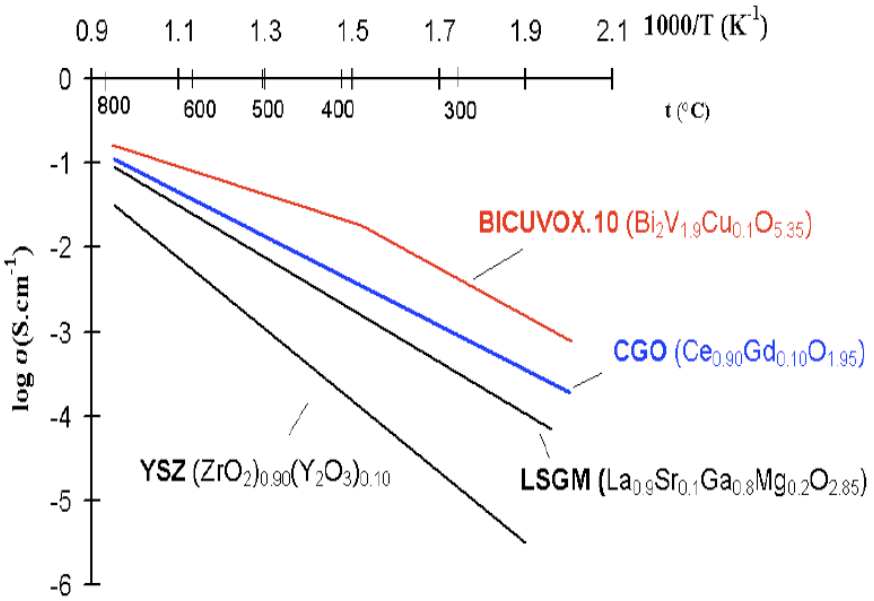

Figure 2.9: *Ionic conductivity versus inverse temperature for different oxide-ion conductors.*

Doped ceria

Pure ceria possesses the same fluorite structure as stabilised zirconia. This crystal structure is stable because the Ce^{4+} cation (R = 0.97 Å) is much bigger than Zr^{4+} (R = 0.84 Å) [59]. The

conductivity of this material can be enhanced substituting Ce^{4+} with aliovalent cations. As in the case of stabilised zirconias, the conductivity of ceria depends on the kind of dopant and on its size. In figure 2.10 the conductivity vs dopant concentration curve is shown for ceria doped with two different cations. A comparison with figure 2.2 will show that doped ceria is indeed a much better conductor than YSZ.

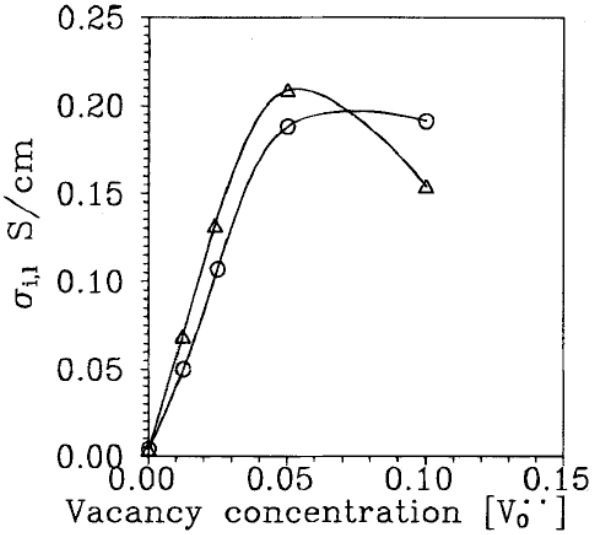

Figure 2.10: *Variation of the ionic conductivity vs dopant concentration for CaO-doped CeO_2 (◯) and Gd_2O_3-doped CeO_2 (△) at 1273 K [60].*

The maximum conductivity for ceria is typically observed for 10 mol % Sm_2O_3. Indeed this material shows a conductivity as high as 5 x 10^{-3} S/cm at 800 K, which makes it attractive for intermediate and low temperature SOFCs. Doped cerias might therefore seem an ideal candidate for the electrolyte. In fact they have very high ionic conductivities, are cubic for every dopant concentration (no degradation problems) and they are cheap. Unfortunately they also present one *major* drawback: at lower oxygen partial pressures, as prevalent on the anode side of a SOFC, these materials become partially reduced. This leads to electronic conductivity in a large volume fraction of the electrolyte extending from the anode side and the overall cell efficiency is drastically reduced. A discussion of the possible solutions for this issue can be found in ref. [5].

Lanthanum gallates

Perovskite-structured, lanthanum gallate, $LaGaO_3$, has attracted considerable attention in recent years as a promising alternative electrolyte for lowering the operating temperature of SOFCs [61, 62, 5]. Increased conductivity is obtained by substituting both the trivalent lanthanum and gallium with divalent cations, generally strontium and magnesium, respectively:

$$\mathrm{La_{1-x}Sr_xGa_{1-y}Mg_yO_{3-x/2-y/2}} \quad \mathrm{(LSGM)} \tag{2.4}$$

A favoured composition in terms of ionic conductivity is $La_{0.9}Sr_{0.1}Ga_{0.8}Mg_{0.2}O_{2.85}$. The ionic conductivity of LSGM, although significantly higher than YSZ, is slightly less than that of Sm_2O_3-doped CeO_2 at 800 K. However, the potential range of operating temperatures of LSGM is greater than Sm_2O_3-doped CeO_2, because it does not suffer from the problems exhibited by Sm_2O_3-doped CeO_2 at higher temperatures associated with electronic conduction. Thus there is interest in the possibility of using LSGM at temperatures around 600 - 700 °C, which are currently too low to obtain adequate power densities with zirconia based SOFCs.

However, there are problems associated with the stability of certain compositions of LSGM. It has also proved difficult to prepare pure single phase electrolytes of LSGM, and additional phases including $La_4Ga_2O_9$ and $SrLaGa_3O_7$, have been detected at the grain boundaries [5]. Such phases raise doubts over the long term durability of SOFCs with LSGM electrolytes, and further research into this material is still required.

2.2 Applications

As mentioned above, oxide ion conducting materials (especially doped zirconias) are the subject of intensive research activity due to their technological applications in Solid Oxide Fuel Cells (SOFCs), oxygen separation membranes, ceramic knives, thermal barrier coatings and gas sensors, *inter alia*. A detailed discussion of all the technological uses for these materials is obviously beyond the scope of this thesis. For this reason, this section will focus on the most important use for these materials which has been the object of an intense research effort in the past 20 years, Solid Oxide Fuel Cells, and the reader is referred to refs. [2, 3, 4, 63, 6] for further information on the other uses.

2.2.1 Solid Oxide Fuel Cells

Fuel cells are currently attracting tremendous interest because of their huge potential for power generation in stationary, portable and transport applications and our increasing need for sustainable energy resources. These devices are very efficient (theoretical efficiencies are close to 100% in certain cases) and present very low emissions of sulphur and nitrogen oxides and hydrocarbon pollutants, and significantly reduced (in some cases virtually zero) emissions of CO_2 [4].

In figure 2.11 a schematic diagram is reported which shows the operating principles of a fuel cell. At the anode, a fuel such as hydrogen, is oxidised into protons and electrons whilst at the cathode, oxygen is reduced to oxide species, and these then react to give water. Depending on the nature of the electrolyte, either protons or oxide ions are transported through an ion conducting, but electronically insulating, electrolyte, while electrons travel round an external circuit delivering electric power. The final output of such a device is therefore water and electricity, an absolute dream considering our currently increasing need for sustainable, "green" energy.

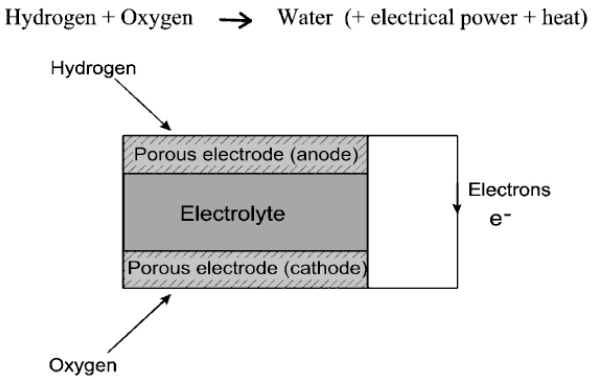

Figure 2.11: *Schematic diagram showing the operating principles of a Fuel Cell [5].*

There are at least five different types of fuel cells, differing in operating temperatures, type of electrolyte and other factors. A summary of these can be found in ref. [5]. This section will focus on Solid Oxide Fuel Cells only, which use a ceramic inorganic oxide as the electrolyte (usually YSZ) and require operation at elevated temperatures, often between 1000 - 1300 K. In figure 2.12 a schematic diagram for a SOFC is shown. In this case, a hydrocarbon (usually natural gas) is typically used as fuel. Due to the high operating temperature and to the reforming nature of the anode, this fuel is then split into hydrogen and carbon monoxide, by using steam

as the oxidant, via the following chemical reaction:

$$CH_4 + H_2O \rightarrow 3\ H_2 + \ CO \tag{2.5}$$

On the cathode, air is used as the oxidant. The final output in this case is the production of water, carbon dioxide and electricity. Although the use of hydrocarbons might seem a step backwards because it results in the production of CO_2, it has to be noted that the amount produced via this route is by far smaller than via conventional power generation [5].

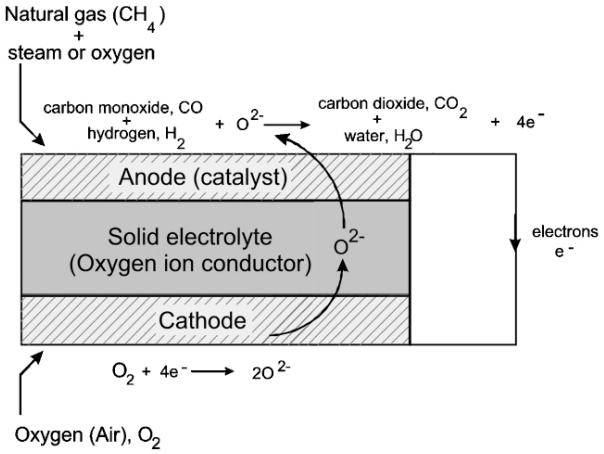

Figure 2.12: *Schematic diagram showing the operating principles of a SOFC running on hydrogen [5].*

The theoretical maximum efficiency of a SOFC is very high, in excess of 80%. Heat is one of the by-products but it can be used in various ways, for example in combined heat and power CHP systems where it is used to provide heat to households, larger residential units and industrial premises, or it can be used to drive a gas turbine to generate more electricity. Multiple cells can be connected electrically to produce larger quantities of power. This is usually achieved using an interconnect, which can be made of either a conducting ceramic material or a metal. The modularity of a SOFC, i.e. the fact that many small units can be combined together to give the desired power is one of the strengths of this technology.

The advantages of this technology are that the reforming of hydrocarbons is performed internally (which makes SOFCs cost-effective), that they have very high efficiencies, especially

Table 2.1: Pros and cons of a Solid Oxide Fuel Cell.

PROS	CONS
Internal reforming	Severe demand on the components
High efficiency	Long start-up time
Flexibility in the choice of fuel	
Tolerance to fuel impurities	
No precious metal used (low cost)	
Simple design	
Modularity	

in CHP systems ($\sim 85\%$), that many types of hydrocarbons can be used, that they tolerate fuel impurities, that they do not use precious metals (which, again, makes SOFC cost-effective) and that their design is generally quite simple. The main drawback of this technology is that the demands placed on the materials used as the electrolyte, electrodes and the interconnect are severe. Each component must meet certain requirements and has more than one function. All components must possess chemical and physical stability in the appropriate chemical environment (oxidising and/or reducing), be chemically compatible with the other components, have high conductivity, and have similar thermal expansion coefficients to the other components to avoid cracking or delamination during fabrication and operation. On top of this, it is also important that the SOFC components are of low cost and strong and yet easy to fabricate[2]! Another disadvantage of the SOFCs for certain applications is the length of time usually required to heat up and cool down the system. This is a consequence of the need to use relatively weak, brittle materials for some components and because of problems associated with thermal expansion mis-matches. This restricts the use of SOFCs in applications that require rapid temperature fluctuations, which is particularly true for transport applications, where a rapid start-up and cool down is essential. In table 2.1 the pros and cons of this technology are summarised. Some of the above-mentioned drawbacks could be avoided if the SOFC could be run at lower temperatures, $T < 850$ K. The main advantage of this would be the use of steel interconnects which are much cheaper than the cermets that have to be used at higher temperatures. However, this requires electrolytes with ionic conductivities in the range of 0.005 - 0.01 S/cm at these temperatures, which is far beyond what can be achieved in YSZ. For this reason, scientist have been looking for alternative electrolyte materials in the past twenty years.

[2]For a review of the requirements placed on each components and of the current best candidates for these, the reader is referred to ref. [5].

As a consequence of the above mentioned properties, SOFCs have a good potential for large scale distributed power generation (hundreds of MW), where the heat from SOFC is used to drive a gas turbine to produce more electricity and increase the system efficiency to levels as high as 80%, significantly higher than any conventional electricity generation. Because cost for this technology are still very high, a rapidly developing market for SOFC is in those applications where there is a real need for high quality, uninterrupted power supply. Such applications include technology companies, airports, hospital and military facilities where there is a willingness to pay a higher price for the guarantee of high quality, uninterrupted power to protect valuable IT, military or life-supporting equipment.

Chapter 3

Computer simulations and data analysis

3.1 Modeling ionic materials

Although the introduction of the Car–Parrinello method [9], some 25 years ago, obviated the need to devise an interaction potential in order to conduct a realistic molecular dynamics simulation, the introduction of a potential remains a necessary step for the investigation of many finite temperature phenomena [64], such as ionic conduction. The principle reason is that to examine these phenomena properly large simulation cells may be necessary and long runs required in order to equilibrate the system adequately in the presence of long relaxation times or to gather good statistics on the property of interest. Despite the benefit of Moores law over the intervening 25 years and the recent progress towards the holy grail of linear scaling algorithms, a full ab initio approach is often prohibitively expensive. A subsidiary reason for the use of potentials in simulations in which the objective is to represent a particular material realistically is that the potential will embody some chemical insight and such calculations may then allow a rather direct way of accounting for the different behaviors of chemically related substances. This reason will become clearer in the later chapters where the role of the cation charges and radii on the conductivity has been studied in depth by directly modifying the interatomic potential.

In the next sections, a series of models for inter-atomic potentials, which have been used in this thesis, will be introduced. This discussion follows, in some regards, that of Madden and Wilson [65]. To start with, one of the simplest model available, the Rigid Ion Model, will be introduced, which considers the ions in the solid state as un-deformable charged spheres.

Although this model was never used in the calculations presented in this thesis, it provides a useful comparison and starting point for the other models. The potentials used in this thesis, on the other hand, allow the electron density to be deformed by the local environment. These deformations are known to play an important role in the case of oxide systems and taking them into account usually yields a much better agreement with the experimental data and a clearer understanding of the materials properties [13].

3.1.1 The Rigid Ion Model

One of the simplest models for the interatomic interaction between ions in the solid state is the so-called Rigid Ion Model (RIM). In this model the ions are considered as undeformable (rigid) charged spheres interacting with each other. Such an interatomic potential usually takes the Born-Mayer form:

$$U_{ij} = \frac{q_i q_j}{r_{ij}} + B_{ij} e^{-a_{ij} r_{ij}} - \frac{C_{ij}^6}{r_{ij}^6}. \tag{3.1}$$

The $\frac{q_i q_j}{r_{ij}}$ term is the Coulombic part of the potential and accounts for most of the attraction between ions of opposite charge and most of the repulsion between like charged ions. The $B_{ij} e^{-a_{ij} r_{ij}}$ part is the short-range repulsion which accounts for the effects of the Pauli exclusion principle which prevents electrons from occupying the same space simultaneously. The B_{ij} parameter controls the magnitude of this interaction whilst the a_{ij} parameter determines the rate at which this interaction decays with distance. Finally, the $\frac{C_{ij}^6}{r_{ij}^6}$ term models the dispersion interaction caused by temporarily induced dipoles on one ion instantaneously inducing a dipole on another ion.

In this simple case, all the terms in the potential depend *only* on the distance, r_{ij}, between two ions, which are regarded in this model to be spherical and incompressible. This potential may be expected to work well for ions whose electron density is less sensitive to changes in the local environment. These simple pairwise additive representations of the repulsive interactions are, on the other hand, computationally inexpensive and allow the study of big systems (up to tens of thousands of ions) for very long times (hundreds of nanoseconds) on a commercial workstation. For these reasons, the RIM has been widely applied in the study of ionic materials, particularly to alkali halides [66, 67], but also to many oxide systems [68, 69, 47, 49, 50].

The oxide ion has, however, an electron density that is very sensitive to changes in the local environment [65]. A clear manifestation of this is the fact that this ion is unstable in the gas phase but commonly occurs in condensed matter. Because of this property, the interaction of

one ion with another cannot be expressed without reference to the environment in which each ion is found. Consequently, the interaction potentials are expected to have an explicit many-body character, unlike the above-mentioned RIM. For this reason, in the next sections a series of potentials will be described, which take into account different environmental effects.

3.1.2 Beyond the RIM

Figure 3.1 shows the electron density of the ions in an AlF_3 crystal [70]. It is clear that the ions are not spherical. The F^- ions, in fact, are elongated towards the neighbouring cations, thus proving that their electron density is indeed influenced by the local environment. This effect appears to be less important for the cations. In view of these findings, it is clear that the RIM which considers the ions as spherical and incompressible should not work in such cases. Figure 3.1 (together with an analysis of the Wannier functions, see below) also shows that the system is still ionic, i.e. that inter-atomic charge transfer and chemical bond formation involving the sharing of electron pairs between atoms are not present. For this reason, it can be expected that an *extended* ionic model, which allows changes (compressions and deformations) in the ionic electron densities, might give a reliable description of the interatomic forces in these systems.

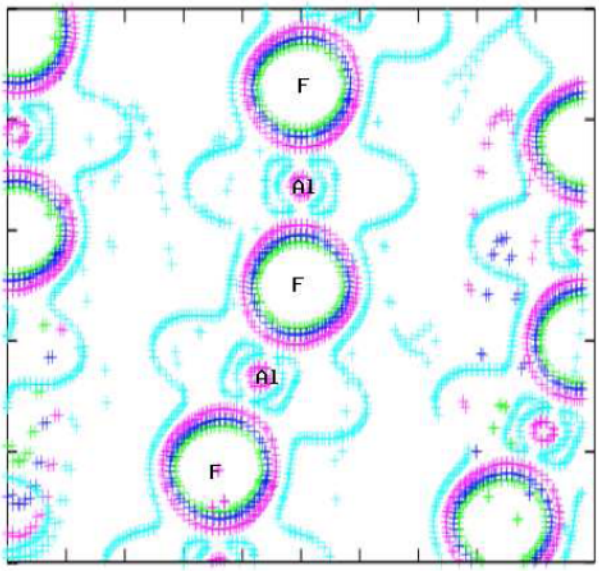

Figure 3.1: *Electron density in an AlF_3 crystal [70].*

The first effects to take into account when making the ionic electron density environment-dependent are compression effects (changes in the radius of the ionic charge distribution) and dipolar and quadrupolar distortions (changes in the shape of the ionic charge distribution). It is

important to note that these will have *two* consequences. Firstly, the central ion will acquire a non-zero electric dipole and quadrupole moment, which will alter its energy through coulombic interactions with the charges and multipoles of the other ions. Secondly, the ions may change their shape as perceived through the short range overlap interaction with its neighbours. The presence of two separate effects can be easily understood by looking at equation 3.1. If dispersion interactions, which contribute to a tiny fraction of the total energy, are neglected, then the potential energy has two terms: a coulombic and a short-range repulsion one. If the ions are deformed and therefore loose their sphericity, then both terms in the potential will have to be "corrected" to take this effects into account. In the next two sections the form and the importance of these corrections will be described in detail.

Polarisation effects

When an ion in the crystal at a relatively large distance (say, greater than next-nearest neighbour separation) from the central ion is displaced off its lattice site, its effect on the potential felt by the electrons in the central ion is simply that of the electric field ($E_\beta(r^i)$) and field-gradient ($E_{\gamma\delta}(r^i)$) at that site. There will be induced dipoles and quadrupoles given by the usual multipole expansion [71]:

$$\mu_\alpha^{i\,as} = \alpha_{\alpha\beta}E_\beta(r^i) + \tfrac{1}{3}B_{\alpha\beta\gamma\delta}E_\beta(r^i)E_{\gamma\delta}(r^i) + ... \tag{3.2}$$

$$\theta_\alpha^{i\,as} = \tfrac{1}{2}B_{\alpha\beta\gamma\delta}E_\gamma(r^i)E_\delta(r^i) + C_{\alpha\beta\gamma\delta}E_{\gamma\delta}(r^i) + ..., \tag{3.3}$$

where the superscript as means that the moments are appropriate when the sources of the fields are *asymptotically* far away from the ion i. Here $\boldsymbol{\alpha}$, and **C** are the dipole and quadrupole polarisabilities and **B** is the dipole-dipole hyperpolarisability. These quantities are usually tensorial, but in the approximation of a spherical ion, they reduce to a single scalar [71].

If a near-neighbouring ion is displaced, there is an additional effect. Figure 3.2 shows what happens when one of the first shell cations is displaced outwards. Beside the field and field gradient (related to the gradient and curvature of the potential at the origin) a dent appears in the confining potential [1]. Whilst the field and field gradient tend to push the electrons away from the displaced cation (this is the above-mentioned asymptotic contribution), this dent-in-

[1] The confining potential is the potential felt by an electron on the central ion caused by the charges and electron densities of the surrounding ions [65]. This potential is responsible for compressing the free-ion charge density into the in-crystal value. This causes the stabilisation of the oxide ion in the solid state and the lower values observed for the ionic in-crystal polarisabilities as compared to the gas phase values

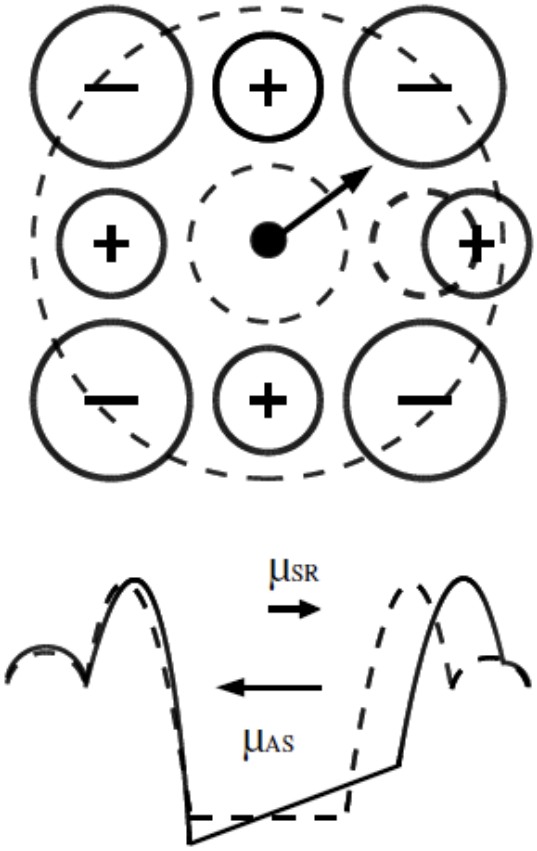

Figure 3.2: *Origin of the asymptotic and short-range contributions to the dipole induced on an anion in a crystal which has been distorted by an outward displacement of one of the first-shell cations. The lower panel shows the confining potential for the undistorted crystal (dashed), and after the distortion (solid): the floor of the potential well has acquired a gradient (the electric field) and the wall of the confining potential has been pushed outwards. These have opposite effects on the electron density. Note that the arrows represent the direction of electron displacement, and are in fact therefore antiparallel to the associated dipoles [65].*

the-wall allows them more freedom to move into the space vacated by the cation. For this reason, there is a short-range contribution to the induced dipole, which is called $\boldsymbol{\mu}^{i\ sr}$, which opposes the "asymptotic" dipole caused by the electric fields. This effect has been studied in electronic structure calculations and it was found to be substantial [72]. The dipole induced by displacing first neighbour cations is reduced below that expected from the asymptotic term alone by about 50 %. For induced quadrupoles this effect is even larger so that sometimes the net quadrupole can have opposite sign to the asymptotic quadrupole.

A similar phenomenon happens to the cations when a first shell anion is displaced outwards. If the signs of the charges on the ions in figure 3.2 are reversed, so as to make the central ion a cation, it can be seen that, as a neighbouring anion is displaced outwards, the electronic field generated will tend to displace the cation electrons towards the displaced anion which is also the direction favoured by the displacement of the cation charge cloud. Again this consideration is true of the higher oder multipoles. It is important to note that this makes the role of the cation polarisation much more substantial than would be suggested by a simple consideration of the relative size of the cation and anion polarisabilities [12].

Ion shape deformation

The development of the multipoles in the less symmetrical structures is a signal that the ion's charge cloud has been distorted from a spherical shape. The polarisation energy results from the classical coulombic interaction of the multipoles with the charges and multipoles of other ions. As mentioned above, this energy represents a correction to the coulombic term that has to be added in the case of non-spherical ions. The deformation of the spherical charge density also has another manifestation, since it affects its overlap with the charge densities of the neighbouring ions, and hence it changes the short-range repulsive interaction with them [2]. This will now be discussed.

When the ion's spherical charge density is deformed, the most important effects to take into account are ion compression, dipolar and quadrupolar distortions. These effects are of par-

[2]This effect is also contained within the shell model of the interionic interactions. The shell is the centre of repulsive interactions and it may be displaced from the ion's centre of mass (and the site of its formal charge) by repulsive interaction - hence, the ion may become anisotropic [73]. A potential difficulty with this approach is that this same displacement is closely tied, in the shell model, to the short-range effect on the induced electric dipole, which was discussed above. Although these phenomena are clearly linked it is believed, on the basis of a limited set of ab initio results, that the connection imposed by the shell model is overly restrictive and that to accurately represent them, the short-range induced dipole and the consequence of the non-spherical deformation on the short-range repulsion should be treated as separate phenomena [65].

ticular importance when studying systems in which the oxide ion might find itself in different coordination environment. This has been discuss in depth by Wilson *et al.* in ref. [18]. A description of these phenomena can be obtained by allowing the ionic radius to depend on the relative position of a number of other ions. For instance, to allow for a deformation of dipole symmetry, a vector property of each ion is introduced, which again depends upon the positions of the other ions in the sample, as illustrated in figure 3.3.

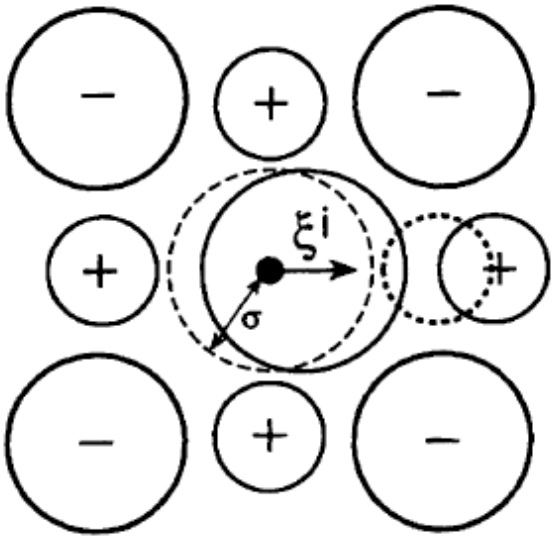

Figure 3.3: *Representation of the ion "deformation effect" in the distorted crystal considered in figure 3.2. In this case, the electron density ceases to be symmetrically disposed about the anion centre - as indicated by the displaced contours in the figure. This affects the repulsive interaction between the anion and its first neighbour cations. The vector ζ^i indicates the direction of the deformation and appears in the modified expression for the repulsive interactions [65].*

3.2 The form of the interaction potential

In the above section a series of effects were described (dipole and quadrupole polarisation, ion-shape deformations *etc.*) which have to be taken into account if one wants to accurately model the many-body, inter-atomic interactions of an ionic material. When studying such a system it can be chosen to either incorporate all these effects into the potential or to select only those

which are believed to be more important [3]. For instance, when studying a system with a very symmetrical crystal structure (like the fluorite structure), it might be decided not to include ion-shape deformation and/or quadrupole polarisation effects because these are likely to play a minor role (see next chapter). This therefore gives a series of models of an increasing degree of sophistication. In the next sections, two of these models (which were used intensively in the work reported in this thesis) will be described in detail and then all the others will be briefly reviewed.

3.2.1 The QUadrupole-polarisable Aspherical Ion Model

This model includes polarisation effects and ion-shape deformations up to the quadrupolar order. For this reason it is dubbed the QUadrupole-polarisable Aspherical Ion Model, or QUAIM. In view of the above discussion, this interionic potential is constructed from four components, describing charge–charge, dispersion, overlap repulsion and polarisation effects. The charge-charge component is purely pairwise additive and therefore identical to the one used in the RIM:

$$U_{ij}^{charge-charge} = \frac{q_i q_j}{r_{ij}} \tag{3.4}$$

where q_i is the formal charge for ion i. The dispersion interactions include dipole–dipole and dipole–quadrupole terms

$$U_{ij}^{disp} = -\sum\nolimits_{n=6,8} \frac{C_{ij}^n f_D(r_{ij})}{r_{ij}^n} \tag{3.5}$$

with C_{ij}^6 and C_{ij}^8 the dipole–dipole and dipole–quadrupole dispersion coefficients, respectively. This description takes into account the short-range corrections to the asymptotic dispersion term (an effect mentioned above for the polarisation effects) by making use of the Tang Tonnies dispersion damping function ($f_D(r_{ij})$, as reported in equation 3.8 [13].

For the short-range repulsive terms of the potential, deformable anions and rigid cations are usually considered. The shape deformations are taken as relatively insignificant for the anion–anion repulsions, which are therefore represented by simple Born–Mayer exponentials, but they are substantial in the shell of nearest neighbours. This leads to the following expression (A stands for anions, C for cation):

[3] It has to be remembered that adding these effects makes the calculation more expensive so that a balance between computational speed and accuracy is needed.

$$
\begin{aligned}
V^{rep} = & \sum\nolimits_{i\in A, j\in C}[A^{+-}e^{-a^{+-}\varrho^{ij}}] + \sum\nolimits_{i,j\in A}[A^{--}e^{-a^{--}r^{ij}}] + \\
& \sum\nolimits_{i\in A}[D(e^{\beta\delta\sigma^i} + e^{-\beta\delta\sigma^i}) + (e^{\zeta^2|\nu^i|^2} - 1) + (e^{\eta^2|\kappa^i|^2} - 1)] + \\
& \sum\nolimits_{i\in A, j\in C}[B^{+-}e^{-b^{+-}r_{ij}^2}] + \sum\nolimits_{i,j\in A}[B^{--}e^{-b^{--}r_{ij}^2}]
\end{aligned} \tag{3.6}
$$

where $\varrho^{ij} = r^{ij} - \delta\sigma^i - S_\alpha^{(1)}\nu_\alpha^i - S_{\alpha\beta}^{(2)}\kappa_{\alpha\beta}^i$ and summation of repeated indices is implied. The variable $\delta\sigma^i$ characterises the deviation of the radius of oxide ion i from its default value; ν_α^i are a set of three variables describing the Cartesian components of a dipolar distrortion of the ion, and $\kappa_{\alpha\beta}^i$ are a set of five independent variables describing the corresponding quadrupolar shape distortions. In the expression for the short range repulsion, $|\kappa|^2 = \kappa_{xx}^2 + \kappa_{yy}^2 + \kappa_{zz}^2 + 2(\kappa_{xy}^2 + \kappa_{xz}^2 + \kappa_{yz}^2)$ and $S_\alpha^{(1)} = (r_\alpha^{ij})/r^{ij}$ and $S_{\alpha\beta}^{(2)} = 3(r_\alpha^{ij}r_\beta^{ij})/r^{ij^2} - \delta_{\alpha\beta}$ are the interaction tensors. The second summation includes the self-energy terms, representing the energy required to deform the anion charge density, with β, ζ and κ as effective force constants. The extent of each ion's distortion is determined at each molecular dynamics time-step by energy minimisations. The last terms, $\sum[B^{+-}e^{-b^{+-}r_{ij}^2}]$ and $\sum[B^{--}e^{-b^{--}r_{ij}^2}]$, are Gaussians which acts as a steep repulsion wall and account for the anion's hard core; these extra terms are used in cases where the ions are strongly polarised to avoid instability problems at very small anion-cation and anion-anion separations [74]. It is worth noticing that although the short-range repulsion term in equation 3.6 looks like a Born-Meyer term, this now has a many-body character because the variables $\delta\sigma^i$, ν_α^i and $\kappa_{\alpha\beta}^i$ are influenced by the position of all the neighbouring ions.

The polarisation part of the potential incorporates dipolar and quadrupolar contributions:

$$
\begin{aligned}
V_{pol} = & \sum\nolimits_{i,j}\{((q^i\mu_\alpha^j f_D(r^{ij}) - q^j\mu_\alpha^i f_D(r^{ij}))T_\alpha^{(1)} + \\
& \left(\frac{q^i\theta_{\alpha\beta}^j f_Q(r^{ij})}{3} + \frac{\theta_{\alpha\beta}^i f_Q(r^{ij})q^j}{3} - \mu_\alpha^i f_D(r^{ij})\mu_\beta^j f_D(r^{ij})\right)T_{\alpha\beta}^{(2)} \\
& + \left(\frac{\mu_\alpha^i f_D(r^{ij})\theta_{\beta\gamma}^j f_Q(r^{ij})}{3} + \frac{\theta_{\alpha\beta}^j f_Q(r^{ij})\mu_\gamma^i f_D(r^{ij})}{3}T_{\alpha\beta\gamma}^{(3)}\right) + \\
& \frac{\theta_{\alpha\beta}^i f_Q(r^{ij})\theta_{\gamma\delta}^j f_Q(r^{ij})}{9}T_{\alpha\beta\gamma\delta}^{(4)})\} \\
& + \sum\nolimits_i(k_1^i|\overrightarrow{\mu}^i|^2 + k_2^i\mu_\alpha^i\theta_{\alpha\beta}^i\mu_\beta^i + k_3^i\theta_{\alpha\beta}^i\theta_{\alpha\beta}^i + k_4^i|\overrightarrow{\mu}^i\cdot\overrightarrow{\mu}^i|^2)
\end{aligned} \tag{3.7}
$$

where μ_α^i is the α component of the dipole moment of ion i, $\theta_{\alpha\beta}^i$ is the $\alpha\beta$ component of the

quadrupole moment of ion i, $k_1^i = \frac{1}{2\alpha^i}$, $k_2^i = \frac{B^i}{4{\alpha^i}^2 C^i}$, $k_3^i = \frac{1}{6C^i}$, $k_4^i = \frac{-{B^i}^2}{16{\alpha^i}^4 C^i}$. α^i, B^i and C^i are the dipole, dipole-dipole-quadrupole and quadrupole polarisabilities on ion i respectively while $T_{\alpha\beta\gamma\delta} = \nabla_\alpha\nabla_\beta\nabla_\delta\nabla_\gamma ... \frac{1}{r^{ij}}$ are the multipole interaction tensors [75]. The instantaneous values of these moments are obtained by minimisation of this expression. The charge-dipole and charge-quadrupole cation-anion and anion-anion asymptotic functions include terms which account for penetration effects at short-range by using Tang-Tonnies damping functions of the form,

$$f_D(r^{ij}) = 1 - c_D e^{-b_D^{ij} r^{ij}} \sum_{k=0}^{4} \frac{(b_D^{ij} r^{ij})^k}{k!} \tag{3.8}$$

$$f_Q(r^{ij}) = 1 - c_Q e^{-b_Q^{ij} r^{ij}} \sum_{k=0}^{6} \frac{(b_Q^{ij} r^{ij})^k}{k!} \tag{3.9}$$

with D and Q standing for dipolar and quadrupolar parts. While the parameters b_D^{ij} and b_Q^{ij} determine the range at which the overlap of the charge densities affects the induced multipoles, the parameters c_D^{ij} and c_Q^{ij} determine the strength of the ion response to this effect.

3.2.2 The DIPole-Polarisable Ion Model

The model described above has the drawback of being computationally very demanding. Most of the studies presented in this thesis required long simulations (up to 10 ns), with many hundreds (or thousands) of ions. For this reason, most of the times a simpler version of this model has been used, in which the ion-shape deformation effects and quadrupolar contributions to the polarisation part of the potential are neglected. This model, which is usually dubbed the DIPole-Polarisable Ion Model, or DIPPIM, was found to describe successfully the systems studied in this thesis (see next chapter).

The first two contribution to the potential (Coulombic and dispersion) are the same as equations 3.4 and 3.5. The short term repulsive terms and the polarisation energy are, however, different. The first reads:

$$\begin{aligned} V^{rep} = &\sum A^{+-} \frac{e^{-a^{+-} r^{ij}}}{r_{ij}} + \sum A^{--} \frac{e^{-a^{--} r^{ij}}}{r_{ij}} + \\ &\sum [B^{+-} e^{-b^{+-} r_{ij}^2}] + \sum [B^{--} e^{-b^{--} r_{ij}^2}] \end{aligned} \tag{3.10}$$

where the 1/r form was selected as this is known to give a better fit of the short-range interaction [74] and to improve the potential's stability. The polarisation energy is identical to equation

Table 3.1: Different potential models.

Name	Features / Description
RIM (Rigid Ion Model)	No polarisation or ion-shape deformation effects
DIPPIM (DIPole Polarisable Ion Model)	Dipole polarisation effects only
QUADPIM (QUADrupole Polarisable Ion Model)	Dipole and quadrupole effects
CIM (Compressible Ion Model)	Ion compression effects
QUAD-CIM (Quadrupole Compressible Ion Model)	Dipole, quadrupole and ion compression effects
QUAIM (Quadrupole Aspherical Ion Model)	Dipole, quadrupole and ion-shape deformation effects

3.7, once the quadrupole moment and polarisabilities are set to zero:

$$V_{pol} = \sum_{i,j}(q^i\mu^j_\alpha f_D(r^{ij}) - q^j\mu^i_\alpha f_D(r^{ij}))T^{(1)}_\alpha - \sum_{i,j}\mu^j_\alpha f_D(r^{ij})\mu^i_\beta f_D(r^{ij})T^{(2)}_{\alpha\beta} + \sum_i(k^i_1|\overrightarrow{\mu}^i|^2). \tag{3.11}$$

3.2.3 Other models

New models can be obtained by systematically including/removing some of the above-mentioned effects. For instance, if quadrupoles are believed to play an important role in the description of the inter-atomic forces for a given system, a potential with dipoles and quadrupoles (but no ion-shape deformation) can be used. This potential is dubbed QUADPIM. Table 3.1 reports the most used combinations.

3.2.4 The relative importance of multipoles and ion shape deformation effects.

In the above sections a series of "corrections" to the simple Rigid Ion Model were presented in order to take into account the effects of distorting the ion's charge. It will now be shown how each of these different corrections influences the physics of a certain system. To this end, this

section will follow the discussion by Wilson *et al.* [76] on ZrO_2, a material which is key to the purpose of this thesis.

Three crystal structures are observed in pure ZrO_2 with increasing temperatures: monoclinic, tetragonal and cubic. Previous models of the ionic type, however, are unable to predict the stability of the ground-state monoclinic structure of ZrO_2 with respect to an orthorombic (rutile) structure. Wilson and co-workers made a detailed investigation of the energies of a number of phases of ZrO_2 using models of increasing degree of sophistication. They used the rigid ion model from ref. [77] and then fitted a RIM, DIPPIM, CIM, QUADPIM and QUAD-CIM potential to ab-initio calculations, in order to evince which factors stabilise the different structures.

Their results show that empirical potentials, like the RIM, all give the rutile structure as the ground state, regardless of the details of the potential. This proves the limitation of such a simple model. Adding compression effects to the potential (CIM) has the effect of stabilizing higher coordinate structures (fluorite and monoclinic) over the 6-coordinated rutile structure. This happens because the ion contracts as its coordination increases and this results in a reduction in the repulsive energy but an increase in the self-energy. It is therefore a more repulsive object (with lower self-energy) at lower coordination. However the reduction in self-energy is not offset by the gain in overlap energy. The result of this is to destabilise lower-coordination structures; in particular the orthorhombic (rutile) structure is brought to a higher energy than the experimentally observed monoclinic structure.

The story is, however, far from complete as this model now gives the fluorite structure as the predicted ground state. It is only with the addition of *both* dipoles and quadrupoles to the compressible ion model (QUAD-CIM) that the correct order is obtained, with the monoclinic structure as the ground state. The stabilisation works because, in the monoclinic structure, the anions sit in a much more asymmetric environment than in the fluorite structure. The driving force for the formation of this structure appears to be the existence of the three-coordinate oxygens sites, which are the sites that experience the largest quadrupole polarisation.

It might therefore seem that all the effects described above will be required for the study of the conducting properties of stabilised zirconias. However, to anticipate the story below, such a level of sophistication was not needed for the work described in this thesis. Indeed, our calculations have been performed on stabilised fluorites only. In this case, all that was needed was a potential which describes reliably the interaction between the ions in this structure only.

The simpler DIPPIM potential was therefore used for most of the work described in this thesis and this successfully reproduced all the experimental properties of interest.

3.3 Parameterizing the potentials: the force-matching procedure.

The use of interaction potentials in simulation studies is wide-spread, and for many ionic systems, such as molten salts and some oxide systems, the parameterisation of these potentials is carried out empirically using experimental data (density, lattice energies and so on) [66, 67, 78, 47]. This technique, however, presents some drawbacks. First of all, this does not work in cases when experimental data for the system in study are not available. In other words, the technique is not predictive. Also, experimental data are usually limited to a small set of thermodynamical states. For instance parameterizing a potential for SiO_2 by reference to experimental data at ambient pressure might not be enough if one is interested in the behaviour of this material at very high pressures, such as the ones found in the Earth's mantle. It is for these reasons that a more systematic approach [13] to the parameterisation of these potentials was used, which makes use of the recent availability of high quality ab initio methods. To this end, a technique was used, which has enjoyed much success in the development of accurate and transferable interaction potentials for oxide systems, that of force-fitting to ab initio information. With this technique, the optimal set of parameters for a certain system can be determined using a force-fitting procedure, where the forces, multipole moments, and, sometimes, stress tensor components of the whole cell, generated by the model for condensed phase reference configurations [4] , are matched to those calculated using an ab initio technique.

The idea behind the development of potentials using a force-fitting procedure is illustrated schematically in figure 3.4. To begin, an existing interaction potential is taken for the system in question, which need not be entirely realistic in its representation of the interatomic interactions, but should be suitable enough to generate representative arrangements of atoms or configurations from high-temperature molecular dynamics simulations, *i.e.* it should give reasonable densities and bond-distances [5]. Ab initio calculations on these atomic configurations are then carried out, and the information extracted about the forces, dipoles, quadrupoles *etc.* of

[4] Using condensed phase reference configurations is of paramount importance for the success of this procedure. In fact, as discussed before, the properties of some ions change significantly from the gas to the condensed phase, the best example of this being the fact that the oxide ions is unstable in the gas phase while perfectly stable in the condensed one.

[5] Alternatively, if no interaction potential is available, one can run a short Car-Parinello molecular dynamics simulation on the system and fit a potential to the forces and dipoles obtained from it.

the individual ions is used in the force-fitting procedure. This new potential can be used to generate additional configurations, and the whole process may be repeated if necessary. In order to generate accurate and transferable potentials, the ions within these configurations must sample a wide range of environments (i.e. high temperatures and pressures and, if possible, different crystal structures). It is hoped that by using a large number of distorted configurations, with the ions sampling various types of coordination environment and a range of interionic separations, it will be possible to acquire a varied data set of ab initio information on which to train the interaction potentials. This process is followed by a testing stage, where the suitability of the new potential is assessed. It is worth noticing that this approach uses thousands of data points (which has to be compared with the few tens of experimental points usually available for such materials). Each ab-initio calculation is, in fact, performed on about 100 ions and each such calculation provides three cartesian force components, three components for the dipole and six components for the quadrupole of each ion.

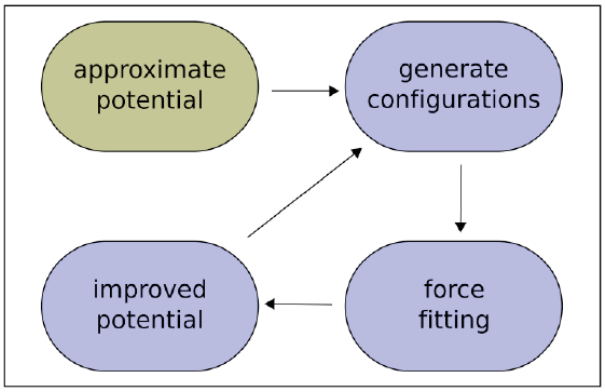

Figure 3.4: *Scheme of the force-matching procedure used in this thesis.*

It is not unusual, during this procedure, to constrain some of the parameters to avoid them taking unphysical values and to limit the number of free parameters in the potential (which sometimes exceeds 40!). Ionic polarisabilities are usually constrained to either their experimental value or to the value calculated via an ab-initio technique [79, 80]. Also, the intensity of the cation-cation and anion-anion short-range repulsion is usually set to zero, since this is not found to influence the fit quality. More details on this procedure will be given, case by case, in the next chapters.

In the fitting procedure the parameters are obtained by *simultaneously* minimizing the fol-

lowing objective functions:

$$A_P(\{\chi\}) = \frac{1}{2}\frac{\sum_{i,\alpha,A}|\zeta^A_{i,\alpha}(\{\chi\}) - \zeta^{A,DFT}_{i,\alpha}|^2}{\sum_{i,A}|\zeta^{A,DFT}_{i,\alpha}|^2} \tag{3.12}$$

$$A_F(\{\chi\}) = \frac{1}{2}\frac{\sum_{i,\alpha,A}|F^A_{i,\alpha}(\{\chi\}) - F^{A,DFT}_{i,\alpha}|^2}{\sum_{i,A}|F^{A,DFT}_{i,\alpha}|^2}. \tag{3.13}$$

In the above expression, $(\{\chi\})$ represents the whole set of parameters which are to be optimised while i runs over atoms and α = x, y, z. The sum over A represents the sum over all the atomic configurations included in the fit. The quantities $\zeta^A_{i,\alpha}(\{\chi\})$ and $F^A_{i,\alpha}(\{\chi\})$ are the multipole components (comprising the dipoles $\mu_{i,\alpha}$ and the five independent quadrupole components $\theta_{i,\alpha\beta}$ for each ion) and the components of the forces obtained from the MD simulation, while $\zeta^A_{i,\alpha}(\{\chi\})$ and $F^A_{i,\alpha}(\{\chi\})$ are the same quantities as obtained from the DFT calculations.

To optimise the objective functions, a non-gradient simplex and MIGRAD method was used, from the standard non-linear fitting package MINUIT [81]. The final values of the objective function can give an indication of the fit quality. In the case of simple systems, like molten halides, it was found that $A_P(\{\chi\})$ and $A_F(\{\chi\})$ can assume values as low as 0.01. Such small values are not expected for oxides systems due to the fact that electron density deformation effects are expected to be larger in these systems. Wilson and co-workers obtained $A_F(\{\chi\}), A_P(\{\chi\}) \sim 0.1$ for Li_2O with the QUAIM model [19]. This value is a good reference for our future work.

3.3.1 Forces and multipole moment from Density Functional Theory

The ab initio methods used in this work are Density Functional Theory (DFT) techniques, which have become popular in recent years for studies of the condensed phase [82]. Application of the Hellman-Feynman theorem allows calculation of the ionic forces [83], which are available from any of the standard DFT packages. In this thesis either CASTEP [84] or CPMD [85] were used, the latter being much faster than the former (see discussion in chapter 6). Obtaining the ionic multipoles however, requires a little more work. The optimum Kohn-Sham eigenvectors derived from the DFT calculations, $\{\Psi_n\}_{n=1,N}$, are delocalised throughout the simulation cell. In order to associate orbitals with individual ions, from which it is possible to calculate ionic multipole moments, one has to switch to a localised representation of the electron density distribution via a Wannier transformation of these eigenvectors [86]. If the

condition of maximal localisation is enforced, a set of Wannier orbitals is obtained which provides a picture of the electron distribution around atoms involved in chemical binding or ions polarised by the electrostatic field. In this work, maximally localised Wannier functions were determined by unitary transformation of the Kohn-Sham eigenvectors according to

$$|w_n\rangle = \sum_{m=1}^{N} \mathbf{U}_{nm} |\Psi_n\rangle \tag{3.14}$$

where the sum runs over all the Kohn-Sham states $\{\Psi_n\}_{n=1,N}$, and the unitary matrix $\mathbf{U}$ was determined by iterative minimisation of the Wannier spread [87]:

$$\Omega = \sum_{n=1}^{N} (\langle r^2 \rangle_n - \langle \mathbf{r} \rangle_n^2). \tag{3.15}$$

In molecular and ionic (closed shell) systems, this transformation localises a set of valence orbitals on each molecule and the molecular charge densities obtained from these orbitals have been shown to give excellent values for the molecular multipoles [88], as judged by their ability to reproduce the values obtained from more conventional quantum chemical methods on embedded clusters and their use in discussing the charge density in interacting systems. This methodology has also been used to predict the ionic polarisabilities of a series of ionic and molecular materials and the results were in good agreement with the experimental data [79, 80].

For each ion i of our systems, the α component of the dipole moment is calculated from the Wannier function center's (WFC) positions, $\mathbf{r}^n$, according to

$$\mu_\alpha^i = -2 \sum_{n \in i} r_\alpha^n, \tag{3.16}$$

where the sum runs over those MLWFs which are close to ion i (usually 4) [6]. To calculate the ionic quadrupoles, the fact that the MLWFs are well-localised inside the periodic cell is exploited, and the components of the quadrupole on an ion i are evaluated from the real-space integral of the charge densities of the MLWFs on that ion :

$$\theta_{\alpha\beta}^i = -2 \sum_{n \in i} \int_{V_{cut}^i} d\mathbf{r} |w_n(\mathbf{r})|^2 (3 r_\alpha^i r_\beta^i - (r^i)^2 \delta_{\alpha\beta})/2 \tag{3.17}$$

Here the integral runs over the space within the radius r_{cut} of ion i, and $\boldsymbol{r}^i$ is the distance from $\boldsymbol{r}$ to the nucleus of ion i, calculated with a minimum image convention.

[6] By this it is meant those Wannier functions which are within a certain cutoff radius from the ion's center. This cutoff radius is usually about 0.5 Å , in agreement with an ionic picture of the system in which the ion's charge distribution is strongly localised around the ion's nucleus.

3.4 Simulation techniques

In this section a summary of the simulation techniques used is provided. For the sake of brevity, and since the work in this thesis did not involve the development of these methods, only a brief discussion will be given, while pointing the reader to more detailed discussions and documentation elsewhere.

The simulations presented in this thesis are molecular dynamics (MD) simulations, and use the Leapfrog Verlet algorithm [89] to integrate numerically Newton's equations for the motion of classically interacting particles. Simulations in the canonical (NVT) ensemble have been performed using the method proposed by Nosé [90, 91] and Hoover [92], with the modifications suggested by Martyna. In fact, it has been shown by Martyna *et al.* [93] that for systems of low dimensionality, the dynamics produced by the Nosé-Hoover equations is not ergodic, and that as a result, the probability distribution obtained does not correspond to the canonical distribution. Extending the Nosé-Hoover dynamics to a chain of thermostats gives the system a higher dimensionality which shows greater ergodicity [93]. For this reason, simulations in the NVT ensemble have been performed using this technique [93]. Those simulations in the NPT ensemble have used a Nosé-Hoover thermostat coupled to a barostat, applying, also in this case, the formalism developed by Martyna *et al.* [94].

In order to simulate a finite system without the properties under study being dominated by surface effects, a simulation cell is used which is replicated infinitely throughout space, and periodic boundary conditions [89, 95] were applied. All short-range interactions, such as the overlap repulsive interactions between ions, are truncated in real space using a simple cut-off procedure, and are calculated with the application of the minimum image convention. The electrostatic interactions in the models of ionic polarisation act over a much larger range of ionic separations than the short-range terms, and must be carefully handled. The most popular technique for treating these long-range interactions is the Ewald summation [95, 96, 97]. In this method, the system is treated as infinite, and each particle interacts with all of the periodic images, in addition to particles of the simulation cell. The energy expression is given in terms of a real space summation of the short-range screened interactions, and a reciprocal space summation arising from the long-range interactions. The Ewald summation method, as implemented within our molecular dynamics code, allows a full treatment of the multipole interactions up to the quadrupolar level. Further details of these methods may be sought elsewhere [97].

The simulation technique used for the work described in this thesis is quite fast. Most of the simulations described in this thesis were done on systems ranging between 500 and 1000

atoms. When a simulation on a system of about 600 atoms (with a potential which includes dipole polarisation effect) is run on a simple commercial Intel Core Duo quad processor (2.8 GHz), then a trajectory of 1 ns can be obtained in less than a day. The advantage over a direct ab-initio approach is evident.

3.5 Data analysis

The main output of a computer simulation are the positions and velocities of each atom at each timestep. This information is extremely beneficial because it is not available experimentally. Usually a first attempt to analyze such output is to visualise the atomic positions. Although such a procedure can be helpful and give some insight on the material's behaviour (see chapter 5), it is usually necessary to calculate other observables from these sets of coordinates. This is needed, for instance, when a direct comparison with an experimental observable is desired.

Our MD code automatically calculates and outputs some of these observables. For example radial distribution functions and partial structure factors are calculated on the fly. There are some quantities, however, which need to calculated *a posteriori*. Total radial distribution functions, mean squared displacements, conductivities, mobility distribution functions, diffuse scattering and vacancy concentrations are examples of these quantities. In the next sections the procedures by which these are calculated will be described.

3.5.1 Radial Distribution Functions

Radial distribution functions describe how the atomic density varies as a function of the distance from one particular atom. For this reason they are very important because they can can provide information on the local structure of a solid. A partial radial distribution function is given by:

$$g_{ij}(r) = \frac{1}{4\pi r^2 dr}\frac{n_{ij}(r)}{\rho_j}, \tag{3.18}$$

where $n_{ij}(r)$ is the number of particles of type j located at a distance between r and r + dr from a particle of type i and ρ_j is the number density of particles of types j. As mentioned before, these functions are calculated on the fly by our MD code and averaged over the entire length of the simulation.

In neutron and x-ray diffraction experiments the total scattering structure factor, $S(q)$, can be Fourier transformed to obtain the corresponding total radial distribution function, $G(r)$, which is the sum of the individual partial rdfs, $g_{ij}(r)$, weighted by the concentrations of the

two species, c_i and c_j and their neutron scattering lengths, b_i and b_j, so that [7]

$$G(r) = \frac{\sum_{i,j=1}^{n} c_i c_j b_i b_j g_{ij}(r)}{(\sum_{i=1}^{n} c_i b_i)^2}. \tag{3.19}$$

This quantity can be trivially calculated from the partial rdfs outputted by our MD code.

3.5.2 Mean squared displacements and conductivity

The simplest way of demonstrating ionic behaviour in the simulation of a certain compound is to show that the mean squared displacements of the mobile ion (the oxide ion in this case) increase linearly with time, whilst those of the immobile ion type remain approximately constant. The mean squared displacement of a given ion species is given by [95]:

$$\langle \Delta r^2(t) \rangle = \frac{1}{n_j} \sum_{i=1}^{n_j} (x(i,t) - x(i,0))^2 + (y(i,t) - y(i,0))^2 + (z(i,t) - z(i,0))^2, \tag{3.20}$$

where n_j in the number of ions of species j and x(i,t), y(i,t) , z(i,t) are the cartesian components of the position of ion i at a time t. When both curves are flat, the material is a solid with no observable ionic diffusion, whereas if both curves are linear the material is a liquid. The gradient of the mean squared displacement is proportional to the diffusion coefficient via [95],

$$D = \lim_{t \to \infty} \frac{1}{6t} \langle \Delta r^2(t) \rangle. \tag{3.21}$$

The diffusion coefficient can then be used to estimate the ionic conductivity of the material via the Nerst-Einstein relationship:

$$\sigma_{NE} = \frac{z_i^2 \rho_i D_i}{k_B T}, \tag{3.22}$$

where z_i is the charge on species i, ρ_i is the number density of species i, k_B is the Boltzmann constant and T is the temperature. This expression is exact only in the case of purely uncorrelated motion. A better value for the conductivity can be obtained, in principle, from an integral over the charge current correlation function J (t) [95]:

$$\sigma = \frac{1}{k_B T V} \int_0^{\infty} J(t) dt \tag{3.23}$$

[7] In the case of x-ray diffraction experiments, the neutron scattering lengths are replaced by the x-ray form factors which are q-dependent. This was done in appendix C.

though this quantity has very poor statistics, especially when diffusion is slow. A comparison between the two values can give some information about the degree of correlation of the ionic motion in a certain system. In this thesis, both approaches were used when possible.

3.5.3 Vacancy analysis

Vacancies in stabilised zirconias are responsible for the impressive values of the conductivity observed in these materials. For this reason, the identification of vacancies is of great importance to better understand the conduction mechanism in these materials. Locating vacancies is not, however, a simple operation. For instance, methods which study the occupancy of a sphere centred on the ideal fluorite lattice site were found unsuccessful [98]. A better way to locate the vacancy is the so-called vector site analysis. The idea behind this method is that all the sites in any crystal are defined by polyhedra composed of triangular faces. In the case of the fluorite structure, each anion is surrounded by four cations, i.e. each anion lies within a tetrahedron whose vertices are delimited by the cation positions. If a mobile ion escapes such a tetrahedron, the ion must pass through one of the triangular faces in order to leave that site. Mathematically this can be defined as the moment when the scalar product of the ion's position vector (with respect to one of the vertices of the plane), with a vector that is normal to the plane, changes sign. This is shown pictorially in figure 3.5. All that needs to be known for this method to be applied to large and long simulations is the identities of the "static" ions (in this case the cations) bordering each site, and a set of all the ion positions at various time intervals. Assigning these vertices is the most arbitrary part of the process, since the only way to do this will require the use of a cut-off in coordination number. However this only has to be done once, and it is possible to use a perfect crystal coordinate file (or one from a simulation at low temperature) to achieve this - in which case the bond lengths are all well defined and so there should be no problem of mis-assignment. The positions of vacancies can be identified for an instantaneous ionic configuration by finding which of the coordination tetrahedra are empty. The position of such a vacancy will be the average position of the surrounding four cations.

Because the oxide ions may perform large amplitude vibrations about their average sites, at the temperatures of interest for dynamical studies, a vacancy is assigned to a tetrahedral site only if the tetrahedron has been empty for a minimum of two frames. For this reason the interval between two frames becomes of critical importance. Too small an interval can lead to a significant vacancy over-counting, as shown in figure 3.6, whereas too long an interval can lead to under-counting because some of the oxide ions might diffuse over such a long interval. It was therefore concluded that the ideal interval between two frames should be 50 - 100 fs. This measure has already been used for the study of PbF_2 [74, 99] and seems to identify vacancies

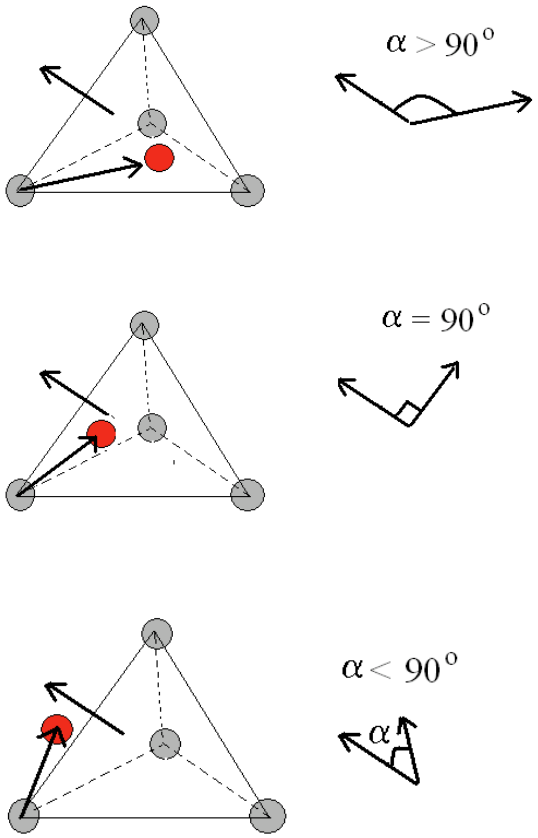

Figure 3.5: *An explanation of the vector site analysis principle. The four cations (gray circles) form a tetrahedron with one anion (red circle) in the middle. If the anion is inside the tetrahedron (top figure), then the scalar product of every vector, normal to one of the surfaces of the tetrahedron, times the position vector of the anion (starting from an arbitrarily chosen cation) is negative. When the anion is on the surface of the tetrahedron (middle figure), then the scalar product is zero. If an anion abandons its tetrahedron (bottom figure), then the product will be positive.*

reasonably faithfully even at high temperatures. This methodology was tested by calculating the number of vacancies in simulations of $Zr_2Y_2O_7$ at 300 K; it was found that the average number of vacancies is ~ 65 in good agreement with the stoichiometric value of 64. At higher temperatures (T = 1500 K), this number goes up to 70. Thermally excited Frenkel pairs make a small contribution to the excess observed at high temperature although an important factor is probably a shortcoming of our way of assigning vacancies. In fact, if a tetrahedral site contains a vacancy, it will induce a substantial distortion of surrounding tetrahedra which lowers the reliability of the geometric criterion used to decide if the site is filled or empty, especially at high temperatures where all the atoms are making large amplitude vibrations. There is therefore a tendency to assign vacancies to sites which neighbour a site containing a true vacancy, and this is manifested in a larger than expected amplitude for the nearest-neighbour peak in the vacancy–vacancy radial distribution function, as will be shown in the next chapters.

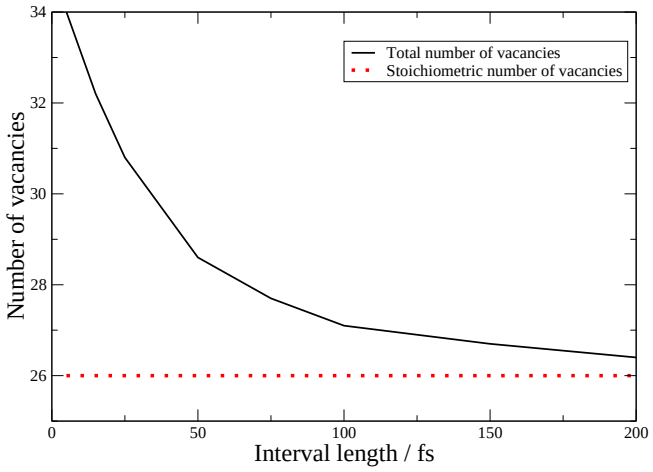

Figure 3.6: *Calculated number of vacancies for $Zr_{0.8}Y_{0.2}O_{1.9}$ at 1200 K as a function of the interval length between two consecutive frames. The red dashed line shows the number of stoichiometric vacancies present in the system.*

Once the vacancy positions have been identified, the radial distribution functions (rdfs) can be calculated for a cation-vacancy and vacancy-vacancy pair. These are then averaged over the entire run. The vacancy-cation radial distribution functions can be very useful because they show whether there is any vacancy binding tendency, i.e. it shows if the vacancy prefer to bind close to a certain cation species (as it is thought to be the case in YSZ). Vacancy-vacancy rdfs,

on the other hand, can show vacancy ordering tendencies like those postulated by Goff *et al.* [7].

3.5.4 Diffuse scattering calculation

The diffuse scattering contains information on the local disorder in a solid. For this reason, ionic conductors have been studied intensively by means of either neutron [7] or electron diffraction [43, 44, 22, 46, 58] techniques, in order to evince the local ordering tendencies and their connection with the conduction of these materials. Calculating diffuse scattering patterns from the output of a computer simulation can be very useful both to validate the reliability of the employed potential and to gain some information on the local ordering in these materials.

We calculate the intensity of the (total) scattering at a point $\mathbf{q}$ in reciprocal space from

$$I(\mathbf{q}) = \langle \sum_i \sum_j a_i a_j^\star e^{i\mathbf{q}\cdot\mathbf{r_{ij}}} \rangle \tag{3.24}$$

where the sums run over all ions in the sample, $\mathbf{r}_{ij}$ is the distance between ions i and j and a_i is the scattering amplitude of the species to which i belongs (for example, the neutron scattering length in the case of neutron scattering). The symbol $\langle ... \rangle$ indicates an average over the whole simulation. Because of the periodic boundary conditions, the accessible vectors $\mathbf{q}$ with a cubic simulation cell of side L are restricted to the set $\frac{2\pi}{L}(m, n, p)$ where m, n, and p are integers, and this provides a limit to the resolution of the simulated pattern. If a simulation box of about 50 Å (corresponding to approximately 12,000 atoms) is used, then the resolution is 0.125 Å^{-1} which is comparable with the experimental resolution of 0.10 Å^{-1} achieved in ref. [7].

If the defects which give rise to the coherent diffuse intensity are static, then the neutron scattering will be elastic, i.e., $\omega = 0$, as in equation 3.24. However, if, for example, the defects become more mobile at elevated temperature, there may be significant quasi-elastic energy broadening in the diffuse scattering. The spectral line shape of $I(\mathbf{q}, \omega)$ versus energy transfer ω then contains information on the temporal nature of the correlations between diffusing ions and the surrounding distorted lattice. This quantity can be measured experimentally and information can be obtained on the dynamics of defect clusters [7]. In the simplest case where the correlations decay exponentially with a lifetime τ, the spatial and temporal behaviour can be separated, such that

$$I(\mathbf{q}, t) = I(\mathbf{q}) e^{-t/\tau}. \tag{3.25}$$

This function can be calculated from the simulation's position file via the expression:

$$I(\mathbf{q},t) = \langle \sum_i \sum_j a_i a_j^{\star} e^{i\mathbf{q}\cdot(\mathbf{r_i}(t)-\mathbf{r_j}(0)} \rangle. \tag{3.26}$$

Plotting the above function versus time can tell whether a certain defect is mobile (if the function decays with time) or immobile (if the function does not decay) with time. The decay time will then contain information on the mobility of the vacancies.

3.5.5 Cation effects on the Mobility Distribution Functions

A detailed investigation of the mean squared displacements of the individual anions within the MD simulations of some of the systems studied in this thesis indicated that the anion mobility can be very different from case to case. In Y_3NbO_7, for instance, some anions move very fast throughout the crystal whereas some others are immobile (see chapter 5). Understanding which factors are responsible for the low mobility of some anions might obviously lead to new ways to optimise the conductivity of these materials.

To understand such a behaviour and link it with the nature of the surrounding environment, a program was developed which divided the MD simulation into a certain number steps (usually 10) of equal length. Each anion moving a distance greater than λ (with λ equal to 1.5 times the average mean square displacement of an anion over that interval) is assigned to be mobile. The distance λ was usually chosen to be comparable to the nearest neighbour anion-anion separation. Thus, it was possible to obtain the distribution of mobility for the anions in these materials, with a maximum value of 10 and a minimum value of 0. At the same time the nature of the surrounding cations was recorded as well. Plotting the average anion mobility vs the average cation environment can help understand which factors hinder the conduction in such materials. In chapter 5, it will be shown that big cations, like Y^{3+}, create trapping sites from which the oxide ions cannot escape and that this lowers the material's overall conductivity.

Chapter 4

Parameterising and testing a potential for Y_3NbO_7-$Zr_2Y_2O_7$

Developing a potential for the $Zr_{0.5-0.5x}Y_{0.5+0.25x}Nb_{0.25x}O_7$ (YNZO) system is quite a challenging operation. This series, in fact, contains three different cation species which differ considerably one from the other. Indeed, on one end there is Nb^{5+}, which is a very small cation (R_{Nb} = 0.74 Å) with a high ionic charge, whereas at the other end there is Y^{3+}, which is a very big cation (R_Y = 1.019 Å) with a relatively small ionic charge. The Zr^{4+} ion is somewhat in between (R_{Zr} = 0.84 Å). Since the cations are so different, it is reasonable to assume that they will prefer different coordination environment with the smaller cations (Nb^{5+} and Zr^{4+}) favouring a 6-fold and 7-fold coordination and the bigger one (Y^{3+}) favouring a 8-fold coordination. An indication of such a trend is found, for example, in some similar systems [100, 46, 101]. These differences in the surrounding environment, together with the very polarisable nature of the oxide ion, make the development of a potential for these materials quite difficult and challenging. It is perhaps for this reason that, up to date, no systematic attempt has been done to study this system by means of MD simulations.

In this chapter the parameterisation of inter-atomic potentials for YNZO is described together with the subsequent tests that have been run to make sure these potentials can properly reproduce the structural and dynamical properties of interest. QUAIM and DIPPIM potentials were parameterised together with simpler models, like the RIM or the RIM with partial charges. The pros and cons of each potential were thoroughly discussed.

4.1 Parameterising the potentials

In this section some details will be given on the DFT calculations used to optimise the potential and on the fitting procedure used in this specific case.

4.1.1 DFT reference calculations

Both the QUAIM and DIPPIM (as well as other) interaction models were parameterised by force-matching to DFT calculations carried out on condensed-phase configurations, as described in section 3.3. Starting from a Born-Mayer potential from the literature [47] for YSZ (with the Nb-O interaction obtained by scaling the Zr-O one with respect to the ionic radius), one atomic configuration for Y_3NbO_7 and one for ZrO_2 were generated by running short MD simulations on small cells (80–96 ions) at 1500 K. These two configurations were used to run DFT reference calculations (see below) and an initial QUAIM model was fitted to the forces, dipoles and quadrupoles. This potential was then used to generate more reference MD configurations, three for Y_3NbO_7 and three for ZrO_2 at high temperatures (> 2000 K). For each of these, the Hellman–Feynman forces acting on individual ions of the simulation cell were calculated using the planewave-DFT code CASTEP [84]. All the calculations used norm-conserving pseudopotentials generated via the OPIUM program [102] and planewave energy cut-offs of 1000 eV and were performed using the generalised gradient approximation (GGA) according to the Perdew, Burke and Ernzerhof (PBE) scheme. For the calculation of ab initio multipoles, the Kohn–Sham orbitals are localised via a Wannier transformation to construct maximally localised Wannier functions (MLWF). From the localised orbitals, ionic dipoles and quadrupoles were calculated as described in section 3.3.1.

4.1.2 Details on the force-matching procedure

The potential parameters are optimised by fitting the forces, dipoles and (when possible) quadrupoles predicted by the QUAIM and DIPPIM potentials for the reference configurations to the respective results from the DFT calculations. The 6 configurations provide a total of around 2500 data points, comprising three Cartesian force components of each individual ion, three components for the dipole and six components for the quadrupole of each ion. While most of the potential parameters are left as free parameters in the fits, there are some exceptions. In both the QUAIM and DIPPIM fits, the cation-cation short-range repulsion terms were set to zero. The cations, in fact, are very small and far away one from the other, so that their electron clouds never overlap at the pressure and temperatures of interest for these materials. In the QUAIM fits, the parameter B_i (hyperpolarisability) was set to zero, as this was not found to significantly

Table 4.1: Objective functions for the dipoles and forces.

Model	A_D	A_F
RIM	-	5.00
RIM (with partial charges)	-	0.399
DIPPIM	0.215	0.365
QUADPIM	0.149	0.352
QUAIM	0.31	0.213

affect the quality of the fit. In addition, the C_i parameter (quadrupole polarisability) was found to be very small for the cations and therefore was set to zero. For this reason, the short-range effects on the cation quadrupoles were also neglected.

One problem with DFT calculations is the uncontrolled representation of the dispersion interaction. Although dispersion energies only contribute a tiny fraction to the total energy, they have a considerable influence on transition pressures and, in particular, on the material's density and stress tensor. For this reason, the dispersion parameters were not included in the fits but were added afterwards, as discussed by Madden *et al.* [13]. The parameters in ref. [20] were used after rescaling with respect to the ionic polarisabilities. The Gaussian parameters were also added after the fit, which was then rerun to check that its quality was unchanged [74].

As described above, the fits are performed by optimizing the objective functions in equations 3.12 and 3.13. Since this is the first time that such potentials are parameterised for a system of transition metal oxides, many potential models were tried to see what the differences are and which one works best. For this reason, table 4.1 reports the values for the objective functions for the dipoles (when applicable) and forces for a series of different potential models. In figure 4.1 the evolution of A_F is shown as more effects are taken into account into the model used. For the sake of comparison, in this table were included also the values obtained from a simple RIM model and those obtained from an RIM model in which the charges too were fitted (partial charges). These two models are the ones which have been most used in the past years for the study of oxide systems [68, 27, 69, 52, 47, 49, 50, 51]. A series of comments can be readily made. First of all, the simple RIM is completely *inadequate* for a good description of the inter-atomic forces in these oxide systems! This appears clear from the very high value the objective function has in this case. As a quick test it was decided to show, in figure 4.2, the total radial distribution function for Y_3NbO_7, obtained from a neutron experiment [103], compared to the one calculated with our RIM potential, in a NVT simulation. The agreement

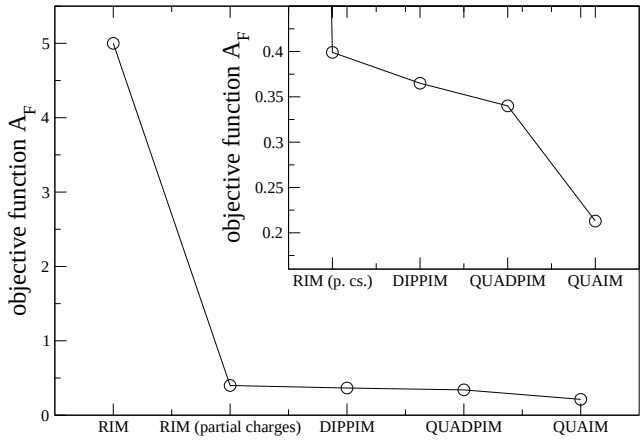

Figure 4.1: *Evolution of A_F for different potential models. The inset shows the same figure without the RIM (which is off the scale).*

is quite poor, especially for the first two peaks, which are caused by the Y-O and Nb-O bonds. The Nb-O distance obtained from the simulation is 2.05 Å, in poor agreement with the experimental value of 1.96 Å. Also the predicted lattice parameter for this material is about 5% greater than the experimental value. The complete failure of the RIM to properly describe this system comes as a surprise, since the vast majority of the studies on stabilised zirconias has been performed by using this model [27, 52, 47, 49, 50, 51].

Next, a RIM with partial charges was tried. This represents a simple attempt at including, on average, polarisation effects by reducing the ionic charges. This procedure seems to work much better, given that the obtained value for A_F is more than *ten* times smaller than for the simple RIM. Also the obtained $G(r)$ and lattice parameters for the Y_3NbO_7 system (not shown) are in better agreement with the experimental data, though the cation-anion distance are still quite different from the experimental values. Although this procedure is simple and fast, it is still preferable to use formal charges. In fact, the use of full formal charges, coupled with a physically based description of induction effects, presents the best chance of deriving models that are truly transferable over a range of different state points and compositions. This was proven, for instance, in the case of GeO_2 (see appendices B and C). The use of partial charges, the values of which are not physically well defined, tends to restrict the applicability of potential models to specific statepoints. Furthermore, the use of the full formal charges

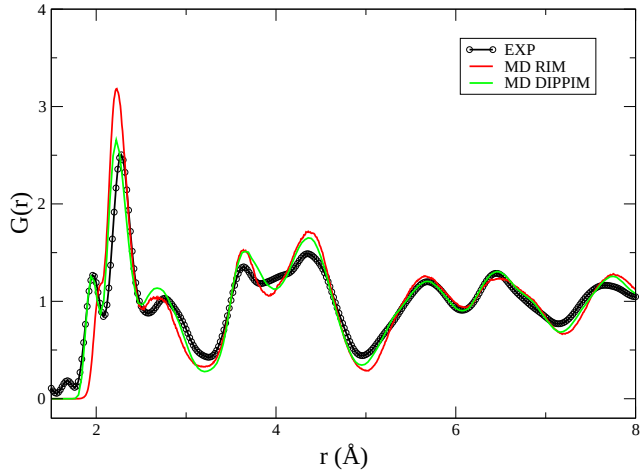

Figure 4.2: *Comparison between the experimental (black points+line) [103], RIM (red line) and DIPPIM (green line) total G(r) for Y_3NbO_7, at 300 K.*

allows a direct comparison between the potential model and the experimental thermophysical quantities (see next chapter).

The DIPPIM model gives a reasonably good agreement with both the DFT dipoles and forces. This agreement with the DFT forces is also better than the one obtained with the RIM with partial charges. As mentioned in the previous chapter, Wilson and co-workers obtained a $A_F \sim 0.1$ for Li_2O with a QUAIM potential. If it is considered that a much simpler model is being used and that our system is a ternary mixture of transition metal oxides, the obtained value can be considered quite satisfactory (see next sections for further discussion on this). This is also confirmed by figure 4.2, which shows that this model reproduces quite well the experimental $G(r)$ for Y_3NbO_7. Figure 4.3 reports the agreement between the DFT-calculated forces and dipoles and those predicted by the fitted potential, for a set of representative ions; the abscissa shows the x component of the forces and dipoles, while the ordinate is simply the ion number.

The QUADPIM potential gives only a small improvement over the DIPPIM. The QUAIM potential, however, gives a much better agreement with the DFT forces, $A_F = 0.213$. This is not surprising as this model is indeed more complex than the DIPPIM. The value obtained for A_F is a bit higher than that obtained for Li_2O in ref. [19]. However, considering that Li_2O

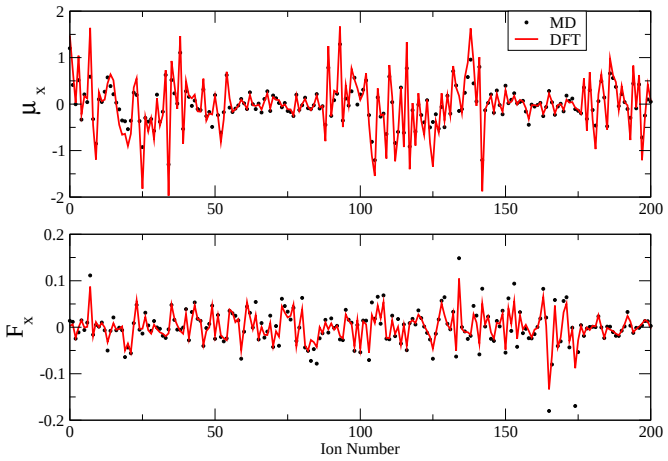

Figure 4.3: *Agreement between the DFT-calculated dipoles (top panel) and forces (bottom panel) and those predicted by a fitted DIPPIM potential model for a set of 200 representative ions. In each panel the ordinate gives the ion number and the abscissa gives the fitted values of the x component of the forces and dipoles as points and the DFT values as the continuous line.*

is a much simpler system than YNZO, this value can be regarded as good. In the next section it will be shown how this potential gives an excellent agreement with the structural properties obtained for different YNZO mixtures.

The parameters obtained for the QUAIM and DIPPIM potentials are summarised in tables 4.2 and 4.3. After fitting such a complicated model with tens of parameters it is useful to check that the derived parameters retain their physical meaning. The oxygen polarisability, for instance, is $\alpha \sim 14$ au (for both potentials) which is in good agreement with that used previously in a similar study [76] and that obtained by extrapolation of ab initio calculations on other oxides [79]. In addition, the Y^{3+} and Zr^{4+} polarisabilities are in good agreement with the value of 4.05 au in [79] (ab initio calculations) and 2.76 au (experimental dielectric properties coupled with ab-initio calculations) [104, 105], respectively.

Table 4.2: Parameters for the QUAIM potentials with values in a.u.. Those short-range parameters which are equal to zero are not reported.

	O-O	Y-O	Zr-O	Nb-O
A^{ij}	0.0	165.19	345.01	159.76
a^{ij}	5.0	1.7586	1.9590	1.7038
B^{ij}	50000	50000	50000	50000
b^{ij}	0.85	1.2	1.2	1.3
C_6^{ij}	44	10	10	5
C_8^{ij}	853	200	200	100
b_{disp}^{ij}	1.0	1.5	1.5	1.5
D	0.1616			
ζ	1.168			
α	14.49	4.86	2.67	2.53
β	3.154			
η	14.842			
C	1.5574			

b_D^{O-O}	2.097	b_D^{O-Zr}	1.778
c_D^{O-O}	1.058	c_D^{O-Zr}	1.674
b_Q^{O-O}	2.363	b_Q^{O-Zr}	1.048
c_Q^{O-O}	4.999	c_Q^{O-Zr}	0.645
b_D^{O-Y}	1.811	b_D^{Y-O}	1.810
c_D^{O-Y}	2.285	c_D^{Y-O}	-0.891
b_Q^{O-Y}	1.837	b_D^{Y-Nb}	1.778
c_Q^{O-Y}	1.442	c_D^{Y-Nb}	0.717
b_D^{O-Nb}	1.845	b_D^{Nb-O}	1.845
c_D^{O-Nb}	1.714	c_D^{Nb-O}	-0.523
b_Q^{O-Nb}	1.865	b_D^{Nb-Y}	1.788
c_Q^{O-Nb}	1.203	c_D^{Nb-Y}	3.500

Table 4.3: Parameters for the DIPPIM potentials with values in a.u.. Those short-range parameters which are equal to zero are not reported.

	O-O	Y-O	Zr-O	Nb-O
A^{ij}	4.97	104.53	55.05	59.11
a^{ij}	22.99	1.389	1.144	1.137
B^{ij}	50000	50000	50000	50000
b^{ij}	0.85	1.35	1.43	1.53
α	13.65	4.73	3.23	3.76
C_6^{ij}	44	10	10	5
C_8^{ij}	853	200	200	100
b_{disp}^{ij}	1.0	1.5	1.5	1.5

b_D^{O-O}	1.99	b_D^{O-Zr}	1.642
c_D^{O-O}	0.689	b_D^{O-Zr}	1.396
b_D^{O-Y}	1.824	b_D^{Y-O}	1.806
c_D^{O-Y}	2.215	b_D^{Y-O}	-0.455
b_D^{O-Nb}	1.844	b_D^{Nb-O}	1.805
c_D^{O-Nb}	1.700	b_D^{Nb-O}	3.50

4.2 Validation of the QUAIM and DIPPIM potentials

In this section the quality of the QUAIM and DIPPIM potentials will be assessed by comparing model predictions to experimental data. Since no experimental data were used in the optimisation of the model parameters, a strong test for the quality of the model is whether it is able to reproduce experimental data of physical properties of the YNZO system at different conditions (high temperatures, different mixtures and so on).

The YNZO system has been recently the object of extensive experimental work [103] which used a combination of impedance spectroscopy measurements of the ionic conductivity (σ) and powder neutron diffraction studies, including analysis of the total scattering to probe the nature of the short-range correlations between ions using reverse Monte Carlo (RMC) modeling [1]. These data, together those in refs. [21, 22], are an obvious testbed.

4.2.1 Structural properties of Y_3NbO_7-$Zr_2Y_2O_7$

All the simulations on the Y_3NbO_7-$Zr_2Y_2O_7$ system were performed using a cubic simulation box with 4 x 4 x 4 unit cells, i.e. 256 cations and 448 oxygen ions. The cation species were randomly distributed over the cation sublattice, since there is no experimental evidence of any ordering [21, 22, 106]. These simulations will be labelled as *d*-fluorite simulations [2]. The time step used was 20 au = 0.484 fs and all the runs were performed at constant temperature and zero-pressure (NPT ensemble). The simulations were started from a perfect fluorite structure and the system was equilibrated at 2000 K for 50,000 steps, to allow both cations and anions to relax in the crystal. The system was then cooled down, first to 1000 K for 10,000 steps and then to 300 K for another 10,000 steps, before a final run of 10,000 steps was performed to accumulate sufficient statistics for the calculation of the radial distribution functions.

QUAIM potential

First the total radial distribution functions were calculated, with the QUAIM potential , for the $Zr_{0.5-0.5x}Y_{0.5+0.25x}Nb_{0.25x}O_7$ system, for x = 0.0, 0.2, 0.4, 0.6, 0.8, 1.0. These are reported in figure 4.4 (top) and compared with the $G(r)s$ obtained by Fourier transform of the experimental neutron structure factor, $S(q)$. The agreement with the experimental data looks

[1] As mentioned in the Introduction, this study is part of a joint research project with Dr Stefan Norberg and Dr Stephen Hull, from the ISIS Neutron Facility, aiming at getting a better understanding of the conduction mechanism in solid oxide electrolytes.

[2] In the next chapter this assumption will actually be reconsidered.

excellent across the entire $Zr_{0.5-0.5x}Y_{0.5+0.25x}Nb_{0.25x}O_7$ series. This indicates that the potential is highly transferable and works for different values of x. The QUAIM model also succeeds in reproducing the lattice parameter increase as x is decreased (see figure 4.4, bottom). The agreement with the experimental values is within 0.5 %.

Next, a comparison is made between the partial radial distribution functions extracted from the neutron diffraction data via bond-valence-sum-constained reverse Monte Carlo [107] and those obtained from the simulations. In figures 4.5 and 4.6 it is shown the comparison between the anion-anion and cation-anion rdfs. These are reported for the two end systems (Y_3NbO_7 and $Zr_2Y_2O_7$) only, for the sake of clarity. In figure 4.5 the $g_{O-O}(r)s$ are compared with those expected from a perfect fluorite structure (green curve). It is clear that both systems are quite disordered, as proved by the big differences observed between the green curves and the experimental points. The agreement between the simulated (black points) and the experimental (red curve) rdfs is excellent, thus proving that the QUAIM potential can successfully account for the structural disorder observed in these systems. The simulations can even reproduce small features like, for example, the peak observed at $\sim$ 3.8 Å in Y_3NbO_7. A more extended discussion of these functions and of the relationship between the observed structural disorder and the conducting properties of these materials will be presented in the next chapter.

Figure 4.6 shows the cation-anion rdfs for the two end members. Again, the agreement with the experimental data is excellent. The location of the first peak is observed at around 2.28, 1.96 and 2.10 Å for Y-O, Nb-O and Zr-O respectively. These differences in the bond distances are consistent with the ionic radii reported by Shannon [59]. Interestingly, the bond distances for Y-O and Zr-O given by the simulations imply an oxygen coordination number of between 6 and 7 whilst the Nb-O bond distance suggests an oxygen coordination number slightly lower than 6. This will be discussed in depth in the next chapter, since it is these differences in the local environment that cause the great differences observed in the ionic conductivity of these materials.

A final test can be performed by calculating the angular distribution functions. In the ideal cubic fluorite structure the cations are situated at the centre of a cube of anions and the expected O–cation–O bond angles are 70.5°, 109.5° and 180°, corresponding to anion pairs that are nearest neighbours along the directions $\langle 100 \rangle$, $\langle 110 \rangle$, $\langle 111 \rangle$, respectively. Figure 4.7 plots the angular distribution functions, $A_{OcationO}(\theta)$, obtained from both the RMC and the MD simulations. The cases of $A_{OYO}(\theta)$ and $A_{OZrO}(\theta)$ show broad peaks centred at the expected angles, whilst the $A_{ONbO}(\theta)$ angular distributions are shifted towards bond angles distributed

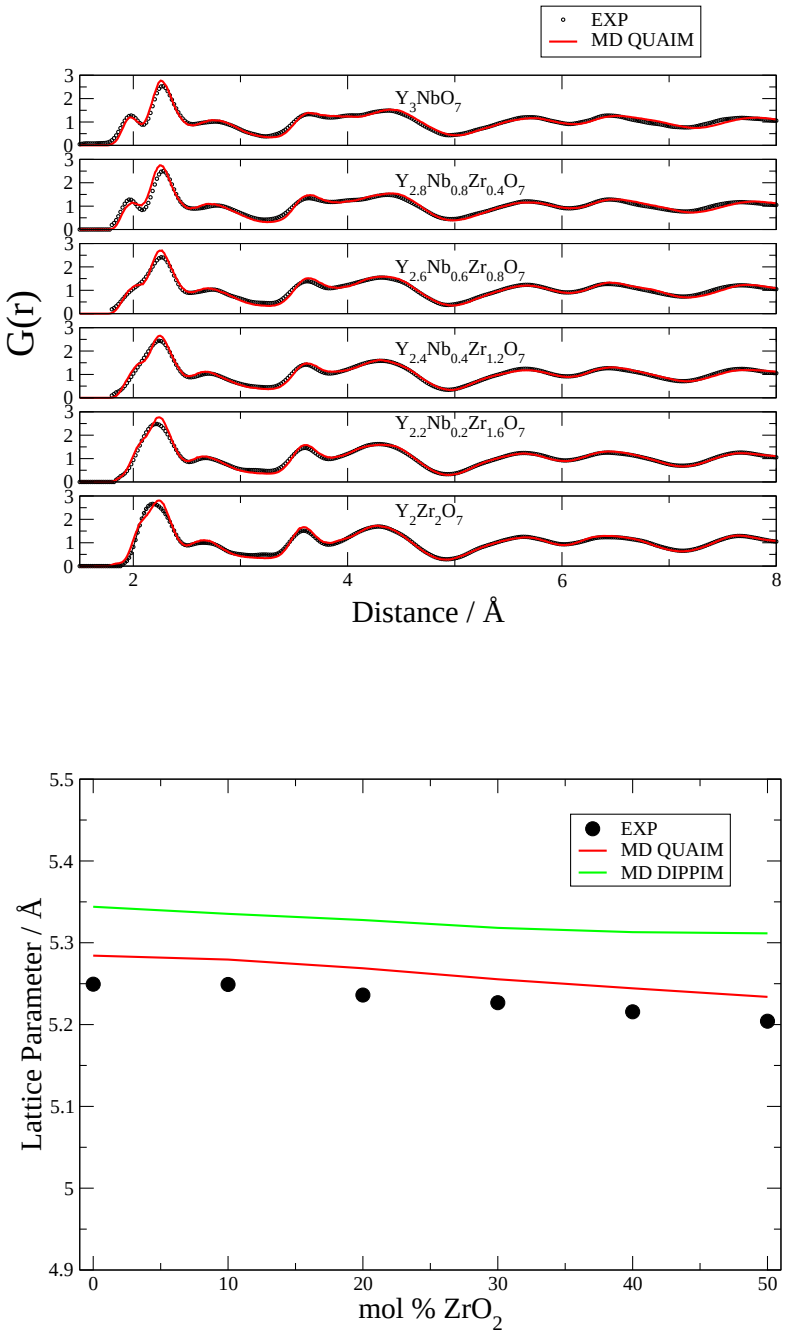

Figure 4.4: *Top: comparison between the experimental [103] and simulated total G(r) for the $Zr_{0.5-0.5x}Y_{0.5+0.25x}Nb_{0.25x}O_7$ system, at 300 K. Bottom: comparison between the experimental lattice parameters [103] and the simulated ones for both the DIPPIM and QUAIM.*

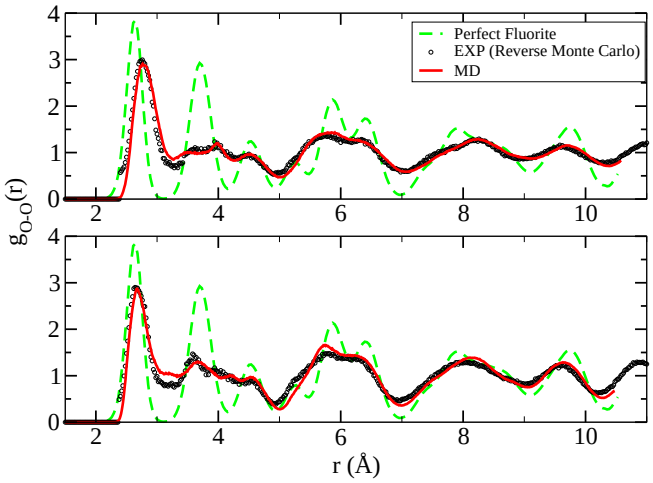

Figure 4.5: *Comparison between the oxygen-oxygen rdf obtained via RMC analysis [103] and the simulated ones for Y_3NbO_7 (top) and $Zr_2Y_2O_7$ (bottom), at 300 K.*

around 85° – 95° and 180°. The agreement between the Reverse Monte Carlo analysed data and the simulations is excellent. This represents an even stricter test because, while the total scattering depends on two-particle correlations, the bond angle involves the relative position of three particles. The Nb–O pair distribution function described above indicates, again, that the Nb^{5+} is coordinated to around 6 surrounding oxygen atoms, as opposed to 7 for Y and Zr. These observations suggest that the Nb^{5+} cation is attempting to adopt a distorted octahedral geometry of surrounding anions, of the type found in several phases of Nb_2O_5 [108, 109]. This will be discussed in depth in the next chapter.

In conclusion, the QUAIM potential seems to be able to reproduce the structural features very well across the whole series. Indeed, the agreement with both the total and partial rdfs and the bond angle distributions extracted from the neutron data is excellent. Unfortunately, this potential has also the drawback of being computationally very expensive. Although this approach is still much faster than a pure DFT approach, the study of relatively big systems ($\sim$ 1000 atoms) for long times (1-10 ns) is still beyond our current computing capacities. For this reason it was decided to test the DIPIPIM potential (which is at least one order of magnitude faster than the QUAIM) to see if this can be used reliably for the study of the conducting properties of these systems.

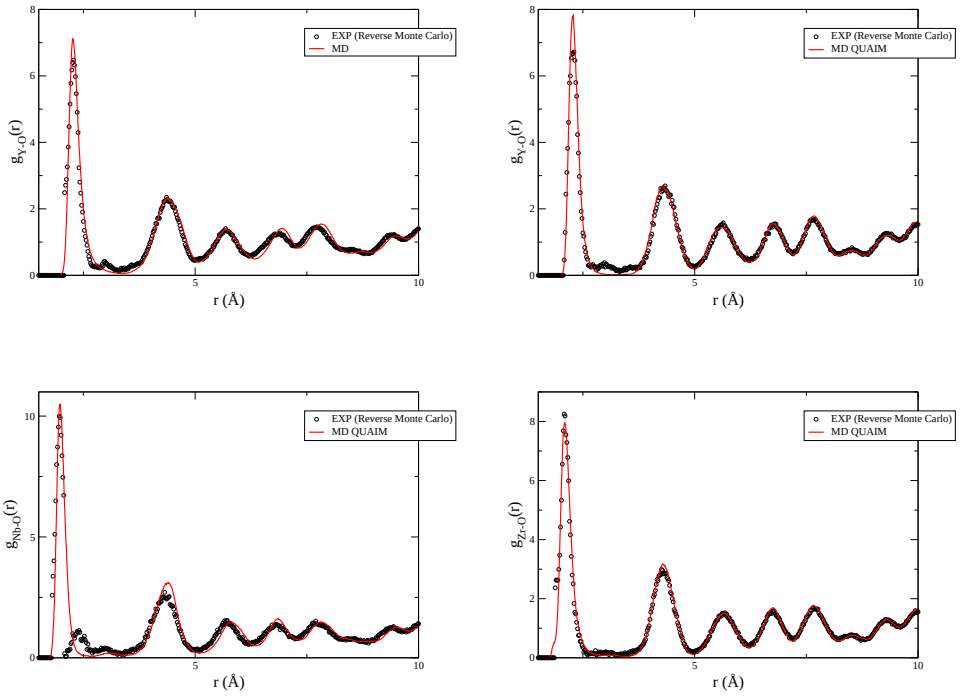

Figure 4.6: *Cation-anion radial distribution functions, $g_{ij}(r)$, as determined from RMC (black dots) and QUAIM (solid red line) simulations at room temperature. The peak at 2.4 Å observed in the experimental data in the Nb-O plot is probably an artifact of the RMC data analysis.*

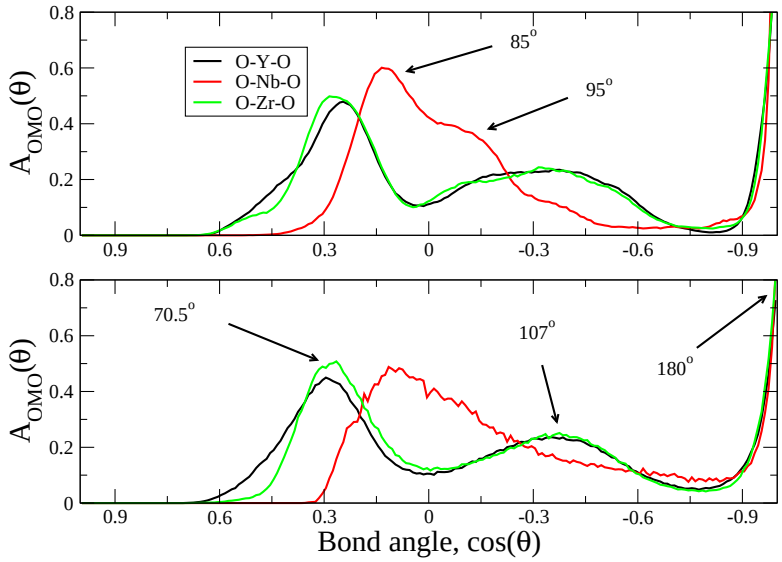

Figure 4.7: *The calculated angular distribution functions, $A_{OYO}(\theta)$ (long dashed line), $A_{OZrO}(\theta)$ (short dashed line) and $A_{ONbO}(\theta)$ (solid line), from both the QUAIM (top) and RMC (bottom) simulations. The arrows indicate the angles in degrees.*

DIPPIM potential

Figure 4.4 (bottom) reports the lattice parameters as predicted by the DIPPIM potential. The difference with the experimental values is greater ($< 1.5\%$) than that observed with the QUAIM potential. This sort of difference is usually considered normal when less sophisticated potentials are used [47, 110]. For this reason, the simulations with the DIPPIM potential have been carried on in the NVT ensemble, at the experimental density. A comparison between the simulated total rdf, $G(r)$, obtained for the YNZO system using DIPPIM potential and the experimental ones is shown in figure 4.8. The agreement with the data is quite good across the whole series, meaning that also the DIPPIM potential is able to properly describe this system.

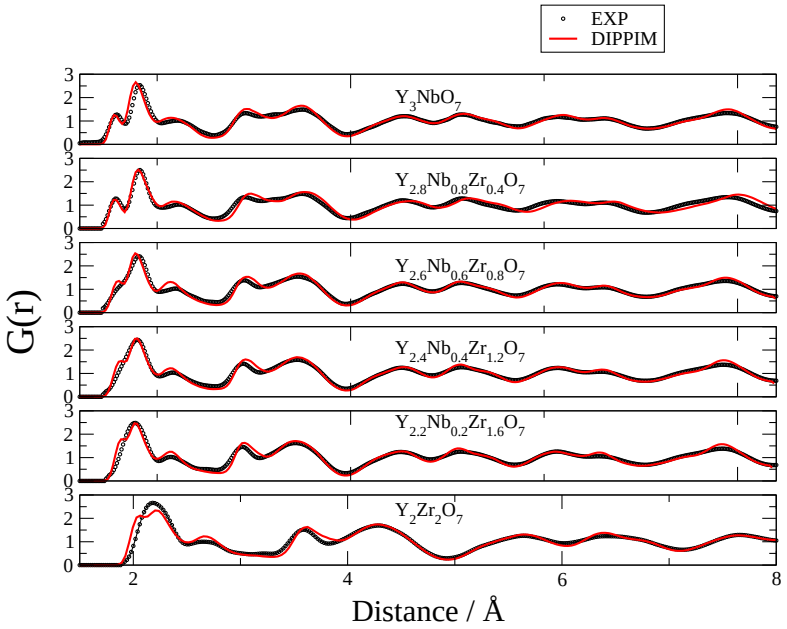

Figure 4.8: *Comparison between the experimental [103] and simulated total G(r) obtained with a DIPPIM potential for the* $Zr_{0.5-0.5x}Y_{0.5+0.25x}Nb_{0.25x}O_7$ *system, at 300 K.*

Next the partial rdfs are compared in the same way as was done with the QUAIM potential. Figure 4.9 reports the O-O rdfs for the two end systems. The agreement with the experimental data is very good for Y_3NbO_7 but less compelling in the case of $Zr_2Y_2O_7$. In fact, while in the first case the DIPPIM potential can successfully reproduce all the small features observed between 3 and 5 Å, it fails to reproduce the small peak at 3.6 Å observed in the $Zr_2Y_2O_7$ rdf. In a way, the structure obtained with the DIPPIM potential is a bit more disordered than the ex-

perimental one. This limitation is however expected not to be relevant at higher temperatures (at which these materials are used in technological applications and which will be the focus of this thesis) where these subtle features in the rdfs will be washed out by the large thermal vibrations the ions perform at those temperatures. A visual comparison of the $g_{O-O}(r)$ (not shown) obtained from a simulation at 2000 K with a DIPPIM and QUAIM potential confirms that at high temperatures the rdfs look identical.

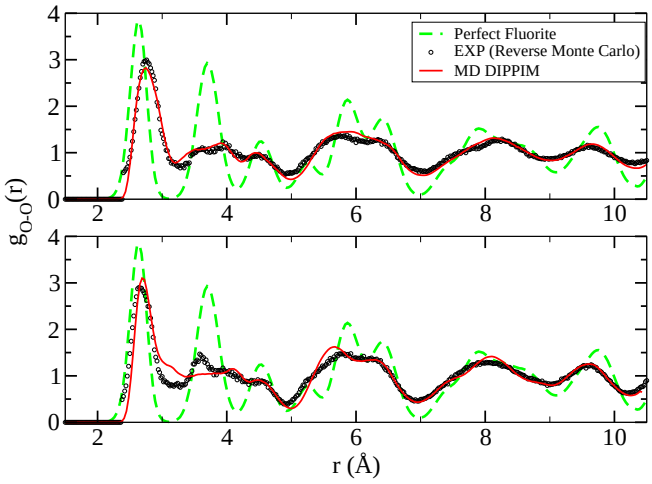

Figure 4.9: *Comparison between the oxygen-oxygen rdf obtained via RMC analysis [103] and the simulated ones, obtained with a DIPPIM potential, for Y_3NbO_7 (top) and $Zr_2Y_2O_7$ (bottom), at 300 K.*

A final comparison was made with the cation-anion radial distribution functions obtained with the DIPPIM potential. This is important because a good agreement with the experimental data would imply that the model can properly reproduce the different cation-oxygen distances. The rdfs are shown in figure 4.10. From these it can be seen that the agreement is very good and the cation-oxygen distances are in perfect accord with the experimental values (2.28, 1.96 and 2.10 Å for Y-O, Nb-O and Zr-O respectively), unlike the case of the RIM. This perhaps is the most important quality indication. In fact, since the main objective of this work is to study the effects that different cations have on the conduction mechanism of this system, it is of primary importance to be able to properly reproduce the differences in size and charge of the cations.

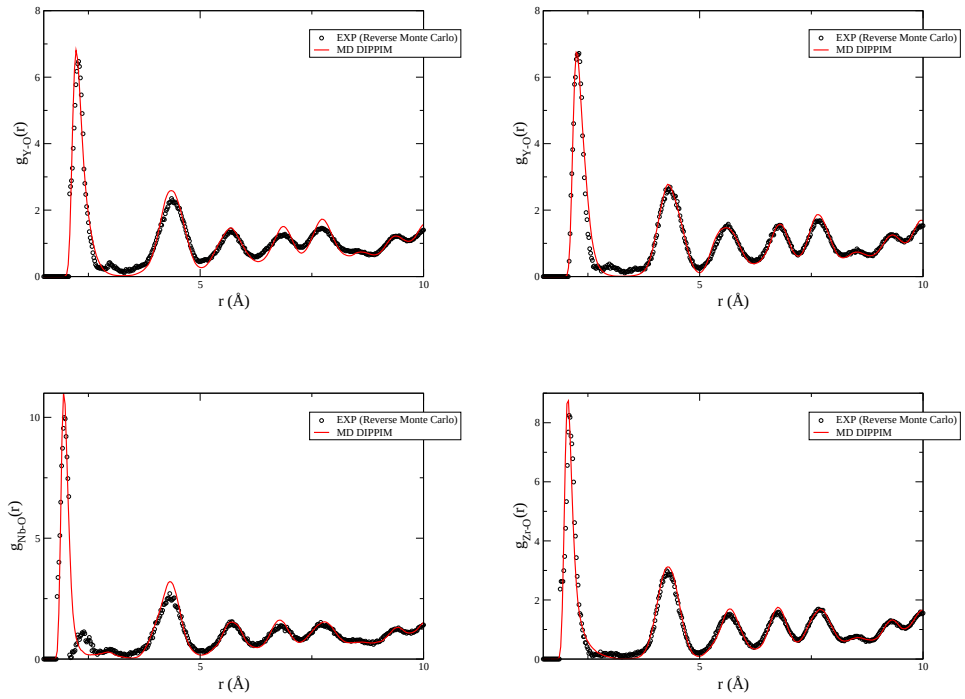

Figure 4.10: *Partial radial distribution functions, $g_{ij}(r)$, as determined from RMC (black dots) and DIPPIM (solid red line) simulations at room temperature.*

In conclusion, both the employed models (QUAIM and DIPPIM) are able to reproduce virtually all of the structural features of this system. The QUAIM potential, being a more accurate model, gives a better agreement with the experimental data than the simpler DIPPIM potential. The latter, however, is computationally less expensive and allows the study of big systems for very long times. In the next section the ability of the DIPPIM and, whenever possible, of the QUAIM potential to reproduce the conductivity data for the YNZO system will be tested.

4.2.2 Conducting properties of Y_3NbO_7-$Zr_2Y_2O_7$

All the simulations were started from the room temperature runs described above. These were equilibrated at the required temperature for at least 100,000 steps (corresponding to $\sim$ 50 ps) and then longer runs were performed to accumulate sufficient statistics for the calculation of the mean squared displacements. All the simulations were performed in the NVT ensemble in which the cell volume was obtained from a previous NPT run. The diffusion coefficients were obtained from the slope of the mean squared displacement curve and from these the ionic conductivities were calculated as described in section 3.5.2.

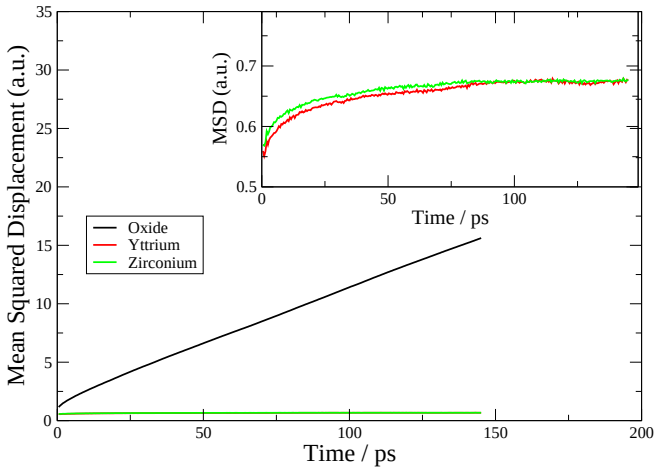

Figure 4.11: *Mean Squared Displacements for the different ions in $Zr_2Y_2O_7$. The inset shows a zoom of the cation mean squared displacements.*

Calculations of the mean squared displacements of the ionic species in YNZO clearly

demonstrate that the oxygen ions are mobile whilst the cations show no diffusive behaviour (see figure 4.11). Figure 4.12 shows the $log\ \sigma\ T$ as a function of the inverse temperature for $Zr_2Y_2O_7$, and compares the data obtained with the DIPPIM potential with the ionic conductivity published by Lee *et al.* [21] and Norberg *et al.* [103]. The simulations had to be performed at high temperatures (T $>$ 1300 K), since the slow dynamics at lower temperatures would require extremely long simulations in order to obtain a meaningful mean squared displacement curve from which a diffusion coefficient can be extracted [3]. The agreement between the experimental and simulated ionic conductivities is quite good, with the differences probably caused by the density of the sample pellets being less than 100% and/or the assumption of uncorrelated motion of the charge carriers (as explained in section 3.5.2). An attempt was made to measure the ionic conductivity by using equation 3.23. However, as discussed before, this methodology is usually affected by very poor statistics, especially when conduction is quite slow, as it is the case for T $<$ 1500 K. For this reason, it was possible to get a reliable value of the true conductivity from very long runs ($>$ 1 ns) for T $\geq$ 1500 K. At 1500 K σ = 0.05 S/cm, which is 1.6 times smaller than the Nernst–Einstein value and in much better agreement with the experimental values in [21, 103]. At higher temperatures the differences between the two methods of calculating the conductivity become smaller. This implies that at these temperatures (T $>$ 1500 K) correlation effects become negligible in these systems.

The inset of figure 4.12 shows the evolution, in $Zr_{0.5-0.5x}Y_{0.5+0.25x}Nb_{0.25x}O_7$, of the ionic conductivity at 2000 K, as x is changed. This has to be compared with figure 2.8. It can be seen that the DIPPIM potential can semi-quantitavely reproduce the change in conductivity observed experimentally. Y_3NbO_7 is in fact a much worse ionic conductor and very long simulations at high temperatures are required to get reliable mean squared displacements. This explains why the simulations were carried out at 2000 K in this case. However, it is found that the DIPPIM potential substantially overestimates the conductivity of Y_3NbO_7 at T = 1500 K. The value obtained from the MD simulation is σ (T = 1500 K) = 0.016 S/cm to be compared with σ (T = 1473 K) = 0.0019 S/cm. As it will be explained in the next chapter, this discrepancy is not a limitation of the employed potential but it is caused by our assumption that local cation ordering is not present in this system. Along the same line, it was also found that the conductivity of this material depends on the cation arrangement. As discussed above, the Y^{3+} and Nb^{5+} cations are usually randomly placed on the cation sublattice. In some cases, simulations on Y_3NbO_7 with different cation placements (but at the same temperature and density) present some important differences in the ionic conductivity (more than 30%). The influence

[3] All simulations are run until each oxygen ion has moved, on average, at least one oxygen-oxygen interatomic distance ($\sim$ 2.6 Å). At T = 1300 K, this requires simulations a few nanosecond long, which is approximately our current computational limit.

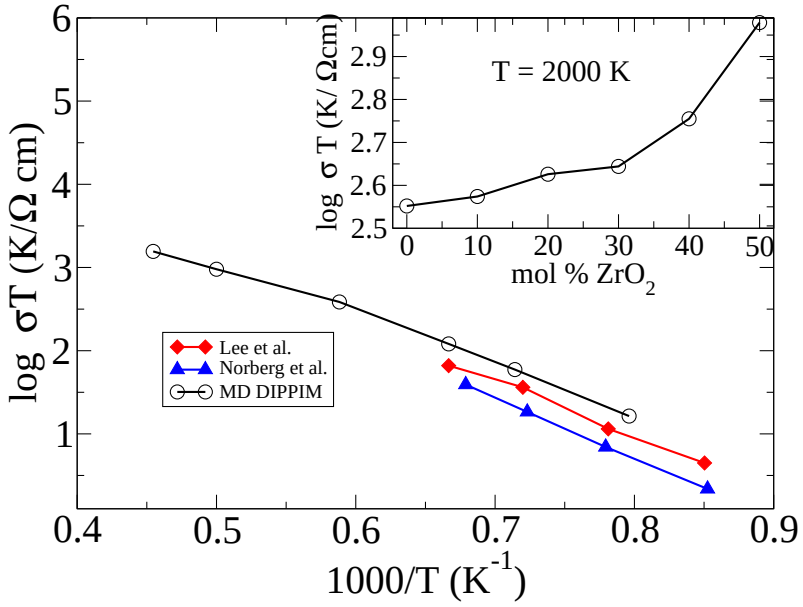

Figure 4.12: *Comparison between the measured conductivity data of Lee et al. [21] and Norberg et al. [103] and the DIPPIM simulations for $Zr_2Y_2O_7$. The inset shows the changes in the MD simulated conductivity at 2000 K as a function of x in $Zr_{0.5-0.5x}Y_{0.5+0.25x}Nb_{0.25x}O_7$.*

of the cation arrangement on the material's conductivity will be discussed in detail in the next chapter.

As mentioned before, it is not feasible to use the QUAIM potential to study the conductivity of this system at the temperatures of interest. However, one simulation on $Zr_2Y_2O_7$ was run at 2000 K to check that the results are consistent with those obtained with the DIPPIM potential (which in turn are consistent with the experimental data). The Nerst-Einstein conductivities were calculated, since at such a high temperature there is no appreciable difference with the values obtained from integrating the charge current. The obtained value was σ_{QUAIM} = 0.29 S/cm, to be compared with σ_{DIPPIM} = 0.50 S/cm. The QUAIM potential gives lower ionic conductivities than the DIPPIM. Since the latter tends to overestimate the conductivity, it might seem that the QUAIM potential gives more accurate results, although further testing is required.

In conclusion, the DIPPIM potential seems to reproduce the main trends in the conductivity quite successfully. The temperature dependence of the $Zr_2Y_2O_7$ conductivity compares well with the available experimental data as does the doping dependence of $Zr_{0.5-0.5x}Y_{0.5+0.25x}Nb_{0.25x}O_7$. The only observed limitation (a severe overestimation of the ionic conductivity of Y_3NbO_7) will be discussed in the next chapter.

Chapter 5

The conduction mechanism in Y_3NbO_7-$Zr_2Y_2O_7$

This first part of this chapter reports a detailed examination of the structure and ion dynamics in the *d*-fluorite simulations which, as showed in the last chapter, successfully reproduce the trends observed in the properties of the YNZO series [1]. In order to clarify how these properties are affected by the cation species, the effects of modifying our first-principles interaction potentials are considered, by equalising the cation charges and the range of the short-range repulsive interactions between the cations and the oxide ions. The structure of the material is then considered from the perspective of the vacancies and cation-vacancy and vacancy-vacancy ordering tendencies are found similar to those observed in the ab initio studies of other stabilised zirconias [8]. In the final part of this chapter the initial assumption that the cations are randomly distributed over the sublattice will be reconsidered and the effects, on the conductivity, of partially ordering the cations will be considered.

5.1 Disorder and mobility in the *d*-fluorite structure of $Zr_2Y_2O_7$ and Y_3NbO_7

All the simulations described in this chapter are thoroughly equilibrated at high temperatures (1500-2000 K) in constant pressure simulations before obtaining dynamical information from constant volume runs at the zero-pressure volume. At these high temperatures the oxide ions

[1] We remind the reader that by *d*-fluorite simulations it is meant simulations in which the cation species are randomly distributed over the cation sublattice.

are diffusing on the simulation timescale but there is no significant exchange of cations (see figure 4.11). Some simulations were also quenched down to room temperature and further short runs were conducted in order to examine structural information and compare with diffraction data collected at the same temperature. Note that, because the ionic mobility drops sharply as the temperature is reduced during the quench, that these runs are not fully equilibrated. To some extent, this will also be true of experimental samples which are prepared at high temperature and quenched [21, 22], though the rate of cooling is much slower than for the simulated systems.

The discussion is started by analysing the results on the *d*-fluorite structure, which are initialised by randomly distributing the cation species over the cation sublattice and randomly assigning oxide anions to the anion lattice. Theoretical calculations show the energy scale associated with cation ordering is very small [8, 34] in yttria-stabilised zirconias and extensive powder diffraction and RMC analyses across the whole series $Zr_{0.5-0.5x}Y_{0.5+0.25x}Nb_{0.25x}O_{1.75}$ provided no strong evidence[2] for cation ordering [103], in agreement with previous studies [21]. For the sake of clarity, the following discussion will focus on the results for the end members (x = 0 and x = 1) of the series, *i.e.* $Zr_2Y_2O_7$ and Y_3NbO_7.

5.1.1 Cation-induced disorder

The disordered character of the anion sublattice can be appreciated from the oxygen-oxygen radial distribution functions taken from the room temperature runs, $g_{O-O}(r)$ (see figure 4.5). They are compared with those expected from a perfect fluorite structure with the same lattice parameter (and with the $g_{O-O}(r)$ obtained from the RMC analysis of the experimental data [103]). The first peak in $g_{O-O}(r)$ for Y_3NbO_7 is shifted by 0.13 Å from the expected position for an ideal fluorite structure and the second peak (which indicates the distance between two next-nearest neighboring oxygen ions) is broadened and presents a number of subsidiary features. $Zr_2Y_2O_7$ shows similar but less marked deviations from the ideal fluorite order, as already noted from the diffuse scattering intensity [103, 21].

In the fluorite structure, the anions sit in a tetrahedral site (see figure 2.1). Because the cation species are distributed randomly in the *d*-fluorite $Zr_2Y_2O_7$-Y_3NbO_7 system, the vertices of these tetrahedra may be occupied by different combinations of cations. A snapshot of the simulation cell in Y_3NbO_7 can be seen in figure 5.1. The two black circles highlight those

[2]It has to be remembered, however, that, because of weak scattering contrast, neutron diffraction experiments are not very sensitive to cation ordering.

oxide ions that are surrounded by Y^{3+} cations only and the red squares those with a significant number of Nb^{5+} ions in their coordination environment. Notice that the former are much more tightly grouped about the lattice site than the latter. The notion that the Nb^{5+} cations are somehow responsible for the disorder observed in Y_3NbO_7 is confirmed by the fact that the Y-O and Nb-O distances, obtained from the RMC analysis of the neutron scattering data in reference [103] (or analogously from our simulations), are quite different ($d_{\mathrm{Nb-O}}$ = 1.96 Å $d_{\mathrm{Y-O}}$= 2.28 Å). In a perfect fluorite structure, the anion-cation distance is $d_{an-cat} = \sqrt{3}/4\ a$ = 2.27 Å, where a is the lattice parameter obtained from the RMC analysis. It is therefore evident that the Nb^{+5} ions are attracting the oxygen ions very tightly, thus disrupting the perfect fluorite order. This effect is less significant in $Zr_2Y_2O_7$ because the cation charges are 3+ and 4+ in this case and because the cation radii are more similar.

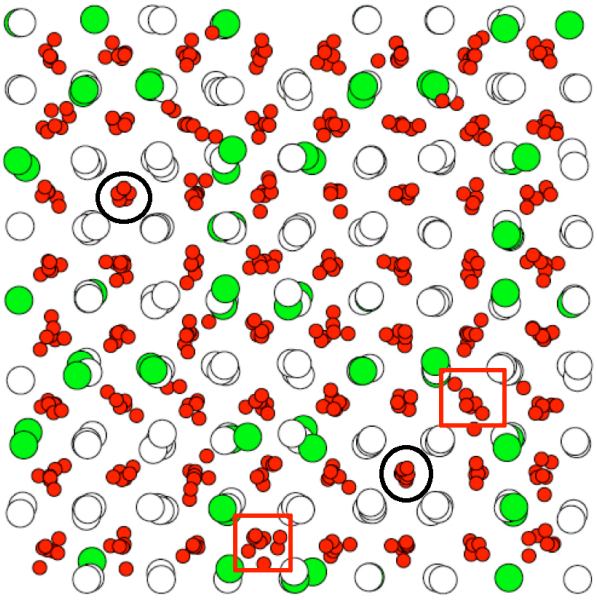

Figure 5.1: *Snapshot along the z axis of the simulation box in Y_3NbO_7. The color code is white, green and red for yttrium, niobium and oxygen ions respectively. The two black circles show those oxygen ions which are surrounded by yttrium ions only, whilst the two red squares show those which are surrounded by both niobium and yttrium ions.*

5.1.2 Cation effects on anion mobility

The inhomogeneities induced by this strain lead to a significant difference in conduction mechanisms between $Zr_2Y_2O_7$ and Y_3NbO_7. Figure 5.2 shows the mobility distribution functions

(calculated as described in section 3.5.5) which analyse the probability for the oxide ions to make a certain number of diffusive hops (by the O-O nearest-neighbour separation) during the course of the simulations at 1500 K. In Y_3NbO_7 a large fraction of anions (about 1/4 of the total number) do not hop at all during the whole simulation whereas a few anions possess a high mobility. The former make no contribution to the conductivity. $Zr_2Y_2O_7$, on the other hand, has a more homogeneous behaviour with fewer immobile oxygen ions and a probability distribution which peaks about the average mobility of 2-3, with relatively few outliers. Further examination (see below) shows that the immobile oxide ions in Y_3NbO_7 are in tetrahedral sites where all the vertices are occupied by Y^{3+} cations.

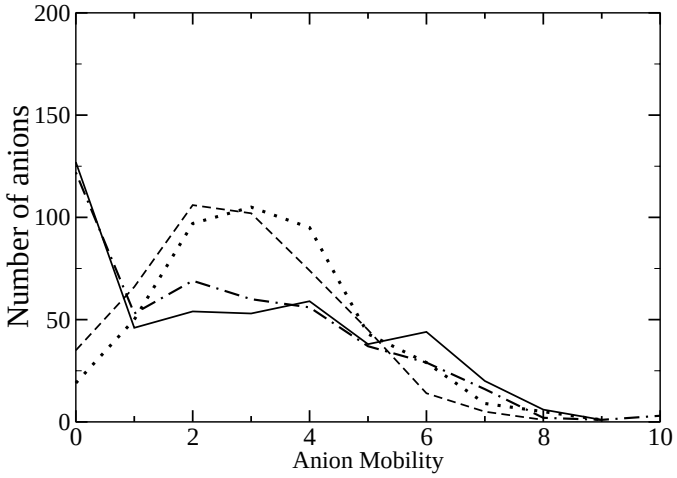

Figure 5.2: *Number of ions with certain mobility against the mobility itself for Y_3NbO_7 (solid line), $Zr_2Y_2O_7$ (dashed line), equal-charge Y_3NbO_7 (dotted line) and equal-radius Y_3NbO_7 (dot-dashed line).*

As a consequence, the conductivity in Y_3NbO_7 exhibits an "aging" effect, especially at low temperatures. The average mobility, shortly after initialising the simulation with randomly placed oxide ions, is high, but drops over a substantial period of time ($\sim$1 ns) presumably because, on this time scale, oxide ions find initially empty Y^{3+}-rich sites and become trapped there. This can be seen in figure 5.3, where both the diffusion coefficient and the number of trapped oxide ions are plotted as a function of the length of the simulation. It is evident that after a certain amount of time ($\sim$ 1 ns), twice as many oxide ions are trapped than at the start of the simulation and that this decreases the diffusion coefficient by a factor of 3 - 4.

Another consequence is that different initial configurations give different mean diffusion coefficients even after very long runs. This is probably caused by the variation in the numbers of different types of tetrahedral sites in the initialisations. Both of these effects make a reliable determination of the conductivity difficult for Y_3NbO_7 in the temperature range (< 1500 K) where experimental measurements have been made. As discussed in the previous chapter, our best efforts (mean squared displacement extracted from a 10 ns long simulation) give a conductivity ($\sigma_{NE} = 0.016\ \Omega^{-1}\mathrm{cm}^{-1}$ at 1500 K of about an order of magnitude larger than measured [103, 21]. This value is considerably lower than the one obtained for $Zr_2Y_2O_7$ ($\sigma_{NE} = 0.08\ \Omega^{-1}\mathrm{cm}^{-1}$), which agrees with the experimental trend [103]. For $Zr_2Y_2O_7$ neither of these effects is observed and reliable conductivity values can be obtained down to the highest temperatures at which measurements are available. In this case, as shown in the previous chapter, the slope of conductivity versus inverse temperature agrees very well with experiment and the actual values of the conductivity at temperatures below 1500 K are only slightly larger than experiment (by a factor of less than 2 for the data in [21]).

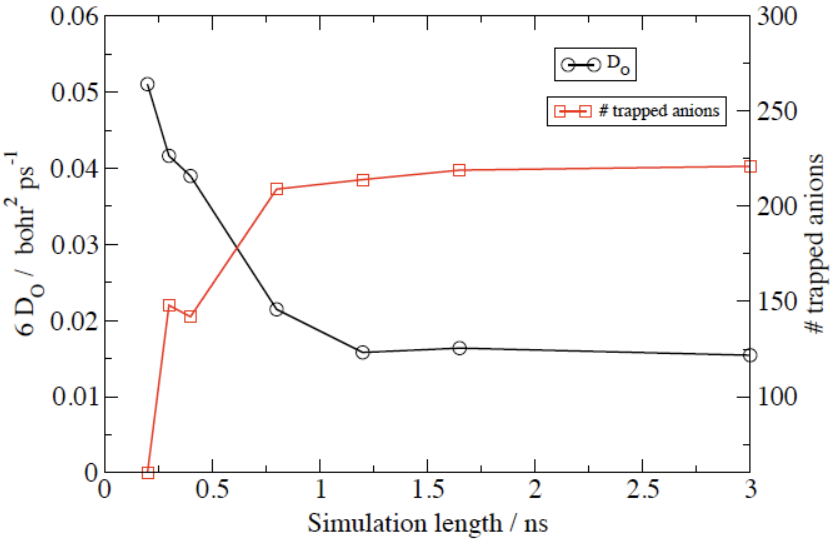

Figure 5.3: *Aging effect on the Y_3NbO_7 conductivity. The red curve shows the number of trapped oxide ions (out of a total number of 448 oxide ions in the simulation) for different lengths of the simulation, whilst the black one shows the calculated diffusion coefficient for that simulation.*

5.2 The effects of cation charges and sizes on the material's properties

The simulations on the $Zr_{0.5-0.5x}Y_{0.5+0.25x}Nb_{0.25x}O_{1.75}$ series in the *d*-fluorite structure give the same trend of decreasing conductivity and increasing disorder with increasing x that is seen experimentally. In this section it will be attempted to distinguish the effects of cation size and charge by comparing the results, obtained with modified interaction potentials, with the realistic models.

5.2.1 The effect of the cation charge

In order to examine the role of the high charge of the Nb^{5+} cation in causing these effects, simulations have been carried out on the x = 1 system in which both the "Nb" and "Y" ions are assigned a charge of 3.5+ (which maintains charge neutrality for this stoichiometry). This system will be called *equal-charge* Y_3NbO_7. All other aspects of the interaction potentials were kept the same as in the runs described above. Starting from a previous high temperature simulation on Y_3NbO_7, the cation charges were equalised. All the simulations were equilibrated at constant pressure for 100,000 steps, during which the velocities were rescaled several times to keep the system at the required (high) temperatures for conductivity studies, and then longer (constant volume) runs were made to study the properties of this material. Some shorter simulations were also run at room temperature to study the static structure and obtain the radial distribution functions.

In figure 5.4 the oxygen-oxygen radial distribution functions are shown for room temperature *equal-charge* Y_3NbO_7 , Y_3NbO_7 itself, and a perfect fluorite structure with a matched lattice constant. It is clear that equalizing the cation charges increases the order of the oxide ion sublattice [3]. The $g_{O-O}(r)$ for the equal-charge system shows a first peak close to the ideal fluorite position and a single prominent second peak, though still not as intense as in the ideal case. It is also found that the cation-anion distances change significantly, $d_{Y-O} = 2.23$ Å and $d_{Nb-O} = 2.19$ Å. This is another sign that the system has become more ordered, as these become closer to the ideal cation-anion distance in this system, given, in this case, by $\sqrt{3}/4\ a_{equal-charge}$ = 2.27 Å. A comparison between figure 5.4 and figure 4.5 shows that *equal-charge* Y_3NbO_7 is also more ordered than $Zr_2Y_2O_7$ which is consistent with the fact that $Zr_2Y_2O_7$ still has two cations with different charges (4+ and 3+).

[3] A movie can be found online at http://www.iop.org/EJ/mmedia/0953-8984/21/40/405403 which shows how Y_3NbO_7 becomes more ordered as soon as the cation charges are equalised.

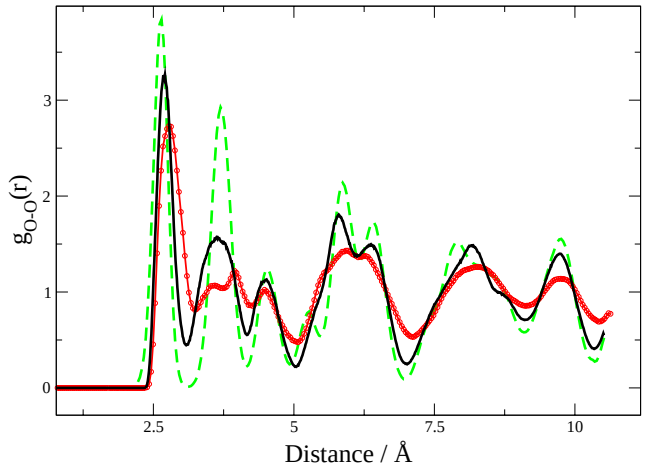

Figure 5.4: *Comparison between the oxygen-oxygen g(r) for Y_3NbO_7 (red dotted line), equal-charge Y_3NbO_7 (black solid line) and a perfect fluorite structure (green dashed line).*

Figure 5.2 shows that equalizing the cation charges (dotted line) greatly reduces the number of immobile oxide ions, relative to Y_3NbO_7. In fact, the distribution comes to resemble that for $Zr_2Y_2O_7$ quite closely and is indicative of a homogeneous pattern of diffusion. The mean squared displacement for the oxide ions in *equal-charge* Y_3NbO_7 was calculated at 1500 K and 2000 K and the respective diffusion coefficients are reported in table 5.1. From this it can be seen that *equal-charge* Y_3NbO_7 is more conducting than Y_3NbO_7. Interestingly *equal-charge* Y_3NbO_7 has a lower diffusion coefficient than $Zr_2Y_2O_7$, whereas it was just shown that the latter system has a more disordered oxide ion lattice. This suggests that there is some other factor at work besides the charge-induced strain in the lattice.

In order to see *how* the dopant cation charge induces the disorder and affects the ionic mobility, the mobility distribution functions were calculated as above, but this time the identities of the four cations surrounding the anion were also monitored . As anticipated, the anions with no mobility (about 1/4 of the total number, see figure 5.2) are in sites with a much higher Y^{3+} content than expected (≈ 3.65 as opposed to the average of 3 Y^{3+} and 1 Nb^{5+} which is expected from the Y_3NbO_7 stoichiometry) and the higher the mobility the higher the content

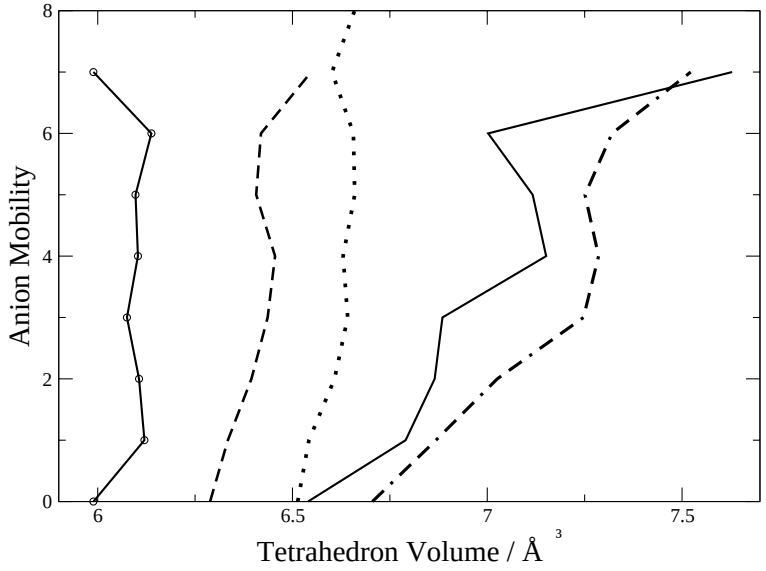

Figure 5.5: *Anion mobility as a function of the average tetrahedron volume for equal-charge (dashed line), equal-radius (dot-dashed line), equal-charge&radius Y_3NbO_7 (circles+line), Y_3NbO_7 (solid line) and $Zr_2Y_2O_7$ (dots).*

Table 5.1: Diffusion coefficients extracted from the MD simulations performed on different materials at 1500 and 2000 K.

Material	$10^6 \times D_O$ (cm ^{2} s^{-1})	
Y_3NbO_7	0.924	
Equal-charge Y_3NbO_7	1.87	$T = 2000$ K
$Zr_2Y_2O_7$	2.87	
Y_3NbO_7	0.072	
Equal-charge Y_3NbO_7	0.21	
$Zr_2Y_2O_7$	0.44	$T = 1500$ K
Equal-radius Y_3NbO_7	0.37	
Equal-charge&radius Y_3NbO_7	2.6	

of Nb^{5+} ions in the tetrahedron surrounding the anion. This effect seems to be associated with the *volume* of the coordination tetrahedron (obtained from the volume of the tetrahedron with the four closest cations at its vertices). The Coulombic repulsion between two Nb^{5+} ions is almost three times stronger than that between the Y^{3+} cations and from the cation-cation radial distribution functions it is found that the nearest-neighbour cation-cation separations are $d_{\mathrm{Y-Y}}$ = 3.69 Å and $d_{\mathrm{Nb-Nb}}$ = 3.86 Å (the ideal fluorite value being $a/\sqrt{(2)} = 3.78$ Å) so that the coordination tetrahedra are strained to an extent which depends on their Nb^{5+} content with the Nb^{5+}-rich ones significantly larger than the average. The anion mobility is plotted against the average volume of the surrounding tetrahedra in figure 5.5 (solid line). Alternatively, the mobility against the average number of Nb^{5+} ions in the coordination shell could have been plotted and this would have shown a very similar curve. Note, firstly, that the tetrahedral volumes for Y_3NbO_7 span an appreciable range, from 6.4 to 7.5 $Å^3$ and secondly, that the anion mobility is a strongly increasing function of the tetrahedron volume. This observation therefore explains the paradox that although highly charged Nb^{5+} cations attract oxide ions strongly they promote *local* mobility but reduce the overall conductivity by straining the cation sub-lattice resulting in the formation of oxide ion trapping sites. The same analysis was also carried on for $Zr_2Y_2O_7$ (dotted curve) and for *equal-charge* Y_3NbO_7 (dashed curve) and the results are shown in figure 5.5. In these cases, the range of tetrahedron volumes is much narrower than for Y_3NbO_7 (< 0.2 $Å^3$) suggesting a much less strained cation lattice and the dependence of the anion mobility on the tetrahedral volume is barely discernable.

5.2.2 The effect of the cation size

Proceeding by analogy with the *equal-charge* study, the effects of equalizing the cation radii in Y_3NbO_7 can also be studied. The short-range repulsion terms in our potentials model the repulsion between two ions and therefore are intrinsically related to the extent of the valence electron density around the ion. Figure 5.6 shows the short-range repulsion terms for the Y-O, Nb-O and Zr-O interactions (recall that these were generated with the *ab initio* force-fitting strategy). It can be seen that the range of these potentials is consistent with the fact that Y^{3+} is the largest ion, Nb^{5+} the smallest, with Zr^{4+} of intermediate size. To generate an equal-radius model for Y_3NbO_7 the Zr-O short-range interaction parameters were used for the Y-O and Nb-O terms, but the Y^{3+} and Nb^{5+} ions keep their formal charges [4]. Simulations are run as previously described for the equal-charge case.

[4]Note that the Y-O and Nb-O nearest-neighbour separations which result from these simulations will differ, because of the stronger Coulombic attraction to the Nb^{5+} ion. From an empirical perspective, *i.e.* the way that the ionic radius is normally assigned [59], the ions do not appear as of equal size; rather they have been treated as if the electron density distributions around the ions are of equal size in the potential model.

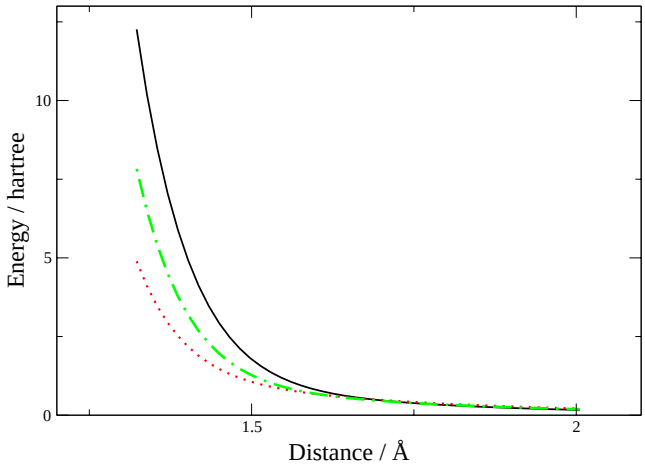

Figure 5.6: *Short-range repulsion parts of the potential for the Y-O (solid line), Nb-O (dotted line) and Zr-O (dot-dashed line) terms.*

The partial radial distribution functions for *equal-radius* Y_3NbO_7 look quite similar to the ones obtained for Y_3NbO_7 itself (figure 4.5) and, for this reason, these are not shown separately. Despite the equal radius potential construction, even the anion-cation distances are comparable ($d_{\mathrm{Nb-O}} = 1.93$ Å, $d_{\mathrm{Y-O}} = 2.29$ Å) to those of the parent compound. This confirms that the observed disorder is caused by the different cation charges in Y_3NbO_7 and that the different ranges of the repulsive cation-anion interactions do not play an important role on this. Given this similarity in structure, it is not surprising that the equal-radius system shows a wide range of tetrahedral volumes like Y_3NbO_7 itself and figure 5.5 (dot-dashed line) shows that, again, the oxide ion mobility tracks the tetrahedral volume like the parent compound. This leads to the inhomogeneous distribution of hopping probabilities, as shown in figure 5.2 (dot-dashed line) with a substantial fraction of immobile ions.

In Table 5.1 the average diffusion coefficient is reported as obtained from a simulation at 1500 K on *equal-radius* Y_3NbO_7 and compared with *equal-charge* Y_3NbO_7, Y_3NbO_7 and $Zr_2Y_2O_7$ at the same temperature. Interestingly, the equal-radius material is more conducting than both *equal-charge* Y_3NbO_7 and Y_3NbO_7 though not as conducting as $Zr_2Y_2O_7$. That *equal-radius* Y_3NbO_7 is more conducting than Y_3NbO_7 itself is probably to be expected, what is more surprising is that it is also more conducting the *equal-charge* system which, as shown

before, has the kind of homogeneous distribution of mobilities seen in the highly conducting $Zr_2Y_2O_7$ system. This is probably a consequence of using the Zr-O short-range interaction parameters for the Y-O and Nb-O terms. As mentioned above, these are softer than the ones for the Y-O interaction but harder than the Nb-O ones. However, since in this system there are three times more Y^{3+} ions than Nb^{5+} ions, this means that, on average, the anion-cation short-range repulsion in this system is softer and this greatly enhances the anion mobility. A similar phenomenon was observed in the case of GeO_2 where rescaling the short-range interaction terms by a factor of 1.6 enhances the oxide-ion diffusivity by several orders of magnitude (see ref. [111] which is also reported in appendix B).

As a final model system, both the cation radii and charges are equalised simultaneously (*i.e.* the Zr-O potential is used for all short-range interactions and all the cation charges are set equal to 3.5). As might be expected this gives a small distribution of tetrahedral volume sizes (figure 5.5, line with circles) and virtually no oxide ion trapping. This material is an incredibly good ionic conductor with a conductivity of $\sigma_{NE} \approx\ 0.6\ \Omega^{-1}\mathrm{cm}^{-1}$ at 1500 K, a value higher than the one found in the best yttria-stabilised zirconias ($\sigma \approx\ 0.6\ \Omega^{-1}\mathrm{cm}^{-1}$ at 1667 K for 8% YSZ [25]).

5.3 Vacancy ordering effects

So far the relationship between disorder and mobility has been studied by examining the ionic positions and the effect of making particular changes in the interaction potential. This study was motivated by reference to the properties of the *vacancies* and the way they are ordered by their interactions with the ions. Their effect is, of course, implicit in the properties which have been examined so far, but an examination of the simulation trajectories will now be performed by considering the vacancies explicitly.

5.3.1 Vacancy interactions

In section 3.5.3 it was explained how vacancies are identified and how the ion-vacancy and vacancy-vacancy radial distribution functions can be obtained. Integration of these can be used to define coordination numbers. For example, integrating the Y^{3+}-vacancy rdf, $g_{\mathrm{Y-V}}(r)$, from zero out to the position, r_c, of first minimum of the $g_{\mathrm{Y-O}}(r)$ gives the average number of vacancies in the first coordination shell of a Y^{3+} ion. In figure 5.7 the cation-vacancy radial distribution functions are reported for Y_3NbO_7 and *equal-charge* Y_3NbO_7 at 1500 K. From

this figure the tendency of the vacancies to bind to the small Nb^{5+} ions is clear[5] for Y_3NbO_7. This tendency is strongly reduced when the cation charges are equalised.

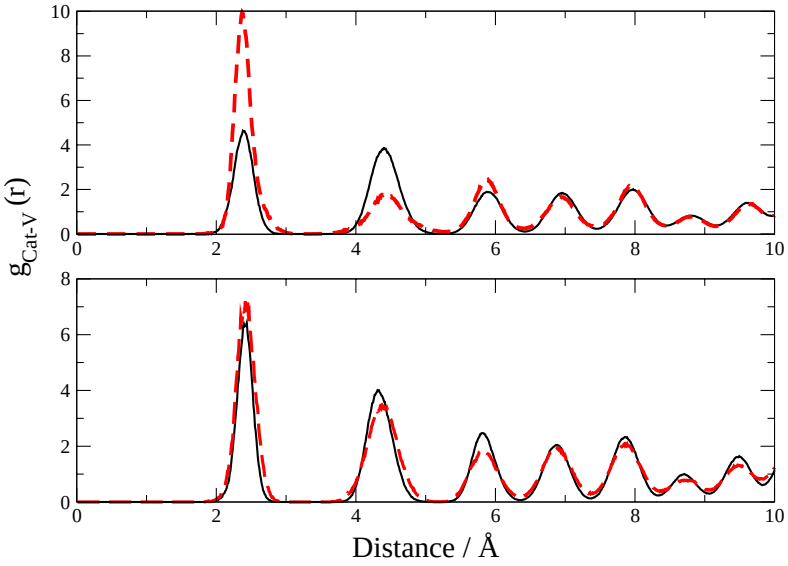

Figure 5.7: *Yttrium-Vacancy (solid line) and Niobium-Vacancy (dashed line) radial distribution functions in d-fluorite structured Y_3NbO_7 (top) and equal-charge Y_3NbO_7 (bottom).*

In table 5.2 are reported the number of vacancies around the different cations compared to the number which would be expected if the vacancies occupied sites randomly. It is clear from the table that vacancies bind very strongly to Nb^{5+} ions in *d*-fluorite Y_3NbO_7 and less strongly to Zr^{4+} in $Zr_2Y_2O_7$. Considering the Coulombic effects, the vacancies (which have a relative charge of 2+) would be expected to bind more strongly to the cation with the lowest charge, *i.e.* Y^{3+} in both materials [21]. The fact that the contrary happens is therefore indicative of the importance of strain effects which are strong enough to outweigh the Coulombic interactions [8] at these temperatures, *i.e.* the vacancies prefer to bind to the smallest cations, despite their higher charges. This was recently confirmed by solid state NMR studies [101] on similar sys-

[5]Note that this is in perfect agreement with what was observed in the previous section with the mobility distribution functions. The fact that vacancies prefer to be nearest neighbours to the Nb^{5+} cations and next nearest neighbours with the Y^{3+} cations is perfectly equivalent to saying that the Y^{3+} cations trap the oxide ions in their lattice sites. This equivalency will be used significantly in the next chapters, as it it much easier to the cation-vacancy radial distribution functions.

Table 5.2: Cation-Vacancy relative coordination numbers extracted from our MD simulations at 1500 K.

Material	n_{Y-V}	n_{Nb-V}	n_{Zr-V}
RANDOM	1	1	1
Y_3NbO_7	0.81	1.53	
$Zr_2Y_2O_7$	0.79		1.21
Equal-charge Y_3NbO_7	0.92	1.23	

tems.

This analysis can now be extended to examine the vacancy-vacancy ordering by integrating $g_{\mathrm{V-V}}$(r) between limits which bound the different coordination shells around an anion site in an ideal fluorite lattice. The first such shell gives the probability of finding a pair of vacancies as nearest-neighbours (*i.e.* along the $\langle 100 \rangle$ direction of the fluorite lattice) whereas the second shell relates to vacancy pairs along $\langle 110 \rangle$ and the third to $\langle 111 \rangle$. These probabilities may be compared with what would be expected if the vacancies were randomly distributed on the simple cubic anion lattice and the ratios are given in table 5.3 for simulations at 1500 K. As discussed in section 3.5.3, it is likely that the way that vacancies are identified leads to an overestimate of the number of vacancy nearest-neighbours, especially if the studied system is very disordered. Nevertheless, it can be seen that there is a specific ordering tendency, with $\langle 111 \rangle$ vacancy pairs appearing with a higher frequency than would be expected for a random distribution, and nearest-neighbour pairs being lower. This order is in accord with Bogicevic's [8] examination of the energetics of vacancy ordering in lightly doped yttria-stabilised zirconia. The observed tendency is, however, not as strong as might be expected from the calculations in that paper. This is probably due to the fact that our calculations have been performed at high temperatures where the ordering is opposed by entropic effects. It is also interesting to notice that the vacancy ordering tendency is found to decrease as temperature is raised and completely disappears at 2000 K. Finally, this tendency seems to be slightly stronger in $Zr_2Y_2O_7$ than in Y_3NbO_7 which might seem at first counterintuitive considering that $Zr_2Y_2O_7$ is a better conductor than Y_3NbO_7. This apparent contradiction will be explained in the next section.

5.3.2 Effects of vacancy interactions on the diffuse scattering

The vacancy ordering influences the diffuse scattering observed in diffraction studies, and it is useful to compare the consequences of the degree of vacancy ordering found in the simulations with those seen experimentally. Our simulations have reproduced extremely well the struc-

Table 5.3: Relative population of the anion vacancy pairs expected from a random distribution of vacancies within a cubic fluorite lattice, compared with those extracted from our MD simulations at 1500 K.

Material	$\langle 100 \rangle$	$\langle 110 \rangle$	$\langle 111 \rangle$
RANDOM	0.231	0.461	0.308
Y_3NbO_7	0.116	0.396	0.487
$Zr_2Y_2O_7$	0.087	0.318	0.594

tures derived from the analysis of the total (*i.e.* Bragg plus diffuse) *powder* diffraction [103] in these systems. However, several Small Area Electron Diffraction (SAED) studies [43, 22] have shown intense diffuse peaks for Y_3NbO_7 at particular positions in reciprocal space. This suggests that the vacancy ordering effects might be considerably stronger and of longer range than is indicated by the propensities shown in tables 5.2 and 5.3. In order to compare with these experimental studies the diffuse scattering has been calculated from the ionic configurations available from the simulations.

It was decided to calculate the electron diffraction pattern of Y_3NbO_7 and $Zr_2Y_2O_7$ along the $\langle 1\bar{1}0 \rangle$ zone axis . This is found to be the most informative pattern in the experimental studies [43, 22, 58] and, for this reason, the experimental electron diffraction patterns for Y_3NbO_7 and $Zr_2Y_2O_7$ are reported in figure 5.8. In the experimental patterns of Y_3NbO_7, a pair of intense and closely-spaced diffuse peaks is seen at $\mathbf{G} \pm \frac{1}{2}\langle 111 \rangle$, where $\mathbf{G}$ is a reciprocal lattice vector of the fluorite-type lattice. In fact, the two peaks correspond to a ring of diffuse scattering centred at these positions which is projected down into the $\langle 1\bar{1}0 \rangle$ plane. The $\mathbf{G} \pm \frac{1}{2}\langle 111 \rangle$ positions correspond to the location of Bragg peaks in the pyrochlore structure and the diffuse scattering seen in Y_3NbO_7 indicates a pattern of vacancy pairs along the $\langle 111 \rangle$ direction which form strings along $\langle 110 \rangle$, as in the pyrochlore structure, but of finite range.

An ideal pyrochlore structure type, $A_2B_2O_7$, is a superstructure of the fluorite (MX_2) structure and is based upon a 2 x 2 x 2 unit cell with $Fd\bar{3}m$ symmetry (figure 5.9 shows the differences between a fluorite and a pyrochlore structure [1, 58].) The cation superstructure of pyrochlore is based upon ordering of A and B cations parallel to the $\langle 110 \rangle$ directions, separated by $\frac{1}{2}\frac{1}{2}\frac{1}{2}$, with respect to the origin. The A and B cations are, respectively, found at the 16c (eight-coordinated) and 16d (six-coordinated) sites whereas the anions are distributed between two tetrahedrally coordinated positions: 48f [O(1)] and 8a [O(2)]. There is another tetrahedral site potentially available for the anions, 8b, which is systematically vacant in fully ordered pyrochlores.

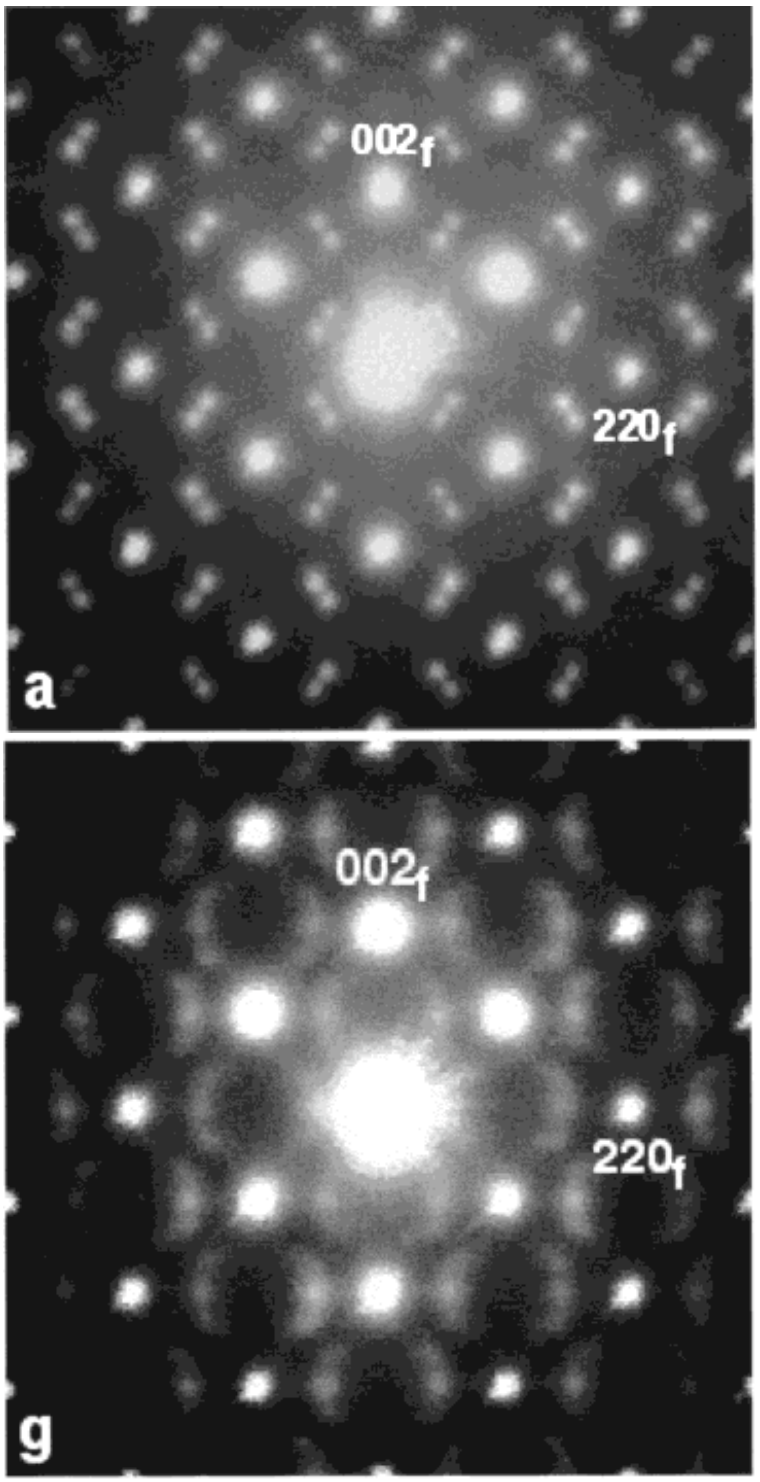

Figure 5.8: *Experimental electron diffraction pattern along the* $\langle 1\bar{1}0 \rangle$ *zone axis for* Y_3NbO_7 *(top) and* $Y_2Zr_2O_7$ *(bottom) [22].*

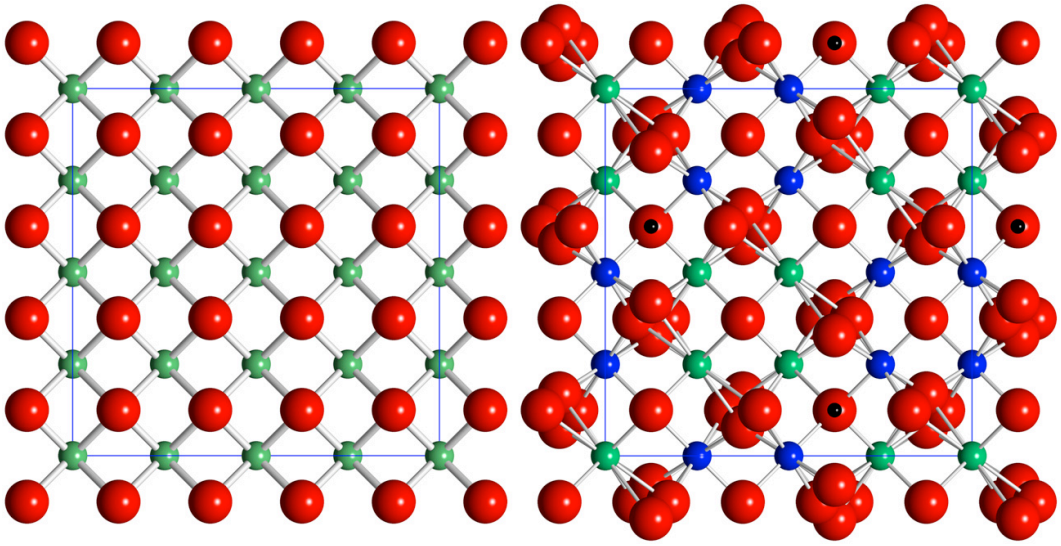

Figure 5.9: *Images of the crystal structures of fluorite (left) and pyrochlore (right), projected along the* $\langle 100 \rangle$ *direction. Large red spheres are oxygen, green spheres represent a large cation and blue spheres a smaller cation. The black dots indicate the unoccupied 8b anion positions [58].*

In $Zr_2Y_2O_7$ the diffuse scattering is considerably weaker and the pattern of peaks is somewhat different. It appears as streaks along $\langle 001 \rangle$ in the studies by Irvine *et al.* [22] (see figure 5.8) and taken as indicative of C-phase ordering of vacancies (*i.e.* vacancy pairs along $\langle 110 \rangle$). Whittle *et al.* [58], however, observe the pattern as 3 peaks centred at $\mathbf{G} \pm \frac{1}{2}\langle 111 \rangle$ and interpret it as another type of pyrochlore-like modulated structure.

The top part of figure 5.10 shows the electron diffraction pattern for Y_3NbO_7 calculated from our MD data (obtained from a simulation on 11,000 atoms, *i.e.* 10 x 10 x 10 unit cells). This simulation was 100 ps long. It was started at 2000 K and the temperature was then lowered down to 300 K with a cooling rate lower than 50 K ps^{-1}. The pattern does not show the diffuse spots at $\mathbf{G} \pm \frac{1}{2}\langle 111 \rangle$ which have been observed in the experimental SAED patterns [43, 22, 58]. The calculated patterns show some diffuse signal at some of these positions but this appears weaker and less sharply peaked than in the experimental studies. This finding was confirmed in longer MD simulations on smaller cells. A similar comparison was made (see next chapters) with the diffuse neutron scattering [7] derived from single-crystal studies of $(ZrO_2)_{1-x}$-$(Y_2O_3)_x$ for $0.1 < x < 0.25$ and this was very successful, thus indicating that the disagreement with the experimental data is probably not a limitation of the way the diffuse

scattering has been calculated or, more generally, of the employed model.

For Y_3NbO_7 a starting configuration was prepared for an MD run in which the cations were distributed randomly over the cation sublattice but in which the oxide ions were placed as if in a pyrochlore structure, to give the associated vacancy-ordered structure. In simulations at 1500 K, this initial configuration rapidly evolved to one in which the extent of vacancy ordering had relaxed to that seen in the previous *d*-fluorite simulations. It therefore does not appear that it is possible to reproduce the evidence for vacancy ordering from the SAED studies with simulations based upon the *d*-fluorite structure with randomly disposed cations.

In summary then, the *d*-fluorite simulations reproduce the experimentally observed *trends* in disorder and conductivity and have enabled us to account for the way that these properties are affected by the cation size and charge. However, there is a suggestion that these simulations overestimate the conductivities, especially on the Nb-rich side of the composition range. Furthermore, although the simulations demonstrate vacancy ordering tendencies similar to those which have been found in more lightly doped zirconias these are not sufficiently strong to reproduce the SAED patterns. This leads us to reconsider one of the underlying assumptions of the work described so far, namely that the different cation species are randomly distributed throughout the lattice.

5.4 Local cation ordering effects

Our simulation studies of Y_3NbO_7 in the *d*-fluorite structure have shown lattice distortions induced by the Nb^{5+} ions, especially when two or more Nb^{5+} ions are found as cation nearest-neighbours (the nearest neighbour Nb^{5+}-Nb^{5+} distance is 3.86 Å as opposed to the ideal cation-cation distance in a fluorite structure, $a/\sqrt{(2)} = 3.78$ Å). The strength of this effect would suggest that the system will try to adapt by ordering the Nb^{5+} ions so as to minimise the strain. Furthermore, the O-Nb-O bond angle distributions extracted from the MD and RMC-generated configurations (see figure 4.7) suggest a tendency towards octahedral local anion co-ordination of the Nb^{5+} sites [103]. Motivated by these considerations and by our inability to reproduce the SAED patterns in Y_3NbO_7, it was decided to examine the consequences of *local* cation ordering in this system. Note that local (rather than long-ranged) ordering presents a significant problem for simulation studies because they necessarily involve periodic replication of a simulation cell which may be too small to allow for the decay of the structural correlations. Nevertheless, Miida *et al.* [43] estimate the correlation length of the order responsible for the diffuse rings in the SAED pattern to be $\sim$22 Å which is the range of 4 fluorite unit cells

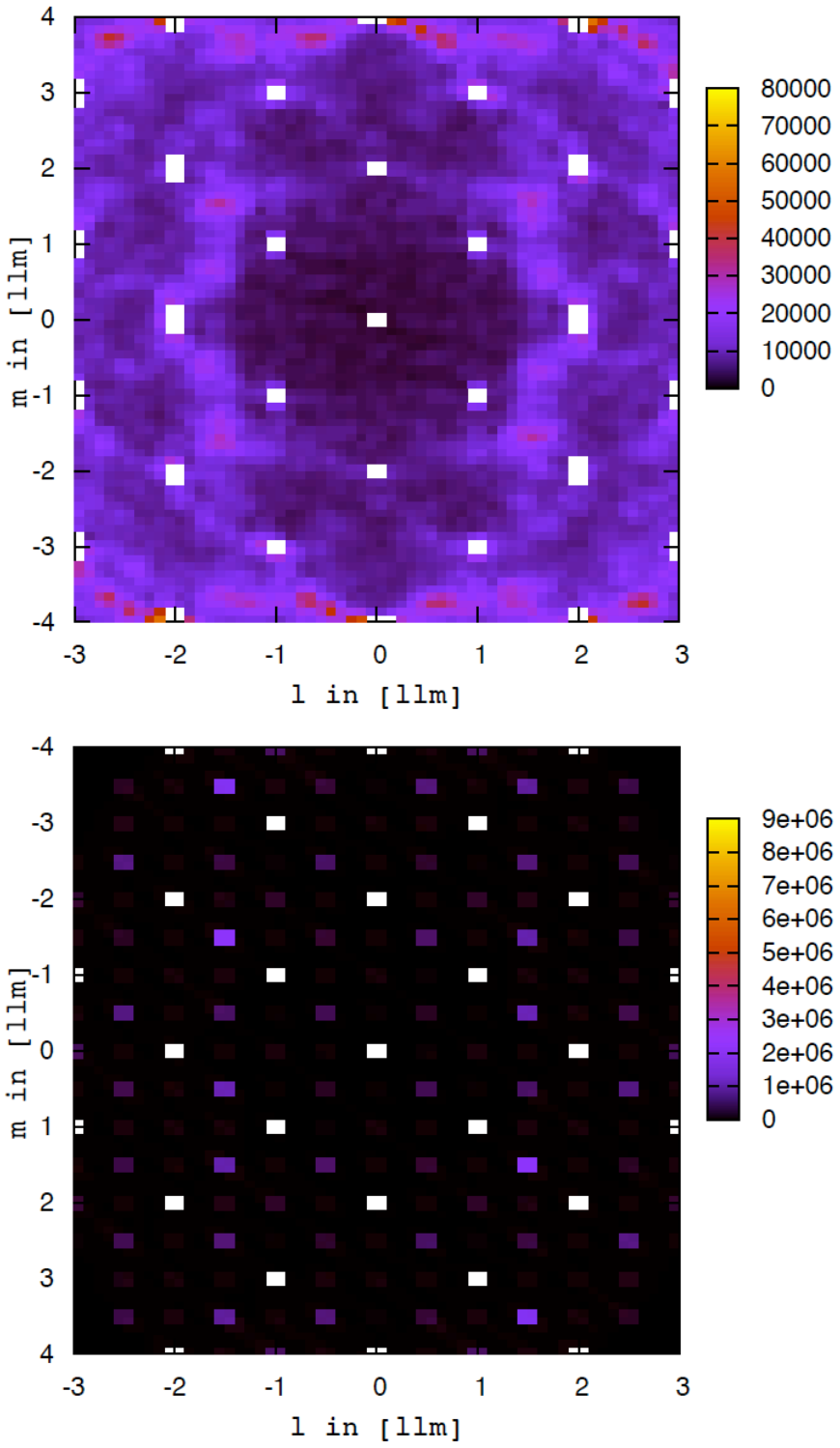

Figure 5.10: *Electron diffraction pattern along the* $\langle 1\bar{1}0 \rangle$ *zone axis obtained from the MD data for d-fluorite (top) and locally cation-ordered (bottom)* Y_3NbO_7.

(the majority of our *d*-fluorite simulations involved 4 unit cells along each cartesian direction, though the 11,000 atom MD cells used in the initial comparison with SAED involved 10). Furthermore, in the calculations to be described below, the cation ordering is imposed upon the system, using intuition and also the insight from the SAED studies to guess a structure which will minimise the lattice strain. In future work a Monte Carlo cation-swapping algorithm will be used to set up the system in a less biased way [112].

The natural stoichiometry for a pyrochlore-structured oxide is $A_2B_2O_7$ where B is a smaller cation which prefers octahedral coordination and A a larger one which prefers 8 oxide neighbours. It has been noticed above that there is a tendency for the smaller Nb^{5+} and Zr^{4+} ions to preferentially bind to vacancies and hence reduce their coordination number relative to Y^{3+}, and adoption of the pyrochlore arrangement would allow this tendency to be accommodated. Opposing this tendency may be long range strain effects, such as that noted above involving Nb^{5+} in particular, and entropy, since the adoption of the pyrochlore structure involves ordering both the cation and anion sublattices with respect to *d*-fluorite. Chao Jiang *et al.* [113] estimate the configurational entropy as

$$\begin{aligned}\Delta S_{ideal} = &- 4k_B[x\ ln\ x + (1-x)\ ln(1-x) \\ &+ 2y\ ln\ y + 2(1-y)\ ln(1-y)]\end{aligned} \tag{5.1}$$

where x is stoichiometric ratio of cations ($\frac{1}{2}$ for $Zr_2Y_2O_7$ and $\frac{1}{4}$ for Y_3NbO_7) and y the fraction of vacancies to oxide ions in the unit cell $\frac{1}{8}$. This gives configurational entropies of 4.986×10^{-4} eV/K and 4.534×10^{-4} eV/K for $Zr_2Y_2O_7$ and Y_3NbO_7, respectively. $Zr_2Y_2O_7$ has the appropriate stoichiometry to adopt the pyrochlore structure but the radius ratio of the cations is not sufficiently large to allow a stable, long-range ordered structure to form [113] - certainly not at the temperatures at which the solid-state synthesis is carried out. The situation must be very marginal however, as $Hf_2Y_2O_7$ does form a pyrochlore [58, 113], and the Hf^{4+} ion is only slightly smaller than Zr^{4+} (note that Chao Jiang *et al.* [113] suggest that "covalent" effects may play a role, alongside ion size, in this comparison). Some *local* pyrochlore-like ordering in $Zr_2Y_2O_7$ does therefore, seem plausible. The stoichiometry of Y_3NbO_7 is not that of a pyrochlore, but that does not rule out a pattern of local cation and vacancy ordering which is pyrochlore-like. Note that Irvine *et al.* [22] consider *cation*-ordering in Y_3NbO_7 likely and Miida [43] has interpreted the SAED patterns by proposing modulated structures in which there is some local ordering of both vacancies and cations. The RMC-interpreted powder neutron studies [103] showed no evidence for cation ordering in either $Zr_2Y_2O_7$ or Y_3NbO_7, but it must be noted that the neutron scattering lengths of Y^{3+}, Zr^{4+}, and Nb^{5+} are very similar and therefore it is unlikely that any evidence of cation ordering can be obtained with this technique.

5.4.1 Partially-ordered Y_3NbO_7

As mentioned above, Y_3NbO_7 does not have the correct stoichiometry to adopt a pyrochlore structure. However, it seems reasonable to assume that the smaller Nb^{5+} ions will prefer to occupy the octahedrally-coordinated B sites and therefore the cations were arranged so that all the Nb^{5+} ions randomly occupy half of the B sites with the Y^{3+} occupying the remaining B sites as well as all the A sites. As a consequence of the random assignment of cations to the B sites the system does not exhibit "long"-range cation order within the simulation cell (though, because of the simulation boundary conditions, the system is periodic). The oxide ions were placed in the O[1] and O[2] positions.

A simulation on this material was run in the same way as explained above on a system with 11,000 atoms. The obtained electron diffraction spectrum is shown in figure 5.10. It can be appreciated that this pattern shows peaks at $G_F \pm \frac{1}{2}\langle 111\rangle$, in reasonable agreement with the experimental data. The reason why a single peak only is observed (instead of two separate ones) is that, because of the periodic boundary conditions, in reality there are some long-range order in the cation positions. The internal energies of the partially cation-ordered Y_3NbO_7 and *d*-fluorite were computed at low temperatures (T = 100 K). This was done by slowly cooling a well-equilibrated high temperature run. These runs contained 704 atoms (four fluorite unit cells in each direction). It was found that the locally-ordered material has an energy which is lower by about $\Delta E \approx 56$ kJ/mol = 0.58 eV/molecule [6] than the *d*-fluorite material, confirming that some degree of cation ordering is indeed favoured on energetic grounds. From this the order-disorder transition temperature can be calculated, as in [113], $T_{O-D} \approx \Delta E/\Delta S_{ideal} = 1160$ K, where Δ_{ideal} is given by equation 5.1. This value goes up to $T_{O-D} \approx 1460$ K if it is assumed that only 2/3 of the vacancies are ordered, *i.e.* if $y = 1/12$ in equation 5.1. Considering that this material is usually synthesised at 1700-1800 K [103, 43, 22], it seems plausible that a certain degree of cation-ordering is observed depending upon how the sample is cooled back to ambient conditions.

Interestingly, it is found that the locally-ordered material is a much poorer ionic conductor than the *d*-fluorite Y_3NbO_7. It is estimated [7] that cation-ordered Y_3NbO_7 has a conductivity of $\sigma_{NE} \leq 0.002\ \Omega^{-1}\mathrm{cm}^{-1}$ at 1500 K, approximately an order of magnitude lower than

[6] This value is found to depend weakly on the cooling rate and on the system history.

[7] The error associated with this number is large because the corresponding mean squared displacement curve is very noisy due to the low mobility of the anions.

Table 5.4: Cation-Vacancy relative coordination numbers extracted from our MD simulations at 1500 K, including the simulations ordered cations.

Material	n_{Y-V}	n_{Nb-V}	n_{Zr-V}
RANDOM	1	1	1
Y_3NbO_7	0.81	1.53	
$Zr_2Y_2O_7$	0.79		1.21
Equal-charge Y_3NbO_7	0.92	1.23	
Partially ordered Y_3NbO_7	0.72	1.85	
Pyrochlore $Zr_2Y_2O_7$	0.15		1.85

Table 5.5: Relative population of the anion vacancy pairs expected from a random distribution of vacancies within a cubic fluorite lattice, compared with those extracted from our MD simulations at 1500 K, including those simulations with ordered cations.

Material	$\langle 100 \rangle$	$\langle 110 \rangle$	$\langle 111 \rangle$
RANDOM	0.231	0.461	0.308
Y_3NbO_7	0.116	0.396	0.487
$Zr_2Y_2O_7$	0.087	0.318	0.594
Partially ordered Y_3NbO_7	0.081	0.219	0.699
Pyrochlore $Zr_2Y_2O_7$	0.038	0.076	0.885

the *d*-fluorite simulations at the same temperature and in much better agreement with the experimental data. The reason for this much lower value of the conductivity is that a partial cation ordering increases the Nb^{5+}-vacancy association (see table 5.4) as well as the vacancy-vacancy pairing along the $\langle 111 \rangle$ direction (see table 5.5) and both factors hinder the vacancy mobility and therefore reduce the overall conductivity. It is worth noting that now prtially-oredered Y_3NbO_7 presents a stronger vacancy ordering tendency along the $\langle 111 \rangle$ direction then *d*-fluorite $Zr_2Y_2O_7$, as expected.

5.4.2 Cation-ordering in $Zr_2Y_2O_7$

Cation ordering in $Zr_2Y_2O_7$, on the other hand, seems to be a less important issue. It has to be remembered that the tendency for Zr^{4+} to preferentially bind vacancies, relative to Y^{3+}, is considerably lower than for Nb^{5+} in Y_3NbO_7, and the strain associated with the different local cation configurations is much less pronounced in this system. The experimental SAED studies show slightly different diffuse scattering patterns [22, 58], suggesting that lattice modulations in this material depend on the details of sample preparation. In all cases, the diffuse features are less intense and sharply peaked than in Y_3NbO_7 (see figure 5.8). Whittle and co-workers [58] have estimated a correlation length of $\approx$ 11 Å for the local order which is much smaller than in Y_3NbO_7.

Since $Zr_2Y_2O_7$ has the correct stoichiometry for a pyrochlore, simulations starting from a fully pyrochlore-ordered configuration (*i.e.* a long-ranged ordered structure) were run. The internal energy of this system at 100 K is slightly lower (ΔE = 49.5 kJ/mol, a value in reasonable agreement with the trends observed in reference [113]) than that of a *d*-fluorite configuration obtained by cooling down a high temperature run and, considering that the ordered system has a lower entropy, it would seem that this structure is unlikely to become stable at higher temperatures (the estimated T_{O-D} is $\approx$1030 K). The ordered system was also simulated at 1500 K to calculate the conductivity (note that there is no cation site exchange at this temperature, so that the system cannot relax to a *d*-fluorite structure on the simulation timescale). The conductivity is found to be very small (at least two orders of magnitude lower than the experimental value). An analysis of the vacancy-vacancy and cation-vacancy rdfs confirms that in pyrochlore structured $Zr_2Y_2O_7$ there is a strong pairing of the vacancies along the $\langle 111 \rangle$ direction and that these bind very strongly to the Zr^{4+} cations (see table 5.4 and 5.5) which explains the very small ionic conductivity shown by this sample. This strong reduction in the $Zr_2Y_2O_7$ conductivity (and the fact that *d*-fluorite simulations give an almost perfect agreement with the measured values), together with the information obtained on the energetics of the pyrochlore

phase, seem to indicate that cation ordering effects are not strong in this material.

5.5 Summary

In this chapter, *d*-fluorite simulations, with a disordered cation sublattice (which were shown to reproduce very closely the neutron powder diffraction data, see previous chapter), were initially examined, and these already allow us to account for a substantial part of the experimentally observed trends in the conductivity and degree of disorder between Y_3NbO_7 and $Zr_2Y_2O_7$. The difference between the two systems can be attributed to differences in cation size and to the different degree of strain imposed on the lattice by the highly charged cations - this creates oxide trapping sites in Y_3NbO_7 and gives an inhomogeneous character to the diffusive dynamics. Although both systems exhibit a tendency to order vacancies so that there is a likelihood of finding the vacancies close to the smaller cation, the vacancy ordering effects are not sufficiently strong to give rise to the diffuse scattering features which have been observed in small-area electron diffraction studies. The fact that the observed trends are recovered from these *d*-fluorite simulations implies that they are primarily associated with the mean cation composition and traceable to the direct influence of ion size and charge, with any influence of intermediate-range vacancy structuring an additional feature.

Because the *d*-fluorite simulations failed to reproduce the diffuse scattering seen in SAED studies, the possible effects of partial cation ordering (based upon the pattern suggested by the pyrochlore crystal structure) were considered. Our results in this context are only indicative as only the properties of "by-hand" ordered systems were examined. Nevertheless, in Y_3NbO_7 it was possible to postulate a structure for which the diffuse scattering was in qualitative accord with the SAED diffuse scattering patterns and which was energetically favoured with respect to *d*-fluorite. In this structure the tendency of vacancies to bind to the smaller cation was considerably enhanced relative to *d*-fluorite and the conductivity was reduced by an order of magnitude, bringing it much closer to the experimental value. For $Zr_2Y_2O_7$ it was not possible to postulate a partially ordered structure which would significantly improve upon the *d*-fluorite calculations across the full range of observations (including the SAED). In $Zr_2Y_2O_7$ the calculated conductivity in the *d*-fluorite structure is already close to the experimental value and the agreement with the powder diffraction is very good. The SAED studies indicate that the intermediate-range order is in any case weaker in this case and our own studies on *d*-fluorite show that the tendency for vacancies to associate with the smaller cation (the driving force for pyrochlore-like ordering) is considerably reduced relative to Y_3NbO_7. In this case a *fully* ordered pyrochlore is slightly favoured energetically over the *d*-fluorite structure but the entropy

cost is high enough that the latter, more disordered structure, will be more stable above ≈1000 K.

As indicated above, the finding that partial cation ordering has an influence on the material's properties presents a challenge for MD simulation because, at the temperatures at which one might hope to equilibrate the system with respect to cation positioning, the ordering tendency has disappeared for entropic reasons. However, the cation ordering also presents a challenge for comparing experimental results. The materials are synthesised at high temperatures but then cooled (according to different protocols in different studies): as the temperature is reduced the cation mobility will be drastically reduced so that the degree of cation ordering found in low temperature studies will depart from the thermodynamic equilibrium value to varying extents.

Chapter 6

A potential for YSZ and ScSZ

The previous two chapters of this thesis focussed on the study of the conduction mechanism in $Zr_{0.5-0.5x}Y_{0.5+0.25x}Nb_{0.25x}O_7$. This material was an ideal test-bed to probe the effects that different cations have on the conductivity and its study evinced the role that the cation's charge and radius play on the conductivity. However, that systems is not of technological interest because its conductivity is too low (for every value of x) for it to be used as the electrolyte in a SOFC. For this reason it was decided to turn to the study of more technologically attractive systems, like YSZ, ScSZ or a mixture of these, $Zr_{0.8}Sc_{0.2(1-y)}Y_{0.2y}$ $O_{1.9}$ (ZYSO). The latter is considered one of the most promising candidates for the electrolyte in a SOFC [56, 46], as it combines the very high ionic conductivity of ScSZ with improved stability properties given by the presence of a small percentage of Y_2O_3 (see section 2.1.2).

In this chapter the parameterisation of new inter-atomic potentials for these system will be briefly described and then these will be tested against a series of experimental data, as was done in chapter 4. In the next chapter these potentials will then be used to study the conduction mechanism in these systems and to underline the role of the vacancy-cation and vacancy-vacancy interactions on the material's conductivity.

6.1 The parameterisation of a potential for Sc_2O_3 and Y_2O_3 stabilised zirconias

In this section the parameterisation of a potential for YSZ and ScSZ will be described. The procedure was quite similar to that described in chapter 4 although in this case only a DIPPIM potential was parameterised, since this was found to be sufficiently good to reproduce all the

experimental properties of interest.

6.1.1 DFT reference calculations

The potential obtained in chapter 4 was used to generate an atomic configuration for $ScZr_3O_{1.875}$ (with the Sc-O interaction obtained by scaling the parameters from the Zr-O interaction with respect to the ionic radius). This configuration was used to run DFT reference calculations (see below) and an initial DIPPIM model was fitted to the forces and dipoles. After that, by combining this result with the parameters in chapter 4, an approximate potential was obtained for Sc_2O_3 - Y_2O_3 - ZrO_2 mixtures. This potential was then used to generate more reference MD configurations on a 2 x 2 x 2 unit cells simulation box (92 ions), two for $ScZr_3O_{1.875}$ and two $YZr_3O_{1.875}$ at high temperatures (3000 - 3500 K). For each of these, the Hellman–Feynman forces acting on individual ions of the simulation cell were calculated using the planewave-DFT code CPMD [85]. This package was found to be at least 20 times faster than CASTEP (both for the single point calculation and the Wannier analysis) and equally accurate (see figure 6.1) [114]. All the calculations used Goedecker norm-conserving pseudopotentials (as taken

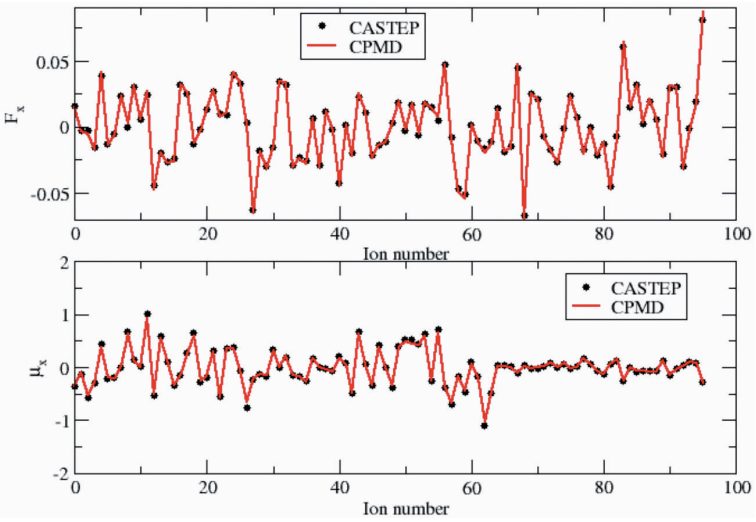

Figure 6.1: Comparison between the forces and dipoles for an oxide system as calculated with CPMD and CASTEP, with the same exchange-correlation functional and pseudopotentials.

from the online psudopotential repository [85]) and planewave energy cut-offs of 1360 eV and were performed using the local density approximation (LDA). For the calculation of ab initio multipoles, the Kohn–Sham orbitals are localised via a Wannier transformation to construct maximally localised Wannier functions (MLWF). From the localised orbitals, ionic dipoles and quadrupoles were calculated as described in section 3.3.1.

6.1.2 Details on the force-matching procedure

The potential parameters are optimised by fitting the forces and dipoles predicted by the DIPPIM potentials for the reference configurations to the respective results from the DFT calculations. The 4 configurations provide a total of around 2200 data points, comprising three Cartesian force components of each individual ion and three components for the dipole. As described in the previous chapter, some parameters are usually constrained. In this case, the cation-cation and anion-anion short range repulsion terms were set to zero, as this made no difference at all to the fit quality.

One problem with DFT calculations is the uncontrolled representation of the dispersion interaction. Although dispersion energies only contribute a tiny fraction to the total energy, they have a considerable influence on transition pressures and, in particular, on the material density and stress tensor. In this case an alternative procedure was used to try to compensate for this shortcoming. In fact, since it was found that the DFT calculations tend to overestimate the unit cell parameters for these materials, by approximately 1.5 %, it was decided to rescale the ionic positions before starting the fit, so that the material retains the correct density. The fit was then started, but this time the dispersion parameters were included and fixed from the start. The resulting potential yields a much better agreement (less then 1% difference) with the experimental densities than that obtained in chapter 4.

The agreement between the DFT and MD values is much closer than the one obtained for YNZO. The objective functions are χ_F = 0.193 and χ_D = 0.155. These values are smaller than those obtained with the QUAIM potential in the case of YNZO. This means that in ZYSO quadrupoles and ion shape deformation effects are less important and this is probably caused by the absence of Nb^{5+} ions in these materials. In fact, such a highly charged cation might cause greater ion shape deformations on the oxide ion, due to its strong coulombic interaction with it. The fact that the values of the objective functions for YSZ and ScSZ are smaller is also in agreement with ref. [8], where they show that, in YSZ and ScSZ, the total electronic contribution to the defect interactions is strongly dominated by simple point-charge electrostatics.

Table 6.1 reports the parameters obtained for these potentials. A comparison with table 4.3 shows that the parameters for the Zr-O and Y-O interactions are quite similar to the previous ones, as expected. The oxygen polarisability too is in good agreement with that previously used in a similar study [76] and that obtained by extrapolation of ab initio calculations on other oxides [79].

Table 6.1: Parameters for the DIPPIM potentials with values in a.u..Those short-range parameters which are equal to zero are not reported.

	O-O	Y-O	Zr-O	Sc-O
A^{ij}	0.00	83.11	65.50	59.19
a^{ij}	5.00	1.294	1.206	1.275
B^{ij}	50000	50000	50000	50000
b^{ij}	1.00	1.25	1.50	1.50
α	14.33	1.90	2.33	1.20
C_6^{ij}	66	15	7	7
C_8^{ij}	1200	300	150	150
b_{disp}^{ij}	1.2	1.9	1.9	1.9
b_D^{O-O}	1.736		b_D^{O-Zr}	1.817
c_D^{O-O}	0.874		c_D^{O-Zr}	1.720
b_D^{O-Y}	1.700		b_D^{Y-Y}	1.926
c_D^{O-Y}	1.559		c_D^{Y-Y}	-1.766
b_D^{O-Sc}	1.832		b_D^{Y-O}	1.700
c_D^{O-Sc}	1.666		c_D^{Y-O}	-2.486
b_D^{Sc-Sc}	1.926		b_D^{Sc-O}	1.832
c_D^{Sc-Sc}	-1.766		c_D^{Sc-O}	-2.797
b_D^{Zr-Zr}	1.135		b_D^{Zr-O}	1.817
c_D^{Zr-Zr}	-0.373		c_D^{Zr-O}	-2.499

6.2 Validation of the potential

In this section the quality of the DIPPIM potential will be assessed by comparing model predictions to experimental data. Since no experimental data were used in the optimisation of the model parameters, a strong test for the quality of the model is whether it is able to reproduce experimental data of physical properties of ScSZ and YSZ at different conditions (high temperatures, different mixtures and vacancy concentrations, *etc.*).

Also in this case, as a result of an on-going collaboration with Dr Stephen Hull and Dr Stefan Norberg at the ISIS Facility and with Prof. John Irvine at the University of St. Andrews, a wealth of yet-to-be-published neutron and impedance spectroscopy data on the ZYSO system could be accessed. These data together with those already available in the literature on stabilised zirconias [25, 26, 23, 7] will be an ideal test-bed for the potential's quality.

6.2.1 Structural properties

Most of the simulations on the YSZO system were performed using a cubic simulation box with 4 x 4 x 4 unit cells, i.e. 256 cations and a variable number of oxygen ions, according to the dopant concentration. The cation species were randomly distributed over the cation sublattice. In the previous chapter, it was concluded that local cation ordering, as observed in Y_3NbO_7, was much less important in $Y_2Zr_2O_7$ and it is presumed that this remains true at other compositions as well as in ScSZ (where the site mismatch between Sc^{3+} and Zr^{4+} is even smaller than in the Y^{3+} and Zr^{4+} case [59]), so that a random distribution of cations is appropriate. This will be confirmed, later on, by the fact that these simulations can successfully reproduce the diffuse peaks observed in the neutron diffraction patterns by Goff and co-workers [7]. The time step used was 41.342 au = 1.0 fs and all the runs were performed at constant temperature and zero-pressure (NPT ensemble). The simulations were started from a perfect fluorite structure and the system was equilibrated at 2000 K for 50,000 steps, to allow both cations and anions to relax in the crystal. The system was then cooled down to 300 K via temperature ramping. The cooling rate was approximately 1.7×10^{13} Ks^{-1}. A final run of 10,000 steps was performed to accumulate sufficient statistics for the calculation of the radial distribution functions.

Figure 6.2 shows the total radial distribution functions obtained from a neutron scattering experimental on the YSZO system, for a series of different dopant concentrations. The $y = 0$ material is not reported because this is not fully stabilised at room temperature, but is a mixture of fluorite-like and orthorhombic-like domains [56, 46, 24]. The agreement with the experimental data is very good across different dopant cation concentrations, once again showing the

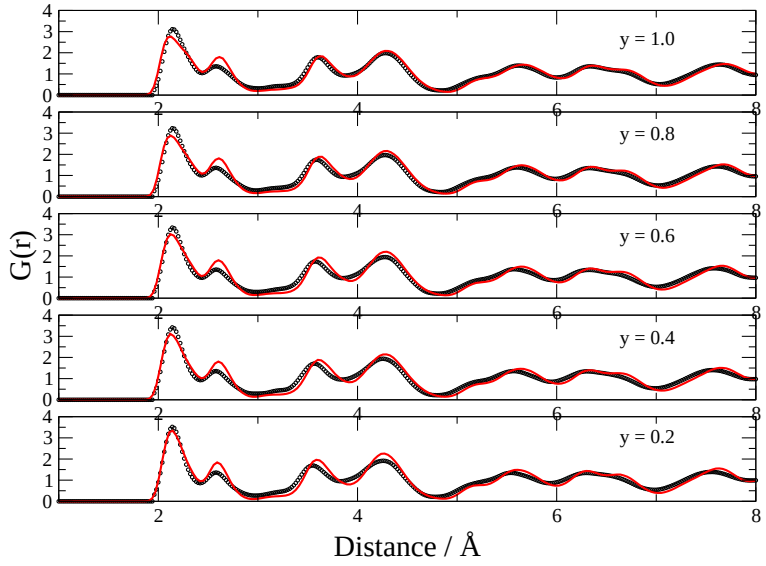

Figure 6.2: *Comparison between the experimental [24] (black dots) and simulated (red lines) total G(r) for the YSZO system, at 300 K.*

transferability of the used model. The lattice parameters (not shown) are within 1% the experimental values. The only shortcoming seems to be the fact that the second peak in the $G(r)$, which should be mostly the O-O nearest neighbour peak, is a bit sharper than the experimental one. This will be discussed below.

In figure 6.3 the partial radial distribution functions are reported for two materials, $Zr_{0.8}Y_{0.2}O_{1.9}$ and $Zr_{0.8}Sc_{0.16}Y_{0.04}O_{1.9}$, compared to the ones obtained by bond-valence-sum-constrained RMC data analysis [107, 24]. The agreement with the experimental data is excellent. The cation-anion distances in $Zr_{0.8}Sc_{0.16}Y_{0.04}O_{1.9}$ are 2.13, 2.18 and 2.32 Å for the Zr-O, Sc-O and Y-O pair, respectively. The potential is indeed able to reproduce the difference in the cations, with the Y^{3+} being significantly bigger than Sc^{3+} and Zr^{4+}. Again, a closer inspection of the O-O rdfs, shows that the peak obtained by the MD simulations is a bit sharper than the experimental one. This seems to imply that the O-O interaction in our potential is slightly harder than in the real material. More sophisticated potentials were parameterised, like the QUAIM potential, but no change was found in the O-O rdf. To see whether this was a shortcoming of our potential or not, a short Car-Parrinello molecular dynamics simulation was performed on $Zr_{0.8}Y_{0.2}O_{1.9}$, using CPMD and the same exchange-correlation functional and pseudopotentials used for the fitting calculations. This simulation was started from a previous MD run using our potential and it was then equilibrated at 3000 K for 10 ps, before being cooled down to 300 K. A subsequent run of 5 ps was then performed at room temperature to accumulate enough statistics for the calculation of rdfs. The O-O rdf obtained from this simulation is shown in figure 6.4 together with the MD and RMC-analysed experimental data. It can be seen that both the DFT and classical MD simulations tend to give a sharper peak than observed experimentally. Different functionals (GGA, LDA) and pseudopotentials were tried, but no improvement was found. Since our potentials are obtained by fitting to DFT data, it is not possible to solve this shortcoming. However, it is believed that this should not influence our results very much, especially at high temperature, as suggested by the good agreement with the conducting properties of these materials (see below).

Next, it was decided to attempt to reproduce the single crystal neutron diffraction patterns for YSZ reported in ref. [7]. This should represent an even more stringent test for the quality of our potentials. In fact, reproducing the data from Goff *et al.*, which shows diffuse scattering peaks caused by vacancy ordering tendencies, is the only way to test, although indirectly, the ability of our potential to correctly reproduce the vacancy behaviour. Unlike when studying Y_3NbO_7, it is expected that, in this case, no problem should be encountered with cation ordering, since these tendencies should be very weak for these materials. For this reason the neutron

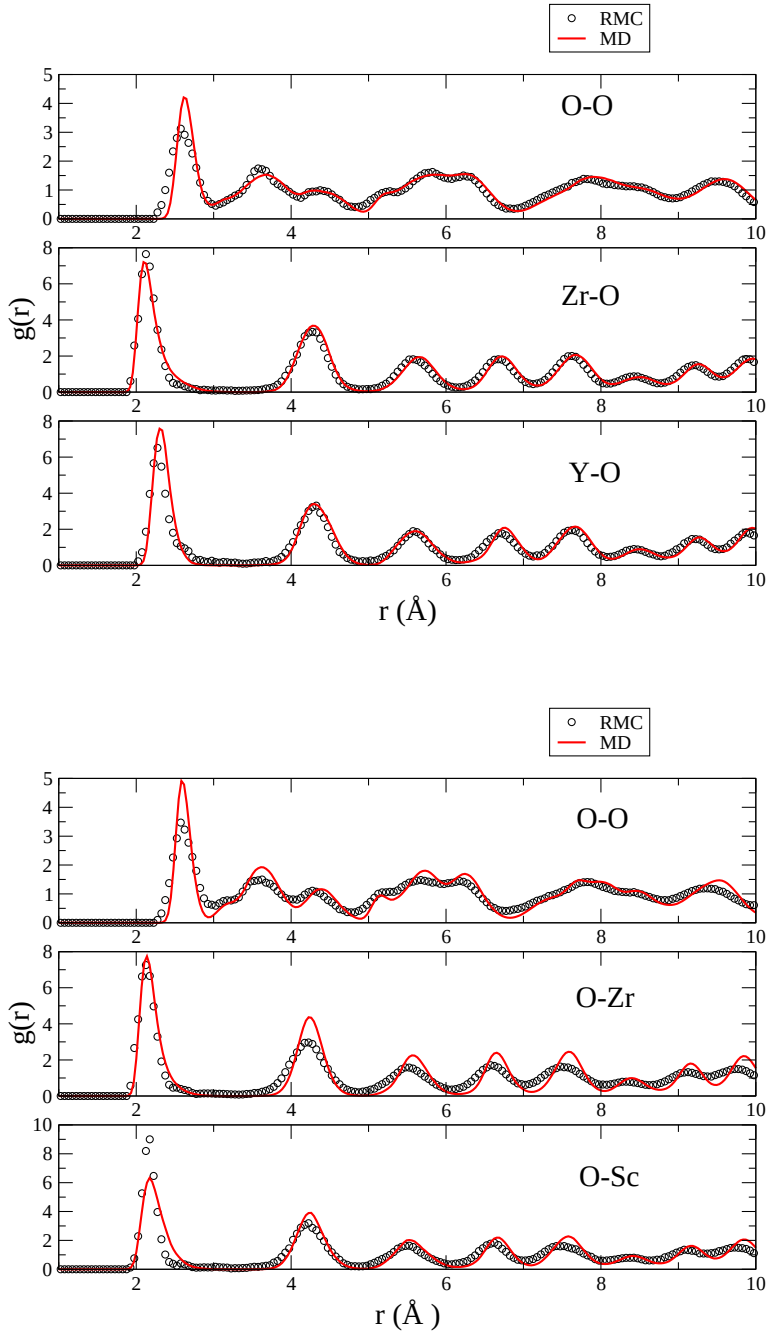

Figure 6.3: *Comparison between the g(r)s obtained from the RMC analysis (black dots) and the MD simulations (thick red line) for* $Zr_{0.8}Y_{0.2}O_{1.9}$ *(top) and* $Zr_{0.8}Sc_{0.16}Y_{0.04}O_{1.9}$ *(bottom).*

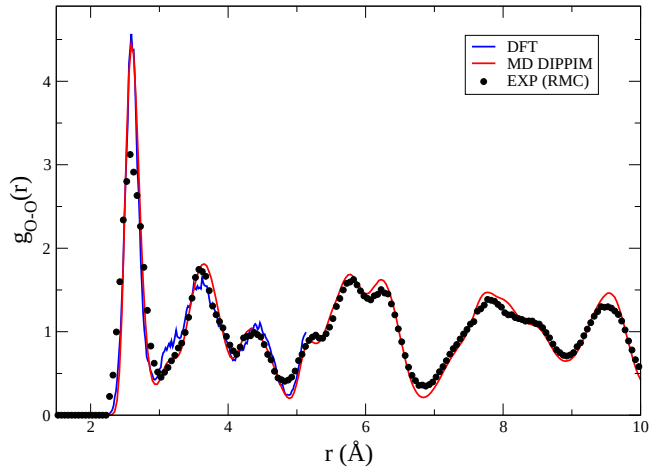

Figure 6.4: *Comparison of the $g_{O-O}(r)$ from the DFT calculation (blue line), MD calculation (red line) and experiment (black dots), as obtained via RMC analysis [24].*

diffraction patterns was calculated as explained in section 3.5.4. The calculation was done for different YSZs on a 6 x 6 x 6 unit cells simulation box. This yields a reciprocal space resolution of $\frac{2\pi}{L} \sim 0.2$ Å $^{-1}$, which is twice as low as the one obtained by Goff *et al.* [7]. These simulations were started at 1800 K and then slowly cooled down to 800 K with a cooling rate of 10^{12} K s^{-1}. In this temperature range, oxygen ion diffusion is observed while, below 800 K, no diffusion can be seen on the available timescale. For this reason the simulations at low dopant content (x = 0.9) were further quenched down to room temperature (300 K). Although this should not influence the vacancy ordering this will increase the tetragonal distortions in the sample (see discussion in chapter 2). The patterns are reported in figure 6.5 for three different dopant concentrations and are compared with the experimental data from ref. [7].

The x = 0.09 (T = 300 K) composition corresponds to the maximum of the conductivity plot for YSZ. The figure shows a $\langle 1\bar{1}0 \rangle$ plane in reciprocal space. Sharp intense peaks are seen in the experimental data at the fcc Bragg positions $\langle 002 \rangle$, $\langle 004 \rangle$, $\langle 111 \rangle$, $\langle 113 \rangle$, $\langle 220 \rangle$, $\langle 222 \rangle$, *etc.*; in the simulation data the Bragg peaks are centred on the same $\mathbf{q}$ values but are broader because of the lower resolution of our calculations as compared with the experimental data. The remainder of the intensity which appears in the pattern is diffuse scattering and is indicative of local structural deformations. At x = 0.09 the most intense diffuse features in the experimental data appear at $\langle 114 \rangle$ and $\langle 112 \rangle$; these are forbidden reflections for the fluo-

rite structure. According to the analysis of Goff *et al.* these peaks are a consequence of local tetragonal distortions of the fluorite structure which occur at relatively low concentrations of Y_2O_3. Recall, in fact, that in pure ZrO_2, a tetragonal phase is more stable than the cubic one and that Y_2O_3 is added to stabilise the latter. At low Y_2O_3 concentrations local tetragonal distortions with random orientation occur even within a single crystal. Comparison with the MD data shows that the same diffuse features are present in the simulation data, together with other features which are comparatively weak in the experimental data. This indicates that the tendency to local tetragonal distortion is reproduced in the simulated system: the differences in the intensity distribution and the widths of the diffuse features compared to experiment may be attributed to the small size of our simulation cell which sets a limit to the range of correlation of the tetragonal deformation which can be accommodated and thus leads to broader, weaker diffuse features. Both sets of data also show a broad, weak feature at $\mathbf{q} = (1.7, 1.7, 1)$ which is associated with a pattern of lattice deformation about isolated vacancies [7].

As the Y_2O_3 concentration is increased to x = 0.13 and x = 0.24 (T = 800 K), the $\langle 114 \rangle$ and $\langle 112 \rangle$ features disappear and the diffuse scattering becomes dominated by new features (highlighted by the arrows in the bottom part of figure 6.5) which may be described as belonging to a superlattice at $\mathbf{G} \pm \langle 0.4, 0.4, \pm 0.8 \rangle$, where $\mathbf{G}$ is an fcc Bragg peak position [7]. This pattern has been interpreted as caused by small aggregates of divacancy clusters (vacancies paired along the $\langle 111 \rangle$ direction) packed along the $\langle 112 \rangle$ direction, as found in the $Zr_3Y_4O_{12}$ compound. These aggregates are typically 15 Å in diameter [7]. This structure is consistent with the most stable arrangement of vacancy pairs found by Bogicevic [8] in his analysis of vacancy-ordering tendencies in YSZ. In the next chapter it will be shown that vacancies do indeed prefer to arrange as pairs along the $\langle 111 \rangle$ direction in these materials, thus confirming the interpretation by Goff and co-workers [7]. Comparison with the simulation data shows that the signature of this particular vacancy-vacancy ordering has been reproduced in the simulation. Interestingly, since our simulations at x = 0.13 and x = 0.24 were run at T = 800 K, this means that these ordering effects are still present at high temperature and that therefore they will affect the conducting properties of these materials at the temperatures of interest for technological applications (see discussion in the next chapter).

In conclusion the obtained DIPPIM potential seems to reproduce very well the experimental structural data. The agreement with the rdfs obtained from neutron powder diffraction experiments [24] is very good for different dopant concentrations. Also the single crystal neutron diffraction patterns from [7], which are more sensitive to longer range ordering tendencies of the vacancies, are well reproduced. In the next section, the ability of this model to reproduce

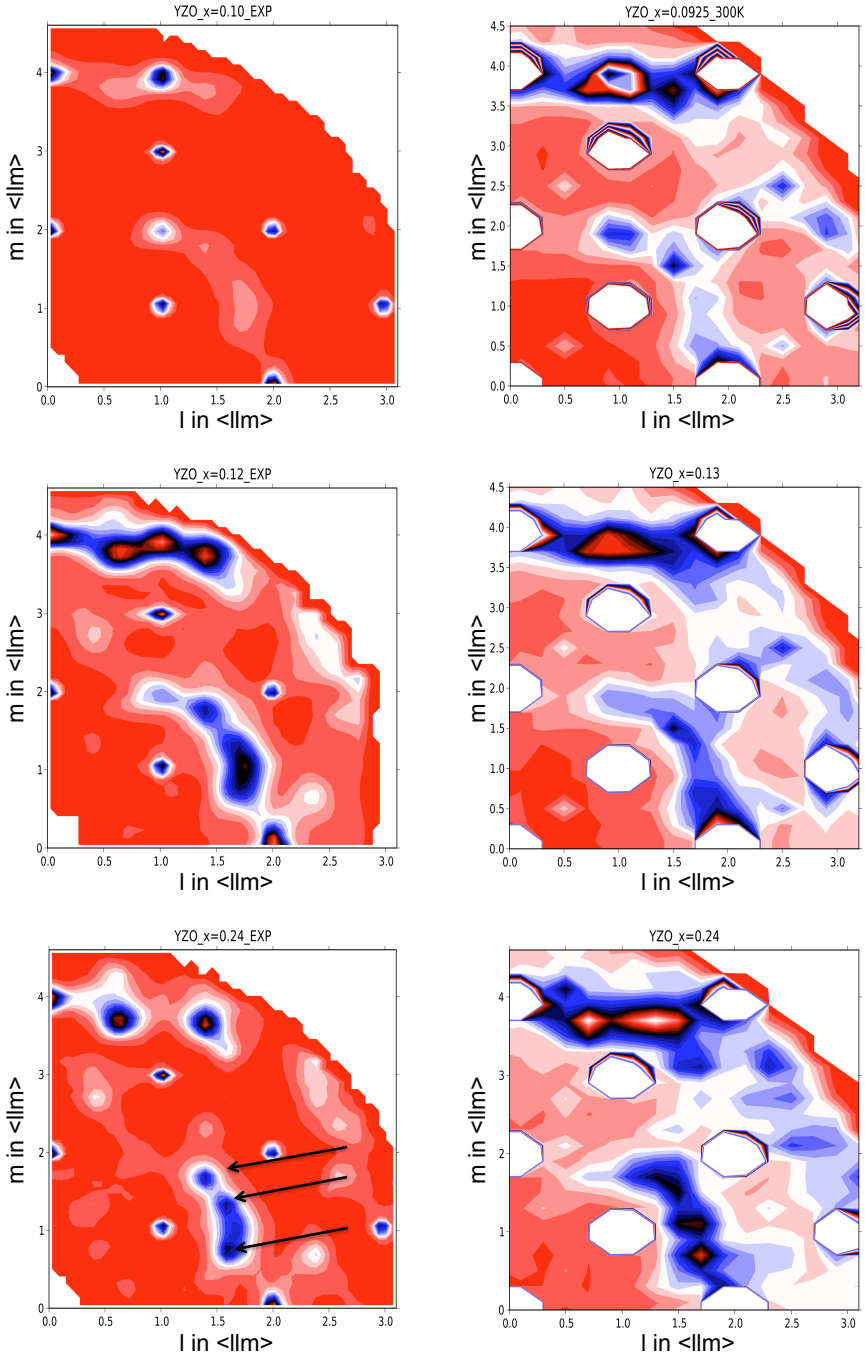

Figure 6.5: *Experimental (left) and computed (right) neutron diffraction patterns for 9 % (top), 13 % (middle) and 24 % (bottom) YSZ. The MD data was obtained at 300 K for 9% YSZ and at 800 K for 13 and 24 % YSZ.*

the conducting properties of these materials will be tested.

6.2.2 Conducting properties

All the simulations were started from the room temperature runs described above. These were equilibrated at the required temperature for at least 100,000 steps (corresponding to $\sim$ 100 ps) and then longer runs were performed to accumulate sufficient statistics for the calculation of the mean squared displacements. Since these materials are, on average, more conducting than those studied in the previous chapters, it was possible to get a reliable estimate of the conductivity for temperatures as low as T = 1000 K. All the simulations were performed in the NVT ensemble in which the cell volume was obtained from a previous NPT run at the same temperature. The diffusion coefficients were obtained from the slope of the mean squared displacement curve and from these the ionic conductivities were calculated as described in section 3.5.2. In some cases, the conductivities were also calculated using equation 3.23. These were found to be identical (within the statistical error) to the Nernst-Einstein conductivities for lightly doped samples ($x < 0.15$). For higher dopant concentrations, greater differences, of the order of 20 - 30 % were observed. Since in no case were the differences very important and since, in this thesis, the main interest is in the trends more than in the absolute values, it was decided to report the Nernst-Einstein conductivities only in the remainder of this chapter.

In figure 6.6 the calculated conductivities are shown for the $Zr_{0.8}Sc_{0.2(1-y)}Y_{0.2y}\ O_{1.9}$ system as a function of y at 1200 K. The experimental trend of increasing conductivity as a function of increasing content of Sc_2O_3 is correctly reproduced, as shown by the comparison with the data at T = 1158 K from [24]. Also the absolute values are in reasonable agreement with the experimental data, if the difference in temperature is taken into account. It has to be noticed that, as in the previous case (see chapter 5), it is observed that the conductivity of this material shows a weak dependence ($\sim$ 10%) on the cation arrangement, especially for the Y^{3+}-rich compositions. This is consistent with what was found in the previous chapters. For this reason it was always made sure that the cations were randomly distributed over the sublattice.

Our MD results can now be compared with the available experimental data on $(Y_2O_3)_x$-$(ZrO_2)_{1-x}$ and $(Sc_2O_3)_x$-$(ZrO_2)_{1-x}$. As was explained in chapter 2, the conductivity in these materials does not increases indefinitely with the number of vacancies but shows a maximum at a dopant concentration, x, of approximately 8 - 13 %. Since most of the remainder of this thesis will be dedicated to trying to explain which factors are responsible for this maximum, it is necessary to test our potentials at different dopant concentrations before any conclusion can be drawn on the conduction mechanism of these materials. Figure 6.7 shows the calcu-

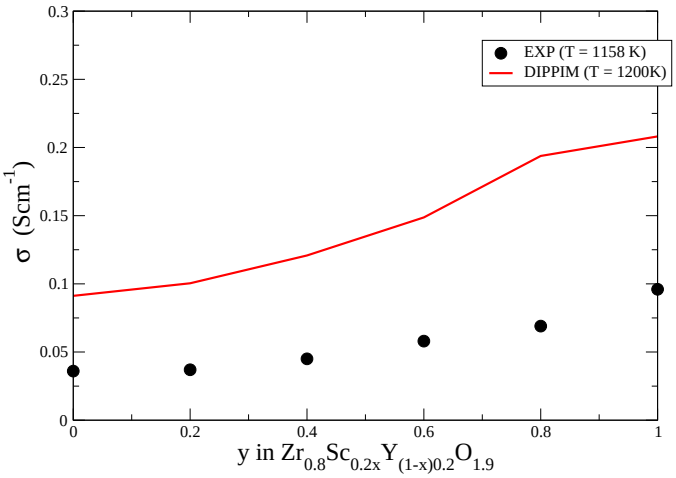

Figure 6.6: *Conductivity isotherm (red line) at 1200 K for the* $Zr_{0.8}Sc_{0.2(1-y)}Y_{0.2y}\ O_{1.9}$ *system. The experimental data (black dots) at 1158 K from [24] are reported as a comparison.*

lated conductivities for both YSZ and ScSZ as a function of dopant concentration at 1670 K. For YSZ, the experimental values from ref. [25, 26] are also reported. The agreement with the experimental data looks promising. Both curves show a peak in the conductivity at 8-9 % and 12-13 % for YSZ and ScSZ respectively, in good agreement with the experimental data. The MD data on YSZ are also in reasonable quantitative agreement although the rise in conductivity shown by our simulation data is smaller than that of the experimental data. This is probably caused by the small systems studied in this thesis, which do not allow the formation of grain boundaries and tetragonal domains. Also, as discussed before, for $x > 0.15$, the Nernst-Einstein conductivities tend to be higher than those obtained using equation 3.23 and this can also explain the differences in high-x region of the plot.

The conductivities shown above were calculated from simulations in which the cubic fluorite symmetry was enforced. This was done by using an isotropic barostat. As described in chapter 2, YSZ and ScSZ are not cubic at low temperatures and dopant concentrations. For this reason, when the same curves as those shown in figure 6.7 are calculated at lower temperatures, a slightly different behaviour is observed (see figure 6.8). The maximum has, in fact, shifted to lower dopant concentrations (approximately 6 % and 8 % for YSZ and ScSZ respectively) and the curve's shape looks very similar to that of Gd_2O_3-doped ZrO_2 (see figure 2.2, a material which, due to Gd's big ionic radius, is cubic for almost all compositions). A shift of the maxi-

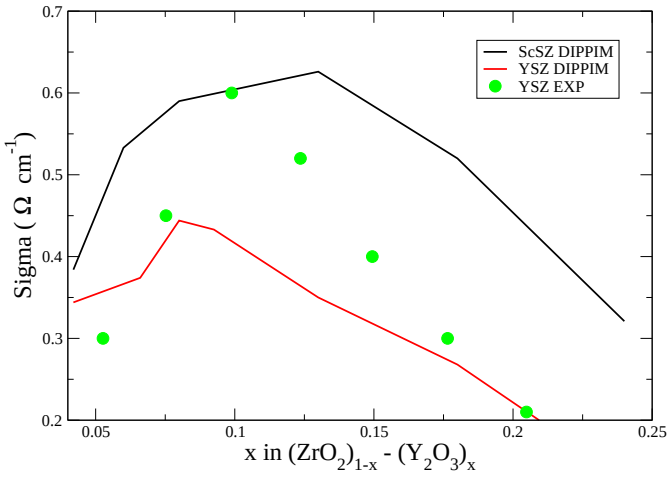

Figure 6.7: *MD conductivities vs doping (x) for YSZ (red curve) and ScSZ (black curve) at 1670 K. The experimental data from [25, 26] for YSZ at the same temperature are also reported.*

mum's position as the temperature is lowered is also observed experimentally [25, 26], though not as strong as that indicated by the comparison of figure 6.8 with figure 6.7.

The observed features in the curves in figure 6.8 are mainly caused by the fact that the real material is not fully cubic at these temperatures and dopant concentrations, so that the simulations tend to overestimate, at low x, the conductivity of these materials. To prove this, the cubic fluorite symmetry was relaxed in a simulation on 4% ScSZ and the simulation box was allowed to change its shape, by using an anisotropic barostat. The simulation quickly turned to a non-cubic symmetry which looked like a monoclinic structure. The conductivity obtained for monoclinic 4 % ScSZ is shown in figure 6.8 as a green diamond. It can be appreciated that this is indeed much lower (more than ten times!) than the conductivity obtained from a cubic simulation. Though it would be tempting to just relax the cubic symmetry for all dopant concentrations and calculate the resulting conductivity, this operation cannot be performed in practice, because a simple DIPPIM potential is not accurate enough to reproduce the correct order of the different crystal phases in pure ZrO_2, as discussed in chapter 3 and in ref. [76]. For this reason, when studying, in the next chapter, the conducting mechanism of these materials, it will have to be kept in mind that the conductivity obtained for lightly doped, cubic YSZ and SSZ are reliable *only* at high temperatures. It still has to be noted that this does not affect at all highly doped zirconias, i.e. all those materials with more than 8 - 10 % of dopant, since these

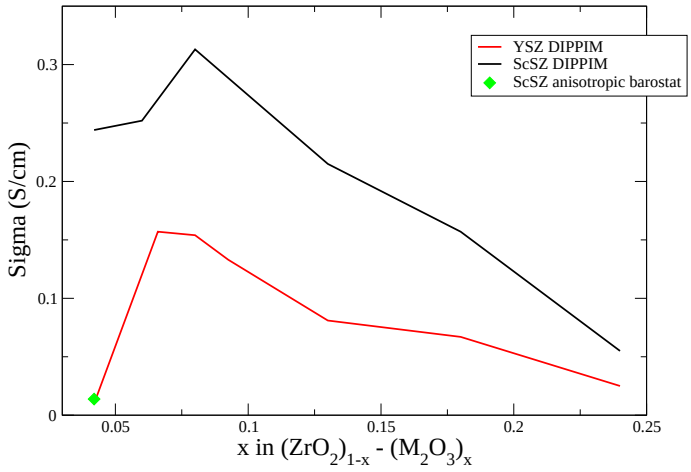

Figure 6.8: *MD conductivities vs doping (x) for YSZ (red curve) and ScSZ (black curve) at 1250 K.*

are fully stabilised at every temperature.

A final test to our model can be reproducing the quasielastic neutron data from ref. [7]. I(**q**,t) was calculated as explained in section 3.5.4, from a simulation at 1800 K on 13 % YSZ. These are the same conditions as found in the experimental work by Goff and co-workers [7]. The three **q** values were taken, in agreement with those from ref. [7], as those points corresponding to isolated vacancies (mobile) and clusters of vacancy pairs (immobile). It can be appreciated that only at **q** = 1.67, 1.67, 1, the intensity I(**q**,t) (which is caused by the presence of isolated, mobile vacancies) decays to zero, in good agreement with the experimental evidence. On the other hand, the functions at the other two **q** vectors do not decay as a function of time, proving that the diffuse scattering observed at those positions in reciprocal space is caused by defect aggregates which are immobile on the time-scale studied. By fitting the curve obtained at **q** = 1.67, 1.67, 1 with an exponential decay as in equation 3.25, an estimate for τ, the single vacancy lifetime, can be obtained. A value of $\tau_{MD} = 1.7$ ps is obtained from our MD simulations to be compared with the experimental value[1] of $\tau_{EXP} = 1.3$ ps. The agreement is very good.

[1]This value is obtained by extracting the characteristic energy transfer, E, from figure 8 in ref. [7]. Assuming this is of the order of 0.5 meV, then the vacancy lifetime is $\tau = \frac{\hbar}{E} = \frac{6.582\times10^{-16}}{0.5\times10^{-3}} \approx 1.3$ ps.

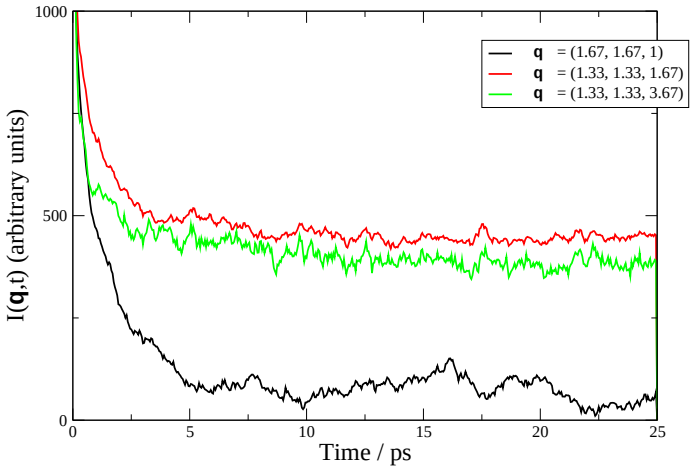

Figure 6.9: *Time scan at constant* **q** *through the quasielastic neutron diffuse scattering from 13 % YSZ at 1800 K.*

In conclusion, DIPPIM potentials were parameterised and tested for mixtures of YSZ and ScSZ. These were used to reproduce a series of experimental data: neutron powder diffraction, neutron single-crystal diffraction, impedance spectroscopy and quasielastic neutron scattering experiments. In all cases, the agreement between the simulations and the experimental data was good. When the agreement was not ideal, this was usually caused by some of the underlying assumptions (imposing a cubic structure, small system size) and not by a limitation of the used model. For these reasons, in the next chapter, these potentials will be used to study the conduction mechanism and the defect interactions in these materials.

Chapter 7

The conduction mechanism in stabilised zirconias

This chapter will start by reporting our study of the conduction mechanism in $Zr_{0.8}Sc_{0.2(1-y)}Y_{0.2y}O_{1.9}$ (ZYSO). The main focus of this part will be to understand why the Sc^{3+}-rich samples are much more conducting than the Y^{3+}-rich ones and which factors are responsible for this. This will be achieved by studying the relative importance of vacancy-vacancy and vacancy-cation ordering tendencies and the effects that different cations might have on these. The second part of this chapter will then examine the conduction mechanism in YSZ and ScSZ. The main focus, in this case, will be on understanding the anomalous trend of the conductivity as a function of the dopant concentration. Cation-vacancy and vacancy-vacancy ordering tendencies will be studied in depth as a possible cause of the observed drop in the conductivity and an attempt will be made to identify which of these factors ultimately limits the conductivity of these materials. Another goal of our investigation will be to find whether there is any scope for further improving their conducting properties by simply doping them with a more suitable choice of cation species.

7.1 The conduction mechanism in $\mathbf{Zr_{0.8}Sc_{0.2(1-y)}Y_{0.2y}O_{1.9}}$

All the simulations described in this chapter were thoroughly equilibrated at high temperatures (1000-2000 K) in constant pressure (isotropic barostat) simulations for about 100 ps before obtaining dynamical information from constant volume runs at the zero-pressure volume. At these high temperatures the oxide ions are diffusing on the simulation timescale but there is no significant exchange of cations (see figure 4.11). As described before, different cation species are randomly placed on the cation sublattice, as there should be no cation ordering in these ma-

terials. Some simulations were also cooled down to room temperature and further short runs were conducted in order to examine structural information and compare with diffraction data collected at the same temperature.

7.1.1 Cation-vacancy interactions

In figure 7.1 the oxygen-oxygen and cation-oxygen radial distribution functions are reported for $Zr_{0.8}Sc_{0.2}O_{1.9}$ and $Zr_{0.8}Y_{0.2}O_{1.9}$ at room temperature [1]. It can be appreciated that the oxygen-oxygen rdfs for the two materials are quite similar, although the one for $Zr_{0.8}Sc_{0.2}O_{1.9}$ is sharper and more structured, thus indicating that this material has a more ordered oxide ion distribution. This difference can be easily understood by looking at the bottom part of figure 7.1 where the cation-anion rdfs for these materials are shown. The Y-O rdf presents a maximum at a much higher distance than the Zr-O and Sc-O functions [2]. This is perfectly consistent with the fact that Y^{3+} has a greater ionic radius than the other cations [59]. This difference in the cation-oxygen bond distances causes the observed disorder in $Zr_{0.8}Y_{0.2}O_{1.9}$ and is still observed at temperatures as high as 1500 K, proving that these effects are significant at the temperatures at which the ionic conductivity of these materials is usually measured. On the other hand, in $Zr_{0.8}Sc_{0.2}O_{1.9}$ the cation-anion bond distances are similar and this system resembles very closely an ideal fluorite structure.

The quickest way to see if the vacancies prefer to bind to a certain cation, thus lowering the overall conductivity, is to calculate the vacancy-cation rdfs, as was done in chapter 5. These are shown in figure 7.2 for $Zr_{0.8}Sc_{0.2}O_{1.9}$ and $Zr_{0.8}Y_{0.2}O_{1.9}$ at 1500 K. It can be readily seen that, even at such a high temperature, there is a very strong binding tendency of the vacancies next to the Zr^{4+} ions in $Zr_{0.8}Y_{0.2}O_{1.9}$, whilst there is virtually no such preference in $Zr_{0.8}Sc_{0.2}O_{1.9}$ This behaviour can also be tested by calculating the anion-cation coordination numbers from the anion-cation rdfs. This was done for the simulation at 1500 K on $Zr_{0.8}Y_{0.2}O_{1.9}$ and it was found that n_{Y-O} = 7.65 and n_{Zr-O} = 7.35, which has to be compared with the stoichiometric value of 7.59. Y^{3+} cations tends to have more oxide ions around them than expected from the sample's stoichiometry whereas Zr^{4+} cations tend to do the contrary. This is consistent with

[1] $Zr_{0.8}Sc_{0.2}O_{1.9}$ is very hard to synthesise in the cubic phase and it is usually found as a mixture of fluorite and orthorhombic domains. In this case, it was forced to the cubic phase by constraining the simulation box. This was done for clarity's sake, as it is much easier to study the two end materials. Also this does not create any problem when studying the conducting properties because this material becomes fully cubic at T = 800 K [46].

[2] As mentioned in the previous chapter, the cation-anion bond distances are 2.13, 2.18 and 2.32 Å for the Zr-O, Sc-O and Y-O pair, respectively, in good agreement with the RMC data [24]

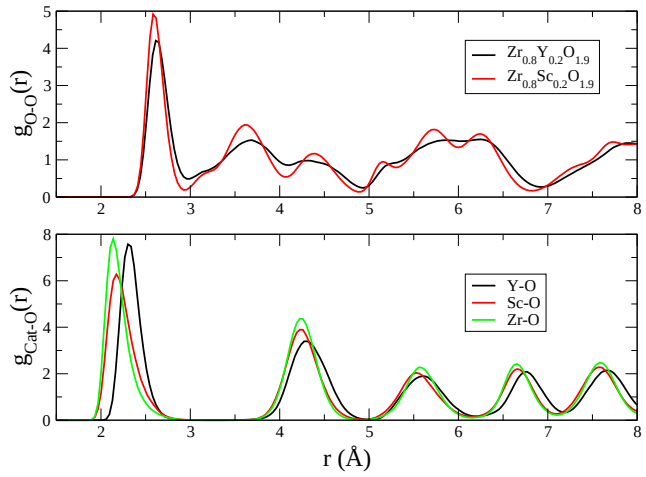

Figure 7.1: *Comparison between the simulated O-O and cation-O rdfs for $Zr_{0.8}Sc_{0.2}O_{1.9}$ and $Zr_{0.8}Y_{0.2}O_{1.9}$ at room temperature.*

Y^{3+}'s tendency to be eight-coordinated and Zr^{4+}'s tendency to be seven-coordinated. These tendencies are equivalent to saying that vacancies prefer to bind to the Zr^{4+} ion. Incidentally, this analysis also confirms the reliability of the methodology described in section 3.5.3.

The tendency for vacancies to be nearest neighbour to the small cations and next nearest neighbour to bigger cations had already been shown and its implications discussed in refs. [27, 34]. However these studies were zero-temperature energy calculations and therefore contained no information as to how important these effects are at high temperatures. Figure 7.3 shows the temperature dependence of these tendencies for T = 1000, 1100, 1200, 1500 and 2000 K. The cation-vacancy binding tendency increases when the temperature is lowered, as expected. It worth noting that the solid curve shows the rdfs for T = 1000 K, which is approximately the temperature at which a solid oxide fuel cell with an YSZ electrolyte is used. At this temperature about twice as many vacancies bind to the smaller Zr^{4+} cations than to the bigger Y^{3+} ones (see table 7.1), thus proving that these effects are indeed very strong at the temperatures of interest for technological applications. The vacancy-cation ordering tendencies are also summarised in table 7.1 where the percentage number of vacancies close to a certain cation species are reported for $Zr_{0.8}Y_{0.2}O_{1.9}$ at different temperatures. Interestingly, even at 2000 K there is still a certain preference for the vacancies to bind next to the Zr^{4+} ions.

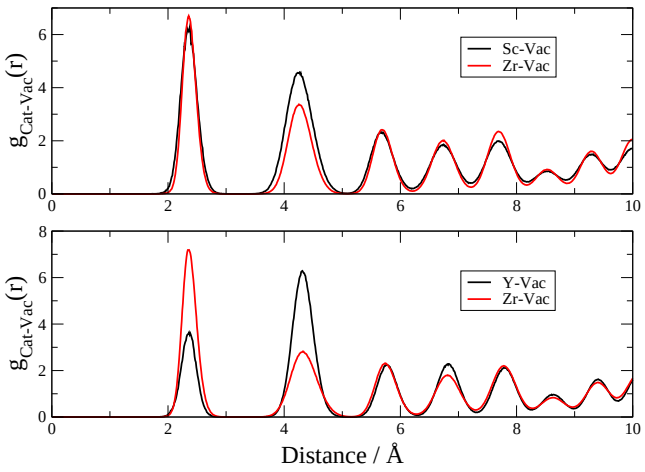

Figure 7.2: *Cation-vacancy radial distribution functions for $Zr_{0.8}Sc_{0.2}O_{1.9}$ (top) and $Zr_{0.8}Y_{0.2}O_{1.9}$ (bottom) at 1500 K.*

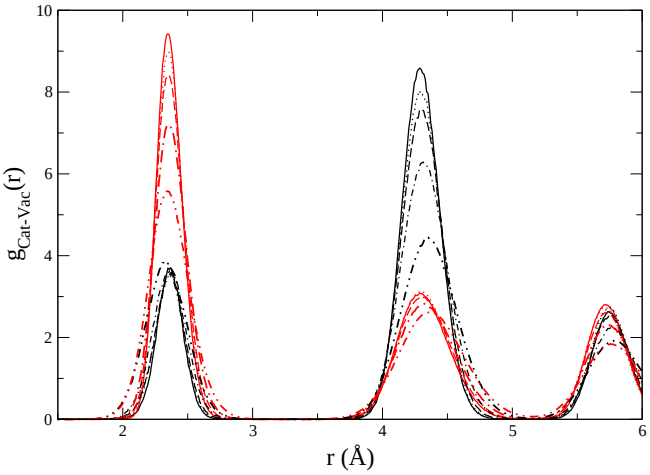

Figure 7.3: *Cation-vacancy radial distribution functions for $Zr_{0.8}Y_{0.2}O_{1.9}$ at 1000 K (solid line), 1100 K (dotted line), 1200 K (dashed line), 1500 K (dot-dashed line) and 2000 K (double-dot-dashed line). Red curves are the Zr-Vac and black curves are the Y-Vac radial distribution functions.*

Table 7.1: Percentage number of vacancies close to a certain cation as extracted from our MD simulations on $Zr_{0.8}Y_{0.2}O_{1.9}$ at different temperatures.

Temperature	n_{Y-V} (%)	n_{Zr-V} (%)
1000 K	29	71
1100 K	30	70
1200 K	31	69
1500 K	34	66
2000 K	41	59

The data reported in table 7.1 can be used to estimate the difference in energy between the two vacancy-cation arrangements. Indeed, if it is assumed that the ratio between n_{Y-V} and n_{Zr-V} has an exponential behaviour (like in a van't Hoff equation [115]), i.e.

$$\frac{n_{Y-V}}{n_{Zr-V}} = A_0 \times \exp(-\frac{E_{Zr-Y}}{k_B T}) \tag{7.1}$$

where A_0 is a constant, k_B Boltzmann's constant and T the temperature in Kelvin, then the energy difference, E_{Zr-Y} can be extrapolated from our data. This is reported in figure 7.4 where the logarithm of $\frac{n_{Zr-V}}{n_{Y-V}}$ is plotted against the inverse temperature. A linear fit is shown as well. The fact that the data can be fitted with a straight line quite successfully confirms the validity of the above assumption. The energy difference obtained via this procedure is E_{Zr-Y} = 0.09 eV. This is value is in reasonably good agreement with those obtained by Bogicevic *et al.*. In the next section, the same analysis will be performed to study the vacancy-vacancy energetics.

It appears clear from the above discussion that cation-vacancy interactions are quite strong in the Y^{3+}-rich side of the ZYSO series whereas they are absent in the Sc^{3+}-rich side. This would explain very well the differences in the conductivity of these materials: vacancies in $Zr_{0.8}Sc_{0.2}O_{1.9}$ do not have any preference for a certain cation species and this lowers the migration energy and makes their motion easier [34]. However, it would be interesting to study vacancy-vacancy interactions (which have been suggested by Goff *et al.* as another factor affecting the conductivity of these materials) in these materials to see if these too contribute to the observed changes in the conductivity of the ZYSO system. This is done below.

7.1.2 Vacancy-vacancy interactions

In figure 7.5 the vacancy-vacancy radial distribution functions are reported for $Zr_{0.8}Sc_{0.2}O_{1.9}$ and $Zr_{0.8}Y_{0.2}O_{1.9}$ at 1500 K, together with the function one would expect if vacancies were

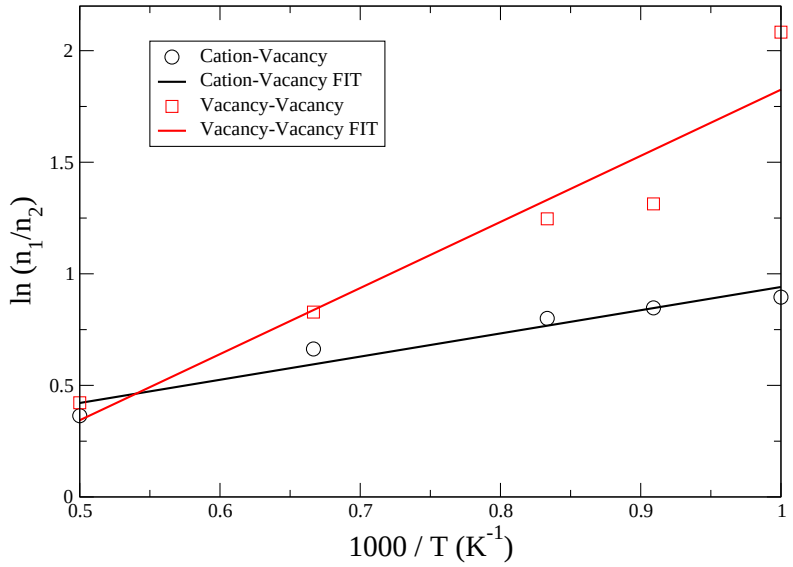

Figure 7.4: *Black dots (curve = fit): logarithm of the ratio between the number of vacancies close to a Zr^{4+}, $n_1 = n_{Zr-V}$, and those close to an Y^{3+} cation, $n_2 = n_{Y-V}$, in $Zr_{0.8}Y_{0.2}O_{1.9}$ versus inverse temperature. Red squares (curve = fit): logarithm of the ratio between the number of $\langle 110 \rangle$ (n_2) and $\langle 111 \rangle$ (n_1) vacancy pairs, in $Zr_{0.8}Y_{0.2}O_{1.9}$ versus inverse temperature.*

randomly distributed [3]. The rdfs have all been rescaled so that the lattice parameters are the same. It can be readily appreciated that vacancies in the ZYSO system are not randomly distributed but they prefer to arrange along specific directions, in this case along the $\langle 111 \rangle$ fluorite lattice direction, as observed before in the case of Y_3NbO_7 and $Zr_2Y_2O_7$. It is interesting to note that occupancy of a pair of positions separated by the $\langle 111 \rangle$ vector results in a substantial lattice distortion, as seen in the position of the corresponding peak in $g_{Vac-Vac}(r)$ compared to the $g(r)$ obtained from a random distribution. It is also clear that the vacancy-vacancy correlations extend well beyond the first unit cell (see figure 7.6) and, indeed, the rdf only begins to match that of the random distribution for separations larger than 9 Å. The $\langle 200 \rangle$ position seems particularly unfavourable, but there is an enhanced occupation of the $\langle 210 \rangle$ and $\langle 211 \rangle$ positions which suggests that the pairs of vacancies are themselves beginning to order. It is well known that at the $Y_4Zr_3O_{12}$ composition, corresponding to x = 0.4, the YSZ system forms a compound which can be described as based on the fluorite structure with ordered $\langle 111 \rangle$ vacancy pairs in positions which are themselves ordered along the $\langle 112 \rangle$ direction and this appears to be the tendency which is being picked up in $g_{Vac-Vac}(r)$ even at considerably smaller x values. The fact that vacancy-vacancy ordering tendencies are so long-ranged is consistent with the fact that these are caused, at least in part, by the coulombic repulsion between vacancies [8].

The relative population of the anion vacancy pairs along the $\langle 100 \rangle$, $\langle 110 \rangle$ and $\langle 111 \rangle$ fluorite lattice directions are reported in tables 7.2 and 7.3 for the two compounds at different temperatures. A series of observations can be made. Firstly, in both materials, vacancy ordering shows a strong dependence on temperature, analogous to what was observed for the cation-vacancy ordering. While at 1500 - 2000 K there is only a weak preference for a $\langle 111 \rangle$ alignment and $\langle 100 \rangle$, $\langle 110 \rangle$ vacancy pairs are present as well, at lower temperatures this trend becomes stronger, with, for instance, almost no $\langle 100 \rangle$ vacancy pairs at 1000 K (the operational temperature for SOFCs). Secondly, by comparing table 5.5 with tables 7.2 and 7.3, it can be seen that the strength of the vacancy ordering at 1500 K is not very different from that observed in Y_3NbO_7 and $Zr_2Y_2O_7$. Finally, the last observation is that there is not a big difference between the vacancy ordering tendencies in $Zr_{0.8}Sc_{0.2}O_{1.9}$ and in $Zr_{0.8}Y_{0.2}O_{1.9}$. In both cases there is a strong preference for vacancy pairs along the $\langle 111 \rangle$ direction whilst the $\langle 100 \rangle$ and $\langle 110 \rangle$ directions are unfavoured. Also, in both cases these tendencies become stronger as the temperature is lowered. The only difference between these two materials is that $Zr_{0.8}Sc_{0.2}O_{1.9}$

[3] The vacancy-vacancy radial distribution functions shown in figure 7.5 are very sharply peaked. This is a consequence of the way locate the vacancy positions. As explained in section 3.5.3, the position of a vacancy is evaluated as the average position of the four surrounding cations. Since the cations are not diffusing at these temperatures and do not perform long vibrations around their lattice position, the resulting vacancy positions are usually quite close one to the other and this results in a very sharp rdf.

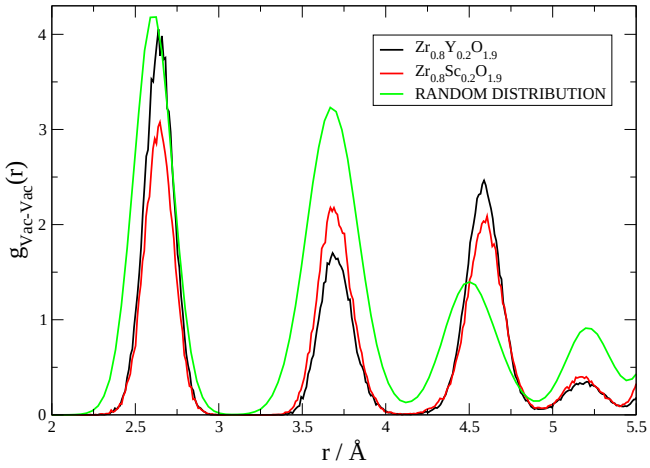

Figure 7.5: *Vacancy-vacancy radial distribution functions $Zr_{0.8}Sc_{0.2}O_{1.9}$ and $Zr_{0.8}Y_{0.2}O_{1.9}$ at 1500 K, together with the function one would expect if vacancies were randomly distributed.*

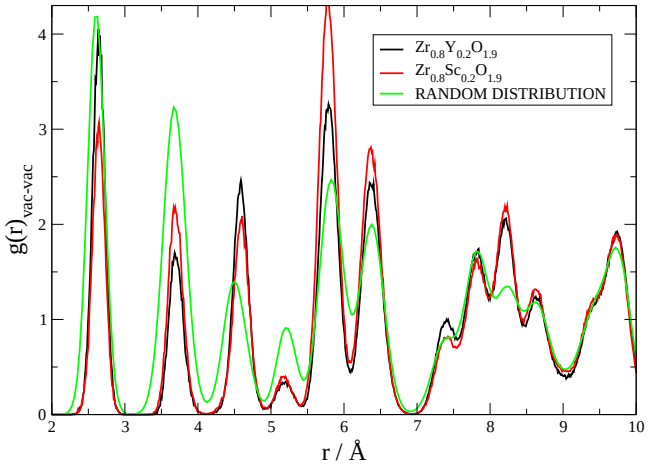

Figure 7.6: *Vacancy-vacancy radial distribution functions $Zr_{0.8}Sc_{0.2}O_{1.9}$ and $Zr_{0.8}Y_{0.2}O_{1.9}$ at 1500 K, together with the function one would expect if vacancies were randomly distributed. This figure shows a greater r range than the previous one.*

Table 7.2: Relative population of the anion vacancy pairs expected from a random distribution of vacancies within a cubic fluorite lattice, compared with those extracted from our MD simulations on $Zr_{0.8}Y_{0.2}O_{1.9}$ at 1000, 1100, 1200, 1500 and 2000 K.

Temperature	$\langle 100 \rangle$	$\langle 110 \rangle$	$\langle 111 \rangle$
RANDOM	0.231	0.461	0.308
1000 K	0.060	0.104	0.835
1100 K	0.160	0.178	0.662
1200 K	0.167	0.186	0.647
1500 K	0.239	0.231	0.529
2000 K	0.243	0.299	0.456

Table 7.3: Relative population of the anion vacancy pairs expected from a random distribution of vacancies within a cubic fluorite lattice, compared with those extracted from our MD simulations on $Zr_{0.8}Sc_{0.2}O_{1.9}$ at 1000, 1100, 1200, 1500 and 2000 K.

Temperature	$\langle 100 \rangle$	$\langle 110 \rangle$	$\langle 111 \rangle$
RANDOM	0.231	0.461	0.308
1000 K	0.011	0.207	0.769
1100 K	0.056	0.207	0.736
1200 K	0.129	0.248	0.622
1500 K	0.190	0.246	0.497
2000 K	0.276	0.329	0.394

systematically presents fewer $\langle 100 \rangle$ and more $\langle 110 \rangle$ vacancy pairs than $Zr_{0.8}Y_{0.2}O_{1.9}$.

The last observation can be caused by a limitation of our way of assigning the vacancies, which was discussed in section 3.5.3. In fact, if a tetrahedral site contains a vacancy, this will induce a substantial distortion of the surrounding tetrahedra which lowers the reliability of the geometric criterion used to decide if the site is filled or empty, especially at high temperatures or in disordered systems, where all the atoms are making large amplitude vibrations. There is therefore a tendency to assign vacancies to sites which neighbour a site containing a true vacancy, and this is manifested in a larger than expected amplitude for the nearest-neighbour peak in the vacancy–vacancy radial distribution function. This seems indeed to be the case for $Zr_{0.8}Y_{0.2}O_{1.9}$. As discussed above, this material has a more disordered structure than $Zr_{0.8}Sc_{0.2}O_{1.9}$, because Y^{3+} introduces a larger-than-expected cation-anion bond distance. This results in our program assigning more vacancies than expected. For instance, at 1200 K, an average of 28.3 vacancies (to be compared with the stoichiometric value of 26) are found in $Zr_{0.8}Y_{0.2}O_{1.9}$ whilst only 27.3 are found in $Zr_{0.8}Sc_{0.2}O_{1.9}$ at the same temperature. This

difference is probably responsible for the slightly higher number of $\langle 100 \rangle$ vacancy pairs found in $Zr_{0.8}Y_{0.2}O_{1.9}$ (see table 7.2).

Despite this limitation, an analysis (similar to the one performed above for cation-vacancy ordering) can be made to obtain an estimate of the energy difference between the $\langle 110 \rangle$ and $\langle 111 \rangle$ vacancy pairs. In fact, the relative population of these two pairs does not seem to be strongly affected by the above-mentioned limitation. For this reason, it can be written that

$$\frac{\langle 110 \rangle}{\langle 111 \rangle} = A_0 \times \exp(-\frac{E_{\langle 111 \rangle - \langle 110 \rangle}}{k_B T}) \tag{7.2}$$

and the data in table 7.2 can be used. The resulting curve for $Zr_{0.8}Y_{0.2}O_{1.9}$ is shown in figure 7.4, together with a linear fit. The obtained energy difference in this case is $E_{\langle 111 \rangle - \langle 110 \rangle} = 0.23$ eV. This value is in good agreement with those obtained by Bogicevic *et al.* [8]. It is worth noting that this value is almost three times greater than the one obtained for cation-vacancy ordering, thus implying that defect ordering in this material is most strongly governed by vacancy-vacancy interactions, in agreement with ref. [8]. The same operation can be repeated for $Zr_{0.8}Sc_{0.2}O_{1.9}$ and in this case $E_{\langle 111 \rangle - \langle 110 \rangle} = 0.20$ eV. The values obtained for both materials are indeed very similar and this seems to confirm our observation that vacancy-vacancy ordering tendencies are not strongly affected by the dopant cation species.

In conclusion, vacancy-vacancy interactions are very strong in these materials. An analysis of the vacancy-vacancy rdfs reported in figures 7.5 and 7.6 has shown that vacancies tend to order and that their arrangement differs significantly from a random distribution over the fluorite lattice. A comparison of these tendencies at 1500 K for $Zr_{0.8}Y_{0.2}O_{1.9}$, $Zr_{0.8}Sc_{0.2}O_{1.9}$, and even Y_3NbO_7 and $Zr_2Y_2O_7$, shows that these are quite similar in all these systems and this therefore seems to imply that the dopant cation species does not have a strong influence over these. This was confirmed by the fact that the energy differences between $\langle 110 \rangle$ and $\langle 111 \rangle$ vacancy pairs in these two materials are very similar. It therefore seems that vacancy-vacancy interactions are more an *intrinsic* effect in these materials which is hardly influenced by any external factor (see also discussion in the next section). For this reason, it can be concluded that the differences in conductivity in the ZYSO system between Sc^{3+}-rich and Y^{3+}-rich samples can be ascribed to the different cation-vacancy interactions, in agreement with the results from the zero-temperature studies in refs. [27, 34, 8].

7.2 Defect ordering in YSZ and ScSZ at different dopant concentrations

The previous section of this chapter dealt with the study of the conduction mechanism in the $Zr_{0.8}Sc_{0.2(1-y)}Y_{0.2y}$ $O_{1.9}$ system. In this system the number of vacancies was fixed and the cation composition was varied across the series, in a similar fashion to $Zr_{0.5-0.5x}Y_{0.5+0.25x}Nb_{0.25x}O_7$. Both vacancy-vacancy and cation-vacancy ordering effects were observed in this system and their effect on the conductivity was discussed. Our focus is now turned to YSZ and ScSZ and to the evolution of the cation-vacancy and vacancy-vacancy ordering tendencies as the vacancy concentration is changed. In the next section this information will then be used to better understand the conduction mechanism in these materials and to explain what causes the anomalous behaviour of the ionic conductivity of these materials.

In figure 7.7 the cation-vacancy radial distribution functions are reported for YSZ and ScSZ for different dopant (vacancy) concentrations at 1250 K. It was chosen to show the concentration at which the maximum in the conductivity is observed (9% and 13% for YSZ and ScSZ, respectively) and then two higher concentrations (18% and 24%). The rdfs for YSZ show that there is a preference for vacancies to be nearest neighbours to the small Zr^{4+} cations. This is in agreement with what was found in the previous section for ZYSO. Interestingly, these binding tendencies become weaker as the dopant cation concentration is increased. This is probably caused by the fact that, as more Y_2O_3 is added, the number of dopant cations increases (as well as the number of vacancies) and it becomes more difficult for the vacancies to completely avoid the Y^{3+} cations. In ScSZ, on the other hand, the vacancies have almost no preference to bind to a certain cation species, for all the studied dopant concentrations, as shown in figure 7.7, which is in agreement with our previous conclusions (see figure 7.2 and table 7.1). This preference becomes even weaker as the dopant concentration is increased.

Figure 7.8 shows the vacancy-vacancy radial distribution functions for both YSZ and ScSZ at 1250 K for the same dopant concentrations as in figure 7.7. As done before, the rdf obtained from a random distribution of the vacancies on the fluorite lattice is shown as well. The functions look very similar to the ones shown in figure 7.6. Tables 7.4 and 7.5 report the relative populations of the first three vacancy pairs for both YSZ and ScSZ. A series of observations can be made. First of all, in both materials there is a strong preference for $\langle 111 \rangle$ pairs for all the dopant concentrations studied and, consequentially, $\langle 100 \rangle$ and $\langle 110 \rangle$ pairs are unfavoured. This is in perfect agreement with what was found in the previous section. The relative populations of the $\langle 111 \rangle$ and $\langle 110 \rangle$ pairs seems to remain unchanged as the dopant concentration is

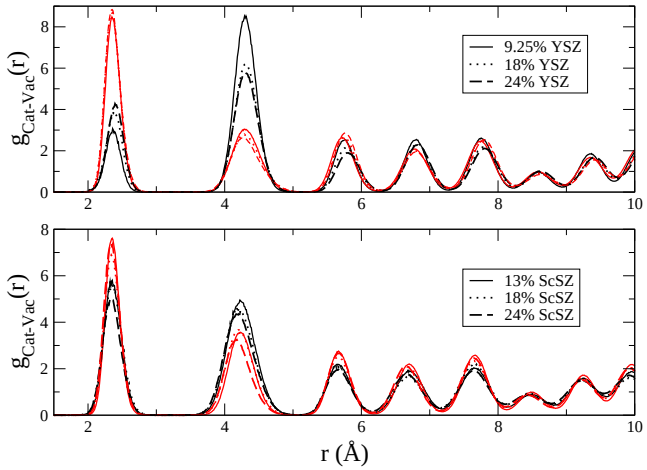

Figure 7.7: *Cation-vacancy radial distribution functions for YSZ (top) and ScSZ (bottom) for different dopant concentrations at 1250 K. The red curves are the Zr-Vac rdfs while the black curves represent the dopant cation-vacancy rdfs.*

changed, whilst $\langle 100 \rangle$ pairs seem to become less favoured as x is increased. This might however be related to the above-mentioned limitation of the way vacancies are identified. Finally, at each dopant concentration, the relative population of different vacancy pairs are quite similar in YSZ and ScSZ, which, again, seems to indicate that these are not strongly affected by the cation species.

The above results seem to confirm what was found for the ZYSO system. Vacancies prefer to bind to the smaller cation, Zr^{4+}, in YSZ and this tendency is present at each dopant concentration. This tendency however almost disappears in ScSZ, because Sc^{3+} has a similar

Table 7.4: Relative population of the anion vacancy pairs expected from a random distribution of vacancies within a cubic fluorite lattice, compared with those extracted from our MD simulations on YSZ at 1250 K for different dopant concentrations.

Dopant concentration	$\langle 100 \rangle$	$\langle 110 \rangle$	$\langle 111 \rangle$
RANDOM	0.231	0.461	0.308
9.25%	0.118	0.141	0.741
18%	0.081	0.229	0.700
24%	0.044	0.239	0.762

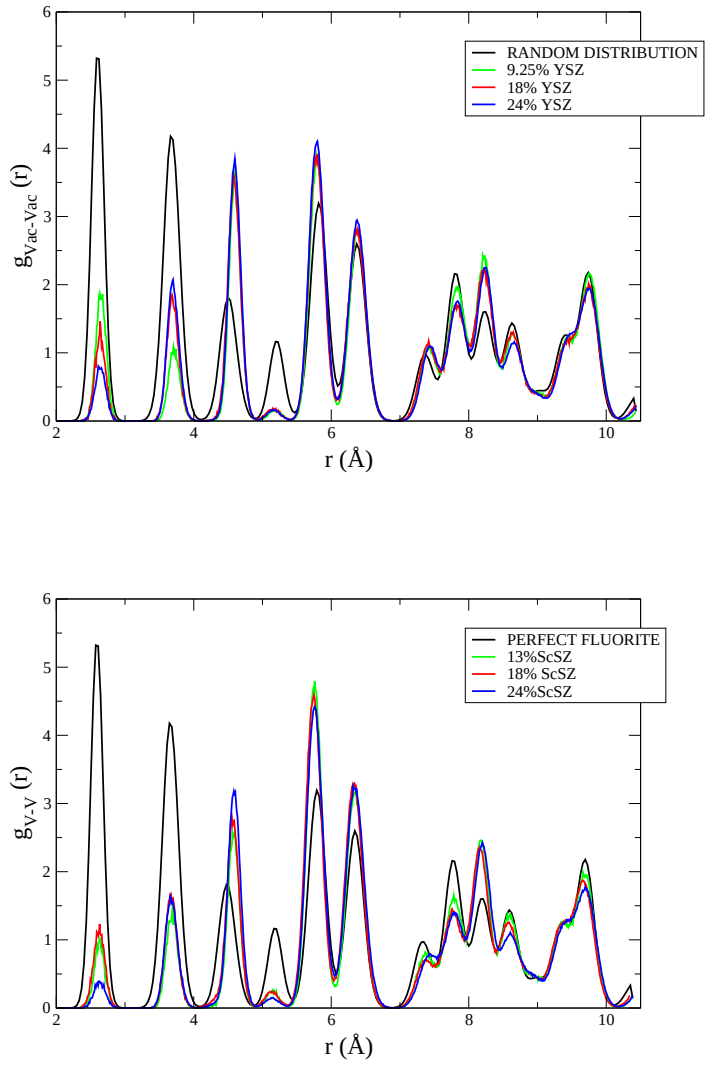

Figure 7.8: *Vacancy-vacancy radial distribution functions for* $(Y_2O_3)_x$ - $(ZrO_2)_{1-x}$ *(top) and* $(Sc_2O_3)_x$ - $(ZrO_2)_{1-x}$ *(bottom) at 1250 K.*

Table 7.5: Relative population of the anion vacancy pairs expected from a random distribution of vacancies within a cubic fluorite lattice, compared with those extracted from our MD simulations on ScSZ at 1250 K for different dopant concentrations.

Temperature	$\langle 100 \rangle$	$\langle 110 \rangle$	$\langle 111 \rangle$
RANDOM	0.231	0.461	0.308
13%	0.068	0.242	0.689
18%	0.042	0.242	0.712
24%	0.023	0.241	0.735

radius to Zr^{4+}. Vacancy-vacancy ordering tendencies, on the other hand, are present in both materials and their strength does not seem to change significantly as the dopant concentration or the cation species is changed. In view of these results it would be quite useful to be able to *decouple* these two effects, by studying, for instance, a system in which only vacancy-vacancy interactions are present. This would allow to separate, quite clearly, the effects that these two interactions have on the properties of these materials. This will be done below by studying a material in which the two cation species have the same radius and charge, in a similar fashion to what was done in chapter 5.

7.2.1 Ideal ZrO_2

In this section, in addition to the "realistic" potentials used above, "ideal" model systems are also constructed (which will be referred to as i-YSZ_x) which contain the same concentration of vacancies as $(Y_2O_3)_x$ - $(ZrO_2)_{1-x}$ with the same x value. In i-YSZ_x *all* the cations carry the same charge, such that the total cation charge balances that of the O^{2-} ions present in the simulation, and all cations have the same short-range interaction potentials as the Zr^{4+} ions in the original potential [4]. This idealised system allows to eliminate the effects of differing charges and lattice strain induced by having host and dopant cations and gives an idealised reference system in which, *by construction*, the cation-vacancy ordering effects are absent.

Simulations on i-YSZ_x were run in the same way as in the case of YSZ and ScSZ, by first equilibrating the simulation in an NPT ensemble for 100 ps and then by running longer simulations in the NVT ensemble. In figure 7.9 the cation-vacancy radial distribution functions are reported for this material at different vacancy concentrations. As expected there is virtually no

[4] It has to be noted that this material has a slightly different potential for each vacancy concentration, since the cation charge changes according to the vacancy concentration, x. For this reason, this material will be called i-YSZ_x, where the subscript is meant to remind the reader of the differences in the potential.

Table 7.6: Relative population of the anion vacancy pairs expected from a random distribution of vacancies within a cubic fluorite lattice, compared with those extracted from our MD simulations on i-YSZ$_x$ at 1250 K for different dopant concentrations.

Dopant concentration	$\langle 100 \rangle$	$\langle 110 \rangle$	$\langle 111 \rangle$
RANDOM	0.231	0.461	0.308
9.25%	0.096	0.239	0.664
18%	0.042	0.244	0.713
24%	0.024	0.248	0.728

preference for vacancies to bind to a certain cation, since the cations have the same charge and short-range repulsion terms in the potential [5]. Next the vacancy-vacancy rdfs are calculated and shown in figure 7.10 for three different vacancy concentrations, at 1250 K. The relative population of the first three vacancy pairs are reported in figure 7.6. A comparison with the values reported in tables 7.4 and 7.4, shows that the vacancy-vacancy ordering tendencies in i-YSZ$_x$ are very similar to those observed in ScSZ and YSZ. The values obtained for i-YSZ$_x$ agree within 5% with those for ScSZ and within 10% for YSZ (if the 9.25% concentration is excluded). The consequences of this must not be underestimated. It has been found that, even if the differences in the cation charges and sizes are removed, i-YSZ$_x$ still presents the same kind of vacancy-vacancy ordering tendencies observed in the "real" materials. This proves that vacancy-vacancy interactions are an *intrinsic* feature of the fluorite lattice and therefore are only weakly affected by the cation species. Figure 7.11 reports the ionic conductivities obtained for i-YSZ$_x$ at 1250 K for different vacancy concentrations. These are compared with the values obtained for the "real" materials, YSZ and ScSZ. Interestingly, i-YSZ$_x$ presents a maximum of the conductivity at the same vacancy concentration for which the maximum is observed in ScSZ, i.e. $\sim 13\%$. Also the shape of the curve is also very similar to that obtained for ScSZ. The consequences of all these findings will be discussed in the next section.

[5] It has to be noted that the polarisation terms for the two cations are still different. These were not equalised because they were not expected to have a great influence on the properties of interest, since the cation polarisabilities are very small in these materials. This is confirmed by the fact that the cation-vacancy rdfs (as well as the cation-anion bond distances) look almost identical for the two cation species. The polarisation energy term is, however, expected to have a greater influence in the case of more polarisable cations, such as in Bi_2O_3 or PbF_2 [98].

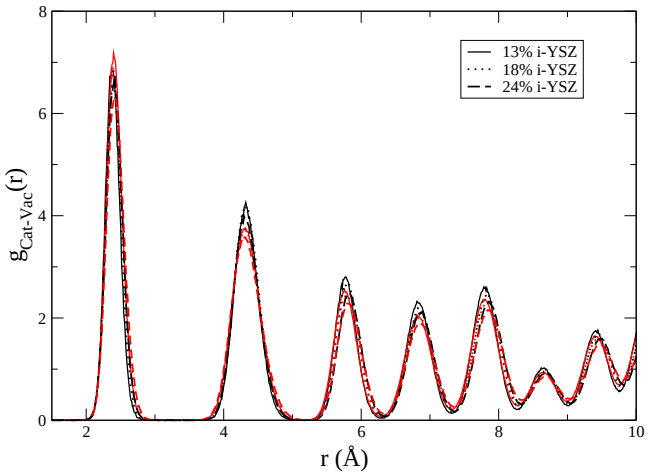

Figure 7.9: *Cation-vacancy radial distribution functions for i-YSZ$_x$ for different dopant concentrations at 1250 K. The red curves are the "Zr"-Vac rdfs while the black curves represent the "Y"-Vac ones.*

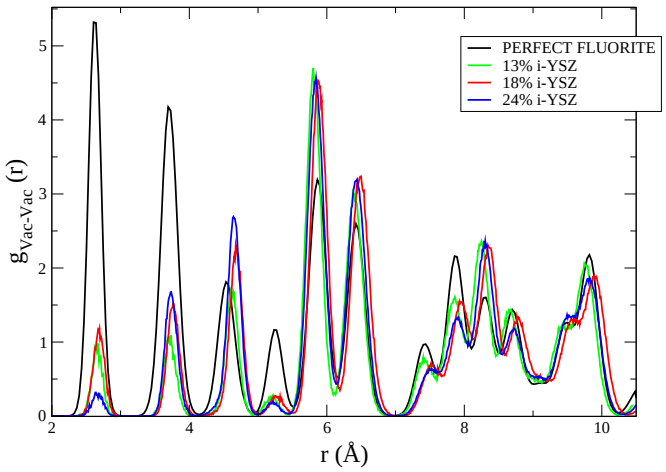

Figure 7.10: *Vacancy-vacancy radial distribution functions for i-YSZ$_x$ at 1250 K, for different dopant concentrations.*

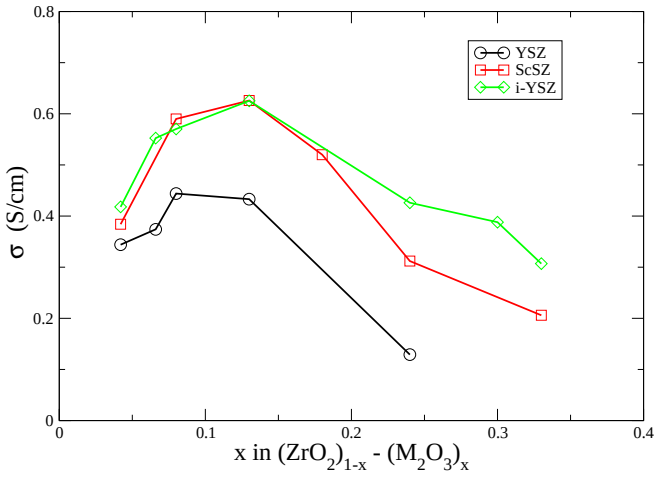

Figure 7.11: *Conductivity versus vacancy concentration for i-YSZ$_x$, YSZ and ScSZ at 1670 K. The data for i-YSZ$_x$ has been rescaled by a factor of 0.8 to facilitate the comparison. That i-YSZ$_x$ has a slightly higher conductivity, at each x, than ScSZ is probably a consequence of the potential which has, on average, a less repulsive short-range interactions (see the discussion in chapter 5).*

7.3 The conduction mechanism in YSZ and ScSZ

As mentioned in chapter 2 and discussed many times throughout this thesis, when ZrO_2 is doped with aliovalent cations, like Y^{3+}, Sc^{3+} or Ca^{2+}, its conductivity increases, at first, as a result of the increasing number of vacancies in the system. In the case of an independent vacancy-hopping mechanism, i.e. if a single vacancy could hop to the next site irrespectively of what the other vacancies are doing, the conductivity should behave like $\sigma \sim c(1-c)$, where c is the vacancy concentration. If this was the case, the conductivity should present a peak at $c = 0.5$, as shown in figure 7.12. However, in reality, this does not happen. The conductivity in stabilised zirconias presents, indeed, a well-known peak but for a much lower dopant concentration (indicated by the red arrow in figure 7.12) of about 8 % (c $\sim$ 0.04) in the case of Y^{3+} and 13 % (c $\sim$ 0.055) for Sc^{3+} (see also figure 2.2) [1]. As discussed in chapter 2, the reasons for such an anomalous behaviour of the conductivity are not well understood and the new information which obtained, in this work, on the vacancy-vacancy and cation-vacancy interactions will now be used to shed some light on this issue. Our final goal will be to try to answer the following question: *What causes the anomalous behaviour of the conductivity of these materials?*

A lot of effort has been made, in the past two decades, to answer this question. In the case of YSZ, it is generally accepted that adding Y^{3+} ions has two competing effects: on the one hand, adding more dopant will increase the number of vacancies and therefore increase the mobility of the remaining anions; on the other hand, since the migration barrier of an oxygen crossing a Y-Zr or Y-Y edge is much higher than in the case of a Zr-Zr edge (because Y^{3+} is a bigger cation than Zr^{4+}), adding more dopant will increase the fraction of cation edges associated with high migration energy barriers, thus effectively reducing the overall number of mobile oxygens. Alternatively [6] this can be seen from a vacancy perspective: vacancies prefer to be nearest neighbours to small cations (Zr^{4+} in this case) and next nearest neighbour to big cations like Y^{3+}. For this reason they tend to bind to the smaller cations and this reduces their overall mobility. If the oxygen diffusion coefficient, D, is expressed as

$$D = D_0 \, exp(-\frac{\Delta H_m}{k_B T}) \tag{7.3}$$

where D_0 is a pre-exponential factor, T the temperature in Kelvin, k_B Boltzmann constant and ΔH_m is the oxygen migration enthalpy, increasing the number of vacancies will increase D_0

[6] This equivalency was shown in chapter 5 where the tendency for Y^{3+} cations to trap the oxide ions was first shown explicitly by calculating the mobility distribution functions and the effects that different cations had on them and then implicitly by calculating the cation-vacancy radial distribution functions for these material, which shown that vacancies preferred to bind to the Nb^{5+} cations.

whereas increasing the number of Y-Zr or Y-Y edges (or analogously the increasing cation-vacancy binding) will increase the migration enthalpy, ΔH_m. The resulting diffusion coefficient, D, will present a peak for a certain dopant concentration, which is indeed smaller that shown in figure 7.12. The idea that this effect *alone* is responsible for the drop in the conductivity observed in this materials is almost universally accepted [52, 47, 48, 53, 49, 54, 50] and has been generalised to other doped fluorite systems [48, 54, 50, 55].

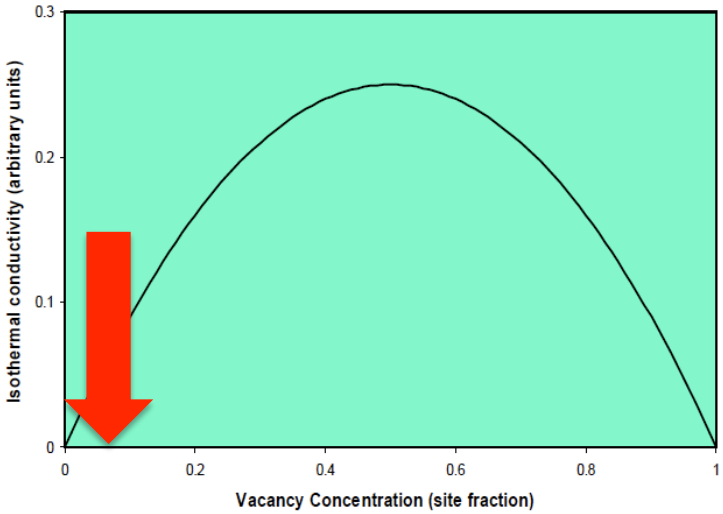

Figure 7.12: *Conductivity as a function of the vacancy concentration in the uncorrelated motion approximation. The red arrow shows approximately the region where the maximum of the conductivity is observed in YSZ and ScSZ.*

In view of the results obtained in this thesis, this explanation is now going to be challenged. In fact, although an increasing migration enthalpy, caused by the strain induced by the bigger dopant cations, might eventually lower the conductivity, this effect *alone* cannot explain the drop in conductivity observed in these materials. Our results on ScSZ (together with the experimental data from the literature) serve as a perfect example of this. In this system, in fact, the ionic radius of Sc^{3+} is very similar (almost identical) to that of Zr^{4+} [59] and therefore vacancies do not have any strong preference to bind to a certain cation (as shown in figure 7.7). However, a similar drop in conductivity is observed at a only slightly higher dopant concentration (see figure 2.2). If the drop in conductivity was caused *only* by the increasing number of cation edges associated with high migration energy barriers, i.e. by vacancy-cation ordering effects, then ScSZ should behave like an ideal conductor and show a $\sigma \sim c(1-c)$ dependence of the conductivity versus vacancy concentration, like the one shown in figure 7.12. A look at

figure 2.2 shows that this is indeed not the case. Furthermore it has to be noticed that, more generally, the position of the maximum of the conductivity versus dopant concentration is only weakly influenced by the dopant cation radius (see, for instance, figure 2.3), which again seems to show that cation-vacancy interactions do not affect the maximum's position very much.

It seems clear from the above discussions that other factors too are responsible for the drop in the conductivity of these materials and it seems almost surprising that, so far, little effort has been done to study and understand these (with the exception of refs. [7, 8, 28]). In the previous sections it was shown that *two* factors seem to affect the conductivity of these materials, namely cation-vacancy and vacancy-vacancy interactions. Vacancy-vacancy interaction might, therefore, be the missing ingredient and explain the above-mentioned (apparent) contradiction. This hypothesis is soon confirmed by the behaviour of the conductivity observed for i-YSZ$_x$ in figure 7.11. Indeed, in this material, vacancy-vacancy ordering tendencies, similar to those in YSZ and ScSZ, are still observed while, since the two cation species have the same radius and charge, any preference for a vacancy to bind to a certain cation is removed. The conductivity of this material, however, still presents a drop at a dopant concentration of approximately 13% (the same value observed in ScSZ). This proves, quite clearly, that the drop in the conductivity observed in these materials is mainly caused by the vacancy-vacancy interaction. This effect leads to an ordering of the vacancies which correlates their motion and therefore reduces the overall conductivity, as explained in ref. [28]. That vacancy-vacancy interactions have a stronger influence on the conducting properties of these materials is also confirmed by our analysis of the energetics of different defect ordering tendencies in $Zr_{0.8}Sc_{0.2(1-y)}Y_{0.2y}O_{1.9}$, which shown that the energy difference associated with two different vacancy-vacancy arrangements is almost three times higher than that associated to two different cation-vacancy arrangements.

Our results also show that vacancy-vacancy is an *intrinsic* effect and therefore a "property" of the fluorite lattice. This is proven by the fact that these ordering tendencies are quite similar in all the materials studied (see tables 7.2, 7.3, 7.4, 7.5 and 7.6), which indicates that these are not strongly affected by the dopant cation species. Vacancy-vacancy interaction are caused by the fact that vacancies are charged and distort the lattice [8]. As more and more vacancies are introduced in the material, these will start interacting with each other and will try to minimise these interactions by ordering over the fluorite lattice. Unlike cation-vacancy interactions, which can be reduced by choosing a suitable dopant cation, which matches the radius of Zr^{4+}, vacancy-vacancy interactions cannot be minimised in such a way. A consequence of this behaviour is that ScSZ is probably the stabilised zirconia with the highest ionic

conductivity achievable. Indeed, in these materials, *two* independent effects combine to hinder the conductivity, namely vacancy-vacancy and cation-vacancy interactions. Since the former is intrinsic and cannot be avoided, only the latter can be minimised by choosing a convenient dopant cation. It therefore appears clear that the highest conductivity can be achieved in those materials in which cation-vacancy interactions are negligible, and it was demonstrated earlier in this chapter, that ScSZ satisfies this requirement (see figures 7.2, 7.7 and table 7.1). This is also confirmed by figure 7.11. In this figure, the conductivity of YSZ shows a peak at 9% dopant concentration whereas i-YSZ$_x$ and ScSZ present the maximum in the conductivity at 13%. The reason for this difference is that, while both cation-vacancy and vacancy-vacancy interactions are responsible for the drop in conductivity in YSZ, in i-YSZ$_x$ and ScSZ it is only the latter which is responsible for that and therefore the maximum is observed at a slightly higher concentration. The fact that i-YSZ$_x$ and ScSZ show the maximum at the same concentration proves, again, that the highest conductivity will be observed in ScSZ and that there is no other cation choice which could yield a higher value. Incidentally this also explains the weak dependence of the maximum's position on the dopant cation's radius shown in figure 2.3. Dopants with bigger radii (Y^{3+}, Dy^{3+}, Gd^{3+}) will indeed increase the cation-vacancy interaction and therefore slightly lower the maximum's position, but will not influence very much the vacancy-vacancy interactions, which is the main cause of the anomalous behaviour of the conductivity of these materials.

Chapter 8

Conclusions

Over the course of this thesis, it has been shown how extended ionic models, in which additional degrees of freedom allow a compact representation of many-body contributions to the interaction energy, can be parameterised using ab initio force-fitting techniques, and successfully applied to a wide range of ionic oxide materials. Interaction models have been developed for ZrO_2 - Y_2O_3 - Nb_2O_5 ternary mixtures, and the level of complexity needed to accurately model these materials has been assessed. For these materials it was shown that the QUAIM potential, which takes into account polarisation and ion-shape deformation energies up to the quadrupolar level, gives an excellent agreement with the structural properties extracted from the neutron scattering data. This model is however computationally very expensive. For these mixtures it was shown that by using potentials whose only source of many-body effects is that of anion and cation dipole polarisation (DIPPIM), it is still possible to accurately predict experimental observables such as the neutron scattering data and high temperature ionic conductivities for different compositions. Other models, like the popular Rigid Ion Model, usually in the Born-Meyer form, were found inadequate for the an accurate description of the interionic forces and therefore for the study of these systems (see also appendices B and C, where a similar issue is found for GeO_2).

The conduction mechanism in the $Zr_{0.5-0.5x}Y_{0.5+0.25x}Nb_{0.25x}O_7$ system was investigated, using the DIPPIM and QUAIM models, by examining simulations with a disordered cation sublattice (*d*-fluorite simulations). These already allowed us to account for a substantial part of the experimentally observed trends in the conductivity and and in the degree of disorder between the two end members, Y_3NbO_7 and $Zr_2Y_2O_7$. The differences in the conductivity and structural properties between the two systems can be attributed to differences in cation size and to the different degree of strain imposed on the lattice by the highly charged cations - this creates

oxide trapping sites in Y_3NbO_7 and gives an inhomogeneous character to the diffusive dynamics. The vacancy ordering tendencies of these systems were studied and it was found that both systems exhibit a tendency to order vacancies so that there is a likelihood of finding the vacancies close to the smaller cation. This tendency was found to be quite strong at temperatures as high as 1500 K, thus implying that this effect will be important at the operating temperature of a SOFC. Vacancies also interact with each other and, therefore, pairs along the $\langle 111 \rangle$ direction are strongly preferred to pairs along the $\langle 110 \rangle$ and $\langle 100 \rangle$ directions. However, the vacancy ordering effects are not sufficiently strong to give rise to the diffuse scattering features which have been observed in small-area electron diffraction studies. For this reason, the possible effects of partial cation ordering, based upon the pattern suggested by the pyrochlore crystal structure, were considered. Our results in this context are only indicative as only the properties of "by-hand" ordered systems were examined. Nevertheless, in Y_3NbO_7 it was possible to postulate a structure for which the diffuse scattering was in qualitative accord with the SAED diffuse scattering patterns and which was energetically favoured with respect to *d*-fluorite. In this structure the tendency of vacancies to bind to the smaller cation was considerably enhanced relative to *d*-fluorite and the conductivity was reduced by an order of magnitude, bringing it much closer to the experimental value. For $Zr_2Y_2O_7$ it was not possible to postulate a partially ordered structure which would significantly improve upon the *d*-fluorite calculations across the full range of observations (including the SAED). In $Zr_2Y_2O_7$ the calculated conductivity in the *d*-fluorite structure is already close to the experimental value and the agreement with the powder diffraction is very good. The SAED studies indicate that the intermediate-range order is in any case weaker in this case and our own studies on *d*-fluorite show that the tendency for vacancies to associate with the smaller cation (the driving force for pyrochlore-like ordering) is considerably reduced relative to Y_3NbO_7. In this case a *fully* ordered pyrochlore is slightly favoured energetically over the *d*-fluorite structure but the entropy cost is high enough that the latter, more disordered structure, will be more stable above $\approx$1000 K.

The second part of this thesis focussed upon a slightly different series of materials, namely ZrO_2 - Y_2O_3 - Sc_2O_3 ternary mixtures. Interatomic potentials were parameterised for these systems, similarly to what was done in the case of ZrO_2 - Y_2O_3 - Nb_2O_5 mixtures. A DIP-PIM potential was found to reproduce rather well the experimental data on the structure (neutron powder and single-crystal diffraction data) and the conductivity (impedance spectroscopy and neutron quasielastic measurements), across a wide temperature and composition range. This model was then used to see how vacancy-vacancy and cation-vacancy interactions affect the conducting properties of these materials. The first material to be considered was $Zr_{0.8}Sc_{0.2-x}Y_xO_{1.9}$. It was found that in this case it is the tendency of vacancies to bind to

the smaller cation in the Y^{3+}-rich samples which causes their lower conductivity as opposed to the case of Sc^{3+}-rich samples which present little, almost zero, vacancy-cation binding preferences and therefore have a higher ionic conductivity. These effects are present up to the highest temperature studied (2000 K), although their strength decreases as temperature is increased. Vacancies were also found to order in these materials and form pairs along the $\langle 111 \rangle$ direction. This tendency was found to depend strongly on the temperature but not on the cation species. An analysis of the energetics of different cation-vacancy and vacancy-vacancy arrangements in these materials shown that defect ordering is most strongly dominated by vacancy-vacancy ordering.

Finally, the last part of this thesis concentrated on the conduction mechanism of YSZ and ScSZ. The main goal was to understand what causes the anomalous behaviour of the conductivity observed in these materials. Cation-vacancy and vacancy-vacancy rdfs were calculated for these two materials at different dopant concentrations. It was found that YSZ presents a certain degree of vacancy-cation ordering and that this tends to diminish as the dopant concentration is increased whereas in ScSZ this ordering is negligible at every concentration. Vacancy ordering effects are, on the other hand, present in both systems for all the dopant concentrations studied. As observed before, vacancies preferably pair up along the $\langle 111 \rangle$ direction and these tendencies are quite similar for both YSZ and ScSZ. In order to separate these two effects, it was then decided to run simulations on an "ideal" model system (i-YSZ_x), in which all the cations carry the same charge and have the same short-range interaction potentials as the Zr^{4+} ions in the original potential. In this system, vacancy-cation ordering effects are not observed because the cations are virtually indistinguishable. The vacancy-vacancy rdfs are very similar to those observed for "real" YSZ and ScSZ, thus confirming their intrinsic nature and the fact that they are not influenced by the cation species. A plot of the conductivity of i-YSZ_x versus the vacancy concentration shows a very similar behaviour to that of ScSZ, with a peak at approximately 13% of dopant concentration. This proves that vacancy-vacancy interactions are what is ultimately responsible for the drop in conductivity observed in these materials and, at the same time, that ScSZ is the stabilised zirconia with the highest conductivity ever achievable, since it is the only material which minimises the cation-vacancy interactions.

The consequences of these finding are not to be underestimated. The first one is that there is no hope to significantly improve the conductivity of these materials by simple choosing a more suitable cation species (or a combination of these) than Sc^{3+}. Co-doping, i.e. doping zirconia with more than one cation, has been recently proposed as a way to improve the material's properties [56, 46]. Although this operation improves the stability of ZrO_2 and reduces

degradation problems [56], in view of the above findings, it is not believed that it might improve the conductivity of these materials as well. Adding more than one cation species will, in fact, increase the preference for vacancies to bind to a certain cation and therefore lower the overall conductivity. Also, more generally, since it was found that vacancy-vacancy ordering is mainly an intrinsic effect, this implies that there is not way to shift the peak in the conductivity towards higher dopant concentrations, thus obtaining a curve like the one in figure 7.12. These considerations should also apply to similar materials, such as doped CeO_2.

This does not mean, however, that there is no hope of further improving the conducting properties of these materials. Indeed, there are some factors that have not been taken into account in this thesis. The first of these factors is the cation's polarisability. This was neglected in the present work because Sc^{3+}, Y^{3+}, Zr^{4+} and Nb^{5+} are not very highly polarisable cations. However, cations like Bi^{3+} and Pb^{2+} present polarisabilities as high as 17 a.u. [74], i.e. comparable to that of the oxide ion, and these might have a positive influence on the conductivity, as it is the case in PbF_2 [74] and Bi_2O_3 [116]. Another field which lately has been considered very promising is that of "nanoionics" in which nanoscale hetero-layered structures were shown as means for significantly increasing the transport properties [117, 118, 119, 120]. For example, it has been shown recently that (Y_2O_3-ZrO_2) / $SrTiO_3$ hetero-interfaces present a much higher (by a few orders of magnitude) ionic conductivity than bulk YSZ [121] and this was interpreted in terms of the positive effects that the lattice mismatch-induced strain has on the conductivity [122].

In conclusion, our results can be summarised this way: in a bulk, fluorite-structured ionic conductor, in which the cation species are randomly distributed over the cation sublattice and present a much lower polarisability than the oxide ion, the conductivity is mainly limited by the vacancy-vacancy interaction and then by the cation-vacancy interaction. Since the former is an intrinsic property of the fluorite structure, the only way to maximise the conductivity is to reduce the latter by choosing dopant cations which are similar to the host cation (as in the case of ScSZ or Gd_2O_3-CeO_2). Alternatively, the conducting properties of this material might be optimised by dropping some of the above constraints (fluorite structure, cations with low polarisability and bulk system) which lead, respectively, to perovskite conductors, Bi_2O_3, and nano-structured (Y_2O_3-ZrO_2) / $SrTiO_3$ hetero-interfaces.

Appendix A

List of publications

Refereed papers

All these paper can be found either on the websites of the respective journals or on my personal research webpage, http://homepages.ed.ac.uk/s0682202/index.htm .

"*The high pressure behaviour of GeO_2: a simulation study*"
D Marrocchelli, M Salanne and PA Madden, published as a Fast Track Communication on *Journal of Physics: Condensed Matter* **22** 152102 (2010)

"*Cation composition effects on oxide conductivity in the $Zr_2Y_2O_7$–Y_3NbO7 system*"
D Marrocchelli, PA Madden, ST Norberg, I Ahmed, S Hull, *Journal of Physics: Condensed Matter* **21** 405403 (2009)

"*The Structural Properties of $CeO_{2-\delta}$ under Reducing Atmospheres*"
S Hull, ST Norberg, I Ahmed, SG Eriksson, D Marrocchelli and PA Madden, *Journal of Solid State Chemistry* **182** 2815 (2009)

"*Local Structure and Ionic Conductivity in the Y_3NbO7-$Zr_2Y_2O_7$ system*"
ST Norberg, I Ahmed, S Hull, D Marrocchelli and PA Madden. *Journal of Physics: Condensed Matter* **21** 215401 (2009).

"*The construction of a reliable potential for GeO_2*"
D Marrocchelli, M Salanne, PA Madden, C Simon and P Turq *Molecular Physics* **107** 443-452 (2009).

"*Conduction and Disorder in* $Y_3NbO_7 - Y_2Zr_2O7$"
D Marrocchelli, PA Madden, ST Norberg and S Hull, in *Solid-State Ionics* 2008, edited by E. Traversa, T. Armstrong, K. Eguchi, M.R. Palacin (Mater. Res. Soc. Symp. Proc. Volume 1126, Warrendale, PA, 2009), 1126-S06-07-PP05-07

Other publications

"*Calculating the dispersion coeffcients for LiF from DFT calculations*"
D. Marrocchelli, HPC Europa 2009 Report,

"*First Principles Interaction Potentials for Ionic Systems*"
D. Marrocchelli, HPC Europa 2008 Report,
available on www.hpc-europa.eu/files/SSCinEurope/CD2008/contents/027-chemi.pdf

Appendix B

The construction of a reliable potential for GeO_2 from first-principles

D. Marrocchelli [1], M. Salanne[2,3], P.A. Madden [4], C. Simon[2,3] and P. Turq[2,3]

[1] School of Chemistry, University of Edinburgh, Edinburgh EH9 3JJ, UK
[2] UPMC Univ Paris 06, UMR 7612, LI2C, F-75005, Paris, France
[3] CNRS, UMR 7612, LI2C, F-75005, Paris, France
[4] Department of Materials, University of Oxford,
Parks Road, Oxford OX1 3PH, UK

Abstract

The construction of a reliable potential for GeO_2, from first-principles, is described. The obtained potential, which includes dipole polarisation effects, is able to reproduce all the studied properties (structural, dynamical and vibrational) to a high degree of precision with a single set of parameters. In particular, the infrared spectrum was obtained with the expression proposed for the dielectric function of polarisable ionic solutions by Weis et al. [J.M. Caillol, D. Levesque and J.J. Weis, J. Chem. Phys., **91***, 5544 (1989)]. The agreement with the experimental spectrum is very good, with three main bands that are associated to tetrahedral modes of the GeO_2 network. Finally, we give a comparison with a simpler pair-additive potential.*

B.1 Introduction

In the vitreous and liquid states, at ambient pressure, germania (GeO_2) (a close structural analog of silica (SiO_2)) forms a tetrahedrally coordinated three-dimensional network [123]. Because of its lower abundance, its usage in practical applications is much less widespread than for the SiO_2. Still, GeO_2 is used in several fields, mainly related to optical technologies. For example, a mixture of SiO_2 and GeO_2 allows precise control of the refractive index in optical fibres and waveguides. It is of interest to develop simulation methods to allow a detailed examination of the local structure in such mixtures and to predict the infrared spectrum, since this determines the long wavelength limit for their use as optical fibres.

The essential similarity between the structures of glassy GeO_2, SiO_2 and BeF_2 was made clear by the study of vibrational properties by Galeener and co-workers [124] who showed that the inelastic neutron, infrared and Raman spectra of the different materials were closely related. More recent infrared studies of GeO_2 have also been reported [125, 126]. Recently a full set of partial structure factors were determined in this system by using the method of isotopic substitution in neutron diffraction experiments [127, 128]. The results show that the tetrahedral network structure is based on corner sharing $Ge(O_{1/2})_4$ tetrahedra with a Ge-O average distance of 1.73 Å and with a mean inter-tetrahedral Ge-O-Ge angle of 132°. They also show that the topological and chemical ordering in the network display two characteristic length scales at distances greater than the nearest neighbour.

Several molecular dynamics (MD) simulations have been undertaken to study the structural and vibrational properties of the disordered phases of GeO_2. Classical MD simulations were performed on glassy and liquid GeO_2 [129, 130], using pairwise additive potentials with partial charges developed by Oeffner and Elliott (OE) for modeling the α-quartz and rutilelike phases of GeO_2 [69]. More recently, first-principles molecular dynamics (FPMD) of glassy GeO_2 have also been reported [131, 132]. In principle, the amount of empirical information needed to set up a first-principles calculation is minimal and it would normally be the method of choice to study the physico-chemical properties of condensed phase systems. However, it is computationally very expensive compared to classical molecular dynamics, which is a major drawback when dealing with glassy systems. Classical and FPMD simulations were also compared one with each other in a combined study [133] for temperatures above 2530 K. In this study *apparent* inconsistencies between the properties predicted by the classical simulations of different authors are noted. In reality, two *different* parameter sets were proposed by OE: an original one, which was fitted from an *ab initio* energy surface, and a so-called rescaled one, which was developed from the previous one in order to give a better reproduction of the vibra-

tional properties. For example, the partial charge of the germanium ion was shifted from 1.5 e in the original potential to 0.94174 e in the rescaled potential. The apparent inconsistencies arise because different classical potentials were being used. Our objective is a single potential which will give a good description of structure and dynamics and allow long simulations on systems of many atoms.

The structure of the simulated system can directly be compared with the neutron / X-ray diffraction experiments. Both classical and FPMD simulation provide structure factors which are in rather good agreement with experiments. For the classical molecular dynamics, the most noticeable difference is a shift to high q-values of the first sharp diffraction peak (FSDP), which was observed with both versions of the OE potential [129, 130]. As this peak is associated to medium range distances [127], this means that the Ge-O-Ge bond angle is too large and the topology of the tetrahedral network is not correctly described. The FPMD simulations provide a diffraction pattern with improved agreement [132], but the small size / timescales explored lead to large statistical uncertainties, mainly in the region of this FSDP. The vibrational properties can also be straightforwardly calculated. The vibrational density of states (VDOS) was estimated from FPMD and classical MD using the rescaled OE potential, with an overall reasonable agreement with the available experimental data extracted from inelastic neutron scattering experiments. The infrared absorption spectrum, which originates from the polarisation fluctuations associated with motion of the atomic charges, has only been reported from the FPMD simulation. The agreement with experiment [124] was overall good, despite a small shift of the peaks towards lower frequencies.

The dynamical properties which involve structural rearrangements are out of reach of the FPMD. The only studies on GeO_2 employ classical MD, and were aimed at determining the diffusion coefficients in the liquid state [129, 133]. Hawlitzky *et al.* [133] observed important differences between their values and those obtained by Micoulaut *et al.* [129]; their hypothesis for rationalizing this discrepancy was inadequate equilibration in the latter. In fact, as noted above, it is due to the use of the two different OE potentials in these studies. Indeed, in simulations performed with the rescaled OE potential the fluidity of the system is enhanced by more than one order of magnitude compared to the results obtained with the original OE potential.

In this work we describe the parameterisation of a new classical MD interaction potential for GeO_2, by using some techniques we have developed for halides and oxides [13, 20], which is entirely based on first-principles electronic structure calculations. In order to provide an accurate, transferable description of the interactions, these potentials include dipole polar-

isation effects and the ions carry full valence charges. The various structural, dynamical and vibrational properties are then compared with the corresponding experimental results. In future work we will use such potentials to study mixtures and the effect of pressure on glassy GeO_2.

B.2 Interaction potential development

The interaction model used in this work is related to that used in previous work [74, 99], with a couple of minor differences. The model (known as DIPPIM) includes a pair potential, together with an account of the polarisation effects which result from the induction of dipoles on the O^{2-} ions. The parameters for these potentials were obtained by force-matching them to first-principles reference data [13]. Such an approach was successfully applied in the case of other oxide materials [20]. Tangney and Scandolo [134] also used a similar interaction model to study silica, in which all the parameters including partial charges on the ions were fitted against first-principles data. Here we use formal ionic charges (Ge^{4+}, O^{2-}) which should ensure a better transferability. In the next paragraphs we will give a brief description of the model used, the first-principles reference calculations and the force-matching procedure.

B.2.1 The DIPole-Polarisable Ion Model (DIPPIM)

The interatomic potential is constructed from four components: charge-charge, dispersion, overlap repulsion and polarisation. The first three components are purely pairwise additive:

$$V^{\mathrm{qq}} = \sum\nolimits_{i \leq j} \frac{q_i q_j}{r_{ij}} \tag{B.1}$$

where q_i is the *formal* charge on ion i. The dispersion interactions include dipole-dipole and dipole-quadrupole terms

$$V^{\mathrm{disp}} = -\sum\nolimits_{i \leq j} [\frac{f_6^{ij}(r^{ij}) C_6^{ij}}{r_{ij}^6} + \frac{f_8^{ij}(r^{ij}) C_8^{ij}}{r_{ij}^8}]. \tag{B.2}$$

Here C_6^{ij} and C_8^{ij} are the dipole-dipole and dipole-quadrupole dispersion coefficients, respectively, and the f_n^{ij} are the Tang-Tonnies dispersion damping function, which describe short-range corrections to the asymptotic dispersion term. The short range repulsive terms are approximately exponential in the region of physical interionic separations. The full expression

used here for the short range repulsion is:

$$V^{\rm rep} = \sum\nolimits_{i\leq j} \frac{A^{ij} e^{-a^{ij} r_{ij}}}{r_{ij}} + \sum\nolimits_{i\leq j} B^{ij} e^{-b^{ij} r_{ij}^2}, \tag{B.3}$$

where the second term is a Gaussian which acts as a steep repulsive wall and accounts for the anion hard core; these extra terms are used in cases where the ions are strongly polarised to avoid instability problems at very small anion-cation separations [74]. The polarisation part of the potential incorporates dipolar effects only. This reads:

$$\begin{aligned} V^{\rm pol} &= \sum\nolimits_{i,j} - \left(q_i \mu_{j,\alpha} f_4^{ij}(r_{ij}) - q_j \mu_{i,\alpha} f_4^{ji}(r_{ij}) \right) T_\alpha^{(1)}(\mathbf{r}_{ij}) \\ &\quad - \sum\nolimits_{i,j} \mu_{i,\alpha} \mu_{j,\beta} T_{\alpha\beta}^{(2)}(\mathbf{r}_{ij}) + \sum\nolimits_i \frac{1}{2\alpha_i} \mid \boldsymbol{\mu}_i \mid^2 . \end{aligned} \tag{B.4}$$

Here α_i is the polarisability of ion i, $\boldsymbol{\mu}_i$ are the dipoles and $\mathbf{T}^{(1)}$, $\mathbf{T}^{(2)}$ are the charge-dipole and dipole-dipole interaction tensors:

$$T_\alpha^{(1)}(\mathbf{r}) = -r_\alpha / r^3 \qquad T_{\alpha\beta}^{(2)}(\mathbf{r}) = (3 r_\alpha r_\beta - r^2 \delta_{\alpha\beta})/r^5. \tag{B.5}$$

The instantaneous values of these moments are obtained by minimisation of this expression with respect to the dipoles of all ions at each MD timestep. This ensures that we regain the condition that the dipole induced by an electrical field $\mathbf{E}$ is $\alpha\mathbf{E}$ and that the dipole values are mutually consistent. The short-range induction effects on the dipoles are taken into account by the Tang-Toennies damping functions:

$$f_n^{ij}(r_{ij}) = 1 - c^{ij} e^{-d^{ij} r_{ij}} \sum\nolimits_{k=0}^{n} \frac{(d^{ij} r_{ij})^k}{k!}. \tag{B.6}$$

The parameters d^{ij} determine the range at which the overlap of the charge densities affects the induced dipoles, the parameters c^{ij} determine the strength of the ion response to this effect. It is important to notice that anion-anion damping terms have been taken into account, contrary to what was done in [74]. The addition of anion-anion damping terms was found to greatly improve the ability to match the first-principles data.

B.2.2 The DFT reference calculations

The parameters in the interaction potential are determined by matching the dipoles and forces on the ions calculated from first-principles on condensed phase ionic configurations [13, 20]. Starting from the empirical pair potential in [129], we obtained atomic configurations for GeO_2

by running short MD simulations on small cells (150 ions); a total of two liquid configurations were obtained for GeO_2; for each of these, the Hellman-Feynman forces acting on individual ions of the simulation cell were calculated using planewave-DFT code CPMD [85]. In all the calculations we used norm-conserving pseudopotentials and planewave energy cut-offs of $1360\ eV$; all calculations were performed using the generalised gradient approximation (GGA) according to the Perdew, Burke and Ernzernhof (PBE) scheme. For the calculation of first-principles dipoles, the Kohn-Sham orbitals are localised via a Wannier transformation to construct maximally localised Wannier functions (MLWF) and the dipoles determined from the positions of the centres of the Wannier functions associated with each ion [88].

B.2.3 Fitting procedure

The potential parameters are optimised by fitting the forces and dipoles, obtained with the DIPPIM potentials for the reference configurations, to the respective results from the DFT calculations; the 2 configurations provide a total of about 1800 data points to fit, comprising three Cartesian force components of each individual ion and three components for the dipoles. While most of the potential parameters are left as free parameters in the fits, there are some exceptions. The O^{2-} polarisability, for instance, was fixed to $\alpha_{O^{2-}} = 11\ a.u.$, i.e. the value Salmon $et\ al$ obtained experimentally in [127]. This value for the oxide polarisability is also compatible with the range of values obtained for this quantity in several magmatic melts from first-principles calculations [135]. One problem in DFT calculations is the uncontrolled representation of the dispersion interaction. Although dispersion only contributes a tiny fraction to the total energy, it has a considerable influence on phase transition pressures and on the material density and stress tensor. For this reason, we decided not to include the dispersion parameters in the fits as discussed in [13] and to add them afterwards. We used the parameters in [103] for the oxygen terms and rescaled these by the Ge polarisability for the anion-cation terms. The Gaussian parameters too were added after the fit and then the comparison with the first-principles data was run again to check that its quality remained unchanged.

In Figure B.1 we report the agreement between the DFT calculated forces and dipoles and those predicted by the fitted potential, for a set of representative ions; the abscissa shows the x component of the forces and dipoles, while the ordinate is simply the ion number. The quality of the representation is quite good and comparable with the one obtained in [136]; this can be regarded as a very good result, considering the simplicity of the model (both ion shape deformation effects and quadrupoles are not taken into account in the present model [13, 20]). The parameters obtained for the DIPPIM potential are summarised in Table B.1.

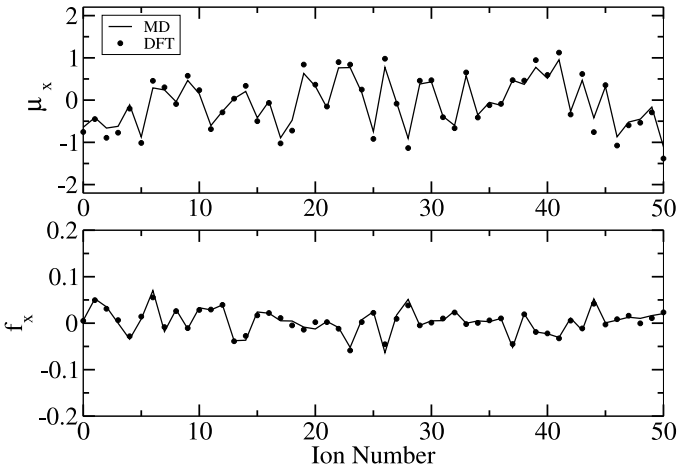

Figure B.1: *Agreement between the DFT calculated dipoles (top panel) and forces (bottom panel) and those predicted by a fitted DIPPIM potential model for a set of 50 representative ions. In each panel the ordinate gives the ion number and the abscissa gives the DFT values of the x component of the forces and dipoles as points and the fitted values as the continuous line.*

B.3 Simulation details

We performed MD simulations in the NVT ensemble through the use of the Nosé-Hoover chain thermostat method [90, 93]. The simulation cell contained 288 oxide and 144 germanium ions, and its volume was set to 6856 Å^3 in order to match the experimental density at 300 K, which is 3.66 g.cm^{-3}. We used a time step of 1 fs to integrate the equations of motion and the minimisation of the polarisation energy was carried out with a conjugate gradient method. The system was studied in both the liquid and amorphous phases.

For the amorphous phase, the system was first equilibrated for 2 ns at the temperature of 4500 K. We have then cooled down the system with a cooling rate of 3.33×10^{11} K.s^{-1}, by rescaling the velocities and decreasing the target temperature of the thermostat in order to reduce the temperature by 50 K every 150000 MD steps. Finally, a 5 ns long simulation was undertaken at 300 K, from which we computed all the data presented in this article. This procedure was performed with two different potentials, the DIPPIM, and the original OE, which

Table B.1: Parameters in the repulsive, polarisation and dispersive parts of the DIPPIM potential. All values are in atomic units. The oxide ion polarisability was set to 11 au.

	O-O	O-Ge	Ge-Ge
A^{ij}	17.78	40.89	2958
a^{ij}	3.893	1.186	5.96
B^{ij}	50000	50000	0
b^{ij}	1.1	1.75	/
C_6^{ij}	44	4	0
C_8^{ij}	853	50	0
c_6^{ij}	1.0	1.0	/
c_8^{ij}	1.0	1.0	/
d_6^{ij}	1.0	1.5	/
d_8^{ij}	1.0	1.5	/
d_{pol}^{ij}	2.208	1.977	/
c_{pol}^{ij}	1.770	1.709	/

has extensively been used in the literature [69]. A simulation at 300 K was also performed with the rescaled OE potential (with one of the configurations obtained from simulations with the original OE potential as a starting configuration) for the study of the vibrational properties.

For the liquid, a series of long simulations with the DIPPIM potential at the temperatures of 3600 K, 3800 K, 4000 K, 4200 K, 4400 K, 4500 K, 4600 K, 4800 K and 5000 K was undertaken. In all the cases, an equilibration run was performed so that the slower species, Ge, moved on average, at least a distance of 5.5 Å; a subsequent run of the same length was made to accumulate enough statistics for the mean-squared displacements curves. At these temperatures, the runs were between 100,000 and 1,000,000 steps. Both the original and rescaled OE potentials were also used within the same simulation conditions at a temperature of 3600 K.

B.4 Static structure

Neutron diffraction experiments with the isotope substitution technique allowed Salmon to determine very precisely the full set of partial radial distribution functions (RDF) [127]. These provide a good check of the validity of the potential.

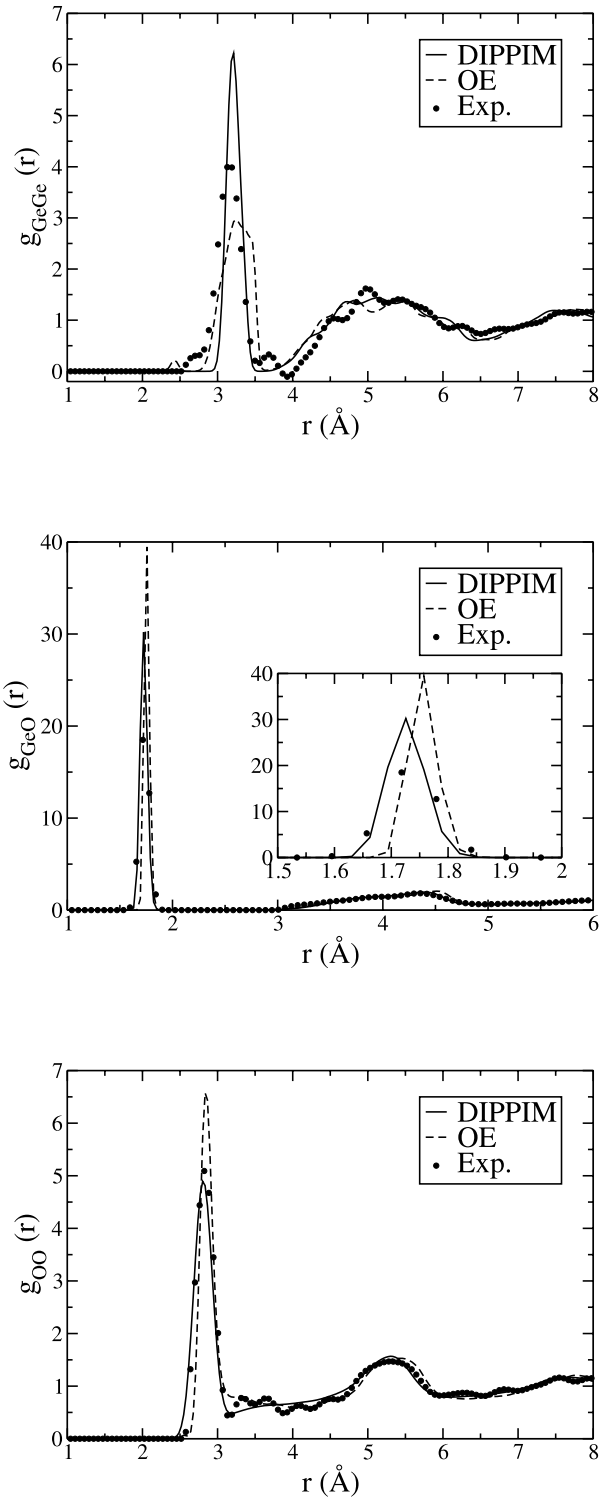

Figure B.2: *Radial distribution functions obtained from the 300 K simulations with the DIPPIM and original OE interaction potentials. These are compared to the experimental ones obtained from neutron diffraction experiments [127].*

The experimental RDFs are given in figure B.2, together with the ones obtained from our simulations at 300 K involving the DIPPIM and the original OE potential; it can be readily observed that our DIPPIM potential gives a closer match with the experimental data than the OE potential, for which all the characteristic first-neighbour distances are slightly overestimated. Concerning the shape of the function, the peaks obtained for the Ge-Ge and Ge-O partials are too sharp but it has be be remembered that other factors, such as system size and cooling rate, also play a role in this aspect of the comparison. The O-O partial RDF is almost in perfect agreement with the experimental one, this is very important since the O^{2-} anions constitute 2/3 of the atoms of the system and their packing arrangement determines the arrangement of the tetrahedral network. The OE potential gives a reasonable description of the static structure (though significantly poorer than the DIPPIM one); one might therefore be tempted to use this potential, due to its simpler form and faster computational time; we will see in the next sections that a reasonable reproduction of the structure might not be sufficient for it to be capable of predicting the dynamical and vibrational properties.

B.5 Dynamics

In this section we will calculate diffusion coefficients for the liquid and compare them both with those obtained with the OE potentials and with the experimental values. The diffusion coefficient of species α can be obtained from the slope of the mean squared displacement at long times, i.e.

$$D_\alpha = \lim_{t\to\infty} \frac{1}{6t} \left\langle r_\alpha^2(t) \right\rangle , \tag{B.7}$$

where

$$\left\langle r_\alpha^2(t) \right\rangle = \frac{1}{N_\alpha} \sum\nolimits_{i=1}^{N_\alpha} \left\langle |r_i(t) - r_i(0)^2| \right\rangle . \tag{B.8}$$

The mean squared displacement curves were evaluated from a series of long simulations at temperatures between 3600 K and 5000 K; these are shown on a log-log scale on figure B.3. No plateau is observed even at the lowest temperature, which shows that the system remains liquid in the range of the study.

The diffusion coefficients were extracted using equation B.7; these are reported in figure B.4 and compared with those obtained with the OE and rescaled OE potentials. Figure B.4 shows many interesting features: first of all, our DIPPIM potential gives approximately the same value for the diffusion coefficients as the original OE potential. Hawlitzky $et\ al$[133] used this potential to calculate the diffusion coefficients and showed that the obtained values

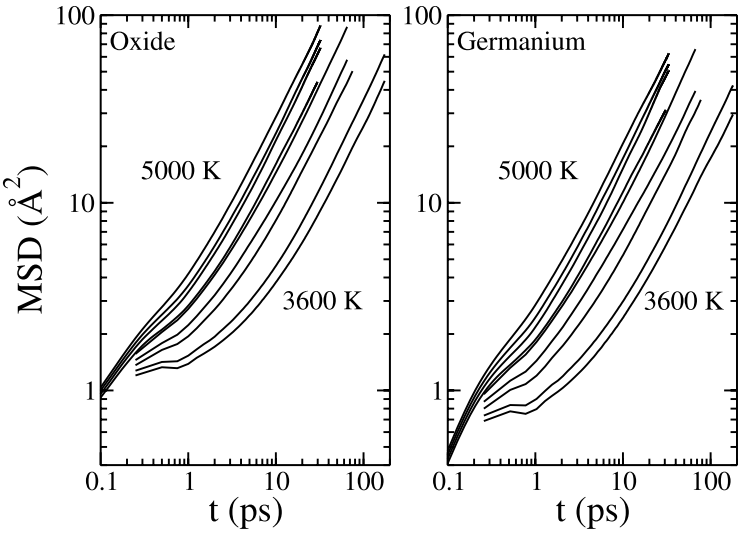

Figure B.3: *Time dependence of the mean squared displacement curves for both the oxygen and germanium ions. The temperatures ranges between 3600 K and 5000 K.*

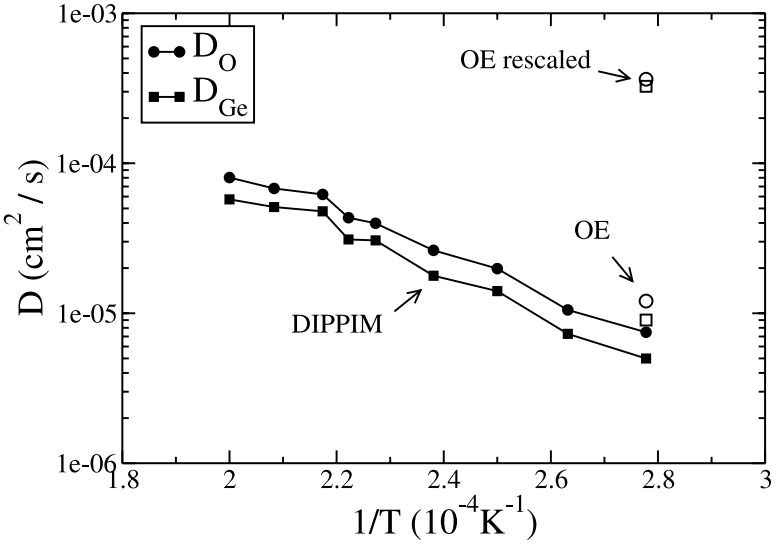

Figure B.4: *Diffusion coefficients obtained with a DIPPIM potential at different temperatures; data points obtained with both the original and rescaled OE potentials at 3600 K are also presented.*

are in good agreement with the experimental ones obtained by converting viscosity data; we can therefore conclude that our DIPPIM potential gives a good agreement with the experimental data as well. A direct comparison with experimental data might be done by using the only published datum ($D_{\mathrm{O}} = 7 \times 10^{-10}$ cm^{2}s^{-1}) on the oxygen diffusion constant [137], at T=1440 K. However, such a low diffusion coefficient would involve an impossibly long simulation run.

It is also interesting to see that the rescaled OE potential yields too fluid a melt if compared with the original OE and DIPPIM potentials and with experimental data. This potential was used by Micoulaut *et al.*[129] and they indeed obtained diffusion coefficients which were more than one order of magnitude larger than the values obtained by Hawlitzky *et al.* [133] (who incorrectly explained this discrepancy in terms of lack of equilibration of the simulations, it is obvious here that the real reason was the difference between the two potentials). The so-called rescaled potential was obtained by taking the normal OE potential and rescaling the ionic charges, the van der Waals coefficient and the repulsive parameters in order to get a better agreement with the experimental vibrational spectrum for the crystal. To do this the parameters which are responsible for the strength of the the O-O and O-Ge short range repulsion were lowered by a factor of approximately 2.5; as a consequence, these ions can diffuse much more easily in a softer environment.

B.6 Infrared spectrum

The infrared spectra of ionic melts with polyvalent cations exhibit discrete bands attributable to the vibrational motion of the local coordination complexes around the cations. They originate from the polarisation fluctuations associated with motion of the ionic charges. The inclusion of polarisation effects for the oxide ions in our model may influence the predicted spectrum in two ways [138]. First, the interactions of the oxide ion dipoles may alter the local structure of the network and the strength of the bonds, which may introduce a shift of the vibrational frequencies. Second, the induced dipoles will themselves be responsible for absorption, as they too contribute to the total polarisation fluctuations.

The absorption coefficient in the presence of these extra moments is calculated from the imaginary part of the total dielectric function $[n(\nu)\alpha(\nu) = 2\pi\nu\Im(\epsilon(\nu))]$, which can be deter-

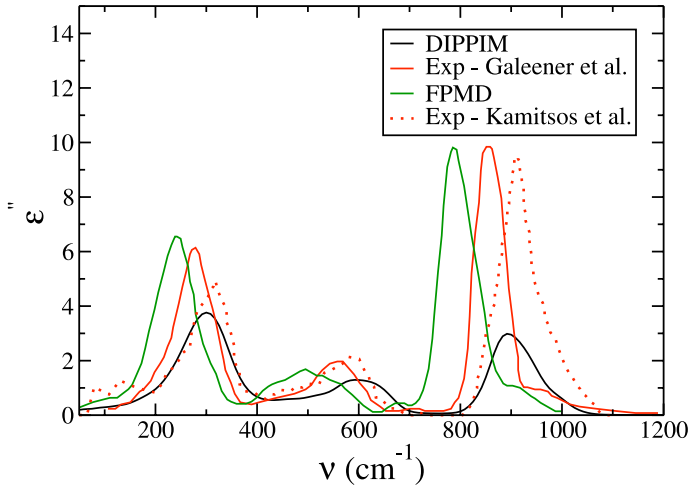

Figure B.5: *Imaginary part of the dielectric function, calculated for simulations carried out with the DIPPIM potential, compared to FPMD simulation [131] and experimental results [124, 125].*

mined following Caillol, Levesque and Weis[139, 140] as

$$\epsilon(\nu) - \epsilon_\infty = \frac{\beta}{3\epsilon_0 V}\left(\langle \mathbf{M}(0)^2\rangle + 2\pi\imath\nu\langle \mathbf{M}\cdot\mathbf{M}\rangle_\nu + 2\langle \mathbf{M}\cdot\mathbf{J}\rangle_\nu + \frac{\imath}{2\pi\nu}\langle \mathbf{J}\cdot\mathbf{J}\rangle_\nu\right) \tag{B.9}$$

where

$$\langle \mathbf{J}\cdot\mathbf{J}\rangle_\nu = \int_0^\infty e^{2\pi\imath\nu t}\langle \mathbf{J}(t)\cdot\mathbf{J}(0)\rangle \mathrm{d}t, \tag{B.10}$$

$\mathbf{J}(t)$ is the charge current $\mathbf{J}(t) = \sum_{i=1}^N q_i \mathbf{v}_i(t)$ and $\mathbf{M}(t)$ is the total system induced dipole moment, $\mathbf{M}(t) = \sum_{i=1}^N \boldsymbol{\mu}_i(t)$.

Figure B.5 shows the imaginary part of the total dielectric function calculated for simulations carried out with the DIPPIM potential, compared to the one obtained from FPMD simulations [131, 132] and from several experiments [124, 125] (the spectrum proposed by Kamitsos *et al.* shows the absorption coefficient, here we transformed it into the dielectric function to facilitate comparisons). Three main bands are observed on the spectra, in good agreement with the other studies. The corresponding characteristic peak frequencies for the absorption spectra are summarised in table B.2. The agreement is very satisfactory; the frequencies obtained match very closely to the various experimental results (even though these

Table B.2: *Characteristic frequencies of the imaginary part of the dielectric function as obtained from the DIPPIM model, compared to previous FPMD simulations [131, 132] and to experimental results [124, 125, 126]. All the frequencies are given in* cm^{-1}.

DIPPIM	300	601	894
FPMD[131]	244	498	787
Exp. 1[124]	280	567	858
Exp. 2[125]	315	585	915
Exp. 3[126]		560	870

show a significant scatter), while the FPMD simulation seems to systematically underestimate them. The relative intensities of the bands is also in good agreement with experiment, though the highest frequency band at around 894 cm^{-1} is not intense enough in our spectrum.

The importance of polarisation effects in determining the relative intensities of the bands can be demonstrated by separating the various contributions to the absorption spectrum. In the case of glassy silica [138] and beryllium fluoride [17], it was observed that the interference between the induced dipoles and permanent charge contributions to the total polarisation, contained in the $\langle \mathbf{M} \cdot \mathbf{J} \rangle_\nu$ cross term, is responsible for the changes of the relative intensities. Figure B.6 shows the decomposition of the absorption spectrum in the case of glassy GeO_2. The two main contributions are the charge fluctuation and the cross term; both show bands at the same intensities. Note that the cross-term strongly reduces the intensity of the two low frequency bands relative to that which would be obtained from the charge fluctuations alone, whereas for the high-frequency band the cancellation is much weaker. For the high frequency band the relationship of the charge-charge and cross-terms is different to that found previously for SiO_2 and BeF_2[138, 17]. In the latter cases, the charge-charge and cross-terms had the same sign, so that the net band intensity was slightly larger than that predicted by the charge-charge term alone. This difference in the behaviour of the calculated spectra might arise from the inclusion of an anion-anion damping term in the polarisation part of the interaction potential here, which was not the case for the previous studies.

We can now attempt to associate these IR frequencies with the vibrational modes of the system. The upper part of figure B.7 shows the vibrational density of states (VDOS) of each ion. Some of these features can be associated to the vibrations of the GeO_4 tetrahedra by comparing them with the tetrahedral-VDOS as obtained from the correlation functions of the velocities of various local tetrahedral symmetry coordinates. The latter would correspond to the velocities of GeO_4 normal modes, if the tetrahedra were isolated (*i.e.* not mechanically linked in a net-

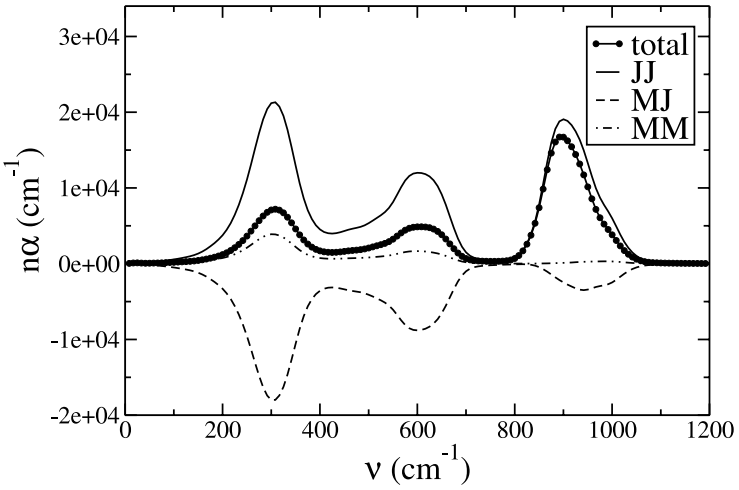

Figure B.6: *Decomposition of the total IR absorption spectrum in its three component parts.*

work). For a tetrahedral molecule, vibrational normal coordinates ν_1 (A_1, symmetric stretch), ν_2 (E, bend), ν_3 (F_2, asymmetric stretch) and ν_4 (F_2, bend) are expected [141]. We may obtain velocities associated with the symmetry coordinates of each GeO_4 unit. For example, for the symmetric stretching motion

$$v_i^A = \sum\nolimits_{i\alpha=1-4} v_{i\alpha}^{\parallel} \tag{B.11}$$

where i labels the Ge of a tetrahedral complex, and $i\alpha$ the four oxide anions at the vertices. $v_{i\alpha}^{\parallel}$ is the projection of the relative velocity of $i\alpha$ along the $i \rightarrow i\alpha$ bond, *i.e.*

$$v_{i\alpha}^{\parallel} = (\mathbf{v}_{i\alpha} - \mathbf{v}_i) \cdot (\mathbf{r}_{i\alpha} - \mathbf{r}_i). \tag{B.12}$$

Similar expressions may be written down for the velocities of the other symmetry coordinates [141]. The corresponding DOS is then obtained by a Fourier transform of the corresponding velocity autocorrelation function:

$$\mathrm{DOS}_A(\nu) = \Re \int_0^\infty e^{2\pi\imath\nu t} \langle v_i^A(t) \cdot v_i^A(0) \rangle \mathrm{d}t. \tag{B.13}$$

Were the network to vibrate as a collection of isolated tetrahedra, the spectra of each tetrahedral-VDOS would exhibit a single peak corresponding to the characteristic frequency of the corresponding normal mode of vibration. The four tetrahedral-VDOS are shown on the lower part of figure B.7, it is clear that it is not the case here. Each spectra consists in the super-

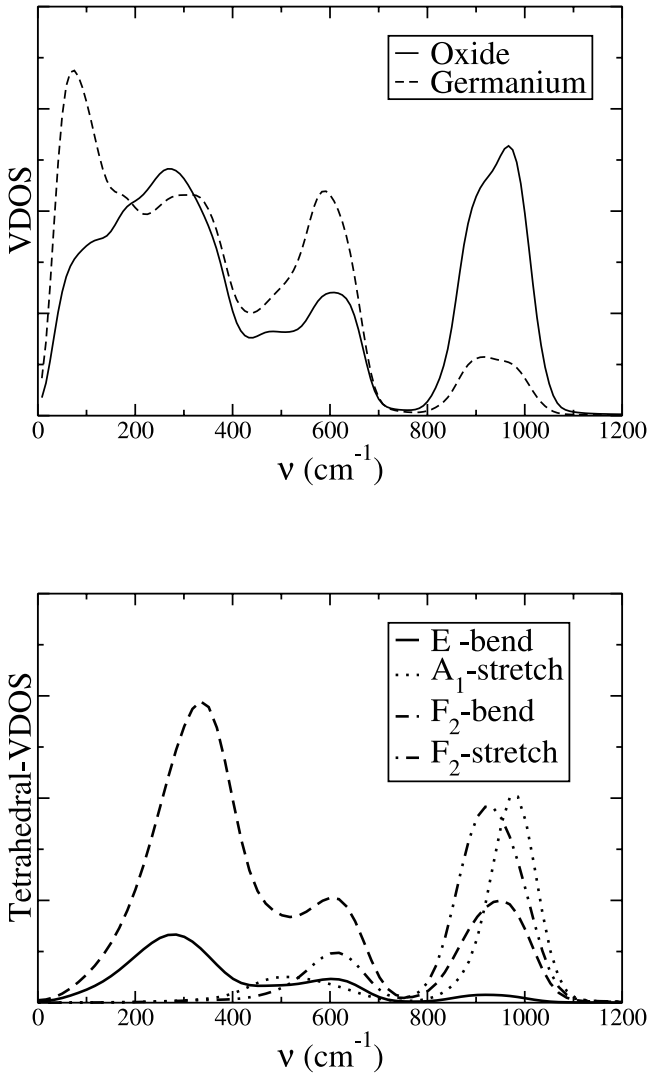

Figure B.7: *The vibrational densities of states, for the DIPPIM, of both type of ions (top panel), and their projections in terms of the A (symmetric stretch), F_2 (asymmetric stretch), E (bend), and F_2 (bend) modes of the $Ge0_4$ tetrahedra (bottom panel).*

position of several bands, which shows the existence of some important coupling between the symmetry coordinates. It is therefore difficult to assign the IR features to the different modes. In particular, all of the three bands observed in the IR spectrum appear in the tetrahedral-VDOS of the bending E and F_2 modes. The other F_2 modes, which is associated to some kind of stretching of the tetrahedra, only exhibits the medium and high frequency modes. Finally, the A_1 stretching spectrum exhibits two bands at frequencies centered on the values of 510 and 970 cm^{-1}, which do not appear on the IR spectrum. Such a mode of this symmetry is indeed not expected to be IR active for an isolated tetrahedral molecule, since it corresponds to the symmetric breathing mode. Coming back to the total VDOS of each ion, the low frequency vibrations are not associated to any of the tetrahedral modes. In fact these are due to some slow collective bending of two tetrahedra linked by a bridging oxide anion [142], so that they would not appear in the DOS of a single tetrahedron.

The vibrational properties of the system as obtained with the original and rescaled OE interaction potentials have also been computed. As these potentials do not include any polarisation effect, it is only possible to compare the charge-charge current contributions to the IR absorption spectrum with the one obtained with the DIPPIM potential. The obtained spectra are given on figure B.8. Unsurprisingly, the original OE potential seem to fail completely in describing the vibrational properties of GeO_2; this is the reason why the rescaled OE potential had to be developed. For that potential, the agreement is better, in particular for both the small and high frequency bands. Concerning the medium frequency band, observed at around 604 cm^{-1} for the DIPPIM potential, it does not appear for the rescaled OE potential. Instead there appears a shoulder to the small frequency band, for frequencies ranging from 400 to 500 cm^{-1}. As these bands were associated to the F_2 stretching and bending modes on the tetrahedral-VDOS, this means that these modes are not correctly depicted by the rescaled OE potential.

B.7 Conclusion

In conclusion, the obtained potential seem to reproduce all the studied properties (structural, dynamical and vibrational) to a high degree of precision. Since there was no reference at all to any experimental data in the parameterisation of this potential, this represents a strong test of the model reliability. The study of pressurised germania is among our top priorities for future work. The potential is of a similar form to that introduced to describe silicates [143]; since these potentials have proved to be transferable, we will be able, in the future, to focus on GeO_2-SiO_2 mixtures as well. These mixtures, as already mentioned in the introduction, attract

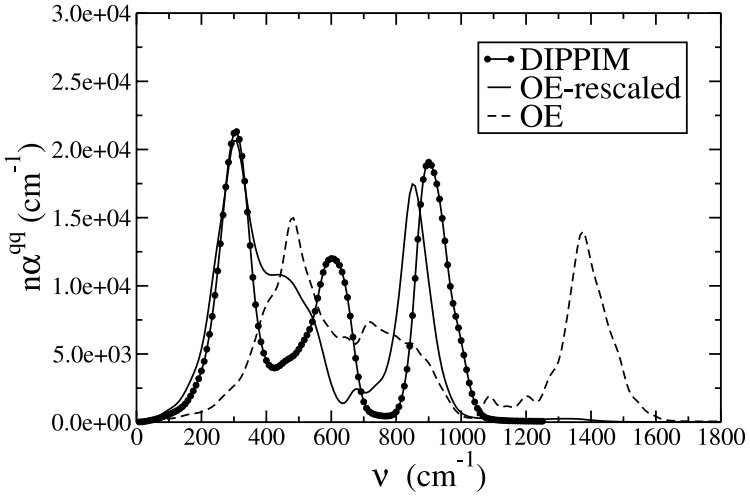

Figure B.8: *Comparison of the charge-charge current contributions to the infrared spectrum obtained with the three different potentials (the two OE curves were rescaled with a factor* $q_{\mathrm{O}}^2/4$*, where* q_{O} *is the partial charge carried by the oxide ion in the corresponding potential.*

great interest as they are widely used in optical fibers and waveguides.

Acknowledgements

We thank Philip Salmon for providing his diffraction data. Calculations were carried out at the EaStCHEM computing facility (http://www.eastchem.ac.uk/rcf). DM thanks the EPSRC and the CMPC for his PhD funding. This work was carried out under the HPC-EUROPA++ project (project number: 211437), with the support of the European Community - Research Infrastructure Action of the FP7 "Coordination and support action" Programme.

Appendix C

High-pressure behaviour of GeO_2: a simulation study.

D. Marrocchelli [1], M. Salanne[2,3] and P.A. Madden [4]

[1] School of Chemistry, University of Edinburgh, Edinburgh EH9 3JJ, UK
[2] UPMC Univ Paris 06, UMR 7612, LI2C, F-75005, Paris, France
[3] CNRS, UMR 7612, LI2C, F-75005, Paris, France
[4] Department of Materials, University of Oxford,
Parks Road, Oxford OX1 3PH, UK

Abstract

In this work we study the high pressure behaviour of liquid and glassy GeO_2 by means of molecular dynamics simulations. The interaction potential, which includes dipole polarisation effects, is able to reproduce the experimental data on glassy germania to a high degree of precision. Our simulations show that the various experimental studies agree well one with each other, even if the initial interpretations that were made of them did not. The proportion of the various GeO_n polyhedra is determined as a function of the pressure: a smooth transition from tetrahedral to octahedral network is observed. Finally, the study of high-pressure, liquid germania confirms that this material presents an anomalous behaviour of the diffusivity as observed in analog systems such as silica and water. The importance of penta-coordinated germanium ions for such behaviour is stressed.

C.1 Introduction

Germania (GeO_2), along with silica and beryllium fluoride, is a "strong" glass-former [144] characterised by a tetrahedral network structure at ambient conditions in the amorphous phase [124]. Its structure is based on corner-sharing $Ge(O_{1/2})_4$ tetrahedra (the $1/2$ index means that each O^{2-} ion is shared by two Ge^{4+}), with a Ge-O average distance of 1.73 Å and a mean inter-tetrahedral Ge-O-Ge angle of 132° [123, 128]. There is considerable interest in the behaviour of such tetrahedrally coordinated glasses under pressure. In the associated crystalline materials high-pressure transitions are observed between four- and six-coordinate structures. Pressure-induced structural changes in the amorphous phases have been linked to anomalous behaviour in the elastic, viscous and thermal properties and to the phenomenon of polyamorphism [145]. In amorphous silica itself, the major structural transition occurs at relatively high pressures ($\sim$25 GPa) where direct structural studies remain difficult [146]. However, because of the larger cation / anion radius ratio in germania relative to silica, the transition occurs in a pressure domain now accessible to structural studies. Despite this, a clear picture of the nature of the pressure-induced structural changes in germania is yet to emerge from the studies which have been performed so far. We have therefore performed computer simulations in an attempt to clarify the relationship of the information emerging from the different experiments.

High-pressure structural studies have been made using EXAFS spectroscopy [147, 148, 149, 150] and X-ray and neutron diffraction experiments [151, 152]. All the experimental studies agreed on the existence of a structural change in the pressure range 3-15 GPa, associated with an increase in the Ge-O separation. Vaccari *et al.*, for example, showed, from EXAFS studies, that this distance switched from 1.74 Å (at 0 GPa) to 1.82 Å (at 13 GPa). On the other hand, the literature is very contradictory about the character of a change in coordination number. The first study to address this issue is that of Itie *et al.* [147] who performed x-ray absorption measurements up to 23.2 GPa and found that the Ge coordination changes from fourfold to sixfold at pressure between 7 and 9 GPa. Vaccari *et al.*, on the other hand, proposed a progressive shift in the coordination number, and found no evidence of a fully six-coordinate structure, even at the highest pressure of their study (13 $\sim$ GPa). Very recent XAFS and EXAFS studies [149, 150] extended the studied pressure range to 53 and 44 GPa respectively and postulated that a complete 6-fold coordination of the Ge ions is only reached at pressures as high as 25-30 GPa. The ability of EXAFS to provide very accurate first-neighbour distances is well established, but so is its limitation for the determination of coordination numbers in amorphous materials [153, 154], due mainly to the low q-range caused by the diamond Bragg diffraction. Only an average coordination number can be extracted, with an important error bar which depends crucially on assumptions about the shape of the radial distribution functions at larger separations, and to estimate proportions of different coordination polyhedra in a material

from EXAFS alone is not normally considered reliable.

In principle neutron diffraction, when employing the isotopic substitution method, gives access to all the partial structure factors, and hence to the corresponding partial radial distribution functions (RDF) which contain all the structural information. In the case of GeO_2, this programme has been fulfilled only at ambient pressure by Salmon *et al.* [155], and at elevated pressures only total X-ray and neutron diffraction patterns are available. A first attempt to study the high pressure system by these means was reported by Guthrie *et al* [151]: unfortunately, the data were too noisy to extract good RDFs. However, a very sharp transition from a tetrahedral to an octahedral structure was proposed, with a small range of pressure in which the system is characterised by five-fold coordination around Ge^{4+} ions. Very recently, Drewitt *et al.* have performed new neutron diffraction measurements up to 8.6 GPa and obtained data of very high quality [152]. Their results show a gradual change of the intermediate range order with increasing density as manifested by an increase in position and reduction in height of the first sharp diffraction peak in the total structure factor. From their data there is no evidence in support of an abrupt transformation of the network structure over the investigated pressure range, in agreement with the most recent EXAFS experiments [148, 149, 152].

Computer simulations could help in resolving the observed differences since they can provide a detailed picture of the structure of a system. Unfortunately, to date, all the molecular dynamics (MD) calculations involving pressurised germania have been performed with pair potentials of limited accuracy [156, 157, 158, 159, 160, 161, 130, 162, 163]. For example, for the most commonly used potential, developed by Oeffner and Elliot [69], *two* different parameter sets were proposed: an original one, which was fitted from an ab initio energy surface, and a so-called rescaled one, which was developed from the previous one in order to give a better reproduction of the vibrational properties. For this reason, some apparent inconsistencies have arisen in the literature because different classical potentials were being used [156, 133, 130]. Finally, since the OE potential is not able to reproduce with a single set of parameters all the ambient pressure properties of amorphous germania, it is also reasonable to suspect that it might fail when studying the pressure behaviour of this material. This might explain the disagreement with the experimental trends found in some papers in the literature. For instance, in ref. [163], the Ge-O bond distance is found to remain constant in the 3-25 GPa pressure interval, whilst in ref. [159] the Ge-O coordination number is found to increase continuously from the lowest pressure (1GPa), both trends being in strong contrast with the experimental evidence [147, 151, 148].

We recently introduced a new interaction potential, which includes many-body polarisation effects, and succeeded in reproducing the structural and vibrational properties of glassy germa-

nia at ambient pressure as well as the dynamical properties of liquid germania in the 3600-5000 K temperature range [111], with a *single* set of parameters. This potential was parameterised with reference to extensive Density Functional Theory (DFT) electronic structure calculations (which have proved as a successful tool to study this system [164]) on condensed-phase configurations. Also, similarly constructed potentials have been shown to provide an excellent, transferable description of a number of complex oxides [103, 20]. The aim of this paper is to show how the use of this potential together with a direct comparison with the available experimental data, can improve our understanding of the behavior of glassy germania at high pressure. In the end, we will emphasise that the various experimental studies are in accord, even if the initial interpretations that were made of them did not.

Once the question of structure is resolved, it is of interest to study the influence of structural changes on the physical properties of the system. A well-known effect is the existence of dynamical anomaly in silica-based systems when the pressure increases [145]. Unlike most other systems which, under compression, tend to show a decreasing mobility of the species, in liquid silica the diffusion coefficients increase until they reach a maximum for a given pressure, and then decrease. This anomaly was linked to the existence of pentacoordinated species [165]. The only evidence for such a behaviour in liquid germania was provided by Sharma *et al.* who showed a decrease of the viscosity with pressure, though the pressure range of this study was very limited (0-1 GPa) [166]. There are also some simulations studies on high-pressure liquid germania but, unfortunately, the results are contradictory. Hoang *et al.* [158] do indeed observe an anomalous behaviour of the diffusivity in GeO_2. However Hung and co-workers [160], who also studied this system by means of classical molecular dynamics, found no evidence of such a phenomenon, but again both of these studies involved classical pairwise additive interaction potentials of limited accuracy. To address this issue we have therefore studied the structural and dynamical properties of liquid germania, at a temperature of 4000 K, on a wide range of pressures.

C.2 Simulation details

The interaction potential used in this study has already been described elsewhere [111]. The ionic species carry their valence charges (Ge^{4+} and O^{2-}), and the polarisation effects that result from the induction of dipoles on the oxide ions are accounted for. The parameters of the interaction potential for germania were obtained from the application of a force- and dipole-matching procedure aimed at reproducing a large set of first-principles (DFT) reference data [13] on the condensed phase. One potential deficiency follows from the fact that the parent DFT calculations do not accurately represent the dispersion interactions between the ions. In

the present case, the dispersion interaction parameters are not determining during the fitting procedure, but added afterwards.

To obtain structural properties in the glassy state, we performed MD simulations in the NPT ensemble using the method introduced by Martyna *et al.* [94]. When dynamical properties were computed, the system was simulated in the NVT ensemble using the Nosé-Hoover chain thermostat method [93]. A relaxation time of 10 ps was used for the thermostats and the barostats. The simulations on glassy GeO_2 (T = 300 K) were performed on a simulation cell containing 432 atoms whereas the NVT simulation cells on liquid germania (T = 4000 K) contained 600 atoms. We used a time step of 1 fs to integrate the equations of motion, and minimisation of the polarisation energy was carried out at each time step using a conjugate gradient method. All simulations were equilibrated for at least 0.5 ns and then a subsequent run of 0.5 ns was made to accumulate enough statistics. Details on the generation of a compressed glassy state will be reported below.

C.3 Compressing a glass: some limitations

Generating a glassy state by means of computer simulations is a challenging operation. Indeed the relatively short time-scales available (a few ns in our case) force us to use unrealistically fast cooling rates. This implies that sometimes the glass we obtained is further away from equilibrium than the experimental one. In fact, even experimentally, glasses prepared in different ways show different properties, implying that even on a time-scale of hours (*i.e.* 12 orders of magnitude higher than what we can afford with MD simulations) there are still some relaxation effects. This problem becomes even more significant when one tries to compress a glass. To this end, Scandolo *et al.* described two different compression methodologies for SiO_2 [167]. The first one is a cold compression route consisting of increasing pressure slowly at ambient temperature while the second one, which they called a 'quench-from-the-melt' procedure, consists of obtaining the compressed glass by a slow cooling of a compressed sample from a temperature where atomic diffusion is observable on the time scale of the MD simulation. By comparing their results with the available experimental data on compressed glass, they showed that the samples obtained with the two procedures are representative of the experimental *in situ* compressed (like, for example, in refs. [148, 149]) and densified forms of glass [168], respectively, and found that structural differences between annealed and cold-compressed forms take place at distances of 3.5–4 Å.

In the case of GeO_2 there has been little effort so far in this direction. Most of the previous work on this system used the cold compression route but a direct quantitative comparison with

experimental data was never attempted. In this work we tried both routes used by Scandolo *et al.* and compared the results with the experimental density vs pressure data. This is shown in figure C.1. It can be appreciated that neither of the two routes reproduces quantitatively the experimental data. In both cases the simulated glass seems to be less responsive to compression, a clear drawback of the limited simulation times. It seems, however, that the quench-from-a-melt procedure gives a closer agreement with the experimental data than the cold-compressed route, once again indicating that a certain degree of diffusion helps the glass relaxation. It has to be remembered, however, that Scandolo *et al.* showed how the quench-from-a-melt route is representative of the densified forms of the glass, so that a comparison with the experimental data on a cold-compressed glass, such as in refs. [151, 155] would not work.

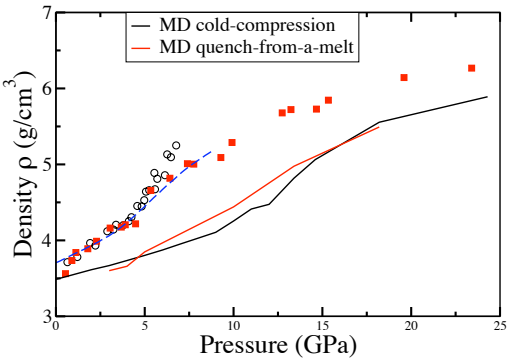

Figure C.1: *The mass density ρ for GeO_2 glass as a function of pressure for cold compression and quench-from-a-melt procedures. Experimental data are from the in-situ compression studies of Hong et al. [169] ((red squares)), Smith et al. [170] (empty circles) and Tsiok et al. [171] (blue broken curve).*

It should be evident from the above discussion that we are unable to reproduce quantitatively the equation of state of glassy germania. This should not be taken as a limitation of out potential but as a consequence of the relatively short time-scales available in computer simulations. For this reason, in the remainder of this paper, we will simulate cold-compressed GeO_2 and report our data as a function of *density*, instead of pressure. When a comparison with experimental data is required, we will convert the experimental pressures into densities by using the data in ref. [171, 169]. In the case of liquid germania, since the the system is very diffusive and reaches equilibrium in a few picoseonds, we do not anticipate any problem with the equation of state and we will therefore report our data as a function of pressure.

C.4 Glassy germania

In the top panel of figure C.2 we report the average Ge-O distance[1] as a function of increasing density. It is compared to the values obtained by Vaccari *et al.* [148] and Drewitt *et al.* [152] *via* EXAFS and neutron diffraction measurements. The agreement is quite good, considering the scatter of the experimental data and the intrinsic error associated with the pressure-to-density conversion. The simulations, like the experiments, show first a Ge-O bond distance which is fairly constant in the 3.66 - 4.5 g/cm^3 density range (corresponding to an experimental pressure range of 0-5 GPa) and then a gradual increase in the Ge-O bond distance, starting at a density of 4.5 g/cm^3.

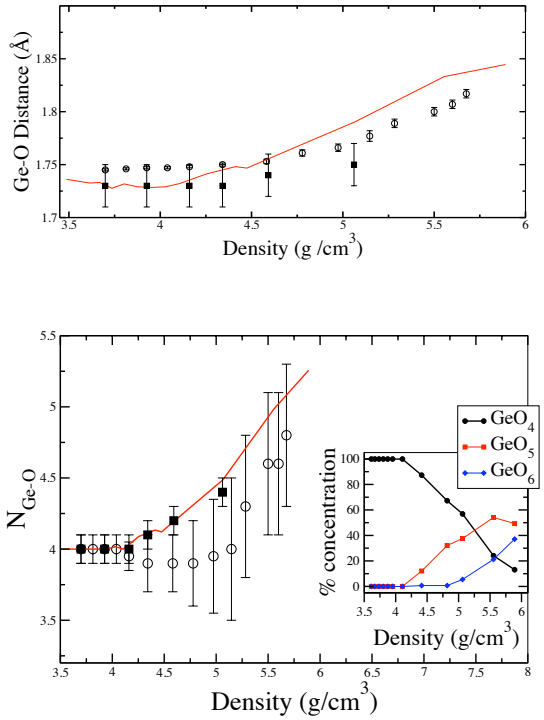

Figure C.2: *Top panel: comparison between the simulated (solid line) and experimental Ge-O bond distance from Vaccari (black empty dots) and Salmon (black filled squares) as a function of increasing density. Bottom panel: comparison between the simulated (solid line) and experimental first shell Ge-O coordination number. The inset in the top panel shows the density dependence of the percentage concentration of GeO_4, GeO_5, GeO_6 units.*

[1]This distance was defined as $d_{GeO} = \frac{\int_0^{r_{cut}} r^3 g(r) dr}{\int_0^{r_{cut}} r^2 g r(r) dr}$ where g(r) is the Ge-O radial distribution function and r_{cut} is the position of the first minimum in the g(r)

We can interpret that data in terms of compression mechanisms. When a tetrahedral system like GeO_2 is compressed, three types of structural changes could be observed. Firstly, the system could keep exactly the same structure, but adapt by allowing the bond lengths to decrease: obviously this is not the case here. Secondly, the tetrahedral units could be kept unmodified, in which case the decrease of accessible volume would imply a rearrangement of the network structure, progressively minimizing the size of the voids [172, 168]. Finally the tetrahedral structure could be lost, and higher-coordinated structural units could be formed. Such an evolution may induce an increase of the Ge-O bond length in order to allow more than 4 oxide ions into the germanium first coordination shell. The analysis of bond length data gives evidence of a succession of the two latter mechanisms, at low and high pressures. This was also confirmed by an analysis of the bond angle distributions (not shown).

To verify this, we have determined the germanium coordination number. The cut-off used for the coordination number calculation was 2.38 Å which corresponds to the first minimum of the Ge-O partial RDF. Again we compare these values with the ones obtained by Vaccari *et al.* [148] and Drewitt *et al.* [152]. Good agreement is found, especially with the neutron data. The simulated coordination number remains constant, at a value of 4, until a density of 4.5 g/cm^3. In this first regime, germania is therefore keeping its tetrahedral structure under compression, but the tetrahedra reorient themselves. Then, in a second régime, more highly coordinated germanium ions begin to be observed. In the inset of the figure, the percentage of GeO_4, GeO_5 and GeO_6 units are given as a function of density. Once again, at a density of 4.5 g/cm^3, some Ge^{4+} ions start to accept 5 O^{2-} ions in their vicinity. Then, at $\rho \sim 5.0$ g/cm^3 (corresponding to an experimental pressure of about 7-8 GPa), GeO_6 units begin to be formed. At the highest density studied experimentally, $\rho \sim 5.85$ g/cm^3 (corresponding to approximately 15 GPa), though, a non-negligible proportion of GeO_4 units is still observed. We find no evidence of a state in which there are only 5-fold coordinated Ge ions in the studied pressure range. These fivefold-coordinated units play an important role in liquid germania as we shall show in the next section.

These results differ significantly from the conclusions of Guthrie *et al.* from their combined X-ray and neutron diffraction study of glassy germania [151] . Qualitatively, they observed an analogous mechanism, but with a much sharper increase in the coordination number. They proposed a complete transition to a GeO_5 units based structure for pressures ranging from 6 to 10 GPa, and a final completely octahedral structure at a pressure of 15 GPa. These values were extracted from a Fourier transform of the X-ray diffraction *total* structure factor (their neutron data being too noisy to allow an attempt to extract partials). To show that the discrepancy observed is due to the analysis of the X-ray data, rather than a deficiency of the representation of the structure in the simulations, we have computed the X-ray structure factor. This was

obtained using the following relationship

$$\begin{aligned} S(q) = \quad & c_{Ge}^2 f_{Ge}(q)^2 [S_{Ge-Ge}(q) - 1] + \\ & 2c_{Ge}c_O f_{Ge}(q) f_O(q) [S_{Ge-O}(q)] + \\ & c_O^2 f_O(q)^2 [S_{O-O}(q) - 1] \end{aligned} \tag{C.1}$$

where c_α and $f_\alpha(q)$ represent respectively the atomic fraction and X-ray form factor of element α. $S_{\alpha\beta}(q)$ is the partial structure factor which can be obtained via a Fourier transform of the partial radial distribution functions:

$$S(q)_{\alpha\beta} = \quad \delta_{\alpha\beta} + \rho \int_0^\infty 4\pi r^2 \frac{sin(qr)}{qr} [g_{\alpha\beta}(r) - 1] dr. \tag{C.2}$$

The q-dependent X-ray form factors are calculated from

$$f_\alpha(q) = \sum\nolimits_{i=1}^{4} a_{\alpha,i} \exp\left[-b_{\alpha,i}(q/4\pi)^2\right] + d_\alpha. \tag{C.3}$$

The parameters we used for the calculation of these form factors factors are reported in table C.1; note they are consistent with an ionic representation of the distribution of electrons (*i.e.* Ge^{4+} and O^{2-}). Figure C.3 has been organised in a similar way to Fig. 1 in ref. [151] in order to facilitate a comparison; in particular, $S(q)$ has been normalised by :

$$(\sum\nolimits_{\alpha=1}^{2} c_\alpha f_\alpha(q))^2. \tag{C.4}$$

The six patterns are reported at the densities corresponding approximately to the following experimental pressures: 0, 3, 5, 7, 10, 15 GPa. In the right-hand panel of figure C.3 we report the calculated neutron diffraction patterns at the same densities; these are obtained from the same expressions but with $f_\alpha(q)$ replaced with b_α, the neutron diffraction length. In this figure we also show some experimental data from the recent study by Drewitt and co-workers [152] at densities close to the simulation ones. These data were collected at the following pressures: 2.2, 4.9 and 8.0 GPa.

By comparing figure C.3 with Fig. 1 in ref. [151], it can be readily appreciated that the agreement with the experimental X-ray structure factors is excellent at all pressures. Our data show that the First Sharp Diffraction Peak position (FSDP) shifts toward higher wavenumbers upon pressure increase until it merges with the principal peak, in agreement with the data in ref. [151].

The comparison with the neutron data from Guthrie *et al.* is inhibited by the noisiness of the experimental data but the data of Drewitt *et al* is of higher quality. For densities above $\rho \sim 5.0$ g/cm^3, corresponding to an experimental pressure of 8-9 GPa, there are, to the best

Table C.1: Parameters used for the form factors [173, 174].

	a_1	b_1	a_2	b_2	a_3	b_3	a_4	b_4	d
O^{2-}	4.174	1.938	3.387	4.145	1.202	0.228	0.528	8.285	0.706
Ge^{4+}	4.758	7.831	3.637	30.05	0	0	0	0	1.594

of the authors' knowledge, no available neutron data. Our simulations are consistent with the main trends observed in the neutron work, namely a diminution in the height and a shift to higher q of the FSDP with increasing pressure. However, the agreement between simulations and experiment is less good than in the X-ray case. The simulations appear to overestimate the height of the FSDP, especially at low pressure, and also to underestimate the amplitude and sharpness of the principal peak at about 2.5 $Å^{-1}$. In the total neutron structure factor of GeO_2 there is a near-total cancellation between the different partial structure factors in the vicinity of the principal peak, so that the "principal" peak in the total $S(q)$ is of much lower amplitude than in the Ge or O partials. The discrepancy we noted above presumably reflects a small error in position or width of the principal peak in these partials. The FSDP on the other hand reflects the intermediate range order in the glass and the implication of a disagreement in this domain is that the quenching method we have used to prepare the glass does not allow this structure to develop in the same way as in the experimental material. In support of this contention, we note that the $S(q)$s calculated from the cold-compressed and densified samples differed most in this region of q-space. The position of the FSDP obtained from the neutron structure factors is shown in the bottom part of figure figure C.3 and increases linearly with density. The corresponding values from the Drewitt *et al* work are also shown.

Overall then, our simulations agree well with the available pressure-dependent diffraction data when we compare directly with the experimentally measured quantity, $S(q)$. There is also good agreement with the density dependence of the nearest-neighbour separation obtained from analysis of the EXAFS data. The examination of the local structure in the simulations supports the conclusion that the transition from a tetrahedral to an octahedral glass is smooth and gradual and probably not completed even at pressures as high as 15 GPa.

C.5 Liquid germania

The high-pressure behavior of liquid germania presents some differences compared with the glassy case. Although a similar increase in mean coordination number is observed, both the Ge-O coordination number and Ge-O distances (not shown) increase more smoothly as pressure is raised. The increase in coordination number begins as soon as the pressure in increased.

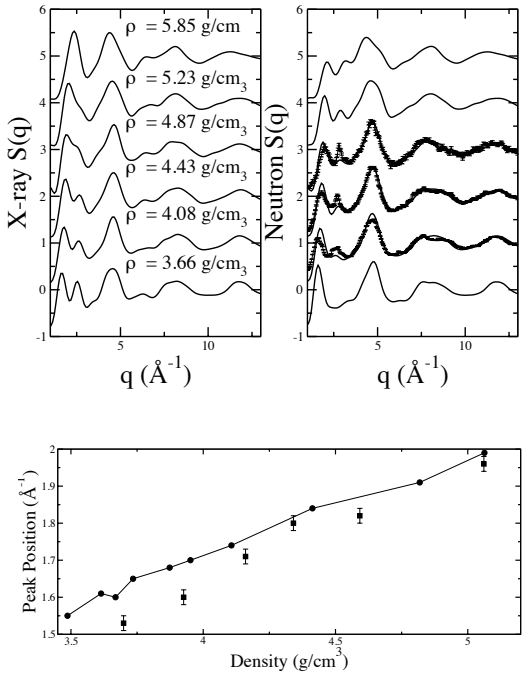

Figure C.3: *Top: simulated X-ray and neutron diffraction patterns as a function of increasing density. The experimental data (line with error bar) are from [152]. Bottom: pressure dependence of the FSDP (extracted from the neutron patterns) position obtained from the X-ray diffaction pattern. The experimental data (filled green squares) are from [152].*

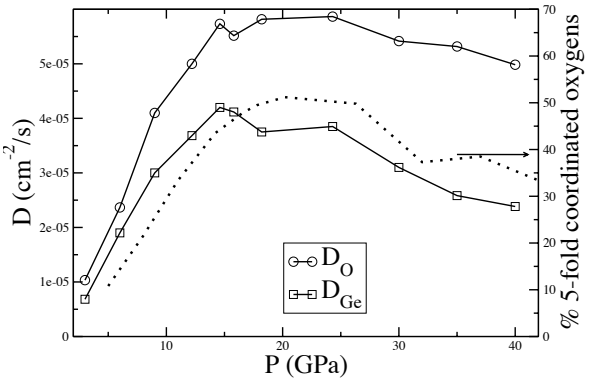

Figure C.4: *Simulated diffusion coefficients on liquid (T = 4000 K) germania and percentage of GeO_5 units as a function of increasing pressure.*

In figure C.4 we show the oxygen and germanium self diffusion coefficients as a function of increasing pressure for liquid germania at 4000 K. It can be seen that the diffusion coefficient exhibits the same anomalous maximum in the P = 15-25 GPa range as observed in other tetrahedral-network materials (like silica and water [145]). In the case of liquid silicates, it was unambiguously shown by Angell *et al.* that such a pressure enhancement of ion mobilities was linked to the formation of fivefold coordinated silicon ions, which act as defects in the original tetrahedral network structure. [165]. The proportion of GeO_5 polyhedra with each coordination number is shown on figure C.4, and we can see that its variation with pressure matches exactly the variation of the diffusion coefficients, in agreement with the silica situation.

C.6 Conclusions

In this work we used a new polarisable interaction potential to study the high pressure behaviour of glassy and liquid germania. For glassy germania, we were able to reproduce all the experimental structural information by making comparisons at the same density. The density-evolution of the Ge-O coordination number, bond distance, X-ray and neutron structure factors was in good agreement with the data from refs. [148, 151, 152]. The only observed shortcoming was the inability of our simulations to properly reproduce the equation of state for glassy germania. This is most likely due to the relatively short time-scale available to computer simulations. From our data and from a comparison with the available experimental evidence, it can be concluded that the transition from a tetrahedral to an octahedral glass is smooth and gradual and probably not completed at pressures as high as 15 GPa. Also, a study of the percentage concentration of GeO_4, GeO_5, GeO_6 units shows that as density is increased, these are present in different proportions but a state with GeO_5 units only was not observed.

As for liquid germania, our results are mainly predictive due to the lack of experimental data available in this case. We find that liquid germania undergoes a transition from a fourfold- to a sixfold-coordinated phase and that this transition is smoother than the one observed in the glassy phase. Most importantly, we find that the diffusivity in germania behaves anomalously as a function of pressure, showing a maximum in the P = 15-25 GPa range, as found in other tetrahedral-network liquid such as silica and water. The cause of this behaviour is traced back to the presence of pentahedrally-coordinated Ge ions.

Acknowledgements

The authors wish to thank Marco Vaccari for sending us the EXAFS data on germania and Philip Salmon for providing us with his neutron data and for fruitful discussions. DM thanks the Moray Endowment Fund of the University of Edinburgh for the purchase of a workstation. DM also wishes to thank the EPSRC, School of Chemistry, University of Edinburgh, and the STFC CMPC for his PhD funding.

The work has been performed under the HPC-EUROPA2 project (project number: 228398) with the support of the European Commission - Capacities Area - Research Infrastructures.

Bibliography

[1] S. Hull. *Reports on Progress in Physics*, 67:1233–1314, 2004.

[2] JW Fergus. The application of solid fluoride electrolytes in chemical sensors. *Sensors and actuators B-Chemical*, 42(2):119–130, JUL 31 1997.

[3] JW Fergus. The application of solid fluoride electrolytes in chemical sensors. *Surface and Coatings Technology*, 108:73–79, 1998.

[4] BCH Steele and A Heinzel. Materials for fuel-cell technologies. *Nature*, 414(6861):345–352, NOV 15 2001.

[5] RM Ormerod. Solid oxide fuel cells. *Chemical Society Review*, 32(1):17–28, JAN 2003.

[6] Kyocera. Info available on www.kyocera.co.uk/.

[7] J.P Goff, W. Haynes, S. Hull, M.T. Hutchings, and K.N Clausen. Defect structure of yttria-stabilized zirconia and its influence on the ionic conductivity at elevated temperatures. *Phys. Rev. B*, 59:14202, 1999.

[8] A. Bogicevic and C. Wolverton. Nature and strength of defect interactions in cubic stabilized zirconia. *Phys. Rev. B*, 67:024106, 2003.

[9] R. Car and M. Parrinello. Unified approach for molecular dynamics and density-functional theory. *Phys. Rev. Lett.*, 55(22):2471–2474, 1985.

[10] P.W. Fowler and P.A. Madden. In-crystal polarizabilities of alkali and halide ions. *Phys. Rev. B*, 29(2):1035–1042, 1984.

[11] P.W. Fowler and P.A. Madden. Fluctuating dipoles and polarizabilities in ionic materials: calculations on LiF. *Phys. Rev. B*, 31(8):5443–5455, 1985.

[12] P.W. Fowler, P.J. Knowles, and N.C. Pyper. Calculations of 2-body and 3-body dispersion coefficients for ions in crystals. *Mol. Phys.*, 56(1):83–95, 1985.

[13] P.A. Madden, R. Heaton, A. Aguado, and S. Jahn. From first-principles to material properties. *J. Mol. Struct.: THEOCHEM*, 771:9–18, 2006.

[14] A Aguado, M Wilson, and PA Madden. Molecular dynamics simulations of the liquid-vapor interface of a molten salt. i. influence of the interaction potential. *Journal of Chemical Physics*, 115(18):8603–8611, NOV 2001.

[15] A Aguado, M Wilson, and PA Madden. Molecular dynamics simulations of the liquid-vapor interface of a molten salt. I. Influence of the interaction potential. *Journal of Chemical Physics*, 115(18):8603–8611, NOV 2001.

[16] A Aguado and PA Madden. Molecular dynamics simulations of the liquid-vapor interface of a molten salt. III. Size asymmetry effects and binary mixtures. *Journal of Chemical Physics*, 117(16):7659–7668, OCT 22 2002.

[17] R.J. Heaton, R. Brookes, P.A. Madden, M. Salanne, C. Simon, and P. Turq. A first-principles description of liquid BeF_2 and its mixtures with LiF: 1. potential development and pure BeF_2. *J. Phys. Chem. B*, 110(23):11454–11460, 2006.

[18] M Wilson, PA Madden, NC Pyper, and JH Harding. Molecular dynamics simulations of compressible ions. *Journal of Chemical Physics*, 104(20):8068–8081, MAY 22 1996.

[19] M Wilson, S Jahn, and PA Madden. The construction and application of a fully flexible computer simulation model for lithium oxide. *Journal of Physics: Condensed Matter*, 16(27):S2795–S2810, JUL 14 2004.

[20] S. Jahn and P.A. Madden. Modeling Earth materials from crustal to lower mantle conditions: a transferable set of interaction potentials for the CMAS system. *Phys. Earth Planet. Inter.*, 162:129–139, 2007.

[21] JH Lee and M Yoshimura. Phase stability and electrical conductivity of the $Zr_{0.5}Y_{0.5}O_{1.75}$-$Y_{0.75}Nb_{0.25}O_{1.75}$ system. *Solid State Ionics*, 124(1-2):185–191, SEP 1999.

[22] JTS Irvine, AJ Feighery, DP Fagg, and S Garcia-Martin. Structural studies on the optimisation of fast oxide ion transport. *Solid State Ionics*, 136(Sp. Iss. SI):879–885, NOV 2000. 12th International Conference on Solid State Ionics, Halkidiki, Greece, JUN 06-12, 1999.

[23] Y Arachi, H Sakai, O Yamamoto, Y Takeda, and N Imanishai. Electrical conductivity of the ZrO_2-Ln_2O_3 (Ln = lanthanides) system. *Solid State Ionics*, 121(1-4):133–139,

JUN 1999. 11th International Conference on Solid State Ionics (SSI-11), HONOLULU, HAWAII, NOV 16-21, 1997.

[24] S.T. Norberg, S. Hull, Li Peng, JR Irvine, D. Marrocchelli, and P.A. Madden. Structural disorder in doped zirconia, part i: Oxygen vacancy order in $Zr_{0.8}(Sc/Y)_{0.2}O_{1.9}$ investigated by neutron total scattering and moleculardynamics. *to be submitted to Journal of Material Chemistry*, 2010.

[25] Subbarao E C and Ramakrishnan T V. *Fast Ion Transport in Solids*. John Wiley & Sons, Inc., 1979.

[26] A Nakamura and JB Wagner. Defect structure, ionic conductivity and diffusion in yttria stabilized zirconia ad related oxide electrolytes with fluorite structure. *Journal of the Electrochemical Society*, 133(8):1542–1548, AUG 1986.

[27] MS Khan, MS Islam, and DR Bates. Cation doping and oxygen diffusion in zirconia: a combined atomistic simulation and molecular dynamics study. *Journal of Materials Chemistry*, 8(10):2299–2307, OCT 1998.

[28] F. Pietrucci, M. Bernasconi, A. Laio, and M. Parrinello. Vacancy-vacancy interaction and oxygen diffusion in stabilized cubic ZrO_2 from first principles. *Physical Review B*, 78(9), SEP 2008.

[29] JM Tarascon and M Armand. Issues and challenges facing rechargeable lithium batteries. *Nature*, 414(6861):359–367, NOV 15 2001.

[30] R.W.G. Wyckoff. *Crystal Structures*. Interscience, New York, 1963.

[31] G. Teufer. Crystal structure of tetragonal ZrO_2. *Acta Crystallogr.*, (15):1187, 1962.

[32] T. H. Etsell and S. N. Flengas. Electrical properties of solid oxide electrolytes. *Chem. Rev.*, (70):339, 1970.

[33] Several Authors. *High-temperature solid oxide fuel cells [electronic resource] : fundamentals, design, and applicatons*. John Wiley & Sons, Inc., 2003.

[34] M. O. Zacate, L. Minervini, D. J. Bradfield, R. W. Grimes, and K. E. Sickafus. Defect cluster formation in M_2O_3-doped cubic ZrO_2. *Solid State Ionics*, (128):243, 1999.

[35] H. Morikawa, Y. Shimizugawa, F. Marumo, T. Harasawa, H. Ikawa, K. Tohji, and Y Udegawa. Local structures around Y-atoms in Y_2O_3-stabilized tetragonal ZrO_2. *J. Jpn. Ceram. Soc.*, (96):253, 1988.

[36] Z. J. Shen, T. K. Li, K. Q. Lu, and Y. Q. Zhao. *Giusuanyan Xuebao / Journal of Chinese Ceramic Society*, (16):270, 1988.

[37] M. H. Tuilier, J. Dexpert-Ghys, H. Dexpert, and P. Lagarde. X-ray absorption study of the ZrO_2- Y_2O_3 system. *J. Solid State Chem.*, (69):153, 1987.

[38] X. Li and B Hafskjold. Molecular-dynamics simulations of yttrium-stabilized zirconia. *J. Phys. Condens. Matt.*, (7):1255, 1995.

[39] P. Li, I-W. Chen, and J. E. Penner-Hahn. X-ray-absorption studies of zirconia polymorphs. ii. effect of Y_2O_3 dopant on ZrO_2 structure. *Phys. Rev B*, (48):10074, 1993.

[40] C. R. A. Catlow, A. V. Chadwick, G. N. Greaves, and L. M. Moroney. Exafs study of yttria-stabilized zirconia. *J. Am. Ceram. Soc.*, (69):272, 1986.

[41] M. Cole, C. R. A. Catlow, and J. P. Dragun. Exafs studies of doped-ZrO_2 systems. *J. Phys. Chem. Solids*, (51):507, 1990.

[42] F. Shimojo, T. Okabe, F. Tachibana, M. Kobayashi, and H. Okazaki. Molecular-dynamics studies of yttria stabilized zirconia .1. structure and oxygen diffusion. *J. Phys. Soc. Jpn.*, (61):2848, 1992.

[43] R Miida, F Sato, M Tanaka, H Naito, and H Arashi. Locally modulated structures of fluorite-related Y_2O_3-Nb_2O_5 solid solutions. *Journal of Applied Crystallography*, 30(Part 3):272–279, JUN 1 1997.

[44] S Garcia-Martin, M. A. Alario-Franco, D. P. Fagg, A. J. Feighery, and J. T. S. Irvine. Modulated fluorite type structure of materials from the (1-x)$Y_2Zr_2O_7$ -xY_3NBO_3. *Chem. Mater.*, 12:1729, 2000.

[45] S Garcia-Martin, MA Alario-Franco, DP Fagg, and JTS Irvine. Evidence of three types of short range ordered fluorite structure in the (1-x) $Y_{0.15}Zr_{0.85}O_{1.93}$-x $Y_{0.75}Nb_{0.25}O_{1.75}$ ($0 \leq x \leq 1$) system. *Journal of Material Chemistry*, 15(19):1903–1907, 2005.

[46] John T. S. Irvine, Jeremy W. L. Dobson, Tatiana Politova, Susana Garcia Martin, and Atef Shenouda. Co-doping of scandia-zirconia electrolytes for SOFCs. *Faraday Discussions*, 134:41–49, 2007. Meeting on Atomic Transport and Defect Phenomena in Solids, Guildford, England, JUL 10-12, 2006.

[47] M. Kilo, C. Argirusis, G. Borchardt, and R. A. Jackson. Oxygen diffusion in yttria stabilised zirconia - experimental results and molecular dynamics calculations. *Phys. Chem. Chem. Phys.*, (5):2119, 2003.

[48] R Krishnamurthy, YG Yoon, DJ Srolovitz, and R Car. Oxygen diffusion in yttria-stabilized zirconia: A new simulation model. *Journal of the American Ceramic Society*, 87(10):1821–1830, OCT 2004.

[49] Devanathan R., Weber W. J., Singhal S. C., and Gale J. D. Computer simulation of defects and oxygen transport in yttria-stabilized zirconia. *Solid State Ionics*, 177(15-16):1251–1258, JUN 15 2006.

[50] Devanathan R, Thevuthasan S, and Gale J D. Defect interactions and ionic transport in scandia stabilised zirconia. *Phys Chem Chem Phys*, 11:5506–11, 2009.

[51] Kai-Shiun Chang and Kuo-Lun Tung. Oxygen-Ion Transport in a Dual-Phase Scandia-Yttria-Stabilized Zirconia Solid Electrolyte: A Molecular Dynamics Simulation. *Chem-Phys-Chem*, 10(11):1887–1894, AUG 3 2009.

[52] N Sawaguchi and H Ogawa. Simulated diffusion of oxide ions in $YO_{1.5}$-ZrO_2 at high temperature. *Solid State Ionics*, 128(1-4):183–189, FEB 2000.

[53] R Pornprasertsuk, P Ramanarayanan, CB Musgrave, and FB Prinz. Predicting ionic conductivity of solid oxide fuel cell electrolyte from first principles. *Journal of Applied Physics*, 98(10), NOV 15 2005.

[54] Manfred Martin. On the ionic conductivity of strongly acceptor doped, fluorite-type oxygen ion conductors. *Journal of Electroceramics*, 17(2-4):765–773, DEC 2006. 2nd International Conference on Electroceramics (ICE-2005), Seoul, South Korea, JUN 12-16, 2005.

[55] Kazuhisa Sato, Ken Suzuki, Keiji Yashiro, Tatsuya Kawada, Hiroo Yugami, Toshiyuki Hashida, Alan Atkinson, and Junichiro Mizusaki. Effect of Y_2O_3 addition on the conductivity and elastic modulus of $(CeO_2)(1\text{-}x)(YO_1.5)(x)$. *Solid State Ionics*, 180(20-22):1220–1225, AUG 17 2009.

[56] TI Politova and JTS Irvine. Investigation of scandia-yttria-zirconia system as an electrolyte material for intermediate temperature fuel cells-influence of yttria content in system$(Y_2O_3)(x)(Sc_2O_3)((11\text{-}x))(ZrO_2)(89)$. *Solid State Ionics*, 168(1-2):153–165, MAR 15 2004.

[57] M Yashima, M Kakihana, and M Yoshimura. Metastable-stable phase diagrams in the zirconia-containing systems utilized in solid-oxide fuel cell application. *Solid State Ionics*, 86-8(Part 2):1131–1149, JUL 1996. 10th International Conference on Solid State Ionics (SSI-10), Singapore, Singapore, Dec 03-08, 1995.

[58] K. R. Whittle, L. M. D. Cranswick, S. A. T. Redfern, I. P. Swainson, and G. R. Lumpkin. Lanthanum pyrochlores and the effect of yttrium addition in the systems La_2-xYxZr_2O_7 and La_2-xYxHf_2O_7. *J. Solid State Chem.*, 79:104203, 2009.

[59] RD Shannon. Revised effective ionic-radii and systematic studies of interatomic distances in halides and chalcogenides. *Acta Crystallographica Section A*, 32(SEP1):751–767, 1976.

[60] M Mogensen, T Lindegaard, UR Hansen, and G Mogensen. Physical-properties of mixed conductor solid oxide fuel-cell anodes of doped CeO_2. *Journal of the Electrochemical Society*, 141(8):2122–2128, AUG 1994.

[61] T Ishihara, JA Kilner, M Honda, and Y Takita. Oxygen surface exchange and diffusion in the new perovskite oxide ion conductor $LaGaO_3$. *Journal of the American Chemical Society*, 119(11):2747–2748, MAR 19 1997.

[62] T Ishihara, JA Kilner, M Honda, N Sakai, H Yokokawa, and Y Takita. Oxygen surface exchange and diffusion in $LaGaO_3$ based perovskite type oxides. *Solid State Ionics*, 113(Sp. Iss. SI):593–600, DEC 1998. 11th International Conference on Solid State Ionics (SSI-11), Honolulu, HI, NOV 16-21, 1997.

[63] A Christensen and EA Carter. Adhesion of ultrathin ZrO_2(111) films on Ni(111) from first principles. *Journal of Chemical Physics*, 114(13):5816–5831, APR 1 2001.

[64] R.J. Heaton. *From first-principles to material properties*. PhD thesis, University of Oxford, 2007.

[65] P.A. Madden and M. Wilson. "Covalent" effects in 'ionic' systems. *Chem. Soc. Rev.*, 25(5):339–350, 1996.

[66] F.G. Fumi and M.P. Tosi. Ionic sizes and born repulsive parameters in the NaCl-type alkali halides - I. *J. Phys. Chem. Solids*, 25:31–43, 1964.

[67] MP Tosi and FG Fumi. Ionic sizes and born repulsive parameters in NaCl-type alkali halides - II generalized. *Journal of Physics and Chemistry of Solids*, 25(1):45–&, 1964.

[68] van Beest B. W. H., Kramer G. J., and van Santen R. A. Force fields for silicas and aluminophosphates based on ab initio calculations. *Phys. Rev. Lett.*, 64(16):1955–1958, Apr 1990.

[69] R.D. Oeffner and S.R. Elliott. Interatomic potential for germanium dioxide empirically fitted to an *ab initio* energy surface. *Phys. Rev. B*, 58(22):14791–14803, 1998.

[70] Lindsay Foy. *Developing Interaction Potentials from First Principles*. PhD thesis, University of Edinburgh, 2008.

[71] A.D. Buckingham. Permanent and induced molecular moments and long-range intermolecular forces. *Adv. Chem. Phys.*, 12:107, 1967.

[72] PW Fowler and PA Madden. In-crystal polarizability of O^{2-}. *Journal of Physical Chemistry*, 89(12):2581–2585, 1985.

[73] Dick BG and Overhauser AW. Theory of the dielectric constants of alkali halide crystals. *Phys. Rev.*, (112):90, 1958.

[74] M.J. Castiglione, M. Wilson, and P.A. Madden. Polarization effects in the simulation of lead (II) fluoride. *J. Phys.: Condens. Matter*, 11:9009–9024, 1999.

[75] A.J. Stone. *Theory of intermolecular forces*. Oxford University Press, Oxford, 1996.

[76] M Wilson, U Schonberger, and MW Finnis. Transferable atomistic model to describe the energetics of zirconia. *Physical Review B*, 54(13):9147–9161, OCT 1 1996.

[77] A Dwivedi and AN Cormack. A computer-simulation study of the defect structure of calcia-stabilized zirconia. *Phylosofical Magazine A - Physics of Condensed Matter Structure Defects and Mechanical Properties*, 61(1):1–22, JAN 1990.

[78] GV Lewis and CRA Catlow. Potential models for ionic oxides. *Journal of Physics C-Solid State Physics*, 18(6):1149–1161, 1985.

[79] R.J. Heaton, P.A. Madden, S.J. Clark, and S. Jahn. Condensed phase ionic polarizabilities from plane wave density functional theory calculations. *J. Chem. Phys.*, 125:144104, 2006.

[80] M. Salanne, R. Vuilleumier, P. A. Madden, C. Simon, P. Turq, and B. Guillot. Polarizabilities of individual molecules and ions in liquids from first principles. *Journal of Physics: Condensed Matter*, 20(49, Sp. Iss. SI), DEC 10 2008. 7th Liquid Matter Conference, Lund, Sweden, JUN 27-JUL 01, 2008.

[81] F. James. *Minuit. CERN Program Library Long Writeup D506.*

[82] Talat S Rahman. Computational methodologies for designing materials. *Journal of Physics: Condensed Matter*, 21(8):080301, 2009.

[83] Jorge Kohanoff. *Electronic Structure Calculations for Solids and Molecules*. Cambridge University Press, 2006.

[84] M.D. Segall, P.J.D. Lindan, M.J. Probert, C.J. Pickard, P.J. Hasnip, S.J. Clark, and M.C. Payne. First-principles simulation: ideas, illustrations and the castep code. *J. Phys.: Condens. Matter*, 14(11):2717–2744, 2002.

[85] The CPMD consortium. *CPMD Version 3.x, http://www.cpmd.org.* MPI Für Festkörperforschung and the IBM Zurich Research Laboratory.

[86] N. W. Ashcroft and D. N. Mermin. *Solid State Physics*. Brooks/Cole: Thomson Learning, 1976.

[87] Nicola Marzari and David Vanderbilt. Maximally localized generalized wannier functions for composite energy bands. *Phys. Rev. B*, 56(20):12847–12865, Nov 1997.

[88] A. Aguado, L. Bernasconi, S. Jahn, and P.A. Madden. Multipoles and interaction potentials in ionic materials from planewave-DFT calculations. *Faraday Discuss.*, 124:171–184, 2003.

[89] M. P. Allen and D. J. Tildesley. *Computer simulation of Liquids*. Oxford Science Publications, 1989.

[90] S. Nosé. A molecular dynamics method for simulations in the canonical ensemble. *Mol. Phys.*, 52:255–268, 1984.

[91] S. Nosé. A unified formulation of the constant temperature molecular dynamics methods. *J. Chem. Phys.*, 81(1):511–519, 1984.

[92] W.G. Hoover. Canonical dynamics: equilibrium phase-space distributions. *Phys. Rev. A*, 31(3):1695–1697, 1985.

[93] G.J. Martyna, M.L. Klein, and M. Tuckerman. Nosé-Hoover chains: the canonical ensemble via continuous dynamics. *J. Chem. Phys.*, 97(4):2635–2643, 1992.

[94] G.J. Martyna, D. Tobias, and M.L. Klein. Constant pressure molecular dynamics algorithms. *J. Chem. Phys.*, 101(5):4177–4189, 1994.

[95] D. Frenkel and B. Smit. *Understanding Molecular Simulations: From Algorithms to Applications*. Academic Press, 2002.

[96] P. Ewald. Evaluation of optical and electrostatic lattice potentials. *Ann. Phys.*, 64:253, 1921.

[97] A. Aguado and P.A. Madden. Ewald summation of electrostatic multipole interactions up to the quadrupolar level. *J. Chem. Phys.*, 119(14):7471–7483, 2003.

[98] M. Castiglione. *Computer Simulation of Superionic Fluorites*. PhD thesis, University of Oxford, 2000.

[99] M.J. Castiglione and P.A. Madden. Fluoride ion disorder and clustering in superionic PbF_2. *J. Phys.: Condens. Matter*, 13(44):9963, 2001.

[100] A Kahnharari, L Mzerolles, D Michel, and F Robert. Structural description of La_3NbO_7. *Journal of Solid State Chemistry*, 116(1):103–106, APR 1995.

[101] Koutaro Kawata, Hideki Maekawa, Takahiro Nemoto, and Tsutomu Yamamura. Local structure analysis of YSZ by Y-89 MAS-NMR. *Solid State Ionics*, 177(19-25):1687–1690, OCT 15 2006. 15th International Conference on Solid State Ionics, Baden Baden, Germany, 2005.

[102] Many. OPIUM package available on http://opium.sourceforge.net/.

[103] S.T. Norberg, I. Ahmed, S. Hull, D. Marrocchelli, and P.A. Madden. Local structure and ionic conductivity in the $Zr_2Y_2O_7$-Y_3NbO_7 system. *J. Phys.: Condens. Matter*, 2009.

[104] WC Mackrodt and PM Woodrow. Theoretical estimates of point-defect energies in cubic zirconia. *Journal of the American Chemical Society*, 69(3):277–280, MAR 1986.

[105] PW Fowler, JH Harding, and NC Pyper. The polarizabilities and dispersion coefficients for ions in the solid group-iv oxides. *Journal of Physics: Condensed Matter*, 6(48):10593–10606, NOV 28 1994.

[106] JH Lee and M Yoshimura. Phase relationship and electrical conductivity in the ZrO_2-$Y_{0.75}Nb_{0.25}O_{1.75}$ system. *Solid State Ionics*, 139(3-4):197–203, FEB 2001.

[107] Stefan T. Norberg, Matthew G. Tucker, and Stephen Hull. Bond valence sum: a new soft chemical constraint for RMCProfile. *Journal of Applied Crystallography*, 42(Part 2):179–184, APR 2009.

[108] K Kato. Structure refinement of h-Nb_2O_5. *Acta Crystallographica Section B - Structural Science*, 32(MAR15):764–767, 1976.

[109] TS Ercit. Refinement of the structure of zeta-Nb_2O_5 and its relationship to the rutile and theoreaulite structures. *Mineralogy and Petrology*, 43(3):217–223, FEB 1991.

[110] M. Saiful Islam and Peter R. Slater. Solid-State Materials for Clean Energy: Insights from Atomic-Scale Modeling. *MRS Bulletin*, 34(12):935–941, DEC 2009.

[111] D. Marrocchelli, M. Salanne, P.A. Madden, C. Simon, and P. Turq. The construction of a reliable potential for GeO_2 from first principles. *Mol. Phys.*, 107(4–6):443–452, 2009.

[112] SH Wei, LG Ferreira, JE Bernard, and A Zunger. Electronic-properties of random alloys - special quasirandom structures. *Physical Review B*, 42(15):9622–9649, NOV 15 1990.

[113] Chao Jiang, C. R. Stanek, K. E. Sickafus, and B. P. Uberuaga. First-principles prediction of disordering tendencies in pyrochlore oxides. *Physical Review B*, 79(10), MAR 2009.

[114] Dario Marrocchelli. First-principles interaction potentials for ionic systems. *HPC Europa Report*, page 115, 2008. available on www.hpc-europa.eu/files/SSCinEurope/CD2008/contents/027-chemi.pdf.

[115] Peter Atkins and Julio de Paula. *Physical Chemistry*. Oxford University Press, 2006.

[116] Chris E. Mohn, Svein Stolen, Stefan T. Norberg, and Stephen Hull. Oxide-Ion Disorder Within the High Temperature delta Phase of Bi_2O_3. *Physics Review Letters*, 102(15), APR 17 2009.

[117] N Sata, K Eberman, K Eberl, and J Maier. Mesoscopic fast ion conduction in nanometre-scale planar heterostructures. *Nature*, 408(6815):946–949, DEC 21 2000.

[118] DC Sayle, JA Doig, SC Parker, and GW Watson. Synthesis, structure and ionic conductivity in nanopolycrystalline BaF2/CaF2 heterolayers. *CHEMICAL COMMUNICATIONS*, (15):1804–1806, 2003.

[119] DC Sayle, JA Doig, SC Parker, GW Watson, and TXT Sayle. Computer aided design of nano-structured materials with tailored ionic conductivities. *PHYSICAL CHEMISTRY CHEMICAL PHYSICS*, 7(1):16–18, 2005.

[120] X. X. Guo, I. Matei, J.-S. Lee, and J. Maier. Ion conduction across nanosized CaF_2/BaF_2 multilayer heterostructures. *Applied Physics Letters*, 91(10), SEP 3 2007.

[121] J. Garcia-Barriocanal, A. Rivera-Calzada, M. Varela, Z. Sefrioui, E. Iborra, C. Leon, S. J. Pennycook, and J. Santamaria. Colossal Ionic Conductivity at Interfaces of Epitaxial ZrO_2:Y_2O_3/$SrTiO_3$ Heterostructures. *Science*, 321(5889):676–680, 2008.

[122] Akihiro Kushima and Bilge Yildiz. Role of lattice strain and defect chemistry on the oxygen vacancy migration at the (8.3% Y_2O_3-ZrO_2) / $SrTiO_3$ hetero-interface: A first principles study. *ECS Transactions*, 25(2):1599, 2009.

[123] M. Micoulaut, L. Cormier, and G.S. Henderson. The structure of amorphous, crystalline and liquid GeO_2. *J. Phys.: Condens. Matter*, 18:R753–R784, 2006.

[124] F.L. Galeener, A.J. Leadbetter, and M.W. Stringfellow. Comparison of the neutron, Raman, and infrared vibrational spectra of vitreous SiO_2, GeO_2 and BeF_2. *Phys. Rev. B*, 27(2):1052–1078, 1983.

[125] E.I. Kamitsos, Y.D. Yiannopoulos, M.A. Karakassides, G.D. Chryssikos, and H. Jain. Raman and infrared structural investigation of $x\mathrm{Rb_2O}.(1-x)\mathrm{GeO_2}$ glasses. *J. Phys. Chem.*, 100(28):11755–11765, 1996.

[126] P.V. Teredesai, D.T. Anderson, N. Hauser, K. Lantzky, and J.L. Yarger. Infrared spectroscopy of germanium dioxide (GeO_2) glass at high pressure. *Phys. Chem. Glasses*, 46(4):345–349, 2005.

[127] P.S. Salmon, A.C. Barnes, R.A. Martin, and G.J. Cuello. Glass fragility and atomic ordering on the intermediate and extended range. *Phys. Rev. Lett.*, 96(23):235502, 2006.

[128] P.S. Salmon, A.C. Barnes, R.A. Martin, and G.J. Cuello. Structure of glassy GeO_2. *J. Phys.: Condens. Matter*, 19(41):415110, 2007.

[129] M. Micoulaut, Y. Guissani, and B. Guillot. Simulated structure and thermal properties of glassy and liquid germania. *Phys. Rev. E*, 73(031504), 2006.

[130] Joaquin Peralta, Gonzalo Gutierrez, and Jose Rogan. Structural and vibrational properties of amorphous GeO2: a molecular dynamics study. *Journal of Physics: Condensed Matter*, 20(14), APR 9 2008.

[131] L. Giacomazzi, P. Umari, and A. Pasquarello. Medium-range structural properties of vitreous germania obtained through first-principles analysis of vibrational spectra. *Phys. Rev. Lett.*, 95(7):075505, 2005.

[132] L. Giacomazzi, P. Umari, and A. Pasquarello. Vibrational spectra of vitreous germania from first-principles. *Phys. Rev. B*, 74(15):155208, 2006.

[133] M. Hawlitzky, J. Horbach, S. Ispas, M. Krack, and K. Binder. Comparative classical and 'ab initio' molecular dynamics study of molten and glassy germanium dioxide. *Journal of Physics: Condensed Matter*, 20(28), JUL 16 2008.

[134] P. Tangney and S. Scandolo. An *ab initio* parametrized interatomic force field for silica. *J. Chem. Phys.*, 117(19):8898–8904, 2002.

[135] M. Salanne, R. Vuilleumier, P.A. Madden, C. Simon, P. Turq, and B. Guillot. Polarizabilities of individual molecules and ions in liquids from first principles. *J. Phys.: Condens. Matter*, 20(49):494207, 2008.

[136] M. Wilson, S. Jahn, and P.A. Madden. The construction and application of a fully flexible computer simulation model for lithium oxide. *J. Phys.: Condens. Matter*, 16(27):S2795–S2810, 2004.

[137] T. Tokuda and W.D. Kingery. Oxygen diffusion and vaporization rates for liquid and solid germanium dioxide. *J. Appl. Phys.*, 34:2104–2105, 1963.

[138] M. Wilson, P.A. Madden, M. Hemmati, and C.A. Angell. Polarization effects, network dynamics, and the infrared spectrum of amorphous SiO_2. *Phys. Rev. Lett.*, 77(19):4023–4026, 1996.

[139] J.M. Caillol, D. Levesque, and J.J. Weis. Electrical properties of polarizable ionic solutions. I. Theoretical aspects. *J. Chem. Phys.*, 91(9):5544–5554, 1989.

[140] J.M. Caillol, D. Levesque, and J.J. Weis. Electrical properties of polarizable ionic solutions. II. Computer simulation results. *J. Chem. Phys.*, 91(9):5555–5566, 1989.

[141] E.A. Pavlatou, P.A. Madden, and M. Wilson. The interpretation of vibrational spectra of ionic melts. *J. Chem. Phys.*, 107(24):10446–10457, 1997.

[142] K. Trachenko, V.V. Brazhkin, G. Ferlat, M.T. Dove, and E. Artacho. First-principles calculations of structural changes in B_2O_3 glass under pressure. *Phys. Rev. B*, 78:172102, 2008.

[143] S. Jahn and P.A. Madden. Structure and dynamics in liquid alumina: simulations with an ab initio interaction potential. *J. Non-Cryst. Solids*, 353(32–40):3500–3504, 2007.

[144] C.A. Angell. Formation of glasses from liquids and biopolymers. *Science*, (267):1924, 1995.

[145] P.F. McMillan and M.C. Wilding. High pressure effects on liquid viscosity and glass transition behaviour, polymorphic phase transitions and structural properties of glasses and liquids. *J. Non-Cryst. Solids*, (355):722, 2009.

[146] M. Wilding, M. Guthrie, C.L. Bull, M.G. Tucker, and P.F. McMillan. (feasibility of in situ neutron diffraction studies of non-crystalline silicates up to pressures of 25 gpa. *J. Phys.: Condens. Matter*, (20):244122.

[147] J.P. Itie, A. Polian, G. Calas, J. Petiau, A. Fontaine, and H. Tolentino. Pressure-induced coordination changes in crystalline and vitreous GeO_2. *Phys. Rev. Lett.*, 63(4):398–401, 1989.

[148] M. Vaccari, G. Aquilanti, S. Pascarelli, and O. Mathon. A new EXAFS investigation of local structural changes in amorphous and crystalline GeO_2 at high pressure. *J. Phys.: Condens. Matter*, 21(12):145403, 2009.

[149] Xinguo Hong, Matthew Newville, Vitali B. Prakapenka, Mark L. Rivers, and Stephen R. Sutton. High quality x-ray absorption spectroscopy measurements with long energy range at high pressure using diamond anvil cell. *REVIEW OF SCIENTIFIC INSTRUMENTS*, 80(7), JUL 2009.

[150] M. Baldini, G. Aquilanti, H-k. Mao, W. Yang, G. Shen, S. Pascarelli, and W. L. Mao. High-pressure EXAFS study of vitreous GeO_2 up to 44 GPa. *Phys. Rev. B*, 81(2):024201, Jan 2010.

[151] M. Guthrie, C.A. Tulk, C.J. Benmore, J. Xu, J.L. Yarger, D.D. Klug, J.S. Tse, H k. Mao, and R.J. Hemley. Formation and structure of a dense octahedral glass. *Phys. Rev. L*, (93):115502, 2004.

[152] J.W.E. Drewitt, P. Salmon, A.C. Barnes, S. Klotz H.E., Fisher, and W.A. Crichton. Structure of GeO_2 glass at pressures up to 8.6 GPa. *Phys. Rev. B*, (81):014202.

[153] Y. Okamoto. Xafs simulation of highly disordered materials. *Nucl. Instr. Meth. Phys. Res. A*, 526:572–583, 2004.

[154] Adriano Filipponi and Andrea Di Cicco. X-ray-absorption spectroscopy and n-body distribution functions in condensed matter. ii. data analysis and applications. *Phys. Rev. B*, 52(21):15135–15149, Dec 1995.

[155] P.S. Salmon. Decay of the pair correlations and small-angle scattering for binary liquids and glasses. *J. Phys.: Condens. Matter*, 18(50):11433–11444, 2006.

[156] M. Micoulaut. Structure of densified amorphous germanium dioxide. *J. Phys.: Condens. Matter*, 16:L131–L138, 2004.

[157] G. Gutierrez and J. Rogen. Structure of liquid GeO_2 from a computer simulations model. *Phys. Rev. E*, (69):031201, 2004.

[158] V.V. Hoang. Static and dynamic properties of simulated liquid and amorphous GeO_2. *J. Phys.: Condens. Matter*, (18):777, 2006.

[159] K.V. Shanavas, N. Garg, and S.M. Sharma. Classical molecular dynamics simulations of behaviour of GeO_2 under high pressures and at high temperatures. *Phys. Rev.* **E**, (73):094120, 2006.

[160] V Hung, L.T. Vinh, and D M Nghiep. Computer simulation of GeO_2 liquid. *J. Non-Cryst. Solids*, (353):2163, 2007.

[161] V.V. Hoang, N.H. Tuan Anh, and H. Zung. Liquid-liquid phase transition and anomalous diffusion in simulated liquid GeO_2. *Physica* **B**, (390):17, 2007.

[162] P. K. Hung, L. T. Vinh, N. T. Nhan, N. V. Hong, and T. V. Mung. Local structure of liquids Al2O3 and GeO2 under densification. *Journal of Non-crystalline solids*, 354(26):3093–3097, MAY 15 2008.

[163] Ting Li, Shiping Huang, and Jiqin Zhu. The structure and void analysis of pressure-induced amorphous GeO_2: Molecular dynamics simulation. *Chemical Physics Letters*, 471(4-6):253–257, MAR 26 2009.

[164] X. F. Zhu and L. F. Chen. First-principles molecular dynamics simulations of the structure of germanium dioxide under pressures. *Physica B - Condensed Matter*, 404(21):4178–4184, NOV 15 2009.

[165] C.A. Angell, P.A. Cheesman, and S. Tamaddon. Pressure enhancement of ion mobilities in liquid silicates from computer simulation studies to 800 kilobars. *Science*, (218):885, 1982.

[166] S.K Sharme, D. Virgo, and I. Kushiro. Relationship between density, viscosity and structure of GeO_2 melts at low and high pressures. *J. Non-Cryst. Solids*, (33):235, 1979.

[167] Yunfeng Liang, Caetano R. Miranda, and Sandro Scandolo. Temperature-induced densification of compressed SiO2 glass: A molecular dynamics study. *High Pressure Research*, 28(1):35–44, MAR 2008.

[168] CE Stone, AC Hannon, T Ishihara, N Kitamura, Y Shirakawa, R Sinclair, N Umesaki, and AC Wright. The structure of pressure-compacted vitreous germania. *Journal of non-crystalline solids*, 293:769–775, NOV 2001. 8th International Conference on the Structure on Non-Crystalline Materials (NCM 8), ABERYSTWYTH, WALES, AUG 06-11, 2000.

[169] X. Hong, G. Shen, V. B. Prakapenka, M. Newville, M. L. Rivers, and S. R. Sutton. Intermediate states of geo_2 glass under pressures up to 35 gpa. *Phys. Rev. B*, (75):104201, 2007.

[170] K. H. Smith, E. Shero, A. Chizmeshya, and G. H. Wolf. The equation of state of polyamorphic germania glass - a 2-domain description of the viscoelastic response. *J. Chem. Phys.*, (102):6851, 1995.

[171] O. B. Tsiok, V. V. Brazhkin, A. G. Lyapin, , and L. G. Khvostantsev. Logarithmic kinetics of the amorphous-amorphous transformations in sio_2 and geo_2 glasses under high-pressure. *Phys. Rev. L*, (80):999, 1998.

[172] M. Wilson, P.A. Madden, N.N. Medvedev, A. Geigerc, and A. Appelhagenc. Voids in network-forming liquids and their influence on the structure and dynamics. *J. Chem. Soc., Faraday Trans.*, (94):1221, 1998.

[173] D.T. Cromer and J.T.Waber. *International Tables for X-Ray Crystallography, Ibers, J. A., Hamilton, W. C., Eds.; Kynoch Press:Birmingham*, page 71, 1974.

[174] M. Tokonami. Atomic scattering factor for O^{2-}. *Acta Crystallogr.*, (19):486, 1965.